U. S. Department of Energy
1000 Independence Avenue, S.W.
Washington, D.C. 20585

Fiscal Year 2021: Third Quarter

Progress Reports:

Advanced Battery Materials Research (BMR) Program & Battery500 Consortium

Released October 2021
for the period of April – June 2021

Approved by

Tien Q. Duong
Manager, Advanced Battery Materials Research Program & Battery500 Consortium
Batteries & Electrification R&D
Office of Energy Efficiency and Renewable Energy – Vehicle Technologies Office
U.S. Department of Energy

ACKNOWLEDGMENTS

This report has been edited by the following team members:

- **T. A. Zachry,** Energy & Environmental Resources Group
- **Simon Thompson,** U. S. Department of Energy – Vehicle Technologies Office
- **Patricia H. Smith,** Naval Surface Warfare Center – Carderock

TABLE OF CONTENTS

TABLE OF FIGURES

TABLE OF TABLES

A MESSAGE FROM THE MANAGER: ADVANCED BATTERY MATERIALS RESEARCH AND BATTERY500 CONSORTIUM

The Vehicle Technologies Office 2021 Annual Merit Review was held June 21–24, 2021. During this event, the Advanced Battery Materials Research (BMR) and Battery500 Principal Investigators had an opportunity to provide a high-level overview of their project objectives, funding level, and milestones, and to spotlight any technology improvements their Team achieved during the past year. I presented an overview of the BMR program (BAT108) describing its charter and the various technical challenges being addressed, as well as a mini-review of one of our newer technology focus areas: solid-state electrolytes. If you missed the review, a copy of the presentations are available at the following link:

https://www.energy.gov/eere/vehicles/2021-vehicle-technologies-office-amr-presentations-program

This BMR and Battery500 quarterly report provides a more in-depth discussion of the Principal Investigators' activities from April 1, 2021, through June 30, 2021. Here, information regarding experimental procedures, techniques, and findings are described. A list of each project's recent publications is also included for even more detailed information.

A few notable achievements from the BMR investigators this quarter are summarized below:

- Stanford University (Z. Bao and Y. Cui Group) demonstrated that applying a polymer film onto a copper electrode can homogenize the electric field distribution and promote uniform lithium deposition. The polymer was synthesized by tethering an electroactive cation (pyrrolidinium) onto a flexible polymer backbone (polydimethylsiloxane).

- G. Ceder's Team at University of California, Berkeley, used a mathematical model to determine that electronic conductivity in solid electrolytes can lead to metal deposition in voids and cause inhomogeneous plating at the electrode/solid electrolyte interface.

- Argonne National Laboratory (K. Amine's Group) demonstrated the effectiveness of designing sulfur composite hosts that not only immobilize polysulfides, but also enable catalytic reactions. A cell containing a 3D-OMSH (ordered microporous sulfur host) / ZnS,Co-N-C composite exhibited both a higher capacity retention (93.9%) and Coulombic efficiency (100%) after cycling at 0.2C for 100 cycles compared to the standard Ketjen-black-sulfur electrode (60.2%, 94%, respectively).

- The J. Zhang and W. Xu Team (Pacific Northwest National Laboratory) analyzed the compositions of the solid electrolyte interface and the cathode electrolyte interface layer formed on the anode and cathode in cycled high-voltage (4.2V) carbon||$NaNi_{0.68}Mn_{0.22}Co_{0.10}O_2$ (NaNMC) cells. The use of high concentration NaFSI-TEP electrolyte was observed to not only form an inorganic rich solid electrolyte interface layer to stabilize hard carbon anode, but also effectively suppress dissolution of transition metals in cathode, therefore improving the electrochemical performance of Na-ion batteries.

Highlights from the Battery500 consortium team include the following:

Keystone Project 1: Materials and Interfaces

- X-ray fluorescence mapping studies were carried out to understand the transition-metal dissolution at high-voltage charging and consequent deposition on the Li-metal anode. The quantitative analysis showed that nickel, rather than the widely believed manganese, is the most dissolved element among nickel, manganese, and cobalt, and that using a new additive can effectively suppress dissolution of all of them.

Keystone Project 2: Electrode Architecture

- Lithium corrosion in a high-efficiency "bisalt" electrolyte was found to be fast during the initial 24 hours but to slow dramatically afterward while a constant-rate corrosion process takes place in a low-efficiency carbonated electrolyte.

Keystone Project 3: Cell Fabrication, Testing, and Diagnosis

- An optimal anode-to-cathode capacity ratio of 1:1 was discovered comparing 0-µm-thick, 50-µm-thick, and 100-µm-thick lithium anodes. Contrary to conventional wisdom, long cycle life is observed by using ultra-thin lithium (20 µm) in balanced cells. A prototype 350 Wh kg^{-1} pouch cell (2.0 Ah) achieved more than 600 long, stable cycles, with 76% capacity retention without sudden cell death.

Our next report is expected to be available in January 2022.

Sincerely,

Tien Q. Duong

Tien Q. Duong
Manager, Advanced Battery Materials Research Program & Battery500 Consortium
Batteries & Electrification R&D
Office of Energy Efficiency and Renewable Energy – Vehicle Technologies Office
U.S. Department of Energy

TASK 1 – Liquid/Polymer Solid-State Electrolytes

Team Lead: Jihui Yang, University of Washington

Summary and Highlights

The BMR Program goal is to develop long-life batteries superior to commercial Li-ion systems in terms of cost, vehicle range, and safety. The BMR Program addresses the fundamental problems of electrode chemical and mechanical instabilities that have slowed development of affordable, high-performance, automotive batteries. The aim is to identify electrode/electrolyte materials that yield enhanced battery performance and lead to greater acceptance of electric vehicles (EVs). Currently, the U. S. Department of Energy (DOE) Vehicle Technologies Office (VTO) supports 14 projects in the BMR Program under this Task. These projects can be categorized into four general topics:

- **Liquid.** The projects for liquid electrolyte (LE) aim to develop electrolyte formulations, based on fluoro-chemistries, to achieve significantly improved operating voltage, increased durability, and increased energy density of Li-ion batteries at a reasonable cost. Nonaqueous polyelectrolyte (PE) solutions with high Li^+ transference numbers will be developed to achieve high rate capabilities at room temperature. In addition, electrolytes with new polymer binders bearing a pentafluorophenyl group on the backbone will be designed, synthesized, and tested.
- **Polymer.** The targets of PE projects include inorganic/polymer and polymer/gel hybrid electrolytes that have flexibility, mechanical strength, thermal stability, high ionic conductivity, stable interfaces against lithium metal, and polysulfide-trapping capability enabling high-energy-density Li-S batteries, with comparable cycle life.
- **Self-Forming & Self-Healing.** The self-forming, self-healing electrolyte projects are focused on developing and implementing Li-metal-based metal fluorite and metal iodide batteries, capable of energy densities > 400-500 Wh/kg and 1000 Wh/L.
- **Solid-State.** The solid-state projects are to develop high conductivities solid electrolytes (SEs) / composite SEs that are scalable, are chemically and electrochemically stable, and will enable low-cost, high-energy-density solid-state lithium batteries (SSLBs).

Highlights. The highlights for this quarter are as follows:

- The Lawrence Berkeley National Laboratory (LBNL) group (B. McCloskey) made progress measuring the self-diffusion coefficients, conductivity, and transference number for an oligomeric 10-repeat unit lithium triflimide appended polystyrene. In a 3:7 ethylene carbonate – ethyl methyl carbonate (EC-EMC) mixture, they measured a conductivity of 1.08 mS/cm at 0.5 molal Li^+ as measured by a conductivity probe. They also measured self-diffusion coefficients of 1.2×10^{-6} cm^2/s and 9.0×10^{-7} cm^2/s for the Li-ion and anionic backbone, respectively, resulting in an ideal nuclear magnetic resonance (NMR) transport number (t_+^{NMR}) of 0.57. Using electrophoretic NMR with platinum electrodes, the group was able to measure the electrophoretic mobilities of the Li^+, backbone, and solvent molecules. They measured mobilities of 3.3×10^{-10} m^2/Vs for the Li^+ ion and 1.75×10^{-9} m^2/Vs for the oligomer backbone, yielding a true transference number of 0.16 and a conductivity of 1.08 mS/cm, in remarkable agreement with their conductivity probe measurements. Their work aims at developing an understanding of how electrolyte composition and molecular interactions can be manipulated to positively impact ion transport of potential electrolytes for Li-metal batteries.
- The Stanford University group (Z. Bao and Y. Cui) examined the stability of the polydimethylsiloxane (PDMS) pyrrolidinium (Py) trifluoromethanesulfonimide (TFSI), or PyTFSI, coating on the Li-metal deposition morphology, a layer of polymer coating was applied to the copper electrodes, and Li||Cu half cells were assembled, with 50 µl of 1 M LiTFSI and 1 wt% $LiNO_3$ in 1,3-dioxolane / 1,2-dimethoxyethane

(DOL/DME) electrolyte. They deposited 0.1 mAh/cm^2 lithium on the copper foil at the current density of 0.5 mA/cm^2 (1st cycle). They observed that a layer of PyPDMS polymer can effectively change the deposition morphology of the lithium metal. When the copper electrode was not coated, the deposited lithium metal was presented as small spherical nucleus. When a layer of coating was present, the deposited lithium nuclei became bigger and flattened. The work demonstrated that the PyPDMS coating can effectively shield the charging tips during lithium deposition and change the lithium deposition morphology. This results in more homogenous lithium deposition structures.

- The University of Maryland (UMD) group (C. Wang) studied electrochemical performance of single-layered anode-free $Ni_{0.8}Mn_{0.1}Co_{0.1}O_2$ (NMC-811) || copper pouch cells with areal capacity of 2 mAh cm^{-2} and lean-electrolyte condition (3 g E Ah^{-1}). The capacity retention over 80% (normalized to the highest usable capacity) was achieved at the 300th cycle. However, before the 20th cycle, the cell capacity slowly increased, indicating that formation at room temperature is insufficient to wet the whole electrode surface. Formation at elevated temperature (45°C) can effectively avoid the capacity variation in the initial cycles, but the capacity decay in the following cycles was also accelerated. The work suggests that it is important to find the appropriate operation time at elevated temperature to reduce the activation cycles as well as to maintain the cycling stabilities. The time and C-rate for formation at elevated temperature will be investigated, and the high-loading NMC-811||Cu will be scaled up in the pouch cell in the future.

Task 1.1 – Characterization and Modeling of Li-Metal Batteries: Characterization of Li^+ Transport in Polyelectrolytes
(Bryan D. McCloskey, University of California, Berkeley)

Project Objective. This task aims to understand lithium plating and stripping in non-traditional electrolyte systems, specifically PE solutions and concentrated binary salt electrolytes that have been proposed to reduce dendrite formation during lithium stripping and plating due to their high Li^+ transference numbers (t_+). The team will develop capabilities that allow them to understand how ion dynamics in these electrolytes impact macroscale transport properties and Li-metal plating and stripping.

Impact. Ultimately, this task will develop an understanding of how electrolyte composition and molecular interactions can be manipulated to positively impact ion transport of potential electrolytes for Li-metal batteries. This will provide a set of general design rules for novel electrolytes enabling stable, efficient high capacity Li-metal stripping and plating.

Approach. To understand various aspects of lithium plating and ion transport in these systems, the team will develop novel diagnostic and computational modeling techniques. Model polyelectrolytes, with pendant triflimide anions, will be used as polyanions, as their properties can be easily tuned via changes in the polymerization chemistry. Solution parameters that can be varied for both polyelectrolyte solutions and concentrated electrolytes include solvent and salt composition, additive inclusion, and the aforementioned polymer properties, all of which can have a profound impact on electrostatic interactions between charged species in solution, as well as interfacial stability and reaction kinetics of the lithium electrode. The team will develop capabilities that allow them to understand the impact of molecular-level ion dynamics in these electrolytes on macroscale transport properties and Li-metal plating and stripping. These computational simulations will be validated and refined by comparing results to experimentally measured transport properties of these electrolytes. The team will optimize electrochemical methods for these electrolytes to evaluate relevant transport properties under the Newman concentrated solution theory framework, which has never been performed on these non-traditional electrolytes. ^1H and ^{19}F NMR diffusometry will also be used to measure single-ion self-diffusion coefficients without an applied electric field; solution viscosity measurements using a state-of-the-art rotating sphere viscometer can be performed under entirely air-free and water-free conditions. The team will develop capabilities to quantitatively understand degradation mechanisms of various electrolytes during Li-metal stripping and plating. Specifically, differential electrochemical mass spectrometry (DEMS) will be used to study outgassing that occurs from electrolyte degradation processes.

Out-Year Goals. The ultimate goal of this project is to understand the influence of electrolytes with novel transport characteristics on the performance of Li-metal electrodes. Work will continue to build toward a complete understanding of Li-ion and counterion transport in polyelectrolyte solutions and concentrated electrolytes, as well as the impact of electrolyte transport properties on Li-metal uniformity during electrochemical stripping and plating. Outgassing measurements using DEMS will be developed to further probe the interfacial reactivity of lithium metal with electrolytes created in this project.

Collaborations. Collaborators on this project include K. Persson (atomistic and coarse-grained modeling) and N. Balsara (electrochemical characterization of PEs), both at LBNL.

Milestones

1. Establish a simple method to measure activity coefficients and thermodynamic factors for a model electrolyte. (Q1, FY 2021; Completed)
2. Synthesize very low molecular weight oligomer triflimide-based polyions (pTFSI). (Q2, FY 2021; Completed).

3. Measure conductivity, self-diffusion, and concentration cells for model pTFSI solutions. (Q3, FY 2021; Completed)
4. Establish electrophoretic NMR techniques for measuring the true Li^+ transference number of pTFSI solutions. (Q4, FY 2021; On schedule)

Progress Report

This quarter, the team progressed on measuring the self-diffusion coefficients, conductivity, and transference number for an oligomeric 10-repeat unit lithium triflimide appended polystyrene. In a 3:7 EC-EMC mixture, they are able to achieve a conductivity of 1.08 mS/cm at 0.5 molal Li^+ as measured by a conductivity probe. They measured self-diffusion coefficients of 1.2 x 10^{-6} cm^2/s and 9.0 x 10^{-7} cm^2/s for the Li-ion and anionic backbone, respectively, resulting in an ideal NMR transport number (t_+^{NMR}) of 0.57. Using electrophoretic NMR with platinum electrodes, the team is able to measure the electrophoretic mobilities of the Li^+, backbone, and solvent molecules. They measured mobilities of 3.3 x 10^{-10} m^2/Vs for the Li^+ ion and 1.75 x 10^{-9} m^2/Vs for the oligomer backbone, yielding a true transference number of 0.16 and a conductivity of 1.08 mS/cm, in remarkable agreement with the team's conductivity probe measurements. They observed small deviations in mobilities measured at high electric field strengths, which is likely indicative of small amounts of convection, and have noted this as an area for technique optimization. The large difference between the true transference number (0.16) and the ideal NMR transference number (0.57) is likely due to significant anion-anion correlation along the polymer backbone. The team hopes to study this phenomenon in upcoming quarters using different molecular weight oligomers including monomeric solutions as well as longer chain polymer solutions.

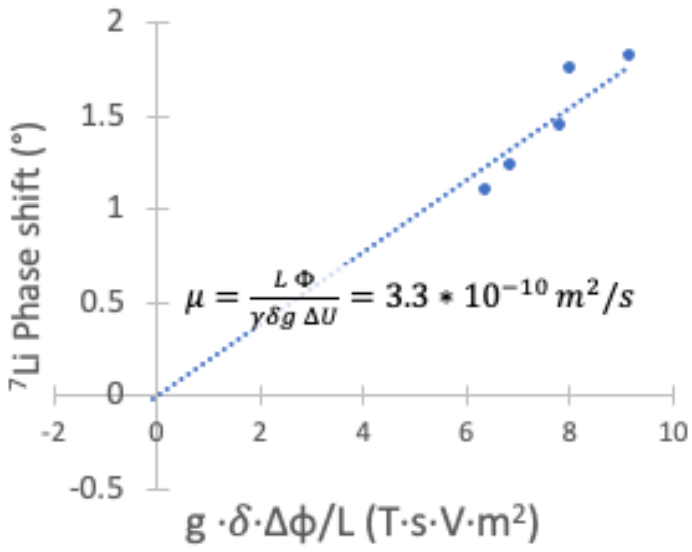

Figure 1. ^{7}Li phase shift (°) versus g·δ·Δϕ/L (T·s·V·m²) measured via electrophoretic nuclear magnetic resonance with a ± 90 V bias in a 0.5 m Li^+ oligomeric triflimide polyanion solution in EC:EMC. From the slope of this line, the mobility and velocity of each species can be calculated.

In addition to progress on electrophoretic NMR measurements, the team has also made progress on implementing Hittorf cells as an alternative low-volume electrochemical method for measuring Li^+ electrolyte transference number. They designed and fabricated a custom low-volume lithium-graphite Hittorf cell out of polytetrafluoroethylene (PTFE). After passing a known amount of current, they extract solutions from each chamber of the 3-chamber cell and measure concentration using ^{7}Li NMR. They are completing validation studies using $LiPF_6$ in EC:EMC; to date, they have measured transference numbers of ~ 0.4-0.5 for 1 M $LiPF_6$ in EC:EMC using this method. They hope to achieve better accuracy through better calibration of the NMR, and by inducing larger concentration gradients using higher current densities. Next quarter, they will apply this method to measuring the transference number of the PE solutions.

Patents/Publications/Presentations

Publication

- Bergstrom, H., K. Fong, and B. McCloskey. "Interfacial Effects on Transport Coefficient Measurements in Li-ion Battery Electrolytes." *Journal of the Electrochemical Society* 168 (2021): 060543.

Task 1.2 – Advanced Polymer Materials for Batteries (Zhenan Bao and Yi Cui, Stanford University)

Project Objective. This project will develop new polymer materials for batteries. The team will develop polymer coatings with specific mechanical properties that can accommodate the volume expansion and contraction of the Li-metal anode associated with deposition and stripping (charging and discharging).

Project Impact. The cycling stability and Coulombic efficiency (CE) of Li-metal electrodes will be increased by implementation of a polymer-based protective layer that functions as an artificial solid electrolyte interphase (SEI) with desired properties. The improved performance will enable further development toward practical utilization of Li-metal anodes with higher cycling efficiency and less susceptibility to dendrite-based failure.

Approach. The project uses soft polymer coatings with dynamic crosslinking to give the resulting polymers liquid-like rheological properties and stretchable and self-healing properties. In previous work, the project has shown that such coatings resulted in uniform deposition/stripping of lithium metal and improved cycling stability of Li-metal electrodes. To understand the design rules for effective polymer coatings, the team chose a few representative polymers to systematically understand structure property relationships. Here, the team investigates the correlation between surface energy of the polymer and exchange current for lithium deposition.

Out-Year Goals. Work will progress toward the correlation between dielectric constant and exchange current. These findings will enable further understanding and development of various polymer coatings for protecting Li-metal anodes.

Collaborations. This quarter, the team is collaborating with J. Qin at Stanford.

Milestones

1. New lithium anode coating design. Analyze the polymer chemistry and mechanical property using NMR, differential scanning calorimetry (DSC), and rheology. (Q1, FY 2021; Completed)
2. Analyze stability of the polymer in electrolyte and its ability to reduce the reaction in the Li-metal surface with electrochemical impedance spectroscopy (EIS). (Q2, FY 2021; Completed)
3. Characterize the impact of the polymeric coating on lithium deposition morphology using scanning electron microscopy (SEM). (Q3, FY 2021; Completed)
4. Coat Li-metal electrodes with the polymeric coating and achieve stable lithium cycling for 150 cycles at 1 mA/cm^2 and 2 mA/cm^2 current density. (Q4, FY 2021)

Progress Report

The team hypothesizes that an effective method to address the lithium anodic interfacial instability is to fundamentally alter the Li-ion deposition pathways by electrostatically blocking the heterogenous surface regions that concentrate lithium ions due to high electric field. This can be experimentally implemented using electro-inactive cations at the interface that can 'shield' the inhomogeneous protrusion on the electrode surface to neutralize the electric field landscape. However, this strategy can be successful only when it is ensured that these electro-inactive cations do not undergo reduction during the lithium deposition process. In other words, their reduction potential needs to be even lower than that of Li^+ ions that already have the lowest intrinsic reduction potentials among metallic cations. Previously, Ding et al. pointed out that Cs^+ can achieve lower reduction potential than Li^+ by tuning its concentration based on Nernst Equation. Furthermore, it was shown that addition of Cs^+ ions in electrolyte resulted in improved lithium deposition morphology and battery operation. However, the concentration dependent electrochemical stability of Cs^+ ions can be undermined by their localized aggregation at the electrode surface, resulting in the reduction of Cs^+.

Instead of using free cations, the team proposes to tether the electroactive cations (Py^+) onto a flexible and stable polymer backbone (PDMS) to form a PDMS-based poly (ionic liquid) (PDMS-Py) coating that would homogenize the electric field distribution on the electrode surface and promote uniform lithium deposition. Based on previous study, Py^+ was selected due to its lower reduction potential compared to Li^+ and its chemical stability with the Li-metal anode. Incorporation of Py^+ in a polymer coating on the lithium anode is a facile method that does not alter existing manufacturing capabilities and also limits their interaction with other battery components. Building on previous studies on anodic coating using polymers [poly(ethylene oxide) (PEO), Nafion, polyvinylidene (di)fluoride (PVDF)], and drawing on the team's knowledge on designing cation-tethered polymeric coating on anode surface, the interfacial material in this work is designed using economically viable chemistry, is chemically and electrochemically inert with lithium metal, possesses conducting pathway for lithium conduction, and is mechanically robust for adapting to rapid volume changes.

Polymer Coating Design

The schematic of Figure 2a illustrates lithium anode coated with PDMS-PyTFSI containing electro-inactive cations and its counter anion TFSI. In absence of any coating, the concentrated electric field at surface protrusion triggers self-amplified surface roughening process of lithium deposition (Figure 2b). The presence of cations is hypothesized to neutralize the radiating electric field and helps to homogenize lithium deposition pathways. Figure 2c showcases the 'cationic shielding' phenomenon where the presence of the PDMS-PyTFSI coating results in redistribution of Li^+ ions away from the surface protrusions, leading to a more uniform topology. The physiochemical prerequisites of the PDMS-Py polymer coating for the cationic shielding mechanism are as follows: (1) the cations in PDMS-PyTFSI backbone should have a lower reduction potential than that of Li^+, and (2) sufficient mobility of the polymer chains is essential for electric-field-based response of the cations.

In previous work, the team has utilized a system of random co-polymer on poly(acrylic) backbone: one of the co-polymer side chains contains the Py^+ cation units, and the other side chain is perfluoroalkyl as an inert component that can also lower the glass transition of the final co-polymer and introduce mobility to the polymer chains.

Instead of using a relatively rigid poly(acrylic) backbone, the new design (Figure 2d) utilizes flexible PDMS backbone, which efficiently brings down the polymer's glass transition temperature (Tg) so there is no longer the need to introduce another fluorinated component and so all of the polymer side chain can be functionalized with the Py^+ cation units. Beyond the benefit of mechanical flexibility, PDMS-based polymer is economically viable in comparison to any fluorinated polymer, its mechanical property can be regulated via controlled crosslinking, and it is inert and electrochemically stable with lithium metal.

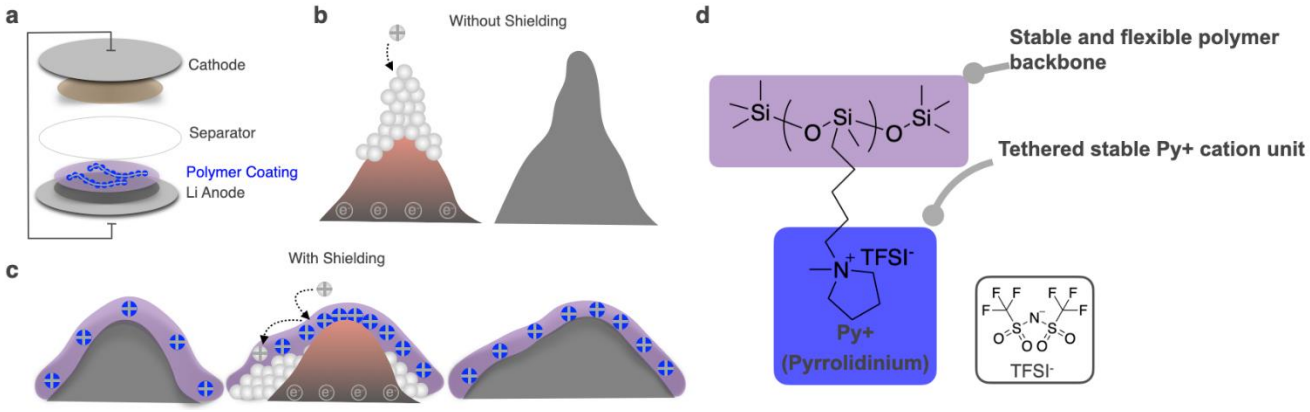

Figure 2. PDMS-Py as the anodic coating for Li-metal batteries. (a) Li-metal battery with polymer-coated anode. (b) Concentrated electric field at vicinity of surface protrusions cause the self-amplifying dendritic deposition of lithium ions. (c) Coating on Li-metal anode. During Li^+ deposition, cations in polymeric ionic liquid coating remain electrochemically stable and can effectively shield the Li^+ ions, resulting in more flat and homogeneous deposition. (d) Chemical structure of the PDMS-PyTFSI coating.

Effect of Polymer Coating on Li-Metal Morphology

To examine the stability of the PDMS-PyTFSI coating on the Li-metal deposition morphology, the team applied a layer of polymer coating to the copper electrodes and assembled Li||Cu half cells, with 50 µl of 1 M LiTFSI and 1 wt% $LiNO_3$ in DOL/DME electrolyte. The team deposited 0.1 mAh/cm^2 lithium on the copper foil at the current density of 0.5 mA/cm^2 (1st cycle).

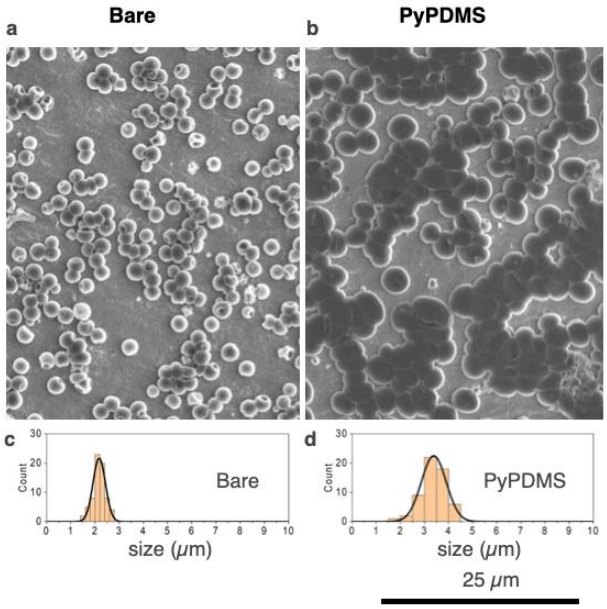

Figure 3. Scanning electron microscopy (SEM) images of lithium depositing on copper foil: (a) bare copper foil, and (b) PyPDMS-coated copper foil. Size distribution of lithium nuclei under SEM: (c) bare copper foil, and (d) PyPDMS-coated copper foil.

Based on the SEM image shown in Figure 3a-b, the team observed that a layer of PyPDMS polymer can effectively change the deposition morphology of lithium metal. When the copper electrode was not coated, the deposited lithium metal was presented as a small spherical nucleus. When a layer of coating was present, the deposited lithium nuclei became bigger and flattened. Furthermore, the team quantified the size distribution of deposited lithium nuclei in Figure 3c-d, which demonstrates that lithium deposition size increased from 2.2 µm to 3.4 µm on application of a coating layer.

This series of characterization shows that PyPDMS coating can effectively shield the charging tips during lithium deposition and change the lithium deposition morphology. This results in more homogenous lithium deposition structures.

Patents/Publications/Presentations

Patent

- Non-Flammable Polymeric Electrolyte with Wide Operational Temperature Range; Application No. 63/219,517.

Publications

- Kim, S. C., X. Kong, R. A. Vilá, W. Huang, Y. Chen, D. T. Boyle, Z. Yu, H. Wang, Z. Bao, J. Qin, and Y. Cui. "Potentiometric Measurement to Probe Solvation Energy and Its Correlation to Lithium Battery Cyclability." *Journal of the American Chemical Society* 143, No. 27 (2021): 10301–10308. doi: 10.1021/jacs.1c03868.
- Wang, H., Z. Yu, X. Kong, W. Huang, Z. Zhang, D. G. Mackanic, X. Huang, J. Qin, Z. Bao, and Y. Cui. "Dual-Solvent Li-Ion Solvation Enables High-Performance Li-Metal Batteries." *Advanced Materials* 33, No. 25 (2021): 2008619. doi: 10.1002/adma.202008619.

Task 1.3 – Improving the Stability of Lithium-Metal Anodes and Inorganic-Organic Solid Electrolytes (Nitash Balsara, Lawrence Berkeley National Laboratory)

Project Objective. The project objective is to establish a new hybrid electrolyte that will be stable against cells with a Li-metal anode.

Project Impact. PEs offer increased stability in lithium batteries in comparison to more widely used LEs. Nanostructured electrolytes containing both soft, ion-conducting domains and rigid, nonconducting domains offer the opportunity to tune both mechanical and electrical properties separately. Such electrolytes are conveniently made by block copolymer self-assembly. Most of the block copolymer electrolytes studied thus far comprise organic polymer chains for both the conducting and rigid domains. The team hopes to synthesize new electrolytes that simulataneously have high transport properties and have greater stability against lithium in comparison to organic diblock copolymers.

Approach. First, the team synthesizes hybrid diblock copolymers by incorporating monomers that contain an inorganic component. Then, electrolytes are prepared by mixing these diblock copolymers with salt. Electrochemical and mechanical characterization of these materials is performed before carrying out cycling X-ray tomography (XRT) experiments and *in situ* small angle X-ray scattering (SAXS) experiments. The combination of these approaches enables rational design of materials that exhibit improved stability against lithium metal.

Out-Year Goals. The project will synthesize a new hybrid electrolyte that is designed to be stable against lithium metal. The material is a block copolymer in which one block contains acryloisobutyl polyhedral oligomeric silsesquioxane (POSS). The second block is a conventional PE (PEO). Electrochemical characterization of this polymer will include measurement of all transport properties including conductivity, diffusion coefficient, and transference number. The stability against lithium metal will be evaluated by cyclic voltammetry (CV), while its applications as an electrolyte will be evaluated and visualized using cycling XRT experiments on symmetric Li-hybrid-Li cells.

Collaborations. There are no active collaborations this quarter.

Milestones

1. Synthesize at least 2 POSS-containing single ion conductors (SICs). (Q1, FY 2021; Completed)
2. Develop the relationship between non-linear mechanical properties and ion transport in solid block copolymer electrolytes. (Q2, FY 2021; Completed)
3. Conduct *in situ* X-ray scattering experiments on Li-polymer-Li symmetric cells to quantify polymer morphology in the presence of an applied field. (Q3, FY 2021; Completed)
4. Conduct XRT experiments on Li-polymer-Li symmetric cells to quantify dendrite growth in block copolymer electrolytes. (Q4, FY 2021)

Progress Report

The following milestones has been completed: *in situ* X-ray scattering experiments on Li-polymer-Li symmetric cells to quantify polymer morphology in the presence of an applied field.

Block copolymer electrolytes are promising materials for Li-metal batteries, due to the combination of an ion conducting block—in this case, PEO—and a mechanically rigid block to prevent dendrite growth—in this case, polystyrene.[1] The polymer used in this study has a polystyrene molecular weight of 19 kg/mol and a PEO molecular weight of 20 kg/mol [polystyrene-*b*-PEO, or SEO (19-20)], and contains a lithium salt, LiTFSI, with 0.16 lithium ions per ethylene oxide monomer unit (r = 0.16). The electrolyte is lamellar at all relevant salt concentrations.

The goals of this study are to use SAXS to characterize the morphology of the electrolyte as a function of position and time under an applied current. A schematic of the setup is shown in Figure 4a. By designing the cell so that the beam is perpendicular to the direction of ion motion, different positions ranging between the two electrodes can be probed, and different azimuthal angles around the scattering pattern provide information about differently oriented lamellar grains relative to the electrodes (Figure 4b).

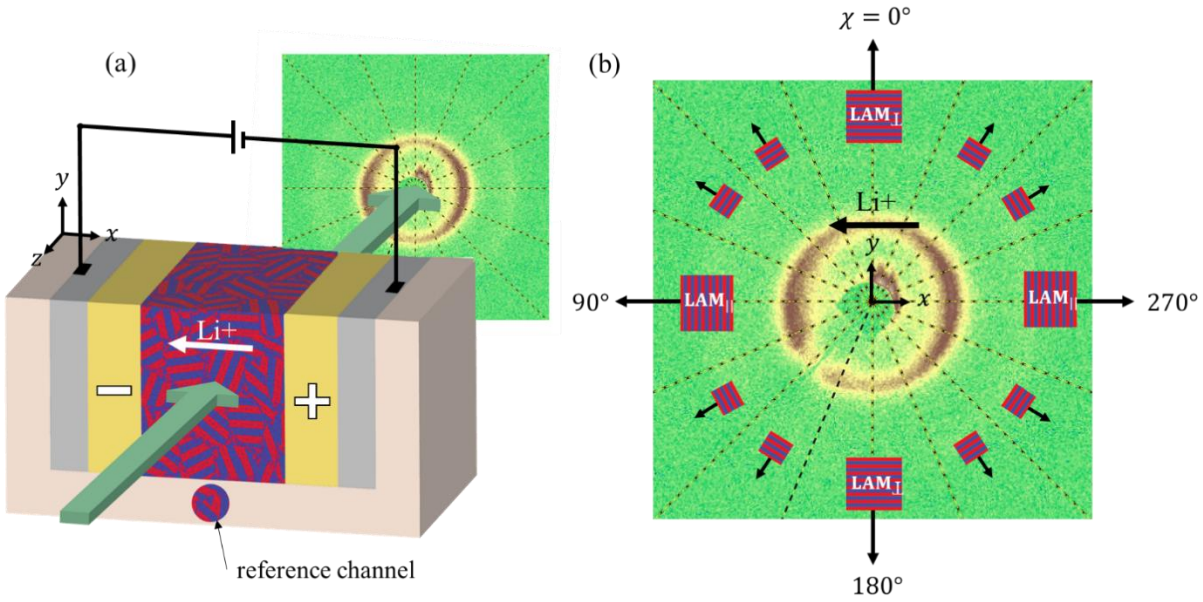

Figure 4. (a) Schematic representation of the simultaneous polarization and small-angle x-ray scattering (SAXS) experiment. An SEO/LiTFSI electrolyte with randomly oriented grains is sandwiched between two lithium electrodes with current passing parallel to the x-axis. X-rays pass parallel to the z-axis, perpendicular to the current. Scanning the beam along the x-axis allows for spatial resolution between the electrodes. A reference channel filled with electrolyte was placed next to the electrochemical cell. (b) Characteristic two-dimensional SAXS pattern obtained from experiments. The pattern is divided into 16 sectors defined by the azimuthal angle, χ. Scattering data in each sector corresponds to lamellae oriented with the angle between the vector normal to the poly(ethylene oxide) / polystyrene interfaces, and the positive y-axis equal to χ. The cartoons in each sector show the lamellar orientation with normal vectors drawn.

Three cells were polarized at three current densities: 0.926 μA/cm, 1.96 μA/cm, and 3.74 μA/cm; their potential response is shown in Figure 5a. By azimuthally averaging the SAXS patterns, the lamellar domain spacing, d, was calculated as a function of position, x/L, over time during cycling (Figure 5b). As a salt concentration gradient builds up during polarization,[2] lamellae near the salt-rich electrode swell, increasing d, to accommodate additional salt, while lamellae near the salt-poor electrode shrink.

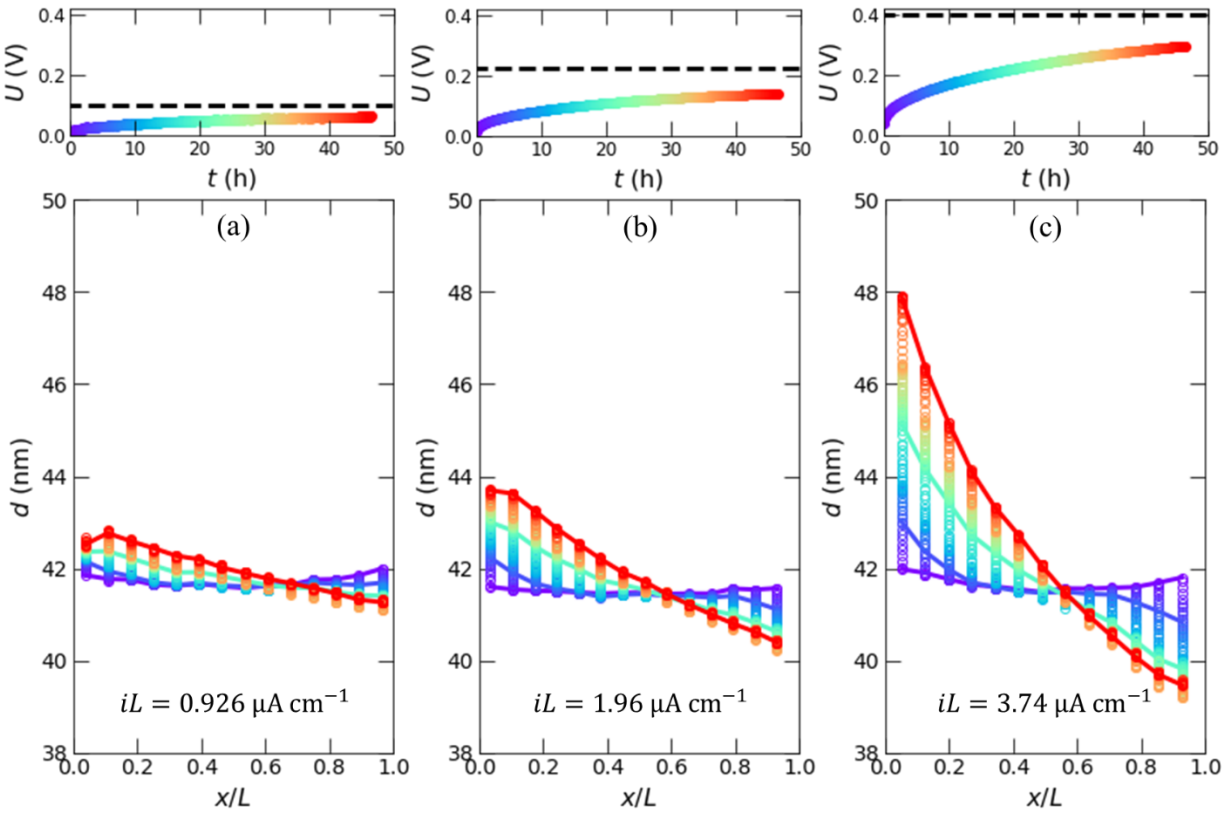

Figure 5. Results from simultaneous polarization and small-angle x-ray scattering experiments at three current densities: (a) The potential drop across the electrolyte, U, versus time, t, is plotted in the top panel of each figure. The dashed line represents the steady state potential (U_{ss}) predicted from concentrated solution theory. In the main panel, the domain spacing, d, is plotted versus normalized cell position, x/L. The color of each data set corresponds with the U versus t plot in the top panel. Purple data sets were obtained at the beginning of polarization (t = 0 h), and red data sets were obtained at the end of polarization (t = 46.6 h).

Figure 5 shows the average domain spacing for lamellae of all orientations. However, lamellae oriented perpendicular and parallel to the electrodes (Figure 4b) swell and contract to differing extents. Figure 6a-b shows the change in domain spacing, Δd, from the initial state to the end of polarization at 1.96 μA/cm, 3.74 μA/cm, and 11.1 μA/cm as a function of azimuthal angle, χ, as defined in Figure 4b. Each curve represents a different position within the cell, with the positions toward the center of the cell swelling or shrinking less than those near the electrodes, as shown in Figure 5. The orientation dependence of the change in domain spacing shown in Figure 6 illustrates that the lamellae oriented perpendicular to the electrodes, or parallel to the direction of ion transport, exhibit much smaller domain size changes during polarization. This shows that while lamellae parallel to the direction of ion transport form important channels to allow ions to traverse the cell, lamellae parallel to the electrodes may also play a crucial role in swelling and shrinking to accommodate formation of salt concentration gradients, enabling application of higher potentials and achievement of faster charging.

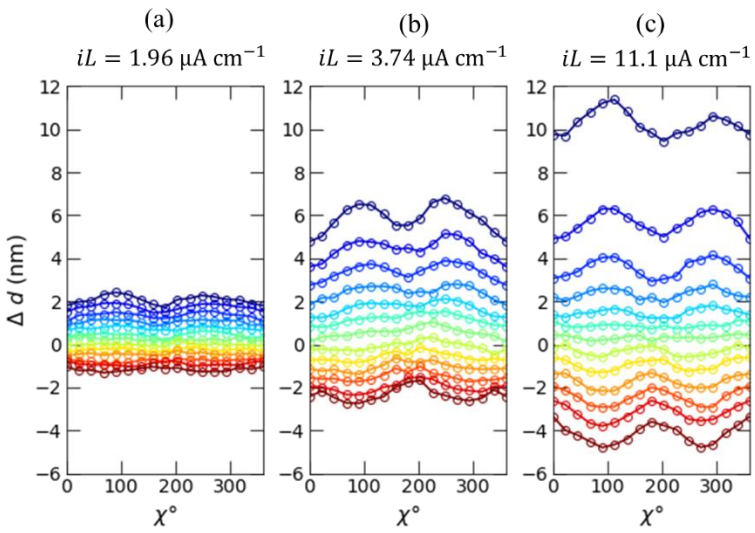

Figure 6. Orientation dependence of lamellar distortion. The change in domain spacing, Δd, a function of azimuthal angle, χ, is plotted for each cell position for the cell polarized at (a) iL = 1.96 μA cm^{-1} at t = 46.7 h, (b) iL = 3.74 μA cm^{-1} at t = 46.7 h, and (c) iL = 11.1 μA cm^{-1} at t = 60.7 h. Each data set is based on the last scan taken at the end of each polarization. (d) Difference in domain spacing between $\mathbf{LAM}_{\perp}$ and $\mathbf{LAM}_{||}$ as a function of normalized position, x/L, for the three data sets in (a), (b), and (c).

References

[1] Tu, Z., P. Nath, Y. Lu, M. D. Tikekar, and L. A Archer. "Nanostructured Electrolytes for Stable Lithium Electrodeposition in Secondary Batteries." *Accounts of Chemical Research* 48, No. 11 (2015): 2947–2956. doi: 10.1021/acs.accounts.5b00427.

[2] Doyle, M., T. F. Fuller, and J. Newman. "The Importance of the Lithium Ion Transference Number in Lithium/Polymer Cells." *Electrochimica Acta* 39, No. 13 (1994): 2073–2081. doi: 10.1016/0013-4686(94)85091-7.

Patents/Publications/Presentations

Publications

- Maslyn, J. A., L. Frenck, V. D. Veeraraghavan, A. Muller, A. S. Ho, N. Marwaha, W. S. Loo, D. Y. Parkinson, A. M. Minor, and N. P. Balsara. "Limiting Current in Nanostructured Block Copolymer Electrolytes." *Macromolecules* 54 (2021): 4010–4022.
- Veeraraghavan, V. D., L. Frenck, J. A. Maslyn, W. S. Loo, D. Y. Parkinson, and N. P. Balsara. "Evolution of Protrusions on Lithium Metal Anodes Stabilized by a Solid Block Copolymer Electrolyte Studied Using Time-Resolved X-Ray Tomography." *ACS Applied Materials & Interfaces* 13, No. 23 (2021): 27006–27018.
- Sethi, G. K., L. Frenck, S. Sawhney, S. Chakraborty, I. Villaluenga, and N. P. Balsara. "Effect of Microphase Separation on the Limiting Current Density in Hybrid Organic-Inorganic Copolymer Electrolytes." *Solid State Ionics* 368 (2021): 115702.

Task 1.4 – Development of Thin, Robust, Lithium-Impenetrable, High-Conductivity, Electrochemically Stable, Scalable, and Low-Cost Glassy Solid Electrolytes for Solid-State Lithium Batteries (Steve Martin, Iowa State University of Science and Technology)

Project Objective. The project objective is to develop new Li^+-conducting mixed oxy-sulfide nitride (MOSN) glassy solid electrolytes (GSEs) that are impermeable to lithium dendrites, have high conductivities, are scalable through low-cost glass manufacturing, are chemically and electrochemically stable, and will enable low-cost, high-energy-density SSLBs. The SSLBs constructed from these new GSEs will meet and exceed all program objectives: usable specific energy @ C/3 ≥ 350 Wh/kg, calendar life 15 years, cycle life (C/3 deep discharge with < 20% energy fade) 1000, and cost ≤ $100/kWh.

Project Impact. This project will enable the team to demonstrate the following: (1) thin MOSN GSE films yield superior performance in a much safer, lower-cost, and Li-dendrite impenetrable form, and (2) high rate and long cycle life can be achieved in SSLBs using thin-film MOSN GSEs. The new GSEs in SSLBs are anticipated to increase energy density (anode basis) from ~ 300 mAhr/g to ~ 4,000 mAhr/g, enabling replacement of internal combustion engines in both light-duty and heavy-duty vehicles. Each 20% reduction in the ~ 1.6 billion liters of gasoline used per day in the United States would reduce CO_2 emissions by ~ 4 billion kg or 2×10^{12} l of CO_2 per day. The team will also increase scientific and engineering knowledge of thin-film GSEs in SSLBs.

Approach. The MOSN mixed glass former (MGF) glasses used for the GSEs in this project have been developed in previous work to have the necessary thermal stability and high ionic conductivity for successful use as a drawn-film electrolyte. In this project, the glass chemistry will be tuned for even more desirable properties, by investigating structure-property relationships and testing variations in glass chemistry.

Out-Year Goals. Work will progress toward developing a glass capable of being drawn to 100-µm thickness, while having high conductivity and electrochemical stability and good cycling ability.

Collaborations. There are no active collaborations this quarter.

Milestones

1. Accomplish: 100 cycles against lithium metal with no cell shorting and < 20% degradation of other properties. (Q4, FY 2021; Completed)
2. Accomplish: Optimize draw conditions for MOSN GSE to achieve 5 m × 5 cm × < 100-µm thin films. (Q4, FY 2021; In progress)
3. Accomplish: Fabricate MOSN MGF Li|GSE|Li cells in small area format, ~ 1 cm^2. (Q4, FY 2021; Completed)
4. *Go/No Go Decision*: Micro-sheet glass ribbon processing facility optimized / design capable of meeting the following performance requirements: glove box enclosing preform redraw facility reaches 10 ppm O_2 and H_2O, and 3 samples of MOSN MGF GSE ribbons have been drawn at 5 m × 5 cm × 100 µm. Analysis indicates technical approach capable of achieving performance targets. (Q4, FY 2021; Completed)

Progress Report

Development of Optimized High Li^+ Ion Conductivity MOSN MGF GSEs

Continue Developing MOSN MGF GSEs with Target Properties Capable of Cycling Lithium against Lithium Metal

In a continuous effort to improve properties of the GSEs developed by Iowa State University (ISU), a new glass series was developed this quarter to increase resistance to crystallization and improve processability. Previous reports demonstrated that while highly conductive and electrochemically stable, all of the ISU GSEs exhibit crystallization temperatures (Tc) ≤ 450°C, making them prone to crystallization during the drawing process. To improve GSE resistance to crystallization, while maintaining conductivity and stability, the ISU-7x series and ISU-8x series have been developed to aid in more thoroughly understanding the effects of nitrogen and aluminum incorporation on properties and performance.

Table 1. Sample IDs, chemical compositions, and compositional formulas of various mixed oxy-sulfide (MOS) and mixed oxy-sulfide nitride (MOSN) glasses.

Sample ID	Chemical Composition	Compositional Formula
ISU-5	$0.60Li_2S + 0.40SiS_2 + 0.1LiPO_3$	$\mathbf{Li_{13}Si_3PS_{12}O_3}$
ISU-6	$0.58Li_2S + 0.315SiS_2 + 0.105LiPO_3$	$\mathbf{Li_{12.05}Si_3PS_{11.52}O_3}$
ISU-7(x)	$0.58Li_2S + 0.315\ SiS_2 + 0.105\ [(1\text{-}x)\ Li_{0.67}PO_{2.87} + xLiPO_{3\text{-}3y/2}N_y]$	$\mathbf{Li_{11.7+0.33x}Si_3PS_{11.52}O_{2.83\text{-}0.36x}N_{0.35x}}$
ISU-8(x)	$Li_{12.05}Si_3P_{1\text{-}x}Al_xS_{11.52}O_{3\text{-}x}$	$\mathbf{Li_{12.05}Si_3P_{0.975}Al_{0.025}S_{11.52}O_{2.975}}$

As highlighted in previous reports, the ISU-6 composition was found to be a promising glass with an ionic conductivity of ~ 7×10^{-4} S/cm at 25°C and a working range of approximately 114°C. For scale-up purposes, the working range needed to be expanded to prevent crystallization of the glass when being drawn. Thus, through the addition of LiPON in the ISU-7x compositional series, thermal stability of these glasses was improved, reaching a working range (ΔT = Tc-Tg) of approximately 121-130°C in the x = 0.0, 0.1, and 0.5 compositions, as seen in Figure 7. The thermal events above 300°C correspond to the glass transition temperature (Tg) and crystallization temperature (Tc), and these values are tabulated in Table 2. The working ranges for these materials are significant when casting these glasses into preforms and drawing them into films. Therefore, the working range is a key parameter in the down-selection process. Further study has been done on these glasses to determine conductivity and electrical properties.

Table 2. Glass transition temperatures, crystallization temperatures, and working range for the ISU-7 Series.

Sample ID	Glass Transition (Tg) (°C) [± 3°C]	Crystallization Temp. (Tc) (°C) [± 5°C]	Working Range (Tc-Tg) (°C)
ISU-7; x = 0.0	338	458	121
ISU-7; x = 0.1	321	451	130
ISU-7; x = 0.2	334	444	110
ISU-7; x = 0.3	339	448	109
ISU-7; x = 0.4	334	438	104
ISU-7; x = 0.5	320	442	121

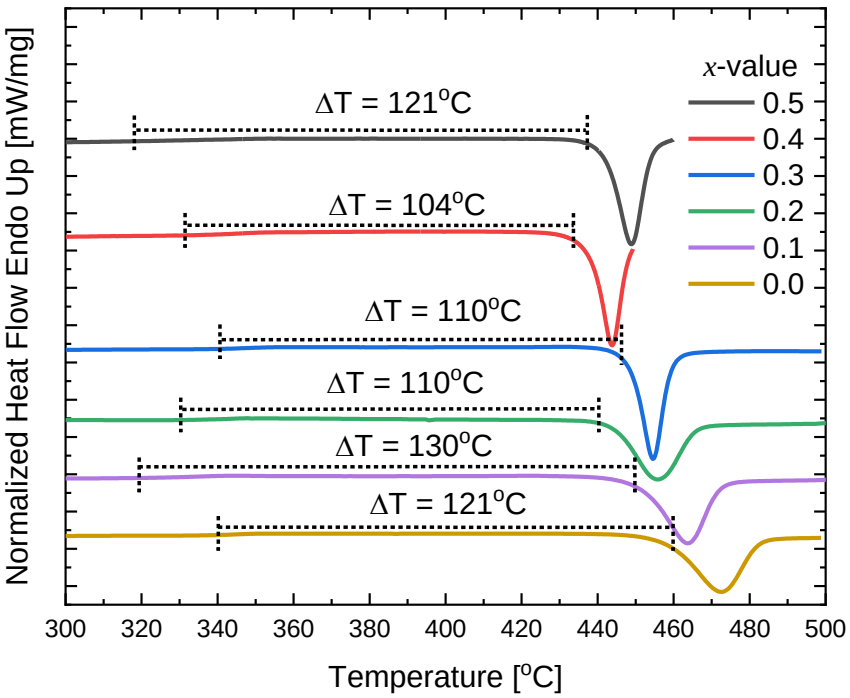

Figure 7. Thermal stability of ISU-7 glasses as shown via differential scanning calorimetry thermograms. All of these glassy solid electrolytes have working ranges that are > 100°C. ISU-7 (x = 0.1), with the largest working range (see Table) found to form a stable glass on cooling.

The ionic conductivity and underlying material structure were investigated further to understand the role nitrogen is playing on these materials. Thus, EIS was used to measure the temperature-dependent ionic conductivity of the ISU-7 GSEs from -60°C to 105°C, as shown in Figure 8a-b. On incorporation of LiPON, the ionic conductivity of the MOSN composition appears to increase slightly for glasses with $x < 0.2$, increasing from 0.44 mS/cm ($x = 0$) to 0.52 mS/cm in the $x = 0.2$ composition. From LiPON incorporation, there is an increase in the amount of lithium and nitrogen and a decrease in the amount of oxygen present in the material. Further additions of LiPON past 0.2 result in a decrease in the ionic conductivity, due in large part to the high field strength oxygen anions trapping lithium.

Work has been conducted to optimize the thermal, chemical, and electrochemical properties of the ISU GSE through compositional development and structural modification through the addition of aluminum to these glasses. The ISU-8 series, with the formula shown in Table, was developed to inhibit the nucleation and growth of crystalline phases observed during the drawing of ISU-5 and ISU-6 GSEs. This work was motived by reports by Eckert et al.[1] that show that incorporation of aluminum ions was able to improve resistance to crystallization by occupying sites with coordination numbers (CNs) ranging from Al_{III} (CN=3) to Al_{VI} (CN=6). Additional work by Zhang et al.[2] also shows that aluminum substitution can increase ionic conductivity of SEs by reducing the jump distance between isolated species. This is particularly important in the highly modified GSEs, as the imparted structural diversity can suppress crystallization processes that arise during material processing. While the work being done on this series is still preliminary, some work has been done to test the ionic conductivity and electrochemical stability of select compositions.

As seen in Figure 8b, conductivity of the ISU-8 series tends to decrease with incorporation of aluminum, with conductivity decreasing to 3.9×10^{-4} at $z = 0.05$ followed by an increase in conductivity at the $z = 0.1$ to 4.4×10^{-4}. Incorporation of aluminum, therefore, tends to decrease conductivity of the MOS glass. More work is being done to further characterize this series.

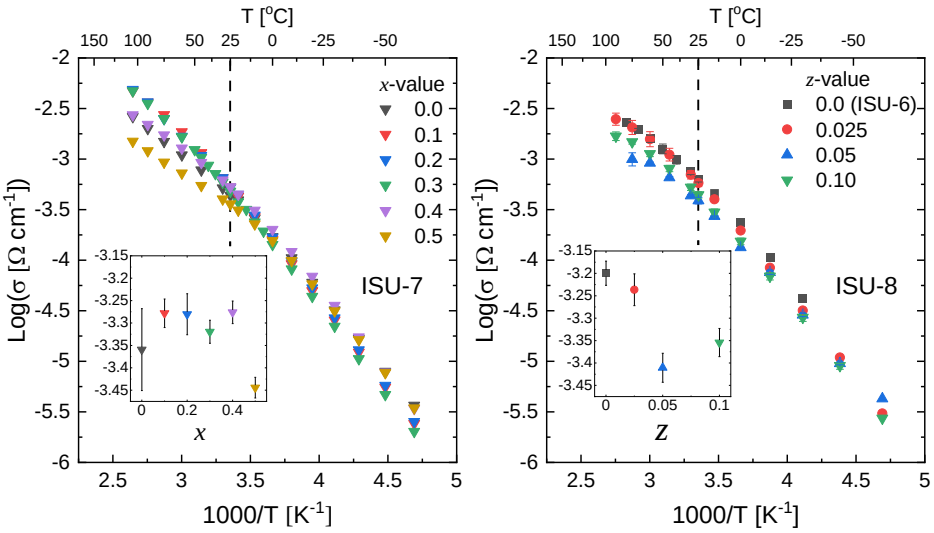

Figure 8. Arrhenius plots of conductivities of ISU-6, ISU-7x, and ISU-8x. (a) Temperature-dependent conductivity measurement for ISU-7 series (x = 0.0, 0.1, 0.2, 0.3, 0.4, and 0.5; y = 0.314) showing that x = 0.1 and x = 0.2 have the highest conductivities of 0.52 mS/cm at 25°C. (b) Arrhenius plot for the ISU-8 (z = 0.0, 0.025, 0.05, 0.1).

Figure 9a shows the electrochemical stability of ISU-8 (y = 0.58, z = 0.025) with little resistance change in contact with lithium metal over a period of 12 hours at no applied voltage. Figure 9b shows the stable cycling of the glass at 0.05 mA/cm^2 for more than 100 cycles. Figure 9c-d shows Nyquist plots taken after the 1st cycle and then after every 20 cycles, and the equivalent circuit fitted resistance values for the bulk and interfacial resistances, respectively. Furthermore, the temperature dependent conductivity of the ISU-8 y = 0.58 series has been determined through EIS and is shown in Figure 8b. More samples of the ISU-8 series will be tested soon to confirm the conductivity values determined.

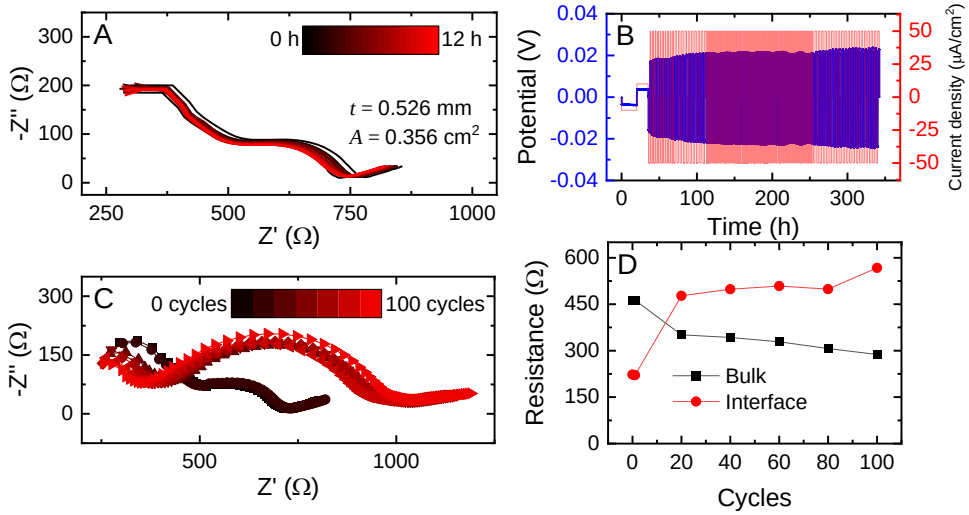

Figure 9. Electrochemical stability graphs for ISU-8 0.58 Li_2S + 0.315 SiS_2 + 10.5 $LiP_{0.975}Al_{0.025}O_{2.975}$. (a) Nyquist plots showing resistance over time at no applied potential. (b) Cycling behavior at 0.05 mA/cm^2 for 100 cycles. (c) Nyquist plots showing resistance change during cycling. (d) Equivalent circuit model fitted resistance values from (c). All graphs have the same electrolyte area and thickness.

Initiate Development of Preforms of MOSN MGF GSEs that Do Not Crystallize

The current series of MOSN glasses allows for production of large preforms without crystallization. A number of conditions, including annealing conditions, raw material cleanliness, and raw material mixing, improve the glass quality to guarantee no crystallization on forming a 250 g preform. However, some crystallization has been observed when reheating the glass for film drawing. This crystallization behavior (on heating rather than on cooling) has been a subject of further testing, as detailed later in this report.

Develop Micro-Sheet Glass Ribbon Processing Facility for GSEs

Continue to Develop and Optimize GSE Micro-Sheet Glass Ribbon Processing Facility

Optimization efforts continued for the micro-sheet glass ribbon processing facility to improve film drawing. As film forming depends on precise temperature control to soften the glass without inducing crystallization, an accurate temperature profile for the draw furnace is extremely important. The temperature profile was measured using a thermocouple assembly in place of the glass preform to accurately determine the effect of various operating conditions on furnace temperature. The temperature controller has a single set point, but the furnace contains one thermocouple on each side. The left and right side of the furnace can differ by ± 30°C at the same set point. Adjusting the external baffles and internal gas flow can provide more temperature control. Figure 10a shows how optimization of settings allows for a focused heating zone for film formation. In addition, temperature overshoot can cause local crystallization in the preform, and these experiments show local temperatures as high as + 40°C from the 350°C set point. Once optimized settings were found, a study was conducted to determine the variation across the furnace at a given depth, as shown in Figure 10b.

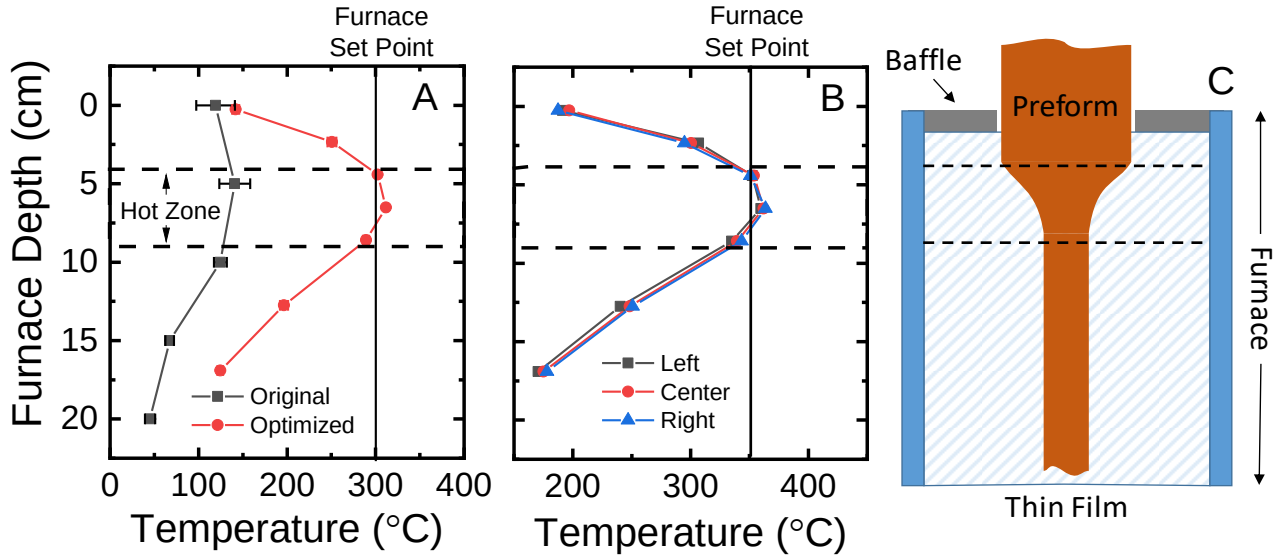

Figure 10. (a) Furnace temperature profiles measured before and after efforts to optimize the gas flow, baffle positions, and other furnace variables. (b) Furnace temperature profiles at different positions and depths following optimization. (c) Representative diagram of glass position during film formation.

Develop Processing Conditions for Micro-Sheet Ribbons of MOSN MGF GSEs

- Complete optimization of draw conditions for optimized oxide GSEs < 500 µm.
- Complete optimization of draw conditions for optimized MOS MGF GSEs < 200 µm.
- Complete optimization of draw conditions for optimized MOS MGF GSEs < 100 µm.

Efforts were made to integrate observations from the drawing of three different GSEs with a predictive model developed to relate characteristic thermal behavior with film drawing conditions. This approach has identified key parameters, determined using DSC measurements, to predict film drawing viability for a given MOSN glass composition. A standardized experimental design has been produced that creates a method to screen potential candidate GSEs for thin film preparation using a series of DSC measurements that require only a small (< 5 g) sample batch. This process reduces both the cost and time required to evaluate new GSEs, allowing for increased compositional screening.

Film drawing has been done with several test glasses, including lithium metaphosphate ($LiPO_3$), lithium-containing MOS glass (ISU-6), and sodium-containing MOSN glass. Both the $LiPO_3$ and sodium MOSN glasses have been successfully drawn into < 100 μm film, multiple times. However, processing the ISU-6 has been unsuccessful due to cracked preforms and sample crystallization. This difficulty resulted in efforts to better understand the material requirements for drawing thin film GSEs.

For successful film processing, the glass has to be heated to its softening point, typically defined as ~ 10^6 (Pa·s). The Mauro–Yue–Ellison–Gupta–Allan (MYEGA) model was used to describe the temperature-dependent viscosity of the different glasses on heating to identify optimal film drawing temperature. A series of DSC measurements allows for creation of a viscosity-versus-temperature curve for the given glass chemistry (Figure 11), giving the softening temperature. For successful film processing, the glass must remain crystallization free during heating and drawing. Previous work found the crystallization temperature with DSC experiment at a heating rate of 20 K/min. However, film processing involves much slower heating rates for the preform (as low as 0.5 K/min), as well as long isothermal holds at temperature. By conducting multiple DSC measurements at different heating rates, the lowest hypothetical crystallization temperature can be extrapolated. This method provides an upper limit, or "cut-off" temperature, for film processing to avoid any crystallization issues, as shown in Figure 11.

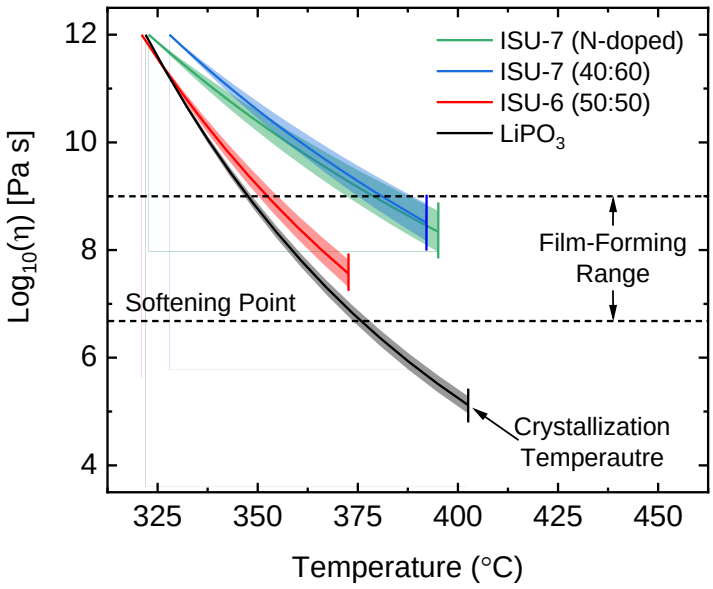

Figure 11. Combining the viscosity curves from the Mauro–Yue–Ellison–Gupta–Allan (MYEGA) model and the crystallization cut-off gives the graph shown, which can be used to evaluate candidate glassy solid electrolytes. Ideal chemistry will have a curve that extends well below the softening point.

Fabricate and Test All-Solid-State Lithium Batteries (ASSLBs) GSEs in Large Area Planar Formats

- Complete testing of optimized MOSN MGF GSE in small-cell-format ASSLBs.
- Initiate testing of optimized MOSN MGF GSE in intermediate-cell-format ASSLBs.
- Initiate testing of optimized MOSN MGF GSE in large-cell-format ASSLBs.

The electrochemical potential window of ISU-7 (x = 0.2) and of ISU-8 (y = 0.58 and z = 0.025) was determined through CV from 0.0-5.0 V versus Li/Li$^+$, as shown in Figure 12. Small oxidation peaks present in both ISU-7 and ISU-8 ~ 1.5-2.5 V versus Li/Li$^+$ can likely be attributed to oxidation of polysulfides due to Li-S impurities in the glass. The peak present in ISU-8 at ~ 1.0 V may be due to an electrochemical conversion reaction between lithium and an aluminum oxysulfide species. Further work and literature review are being done to better characterize this feature. The low currents of these peaks indicate that the reaction is minimal and will be negligible during cycling. Both ISU-7 and ISU-8 appear to be stable from 0.0-5.0 V, with no major oxidative or reductive peaks between 3.0-5.0 V and only minor peaks present below 3.0 V.

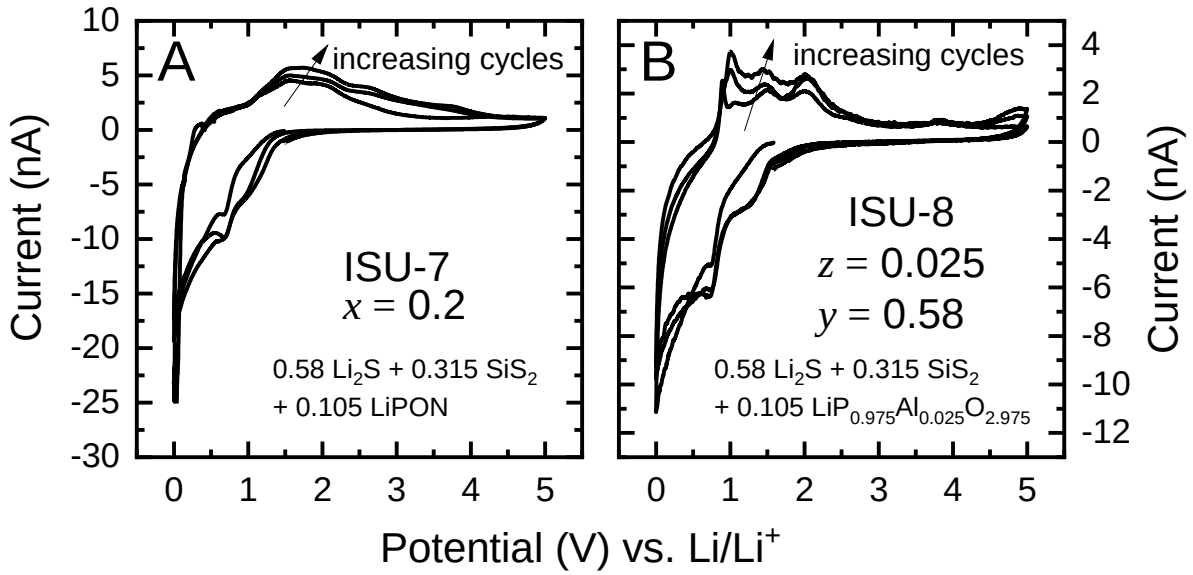

Figure 12. Cyclic voltammetry of (a) ISU-7 (x = 0.2) and (b) ISU-8 (y = 0.58; z = 0.025) from 0.0-5.0 V versus Li/Li$^+$ showing oxidative and reductive stability of glassy solid electrolytes.

Critical current density (CCD) testing of ISU-8 (y = 0.58, z = 0.05) was conducted on a sample following 100 charge/discharge cycles at 0.05 mA/cm^2. Three cycles were completed at each current density before a stepwise current increase, while cycling capacity was kept constant. Results of the CCD experiment are shown in Figure 13. The cell was cycled with stable overpotentials up until a current density of 0.25 mA/cm^2, upon which the impedance of the cell increased significantly, causing the overpotential to exceed cycling limits. The cell was saved for future testing. The CCD measurement is extremely sensitive to the electrode contact area and the preparation of the cell itself, and it is believed that better contact through lithium evaporation may increase the CCD and allow for a more accurate measurement.

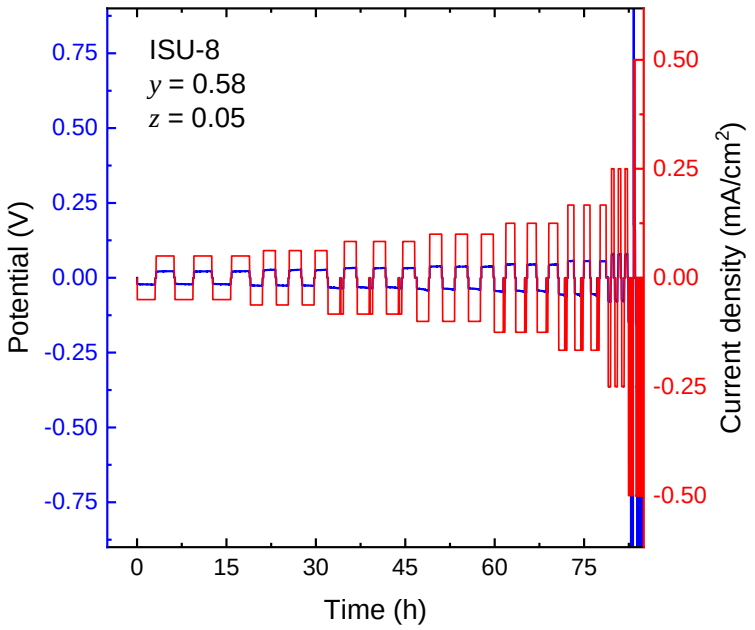

Figure 13. Critical current density (CCD) test for ISU-8 showing CCD of 0.25 mA/cm² at room temperature prior to a spike in cell resistance.

Thin-film glass has been prepared using the ISU-6 composition; the glass was cut into rough disks and the electrochemical stability was evaluated using EIS measurements in symmetric cells. Using a 250-µm thin film, a symmetric cell was prepared; impedance was repeatedly measured during the 24 hours following assembly, with results shown in the Nyquist plot in Figure 14a. While the film exhibits a low bulk glass resistance, two other semi-circles are present, indicating the presence of an interfacial layer and a crystalline phase. The crystalline phase can be visually observed, as the glass appears foggy compared to analogous bulk samples. The resistance of the crystallites and the interface is significantly higher than the resistance of the bulk. Further work is being done on new glass chemistries and different drawing conditions to prevent crystallization during the drawing process.

To evaluate electrolyte performance and cycling stability, full-cell batteries were prepared using several cathode designs with a small-cell format. A hybrid cell design, in which small amounts of LE are used to mediate the cathode SEI was explored. Full cells were assembled using a hybrid design, with a Li-foil anode in direct contact with a GSE disk, while a $LiFePO_4$ (LFP) cathode containing a small amount of LE was used to complete the cell. As shown in Figure 15, preliminary cycling experiments have demonstrated that cells cycle with good reversibility. However, cell resistance is seen to increase during cycling, leading to high polarization between charge and discharge cycles. This is likely due to formation of an unstable SEI or dissolution of the GSE by the carbonate solvent in the LE. Further experiments will be performed to better understand the interaction between the GSE and LE additives.

Recently, several alternative electrolytes based on solvate ionic liquids (SIL) have been prepared to replace the carbonate-based LEs. Past studies have shown these SILs to have a reduced reactivity toward sulfide species, potentially allowing for formation of a more stable hybrid full cell. The behavior of full cells produced with cathodes containing small amounts of SIL electrolytes will be investigated next quarter.

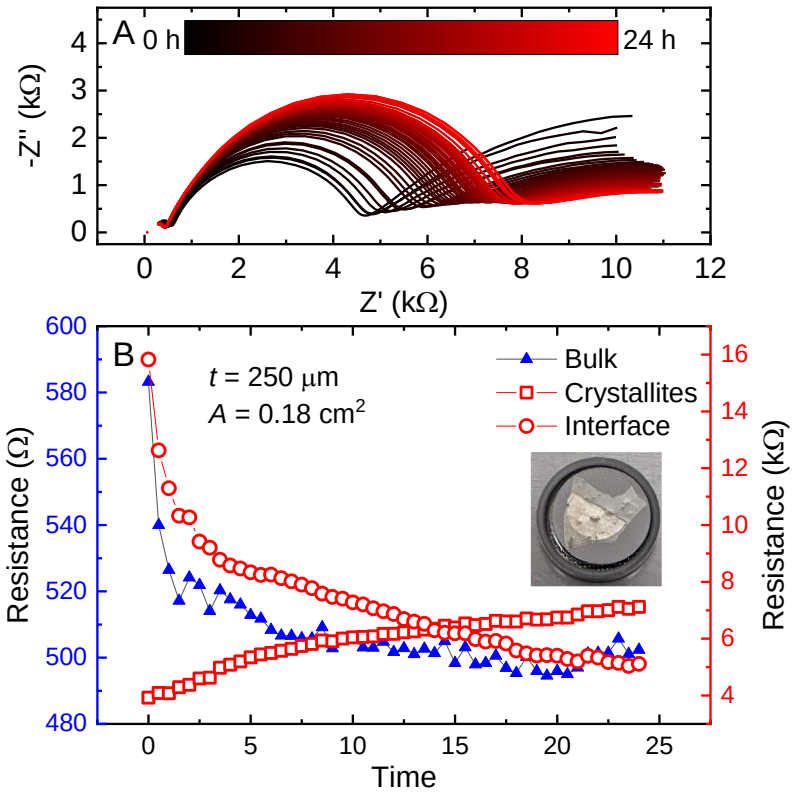

Figure 14. (a) Nyquist plot showing interfacial growth over time for a thin-film cell of 250 μm. (b) Equivalent circuit fitted resistance values for the bulk, crystal, and interfacial resistances of the thin-film symmetric cell.

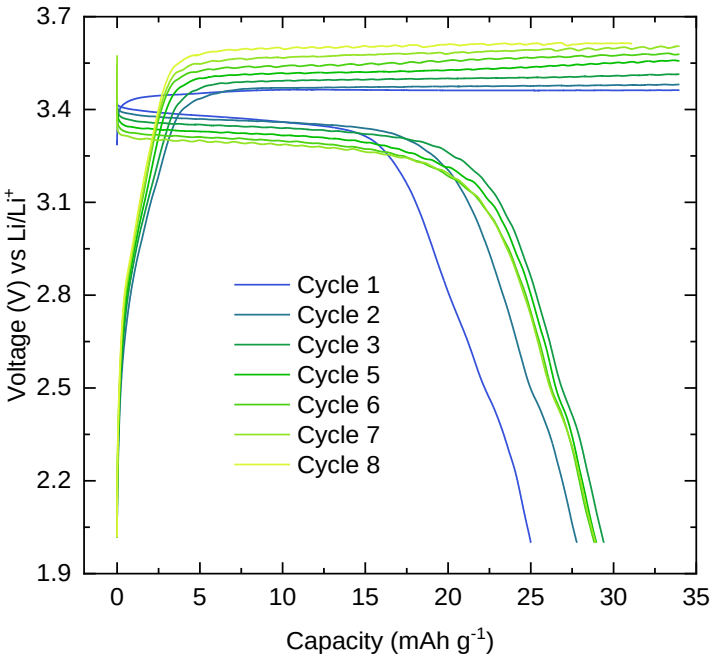

Figure 15. Preliminary cycling results of a hybrid full cell using a mixed oxy-sulfide nitride glassy solid electrolyte with a Li-foil anode and a $LiFePO_4$ cathode.

References

[1] Deshpande, R. R., and H. Eckert. "Sol-Gel Preparation of Mesoporous Sodium Aluminosilicate Glasses: Mechanistic and Structural Investigations by Solid State Nuclear Magnetic Resonance." *Journal of Materials Chemistry* 19, No. 21 (2009): 3419–3426.

[2] Zhang, Z., J. Zhang, H. Jia, L. Peng, T. An, and J. Xie. "Enhancing Ionic Conductivity of Solid Electrolyte by Lithium Substitution in Halogenated Li-Argyrodite." *Journal of Power Sources* 450 (2020): 227601.

Patents/Publications/Presentations

Publication

- Zhao, R., G. Hu, S. Kmiec, R. Gebhardt, A. Whale, J. Wheaton, and S. W. Martin. "New Amorphous Oxy-Sulfide Solid Electrolyte Material: Anion Exchange, Electrochemical Properties, and Lithium Dendrite Suppression via *In Situ* Interfacial Modification." *ACS Applied Materials & Interfaces* 13, No. 23 (2021): 26841–26852.

Presentation

- 239th Electrochemical Society (ECS) Meeting, Virtual (May 30, 2021): "Electrochemical Characterization of a Drawn Thin-Film Glassy Oxide Electrolyte Material for Solid-State Battery Applications"; J. Wheaton, S. Kmiec, and S. W. Martin.

Task 1.5 – Composite Solid Ion Conductor with Engineered Lithium Interface (Kyler Carroll and Cam Peebles, Wildcat Discovery Technologies)

Project Objective. In this project, Wildcat seeks to perform focused, fundamental research and development on composite polymer/ceramic electrolytes and for the protection of Li-metal anodes to develop a Li-metal all-solid-state battery (ASSB) that achieves DOE requirements for performance to enable potential commercialization of this technology. Wildcat will leverage its high-throughput (HT) battery platform to explore a broad composite electrolyte compositional space. Additionally, the HT platform will allow the team to screen hundreds of inorganic and organic coatings for Li-metal protection and translate the best results to all solid cells.

Project Impact. Successful widespread commercialization of EVs is contingent on developing safe high-energy-density batteries capable of long cycle life. Lithium metal affords the highest theoretical capacity (3,860 mAh/g) and lowest electrochemical potential (-3.04 V versus self-healing electrolyte), which offers the highest specific energy density of anode materials today. However, significant progress toward the passivation of lithium metal must occur before the energy density benefit can be realized. The intrinsic high reactivity between lithium metal with conventional Li-ion electrolytes (organic carbonate-based solvents) makes it extremely difficult to overcome these problems. The proposed composite polymer/ceramic electrolyte and a protected Li-metal anode will enable a Li-metal ASSB. It is expected that the outcomes from this effort will deliver a safe all-solid-state Li-metal pouch cell with over 350 Wh/kg and over 1,000 cycles (C/3) with the cost estimate below $100/kWh.

Approach. The project approach involves (1) identifying a suitable combination of solid ion conductor, polymer, and additive that minimizes overall interfacial impedance between the PE and solid ion conductor, and (2) identifying stable Li-metal protection agent or combination of agents that shows enhanced cycling performance (relative to a non-protected system) using the down-selected cell architectures.

Out-Year Goals. The out-year goals involve screening of cathode composites to minimize interfacial resistance, down selection of the best solid-state electrolyte (SSE), and down selection of the best passivation approach for lithium metal. Following these developments, the final tasks will be to integrate these three components into a full ASSB with improved cycle life.

Collaborations. All project tasks will be performed at Wildcat Discovery Technologies.

Milestones

1. Down select passivation approaches. (Q1, FY 2021; Completed)
2. Optimize SE. (Q2, FY 2021; In progress)
3. Integrate SE with cathode. (Q3, FY 2021; In progress)
4. Final testing. (Q4, FY 2021; In progress)

Progress Report

This quarter, Wildcat utilized its HT platform to further improve ionic conductivity of high-voltage PE used in ceramic-polymer composite. Various approaches were proposed and tested. As a result, the team successfully identified a LiFSI/co-polymer system that offers almost 100-times higher ionic conductivity than the PE used in the previous composite electrolyte.

Protection materials were applied to the lithium metal, with the goal of finding a system that showed reduced resistance compared to a baseline (non-protected) system. Systems with reduced resistances have been shown at Wildcat to have better cycling performance when current is passed through them. Once a system with minimal resistance was found, that system was further optimized and then tested in combination with various SSEs that have been developed in another part of this project.

Optimization of Composite Electrolyte

In previous quarters, the team investigated different types of PVDF polymers on their impact on ionic conductivity of ceramic-polymer composite as well as their full-cell performance. Initial results suggest that the polymer could significantly affect the full-cell performance, hypothetically on both the cathode/electrolyte and anode/electrolyte interface. Considering the larger amount of PE in the composite ceramic-polymer electrolyte, having the conductivity of pure PE as high as possible could be an easy approach to improve the composite ceramic-polymer electrolyte conductivity. The PE used in the composite electrolyte reported last quarter was prepared as the control sample, and the conductivity was measured by impedance spectroscopy using blocking electrode. As shown in Figure 16, the pure PE used in previous ceramic-polymer composite electrolyte showed low conductivity, which is 1.6×10^{-7} S/cm at 30°C.

Various approaches have been tried to improve the ionic conductivity of the PE. Figure 16a shows the conductivity of nine polymers that have the same salt/polymer weight ratio (32:68) and same polymer component (PVDF-A). Different colors represent different lithium salts being used. Clearly, lithium salt had a significant impact on the polymer conductivity. Five lithium salts showed much improved conductivity over LiTFSI, which is the salt used in the previous baseline PE. As a result, the team identified several promising salts such as LiFSI, LiOTf, and $LiClO_4$, showing 5-10 times higher conductivity than LiTFSI. The results suggest that an anion of the lithium salt could significantly impact how Li^+ interacts with polymers by changing the crystallinity of the polymer, which could result in a very different Li^+ pathway within the polymer phase.

Organic or inorganic fillers had been widely used to alter crystallinity of polymer in many industrial applications. Another approach the team tried is to investigate several PVDF copolymers with different crystallinity, which may possibly improve ionic conductivity of the PE. Figure 16b shows the efforts in this direction. It turns out that when the team replaces the homopolymer PVDF with PVDF-HFP copolymer with the same exact weigh ratio of LiFSI (32 wt% LiFSI / 68 wt% polymer), the ionic conductivity of the co-polymer is almost 100 times higher (~ 1.8×10^{-5} S/cm). However, introduction of other organic or inorganic fillers did not show significant beneficial effects as expected. This is possibly due to the intrinsic property of the polymers. Nonetheless, the team plans to continue screening more types of organic and inorganic fillers aiming to further improve ionic conductivity with a co-polymer system.

The team also investigated the salt/polymer ratio effect on PE conductivity, as shown as Figure 16c. They down selected the most promising PEs in earlier studies. As expected, the higher the salt concentration, the higher the polymer conductivity. It is worth to noting that the resulting PE still showed good processibility and film quality, even in the presence of up to 50 wt% LiFSI.

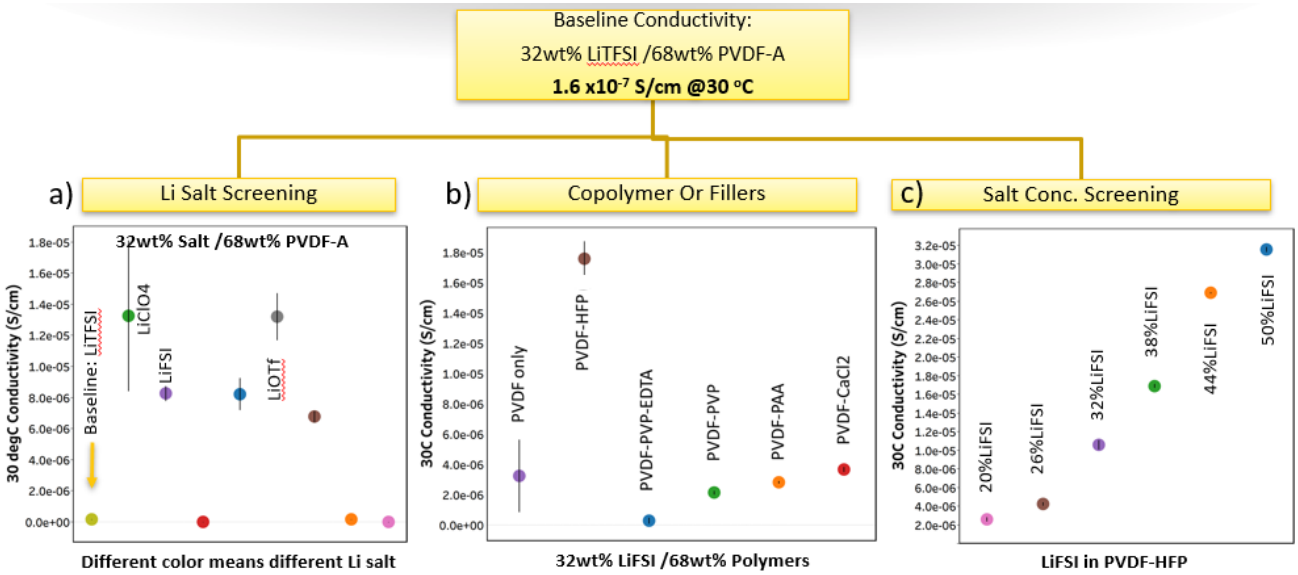

Figure 16. Screening of various polymer electrolytes using stainless-steel / stainless-steel blocking electrode. (a) Lithium salt screening. (b) Co-polymer or filler screening. (c) Salt concentration screening.

Future work in this thrust includes further screening of different types of homo- and co-polymers with different molecular weight, exploring the possible salt/polymer synergy effect; the team will check promising PE effects in the composite ceramic-polymer electrolyte. In parallel, some of the most promising PEs will be tested in Li/Li symmetric cells to understand their intrinsic reactivity toward either protected or non-protected Li-metal surface.

Catholyte Development

Last quarter, Wildcat evaluated different PVDF polymer types in the composite SSE using its HT platform; they shortlisted a few promising candidates based on their conductivities. Wildcat also demonstrated all-solid-state full cells that can charge fully up to 4.3 V versus Li^+/Li. From this evaluation, a PVDF polymer type was chosen for integration with other optimized SSE constituents. This quarter, Wildcat started evaluating composite SSEs containing the chosen PVDF polymer type and two ceramic materials, denoted as SSE A and SSE B. All-solid-state full cells were built with these two composite SSEs, the optimized catholyte selected from last quarter, and the protected Li-metal from Thrust 2. The full cells were cycled in the voltage range of 3.0-4.3 V at a temperature of 60°C. Figure 17a shows the cycle life plots of the all-solid-state full cells. The initial discharge capacities of the full cells with SSE A and SSE B were 206 mAh/g and 213 mAh/g, respectively, which were comparable to the values obtained in a LE cell. After a series of rate capability test steps carried out at 0.1C and 0.2C, the cycle life test step was started at 7^{th} cycle. At the end of 80 cycles, the discharge capacities were 137 mAh/g and 157 mAh/g, corresponding to capacity retention values of 71.7% and 76.2%. Figure 17b shows the voltage traces of the full cells built with the two different SSE types at 1^{st}, 20^{th}, and 60^{th} cycles. The voltage traces at all cycles showed smooth and full charge profiles up to 4.3 V, demonstrating the cyclability of the all-solid-state full cells. Next quarter, Wildcat aims to continue screening catholyte compositions to couple with the optimized SSE composition (SSE B) demonstrated this quarter. Efforts will also be made to test the full cells at a lower temperature and achieve a comparable cycling performance.

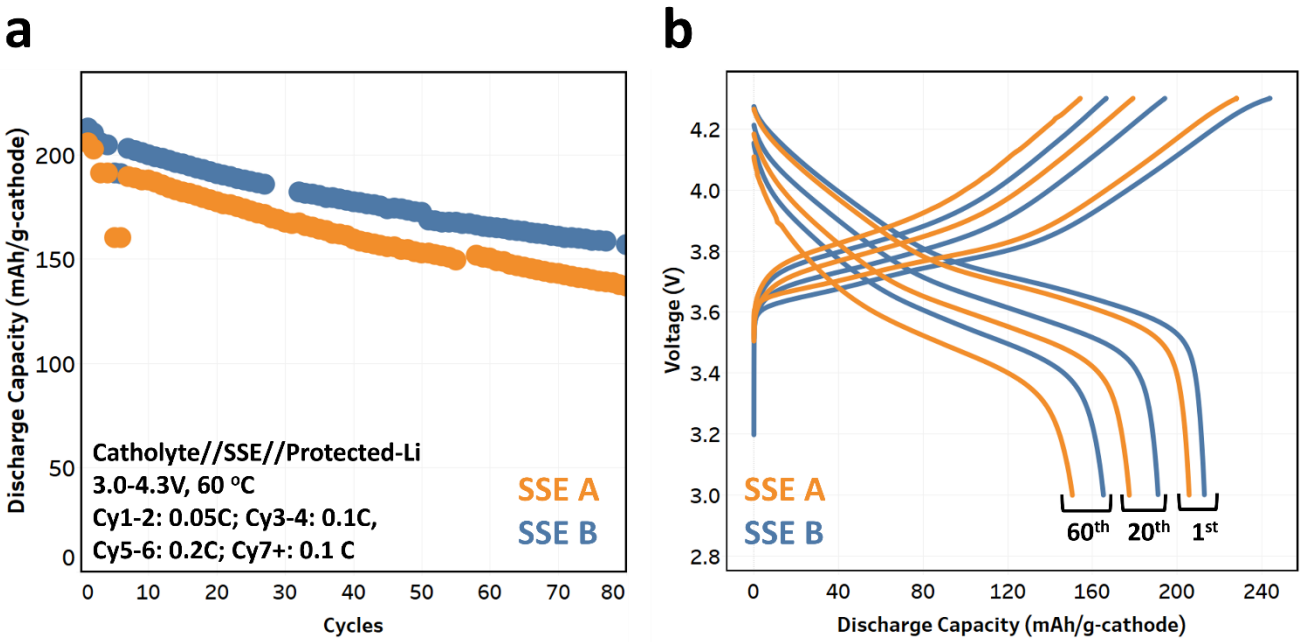

Figure 17. Performance of all-solid-state full cells. (a) Cycle life plot of all-solid-state Li//NMC full cells with different solid-state electrolyte (SSE) types. (b) Voltage traces of Cycles 1, 20, and 60 of all-solid-state full cells with different SSE types.

Patents/Publications/Presentations

Presentation

- DOE VTO Annual Merit Review Meeting, Bat479 (June 24, 2021): "Composite Solid Ion Conductor with Engineered Lithium Interface"; G. Cheng.

Task 1.6 – Physical and Mechano-Electrochemical Phenomena of Thin-Film Lithium-Ceramic Electrolyte Constructs
(Jeff Sakamoto, University of Michigan)

Project Objective. While a small number of SEs exhibit high ionic conductivity (~ 1 mS cm at 298 K), few are stable against lithium metal. The garnet-type SE, based on the nominal formula $Li_7La_3Zr_2O_12$ (LLZO), is unique in that it is a fast ion conductor and—as demonstrated in the team's recent project (DE-EE-00006821)—is stable against lithium. Moreover, the team's former project successfully demonstrated a decrease in Li-LLZO interface resistance from 12,000 $\Omega\,cm^2$ to 2 $\Omega\,cm^2$ and stable cycling at 1 $mA\,cm^2$ for 100 cycles (± 15 µm of lithium per cycle). Although the past project demonstrated that LLZO is a viable SE for enabling batteries using metallic lithium, the studies used thick pellets (1 mm) and thick anodes (~ 500 µm). The goal of this project is to acquire a deep fundamental understanding of the physical and mechano-electrochemical phenomena that control the performance of cells consisting of thin LLZO (~ 10 µm), thin lithium anodes (~ 20 µm), and thin solid-state composite cathodes.

Project Impact. If successful, the project will gain knowledge to guide closely related commercialization efforts to scale the production of LLZO-based solid-state batteries (SSBs).

Approach. The team believes that to achieve a step increase in technology readiness level (TRL), the same performance characteristics previously shown should be demonstrated in technologically relevant cells, for example, thin LLZO and thin lithium.

Out-Year Goals. Out-year goals involve the following: custom thin-film composite (TFC) development, preliminary cycling studies, Vis cell development, lithium cycling, and polymer gel electrolyte (PGE) screening.

Collaborations. This project collaborates with N. Dasgupta and D. Siegel of University of Michigan (UM), Mechanical Engineering.

Milestones

1. Initial design, fabrication, testing, and optimization of custom *operando* optical visualization cell. (Q1, FY 2021; Completed)

2. Initial integration of precision micro reference electrodes with thin lithium and TFC for 100 cycle tests. (Q2, FY 2021; Completed)

3. In thin lithium and thin LLZO TFC, determine max cycling rates versus lithium thickness ranging between 2-17 µm. (Q2, FY 2021; Completed)

4. Refinement of custom *operando* optical visualization cell to quantify topographic lithium plating homogeneity versus cycle number. (Q4, FY 2021; In progress)

Progress Report

The pressure needed for operation is an on-going debate within the Li-metal SSB community. This quarter, the effect of creep was studied as a function of lithium anode thickness and pressure (Figure 18). The team has determined that creep behavior dramatically changes with lithium thickness. Typically, creep behavior is controlled by constitutive equations and should not be affected by geometric effects such as thickness. However, owing to the clear effect of thickness, other physical phenomena influence lithium behavior. Owing to adhesion among lithium, SE, and a current collector, it is likely that hydrostatic stress states are created. As lithium anode thickness decreases, the effect of adhesive forces increases, thus creating hydrostatic stress.

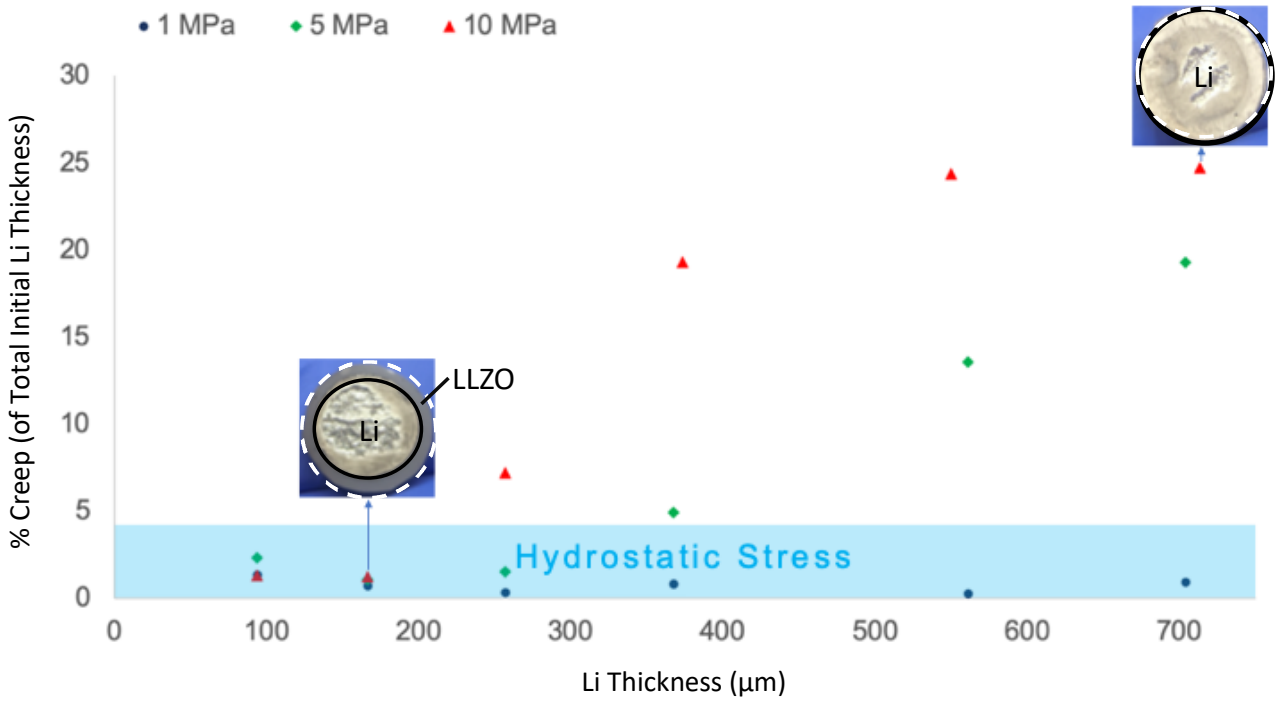

Figure 18. Percentage of creep versus lithium thickness.

As the thickness of the Li-metal anode decreases (LLZO/Li/Ni configuration), the creep deformation of lithium also decreases (lithium area = 1.26 cm^2; pellet diameter = 1.26 cm). As the pressure increases, and Li-anode thickness is > 150 µm, the creep deformation increases. The insets in Figure 18 show that after creep tests at 10 MPa, the 150-µm-thick lithium anode retains close to its original diameter, while the 700-µm-thick lithium anode covers the whole diameter of the LLZO pellet, which is beneath the lithium anode and cannot be seen. These results have implications for stack pressure requirements for solid-state Li-metal batteries (SSLMBs).

Patents/Publications/Presentations

Patent

- Issued: Sakamoto, J., T. Thompson, and A. Sharafi – U. S. Patent 10,938,061; 2021 System and Method for Treating the Surface of Solid Electrolytes. https://patents.google.com/patent/US10938061B2/en.

Presentation

- DOE VTO Annual Merit Review Meeting (June 2021): "Project Summary."

Task 1.7 – Lithium Dendrite-Free Li_7N_2I-LiOH Solid Electrolytes for High-Energy Lithium Batteries (Chunsheng Wang, University of Maryland)

Project Objective. The objective of this project is to research, develop, and test Li-metal-based batteries that implement solid Li-ion conductors (LICs) equipped with Li_7N_2I-LiOH SE capable of achieving cell performance of 350 Wh/Kg energy density for 1000 cycle life with a cost of ≤ $100/kWh.

Project Impact. Lithium dendrite growth during charge/discharge cycles limits the use of ASSBs. A criterion for lithium dendrite suppression that is developed through systematical investigation on thermodynamics and kinetics of lithium dendrite growth will guide the electrolyte design. Li_7N_2I-LiOH and Li_3YCl_6 SE with high ionic conductivity and low electronic conductivity will be used to validate the criterion for lithium dendrite suppression, to achieve the project objective.

Approach. The team will establish the relationship among interface energy, lithium plating/stripping overpotential, interface resistance, SE stability with lithium, and CCD. The dendrite suppression criterion will be developed based on the relationship. The dendrite suppression capability for the Li_7N_2I-LiOH pellet will be evaluated by testing the CCD.

Out-Year Goals. The project will study the thermodynamics and kinetics of lithium dendrite growth in SSEs and develop lithium dendrite suppression criterion in SSEs. The Li_7N_2I-LiOH electrolytes and Li_7N2I-LiOH/Li_3YCl_6 bi-layer electrolytes will be used to validate the developed dendrite suppression criterion and support NCM cathodes.

Collaborations. There are no reported collaborations this quarter.

Milestones

1. Determine critical overpotential of Li_7N_2I-LiOH, Li_3PS_4 (LPS), and LLZO electrolytes. (Q1, FY 2021; Completed)
2. Develop lithium dendrite suppression criterion for SSEs. (Q2, FY 2021; Completed)
3. Develop a kinetics model of SSEs. (Q3, FY 2021; Completed)
4. Critical current of Li_7N_2I-LiOH electrolytes should be > 4 mA/cm^2 at 3 mA/cm^2 of current. (Q4, FY 2021)

Progress Report

Kinetics for Dendrite Growth in SSE

Lithium dendrite growth in SSEs depends on driving force (applied lithium plating potential, η_{app}) and resistance (critical lithium plating overpotential in SSE, η_{cri}). The η_{cri} is determined by the properties of SSEs, including thermodynamic stability, ionic conductivity, electronic conductivity, porosity, interface energy, and mechanical strength. Once the η_{app} exceeds the η_{cri}, lithium dendrites begin to grow. As shown in Figure 19a, the standard free energy profiles along the reaction coordinate have parabolic shapes, and $Li^+ + e^- \rightleftharpoons Li_{(inside\ SSE)}$ reach equilibrium (red dash lines). During lithium plating, the η_{app} is applied to the anode, resulting in an overpotential inside the SSE (η_1). The correlation between the η_{app} and η_1 is governed by the electronic conductivity and area specific resistance (ASR) of SSE. Lithium dendrite growth in SSEs can be analyzed by Butler-Volmer (BV) reaction kinetics. At an open circuit potential, lithium stripping is favored rather than lithium plating inside SSE. After applying η_1 overpotential during lithium plating on lithium anode, lithium plating inside the SSE energy curve moves up by $F\eta_1$, which reduces the energy barrier for lithium plating ($\Delta G'_{Li^+ + e \rightarrow Li}$) and increases the energy barrier for lithium stripping ($\Delta G'_{Li + e \rightarrow Li^+}$). At the same time, the local stress and the interface energy against lithium (E_{Li}^{SSE}) of the SSEs will provide overpotential (η_2 and η_3 in Figure 19b) for the dendrite formation. The energy barrier for lithium nucleation and growth inside SSE ($\Delta G''_{Li^+ + e \rightarrow Li}$) will be increased by the η_2 and η_3. To suppress lithium dendrite growth in SSEs, η_1 needs to be reduced by increasing ionic conductivity and also reducing electronic conductivity and ASR. Meanwhile, the $\eta_{cri} = \eta_2 + \eta_3$ of SSEs should be increased to enhance local stress and interface energy of SSEs. As shown in Figure 19b, for the electrolytes that are not dense, lithium infiltration into porous SSEs behaves like an incompressible work fluid, driven by the chemical potential/pressure gradient and interface energy of Li/SSEs. The dendrite can easily propagate in the SSEs with high electronic conductivity and low interface energy. However, for the SSEs that are electronic insulators with a high interface energy, the nucleation and growth should be suppressed. In summary, to suppress dendrite growth inside porous SSEs, the kinetics of lithium dendrite formation inside SSEs should be carefully studied.

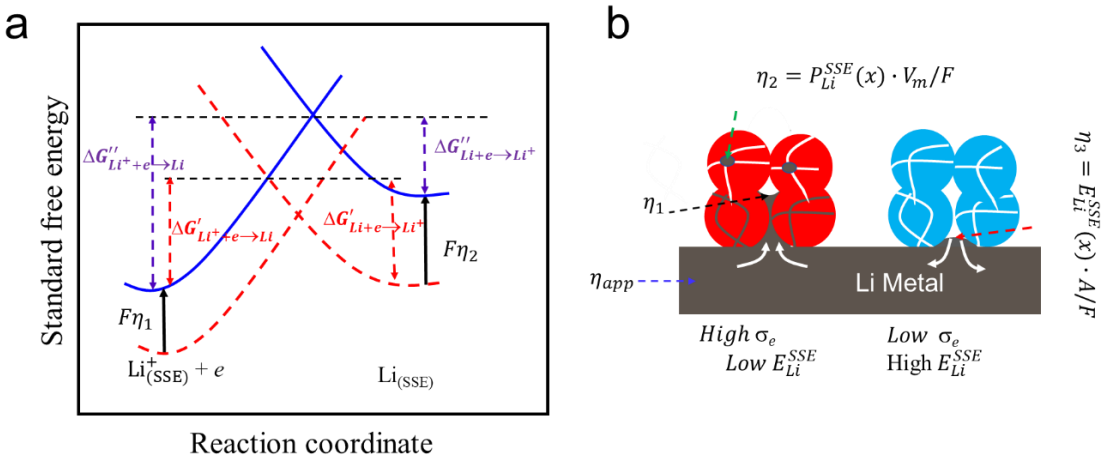

Figure 19. Kinetics of lithium dendrite growth in solid-state electrolytes (SSEs). (a) Illustration of Butler-Volmer kinetic model for lithium plating in SSE. (b) Lithium dendrite growth in stable SSE, which is not dense and has different electronic conductivity and interface energy; P_{Li}^{SSE} is the stress of lithium nucleation site, E_{Li}^{SSE} is the interface energy of SSE against lithium, V_m is the lithium molar volume, A is the interface area, and F is the Faraday constant.

Decomposition Kinetics of the Sulfide SSE

The thermodynamics of decomposition of SSEs have been widely investigated using the phase diagram calculated using density functional theory (DFT). However, the equilibrium stability window that is calculated by using the Gibbs energies thermodynamic stable phases did not take kinetics of decomposition into account. Many experimental works reveal the importance of the kinetics of decomposition, and some SSEs can be kinetically stable during the electrochemical process. This quarter, the team studied the detailed decomposition process of sulfide SSEs using *ab initio* molecular dynamics (AIMD) and defect formation energy (DFE) calculations.

To give an atomic picture of the dynamic decomposition process, the lithium | $Li_{10}GeP_2S_{12}$ (LGPS) interface reaction was simulated at room temperature using AIMD (Figure 20). Significant decompositions at the interface after 20 ps of AIMD simulations are noteworthy (blue rectangles), with P-S and Ge-S bonds broken and new Li-S bonds formed. Specifically, for Li|LGPS interface (Figure 20a-b), lithium atoms can insert into LGPS, while germanium and sulfur atoms can move into the lithium bulk, indicating a strong mass exchange at this interface. Since simulations were carried out at room temperature for a short time (20 ps) before applying external voltage, the strong interfacial reaction indicates that the LGPS is kinetically unstable against lithium. During the electrochemical process, especially with extra negative voltage applied, decomposition would be intensified.

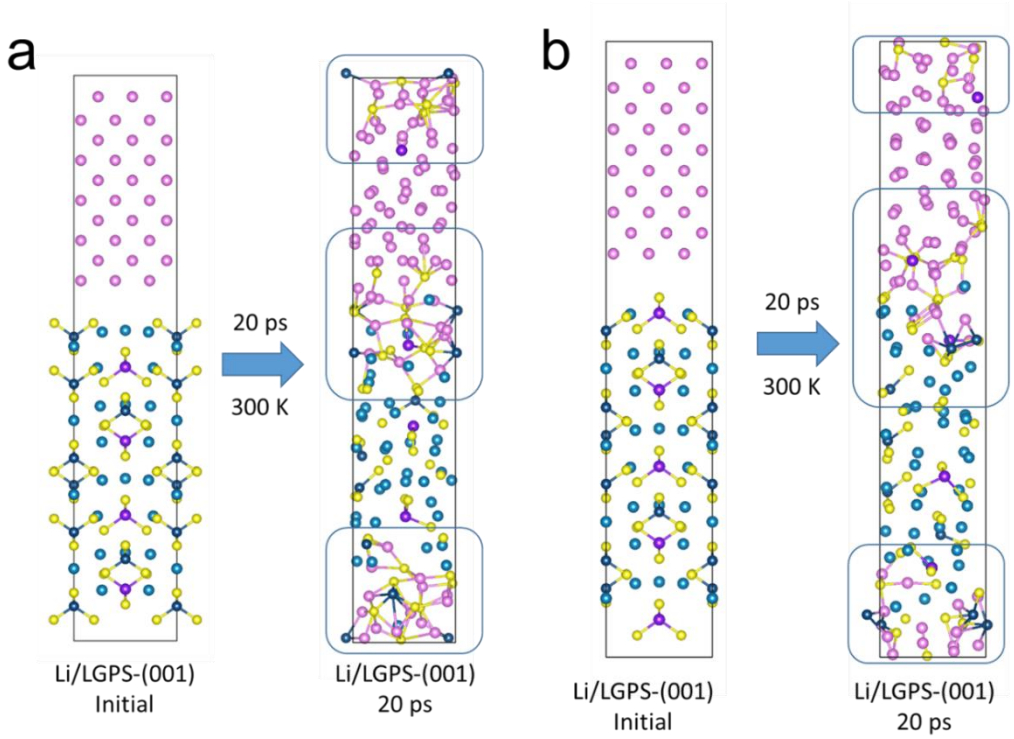

Figure 20. Illustration of structural change of (a) Li|LGPS-(001) with the Ge-S terminated and (b) LiMg|LGPS-(001) interface with P-S terminated LGPS surface after *ab initio* molecular dynamics simulations (20 ps at 300 K) compared with initial configuration. Blue rectangles indicate the formed interphases.

The interface energy of SSE against lithium is one of the most critical properties for SSEs, in addition to high ionic conductivity and low electronic conductivity. An SSE with high interface energy can prevent lithium dendrite nucleation and growth inside the SSE, even if the SSE has a high porosity. Since the most highly ionic conductivity electrolytes are unstable with lithium, SEI will generate because of the chemical reaction. If the formed SEI has a high interface energy with lithium, the SEI still can suppress lithium dendrite nucleation and growth. However, if the SEI has a low interface energy and high electronic conductivity, the SEI will accelerate lithium dendrite growth.

By taking the typical LPS electrolyte as an example, the team calculated the DFE of LPS from the DFT by using first-principles calculations. Figure 21a shows the DFT models for the defect LPS crystal, and Figure 21b demonstrates their corresponding DFE at the chemical potential of Li-rich LPS (μ_{Li} = -1.71 eV). The DFEs indicate that S-vacancy (V_S) and Li-vacancy (V_{Li}) are the main intrinsic defects at that chemical potential and 300 K. The V_S will lead to decomposition of the anion framework and formation of Li_2S. Figure 21c exhibits the Fermi level determined by the charge neutrality at 300 K and defect concentration as the function of lithium chemical potential (μ_{Li}). The stability window of LPS is indicated by the solid vertical lines in Figure 21c. V_{Li} and lithium interstitial (Li_i) are the main intrinsic defects, with similar concentrations that suggest lithium vacancies and interstitials are perceived as the mobile charger species. The lithium chemical potential reaches to 0.0 eV, which is consistent with the situation that LPS contacts to lithium metal. The increases in concentration of V_S indicate that the PS_4 anion framework fails. The high V_S concentration as charge carriers denies the unit transference number at the interface region. As the lithium chemical potential increases, the Fermi level increases because the defects create additional states in the band gap. The up shift of the Fermi level at the increasing of μ demonstrates that more electrons can migrate and cumulate in the LPS SSEs, increasing electronic conductivity. The energy diagram (Figure 21d) between the lithium metal and LPS interface has been calculated to show the space charge region. The electrostatic potential difference (φ_{Li}^{SSE}) at the interface is proposed to be 1.39 V, which is considered as a large driving force for the redistribution of charge carriers, decomposing the LPS. The detailed energy diagram parameters were listed in Table 3.

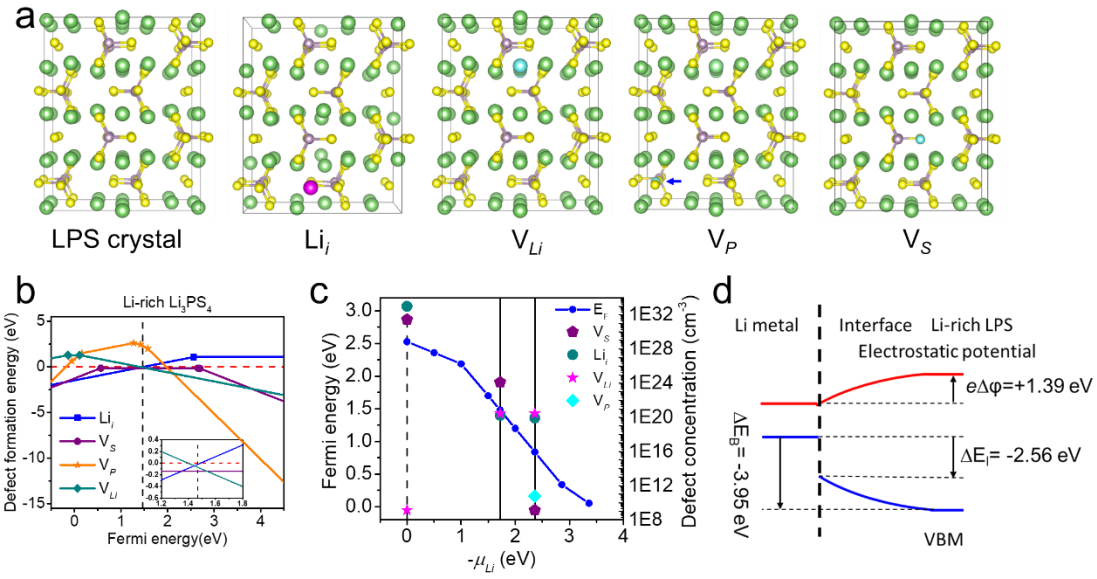

Figure 21. Defect formation energy (DFE) calculations on the chemical decomposition of the Li|LPS interface. (a) Schematic density functional theory models for defect Li_3PS_4 (LPS) crystal. (b) DFE as a function of Fermi energy in Li-rich Li_3PS_4 (μLi = -1.71 eV). The Fermi energy is referenced to the valence-band maximum (VBM). The slopes of the lines are the charge states of the defects. The symbols at the kinks are the charge-state transition levels. Inset shows details near the charge-neutrality Fermi energy (dash line) at 300 K. (c) Fermi level reference to VBM determined by charge neutrality at 300 K and defect concentration as a function of lithium chemical potential. (d) Schematic of the electrostatic potential and valence bands at the Li/LPS interface (see details in Table 3 below).

Table 3. Density functional theory calculated bulk quantities for Li_3PS_4 and band offsets and electrostatic potential drops for Li|Li_3PS_4 interface.

	E_f	IP	$\tilde{\mu}_e$
Li metal	0	3.14	0
Li_3PS_4 (Li-rich)	2.53	5.70	-1.42
	ΔE_B	ΔE_I	$\Delta\varphi$
Li|Li_3PS_4	-3.95	-2.56	1.39

The calculation details are the same with the previous work. E_f : Fermi energy; IP: ionization potential; $\tilde{\mu}_e$: electrochemical potential of electrons; ΔE_B: the difference in bulk valence band maximum (VBM), $\Delta E_B = \Delta\tilde{\mu}_e - \Delta E_f$; ΔE_I: the intrinsic valence band offset at the interface, $\Delta E_I = -\Delta IP$; and $\Delta\varphi$: the interfacial potential drop, $\Delta\varphi = (\Delta E_I - \Delta E_B)/e$.

Electronic Conductivity and Interface Energy for the Interphases

The electronic conductivity of LPS and the decomposed products was evaluated by calculating the density of states (DOS). According to the thermodynamic phase diagram and experimental results, the decomposition products of LPS are Li_2S and Li_3P. Figure 22a-c shows the DOS of LPS, Li_2S, and Li_3P. LPS and Li_2S can be treated as electronic insulators for their large band gaps of 3.86 eV and 4.14 eV. However, the small band gap (1.25 eV) of Li_3P crystal indicates its electronic semiconductor characteristic. At the electron leakage site, the chemical potential of lithium atom in SEI layer is $\mu_{Li}^{SEI} = 0$. The mass spatial distribution of the reduction products will lead to electric field distribution, making $\mu_{Li}^{SEI} \ll 0$ with the applied external circuit (η_1). The reduction reaction also leads to volume change, thus introducing cracks in the SSE layer and reducing the stress (η_2). The reaction-induced cracks will also provide opportunity for physical lithium dendrite formation pattern.

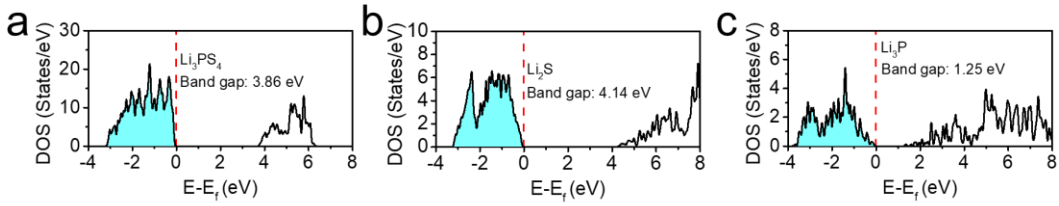

Figure 22. The density of states (DOS) and HSE06 band gap for (a) LPS, (b) Li_2S, and (c) Li_3P. The Fermi levels are set to be 0 eV (red dashed lines).

The interface energy of LPS, Li_2S, and Li_3P against lithium was also calculated (Figure 23). That of LPS and lithium metal is calculated to be -88.92 eV/Å^2. The negative interface energy indicates spontaneous chemical reaction between lithium and LPS. The P-S tetrahedron breaks and sulfur atoms migrate to the surface, re-bonding with the lithium atoms from lithium metal. The low interface energy of Li_2S against lithium metal (19.01 eV/Å2) indicates its low capability in blocking lithum dendrite growth. Li_3P has a higher interface energy than Li_2S, but its interface energy is much lower than LiF. In addition, the high electronic conductivity of Li_3P promotes lithium dendrite growth. Based on the interface energy calculation, the team concludes that LPS is unstable against lithium metal; the LiF is stable and highly lithiophobic, which can block dendrite penetration inside the SSE for the large η_3.

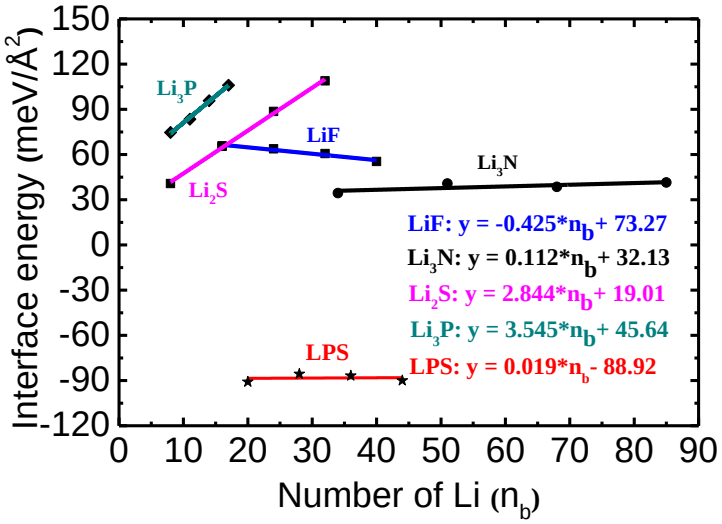

Figure 23. Plot of the relationship between interface energy for Li_3PS_4 (LPS), LiF, and Li_3N and number of Li-metal formula units. The data for LPS and LiF are obtained from a previous publication, while the data for Li_3N are calculated using the same method as in the previous work. The interface energy can be obtained from the intercept of the fitted lines. The negative interface energy (-88.92 meV/Å^2) of LPS indicates that it is unstable against lithium metal. The interface energies for LiF and Li_3N are 73.27 meV/Å^2 and 32.13 meV/Å^2, respectively.

Interface Designed Based on the Kinetic Principles

With the guidance of the kinetic model, a new $LiYO_2$-based interface is developed to suppress dendrite growth inside SSEs. The CCD measurement shows that the formed $LiYO_2$ interface can reach a high CCD of 1.15 mA/cm^2 (Figure 24a). The comparison of the LiAu anode and LiY anode with different concentrations is shown in Figure 24b. The LiY anode with the $LiYO_2$ interphase exhibits much higher CCD than the LiAu anode. The depth profiling of the yttrium from time-of-flight secondary ion mass spectrometry (TOF-SIMS) validated the aggregation of yttrium at the interface (Figure 24c). The DFT calculations shown in Figure 24d further confirm the thermodynamic stability of the $LiYO_2$ against lithium metal. The decent electrochemical performance and interfacial characterization confirm the proposed kinetic principles.

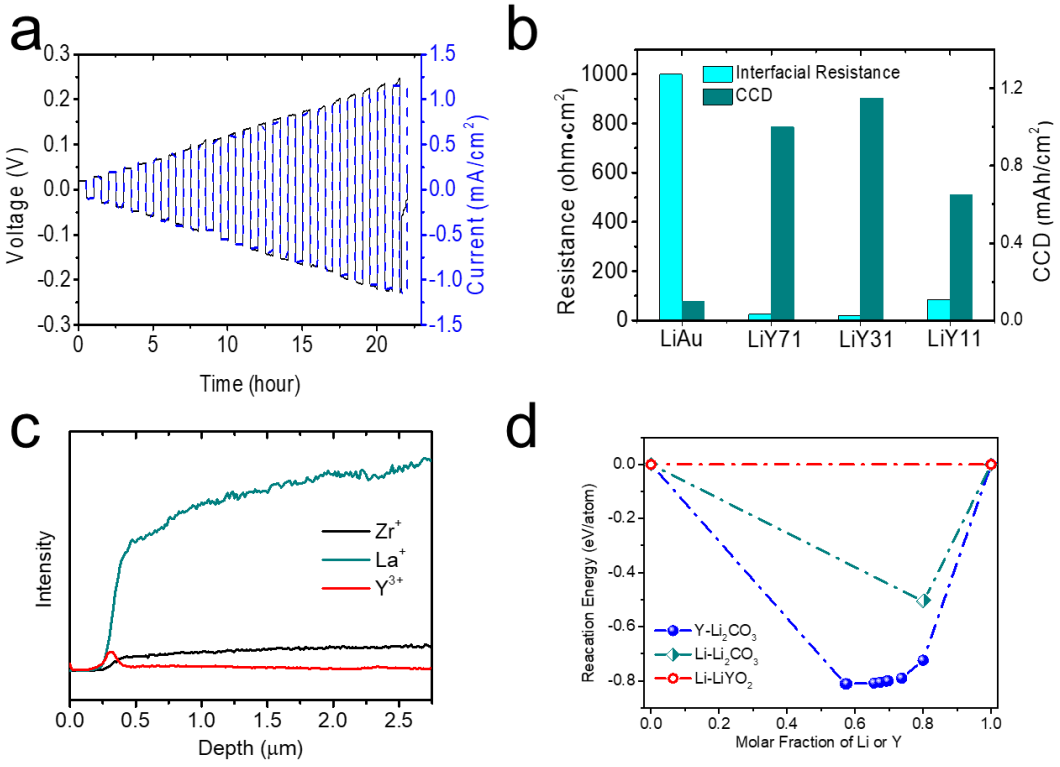

Figure 24. Novel interface design based on the kinetic principles for dendrite suppression. (a) Critical current density (CCD) measurement for the LiY_{31}|LLZTOLiY_{31} cell at a step-increased current density with a fix charging/discharging time of 0.5 hours. (b) Summary of interfacial resistance and measured CCD for cell with Li-Au and Li-Y anode. (c) Depth profiling of spatial distribution of zirconium, lanthanum, and yttrium element at the interface. (d) Thermodynamic equilibrium reaction energy for Y-Li_2CO_3, Li-Li_2CO_3, and Li-$LiYO_2$ interfaces.

Engineered Lithium Anode for High-Capacity SSBs

Based on the thermodynamic and kinetic analysis of the interface of Li/SSE, a robust and Li-ion conductive SEI should be formed between the SSEs and lithium anode, which has sufficient strength to suppress lithium dendrite penetration while maintaining close contact with SSEs. In this part, the team explored a new interfacial engineering method to manufacture Li-metal anodes for real application: the engineered lithium (eLi) is thin with known capacity (4 mAh cm^{-2}) for well-known SSEs, including garnet-types electrolytes, sulfide-based electrolytes argyrodite-Li_6PS_5Cl (LPSCl) and composite polymer electrolytes (CPEs). This surface engineering method for eLi anode not only stabilizes the Li-SSEs interface, but also provides a cheap option for large-scale production in SSLB application.

First, the team assembled the lithium symmetric cells with LPSC electrolyte to demonstrate the dendrite suppression capability and cycling stability (Figure 25). As shown in the inset of Figure 25a, the thin LPSC film with a thickness of 15-20 μm was prepared by grinding the LPSC powder with PTFE binder, followed by

by mold-cutting into discs with diameter of 10 mm. CCD measurement was conducted to demonstrate the capability of eLi anode to suppress lithium dendrite penetration using the lithium symmetric cell eLi|LPSC|eLi under fixed areal capacity of 0.25 mAh cm^{-2}. As shown in Figure 25a, the cycling of symmetric cell is fairly stable, and its potential response highly follows with Ohm's Law under different current densities (0.2-1.6 mA cm^{-2}). The cell voltage is ~ 40 mV at 0.2 mA cm^{-2} due to the enhancement of surface contact and formation of Li-ion conductive SEI. With the increase of current density, the corresponding voltages present arc-like shape due to limited kinetics of lithium ions near the interface. Finally, the cell was shorted by lithium dendrite when the current density reached to an extreme high value of 1.6 mA cm^{-2}, which has never been reported for the dry and thin film of sulfide-based SSEs.

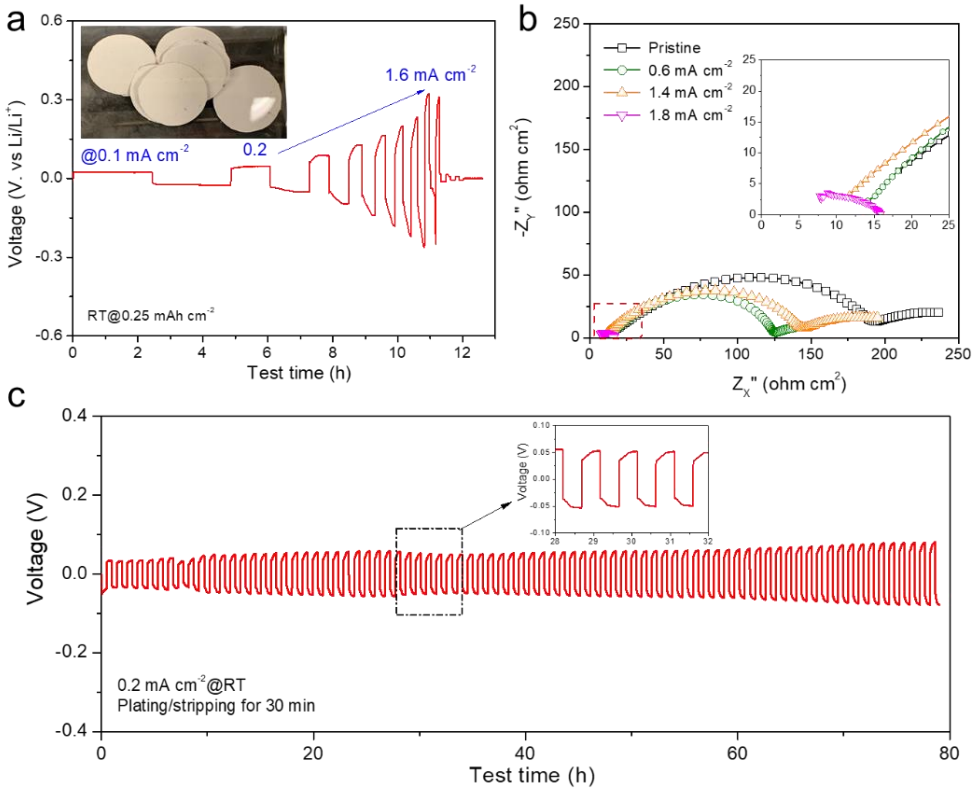

Figure 25. Electrochemical performance of eLi|LPSC|eLi symmetric lithium cell at room temperature: (a) Voltage profiles of the cell under step-increased current densities from 0.2-2.0 mA cm^{-2} for lithium plating/stripping under fixed areal capacity of 0.25 mAh cm^{-2}, 0.2 mA cm^{-2}/per step. (b) Nyquist plots of the symmetric cell under different current densities, confirming the short circuit occurred at 1.6 mA cm^{-2}. (c) Galvanostatic cycling of eLi|LPSC|eLi cell at current density of 0.2 mA cm^{-2} with constant plating/stripping time of 30 minutes; cycling continues.

Figure 25b shows the impedance change of the symmetric lithium cell during the CCD testing. Only one semicircle can be observed in the EIS curves: the interception at high frequency range is attributed to the bulk resistance of the LPSC film electrolyte (~ 15 Ω cm^2), while the semicircle in the intermediate frequency could be caused by the resistances from SEI, grain boundary (GB) structure, and surface layer of eLi (130 Ω cm^2 in total). Overall, the total resistance of the lithium symmetric cell remains almost stable before short circuit occurs. The team further tested the cycling stability of eLi|LPSC|eLi cell at constant current density of 0.2 mA cm^{-2}. The cell presents fairly stable cycling with small increase of polarization after 80 cycles (Figure 25c). The cell is still running, and the team is expecting to increase the plating/stripping time or areal capacity for demonstrating the high-capacity cycling. In general, these results demonstrate that the designed eLi anode can effectively stop the continual reduction of electrolytes and simultaneously protect the Li-SSE interface by suppressing lithium dendrite penetration and preventing loss of surface contact due to morphology change.

With the similar testing apparatus and methods, the team further tested the symmetric lithium cells based on CPE film electrolyte under constant plating/stripping time of 30 minutes at 0.2 mA cm^{-2} (Figure 26). As can been seen in Figure 26a, the cell presents very small and stable voltage (~ 30 mV) even after more than 500 hours of cycling. On the contrary, the lithium symmetric cell Li|CPE|Li shows continual increased polarization (~ 50 mV) when cycled at 0.2 mA cm^{-2}. The uneven lithium dissolution/deposition caused by unstable interphase formation leads to lithium dendrite formation and finally shorts the cell at 48 hours due to dendrite penetration. From the enlarged view of voltage profiles, the team found that the lithium symmetric cells with CPE film display miner "arc" voltage curves, which highly relates to the softness of polymer and good surface contact. The sudden drop of cell voltage for Li|CPE|Li cell might be related to dead lithium accumulation near the Li/CPE interface or lithium propagation along the CPE film. Figure 26b shows the impedance change of the eLi|CPE|eLi cell during lithium plating and stripping. It shows a semicircle at a high frequency range of Nyquist plots due to formation of SEI formation and introduced polymer layer on eLi anode. The almost constant resistance indicated by Figure 26b confirms the stability of eLi anode to CPE film electrolytes.

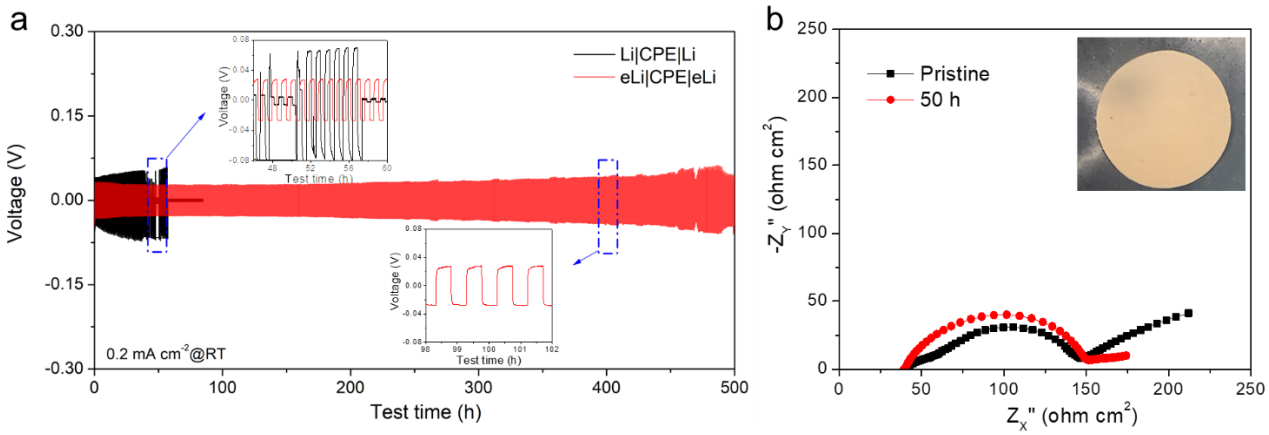

Figure 26. Performance comparison of eLi|CPE|eLi and Li|CPE|Li symmetric lithium cells at room temperature: (a) Galvanostatic cycling of symmetric lithium cells at current density of 0.2 mA cm^{-2} with constant plating/stripping time of 30 minutes. (b) Nyquist plots of the eLi|CPE|eLi symmetric cell, showing stable cell interfaces in cycling.

The team also observed the deposited lithium particles on the surface defects of cycled CPEs, which might help explain the partial short of CPE in long cycling. Figure 27a compares the X-ray diffraction (XRD) patterns of pristine CPEs with the shorted CPEs at 0.5 mA cm^{-2}. The picture of cycled CPE membrane (the inset of Figure 27a) shows some dark yellowish area due to the corrosion of reactive lithium metal. In addition, the XRD pattern indicates that the coloration of CPEs leads to formation of Li_2CO_3 (200, 111, 002, and 020) and LiF compounds via PVDF decompostion, which also accumulated on the top of cycled lithium metal in Figure 27b. What is more, the shorted region of CPE membrane shows irregular morphology with dead lithium attached on the top and CPEs (Figure 27b-c). These results illustrate the necessity to form a stable SEI for Li/CPE interface to achieve uniform lithium dissolution and deposition.

In summary, the team used a novel method to engineer the thin lithium anode to realize stable, long cycling of SSLBs, which accelerates the transformation from cell component research to real battery technologies. Further efforts should be devoted to increasing the plating/stripping capacity or time of symmetric cell and preparing the full cell with high capacity based on the thin SSE films.

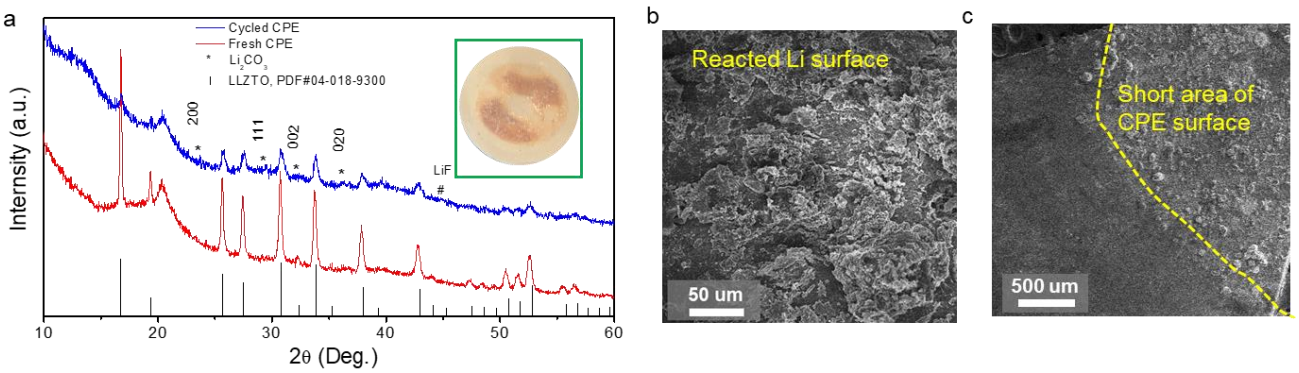

Figure 27. Post-mortem characterization of shorted composite polymer electrolyte (CPE) cell. (a) X-ray diffraction patterns of pristine CPE and shorted CPE obtained from Li|CPE|Li cell at 0.5 mA cm^{-2}, indicating the decomposition of PVDF by lithium metal after long cycling. (b) Scanning electron microscopy (SEM) image of the surface of cycled lithium metal with decomposed products on the top. (c) SEM image of the shorted CPE showing the reacted surface by lithium metal.

Patents/Publications/Presentations

The project has no patents, publications, or presentations to report this quarter.

Task 1.8 – Low Impedance Cathode/Electrolyte Interfaces for High-Energy-Density Solid-State Batteries (Eric Wachsman and Yifei Mo, University of Maryland)

Project Objective. The project objective is to research, develop, and test Li-metal-based batteries that implement solid LICs equipped with NMC cathodes integrated into the Li-metal / Li-La-Zr (LLZ) tri-layer architecture. Specifically, the team will achieve the following: (1) identify and demonstrate interfacial layers to achieve low-impedance and stable NMC/LLZ interfaces; (2) develop novel processing techniques to fabricate NMC/LLZ composite cathodes with low interfacial resistance; and (3) enable high-performance ASSBs with an energy density of 450 Wh/kg and 1400 Wh/L and negligible degradation for 500 cycles.

Project Impact. Instability or high resistance at the interface of high-energy cathode materials with Li-garnet SEs limits the high-energy-density ASSLBs. This project will lead to a fundamental understanding of solid-electrolyte/solid-cathode interfaces and a unique and transformative LLZ framework to enable high-energy-density, safe Li-metal batteries approaching ~ 400 Wh/kg.

Approach. In this new project, the team will build on their demonstrated expertise with garnet electrolytes and ASSB cells to accomplish the following: (1) engineer interfaces to overcome high NMC/LLZ interfacial impedance and interfacial degradation; (2) develop processing and fabrication techniques to achieve high-loading NMC/LLZ composite cathodes with low resistance and high cyclability; and (3) integrate the NMC/LLZ cathodes into all-solid-state Li-metal/LLZ cells to achieve high-energy-density batteries.

Out-Year Goals. The project will solve the current challenges of integrating garnet SE with a cathode to achieve a high-performance ASSB using a high-energy-density Li-metal anode. The resultant high energy density and stability using both high-energy-density Li-metal anodes and NMC cathodes will open new applications in portable electronics, EVs, and beyond.

Collaborations. This project funds work at UMD. The principal investigator (PI), E. Wachsman, will have management responsibility and will lead experimental efforts including garnet synthesis, interface processing, cell fabrication, and testing. The Co-PI, Y. Mo, will lead computational efforts on understanding stability between garnet and cathode and on identifying promising coating materials. In addition, E. Wachsman is actively collaborating with several universities and national laboratories through the U.S.–German cooperation on SSB interfaces.

Milestones

1. Experimentally determine thermochemical stability between interface-coated LLZ and infiltrated NMC. (Q1, FY 2021; In progress)
2. Perform computations of promising coating materials to determine appropriate compositions to stabilize the LLZ-NMC interface. (Q2, FY 2021; Completed)
3. *Go/No-Go Decision*: Demonstrate a 10-times reduction in interfacial impedance between coated and uncoated LLZ/NMC interfaces. Design capable of meeting performance requirements. (Q4, FY 2021; In progress)

Progress Report

Filling of garnet trilayer structures with $Ni_{0.6}Mn_{0.2}Co_{0.2}$ (NMC-622) was performed by a simple suspension in ethanol and subsequent drop-casting onto both sides of the trilayers. In the backscatter SEM image (Figure 28), the dark particles are NMC and the light portions are LLZO.

Co-sintering of these samples was subsequently carried out at 500°C, 700°C, and 800°C for 3 hours on both uncoated and Al_2O_3 atomic layer deposition (ALD) coated structures under argon atmosphere. These were then assembled into symmetric cells, and EIS was performed from 1 MHz to 100 Hz to observe the effect of the ALD layer on the impedance of these cells.

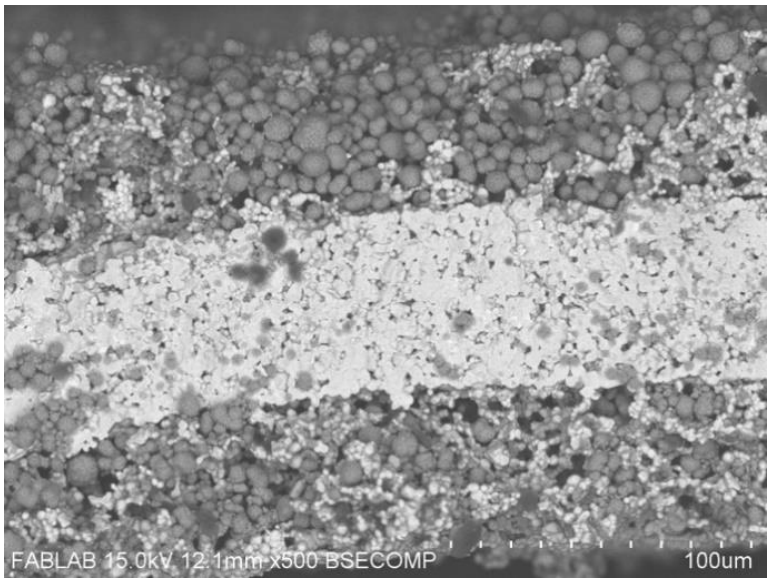

Figure 28. A scanning electron microscopy image of an example LLZO trilayer with the pores filled with NMC-622.

Figure 29 contains the EIS Nyquist plots and distribution of relaxation times (DRT) analysis for the symmetric cells co-sintered at various temperatures. At 500°C, no significant difference between uncoated and coated trilayers could be distinguished. This is likely due to poor contact between particles since the sintering temperature is too low as evidenced by the noisy data, especially in the low-frequency region, shown in the Nyquist plot (Figure 29a). At 700°C, both the Nyquist and DRT plots (Figure 29c-d) show a decrease in the overall impedance for the sample with the ALD coating. The semicircle in the Nyquist plot is smaller and the peak in the DRT plot is smaller. Additionally, only slight noise is present in the low-frequency region of the samples co-sintered at 700°C, indicating that interparticle contact is improved compared to co-sintering at 500°C. At 800°C, the trend continues as the total impedance of the cells is still lower for the ALD-coated samples. The size of the visible high frequency semicircles in the Nyquist plot appears to be similar; however, the lower frequency semicircle is lower for the ALD-treated sample. This is even more apparent in the DRT plots (Figure 29d-f) where the low-frequency component has dramatically lower impedance for the ALD-treated samples.

Unfortunately, XRD and X-ray photoelectron spectroscopy (XPS) facilities at UMD have been down for the past two months, so further information regarding the thermochemical stability between the LLZO trilayer and NMC-622 could not be obtained. Future planned experiments include increasing the thickness of the coating layer to determine the optimal thickness, if a thicker coating may allow for co-sintering at temperatures above 800°C, and extending these experiments to other ALD layers including ZnO.

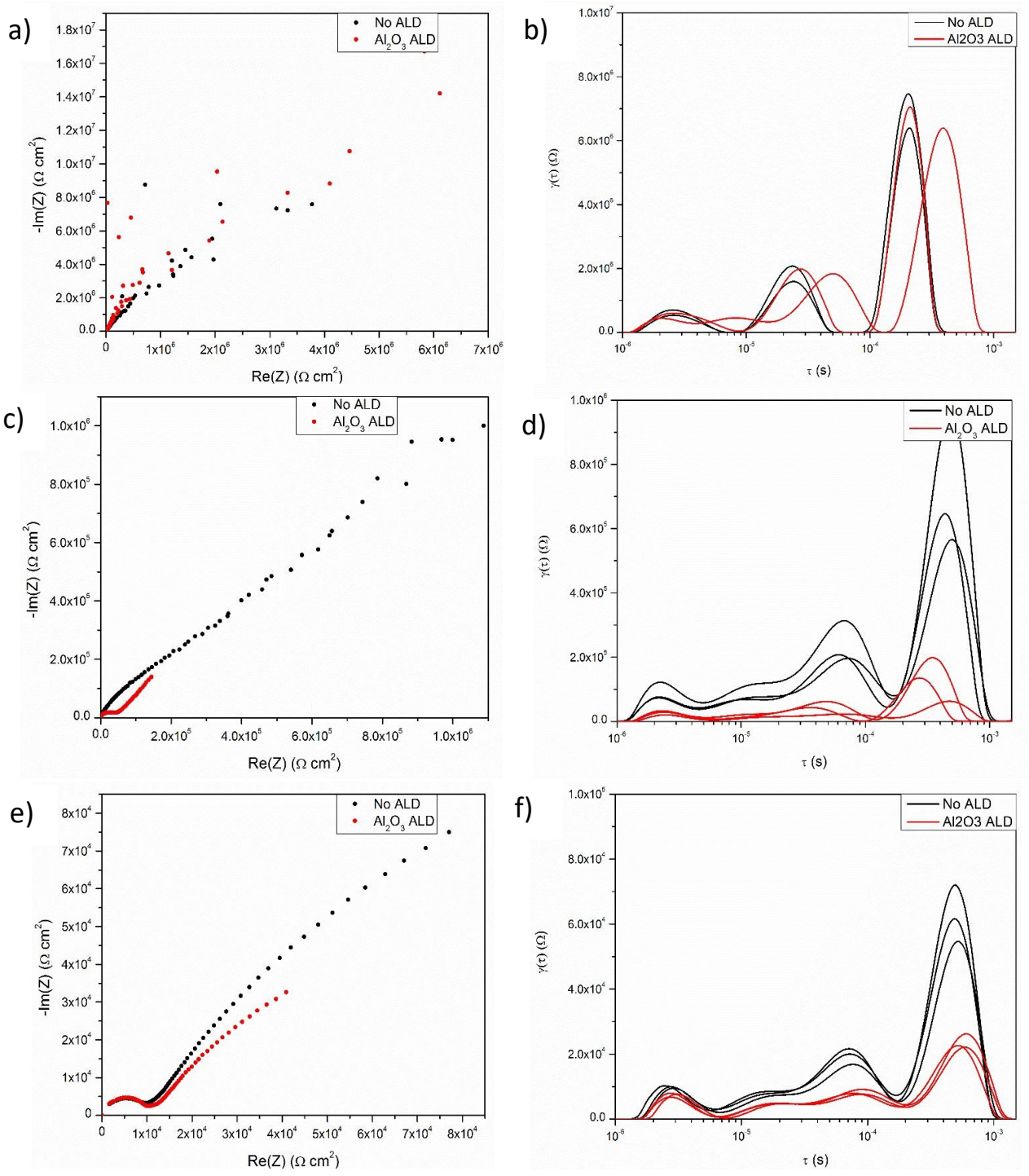

Figure 29. Electrochemical impedance spectroscopy for symmetric NMC-622|LLZO|NMC-622 cells co-sintered at various temperatures comparing uncoated and ALD-coated samples. (a) Nyquist plot and (b) distribution relaxation times (DRT) analysis of samples co-sintered at 500°C. (c) Nyquist plot and (d) DRT analysis of samples co-sintered at 700°C. (e) Nyquist plot and (f) DRT analysis of samples co-sintered at 800°C.

Patents/Publications/Presentations

Publication

- Nolan, A. M., E. D. Wachsman, and Y. Mo. "Computation-Guided Discovery of Coating Materials to Stabilize the Interface Between Lithium Garnet Solid Electrolyte and High-Energy Cathodes." *Energy Storage Materials* 41 (2021): 571–580.

Presentations

- Beyond Lithium Ion XIII, Argonne National Laboratory, Virtual (June 2021): "Interfacial Failure of Lithium Metal in Solid-State Batteries: Insight from Large-Scale Atomistic Modeling"; Y. Mo. Invited.
- Phonon Science Seminar, Stanford Linear Accelerator Center (SLAC) National Accelerator Laboratory, Virtual (May 2021): "Computation Accelerated Design of Materials and Interfaces for Solid-State Batteries"; Y. Mo. Invited.
- Materials Research Society (MRS) Spring Meeting, Seattle, Washington (April 2021): "Computation-Guided Discovery of Materials for Stabilizing Interfaces in High-Energy Solid-State Lithium-Ion Batteries"; A. Nolan and Y. Mo.

Task 1.9 – Developing an *In Situ* Formed Dynamic Protection Layer to Mitigate Lithium Interface Shifting: Preventing Dendrite Formation on Metallic Lithium Surface to Facilitate Long Cycle Life of Lithium Solid-State Batteries
(Deyang Qu, University of Wisconsin, Milwaukee)

Project Objective. The objective of this project is to research, develop, and test Li-metal-based batteries that implement solid LICs equipped with a formed dynamic protection layer. The proposed project aims to enable safe, long-cycle lithium anodes to achieve cell performance targets of 400 Wh/Kg, over 100 cycles, with 15-year shelf life, and < $100/KWh cost.

Project Impact. Project efforts are to contribute an in-depth understanding of the lithium interface and dendrite growth prevention to the field of Li-metal batteries, which will pave the way for eventual development of high-energy-density, low-cost, and long-lasting lithium batteries. This advancement could be a crucial selling point for the greater adoption of EVs. This project will make possible the translation of fundamental research into practical implementation of high-energy lithium anodes, enabling eventual achievement of cell performance targets.

Approach. The novelty of this approach is that the team intends to mitigate the dendrite problem by creating a dynamic protection layer during the interface shift to prevent dendrite formation throughout battery operation.

Out-Year Goals. The project has three out-year goals: (1) *in situ* diagnostic tools are fully functional; (2) potential candidates for Li-anode modifications are identified; and (3) synthesis routes are designed.

Collaborations. The PI is the Johnson Control Endowed Chair Professor, who has close and frequent collaboration with Johnson Controls' scientists and engineers. The collaboration enables the team to validate the outcomes of fundamental research in pilot-scale cells. The PI also has been working closely with top scientists at Argonne National Laboratory (ANL), Brookhaven National Laboratory (BNL), LBNL, and Pacific Northwest National Laboratory (PNNL) and with U. S. industrial collaborators, for example, General Motors (GM), Millipore Sigma, and Clarios. In addition, the team works with international collaborators in China, Japan, and South Korea. These collaborations will be strengthened and expanded to give this project a vision with both today's state-of-the-art technology and tomorrow's technology in development, while incorporating feedback from the material designers and synthesizers upstream, as well as from the industrial end users downstream.

Milestones

1. Lithium anode electrochemical performance evaluation. Synthesis n-type polymer materials and evaluation of the electrochemical performance. (Q1, FY 2021; Completed)

2. Roll-press coating development. Complete the process development of roll-press coating. (Q2, FY 2021; Completed)

3. Polycyclic aromatic hydrocarbon (PAH) derivative structure identified. Identification of the synergy of the parameters and their impact on dendrite growth. (Q3, FY 2021; Completed)

4. Synthesis and test of PE with PAHs. Synthesis of PE with various PAH functionalities, and test with lithium anode in a half cell. (Q4, FY 2021; In progress)

5. Dendrite suppression demonstrated; interim cell performance verified. Dendrite suppression on coated lithium anode demonstrated, and analysis indicates technical approach capable of achieving performance targets. (Q4, FY 2021; In progress)

Progress Report

Last quarter, the team reported the success of halide (Li_3YCl_6, LYCl) SSE synthesis, the creation of a dynamic and self-limiting protective layer on lithium anode, and demonstration of a high-performance ASSB. This quarter, they tried to better understand the mechanism of the high-performing chemistry.

To analyze the reaction products at the Li/LYCl interface, lithium pieces and the as-synthesized white LYCl powder were hand-ground at a molar ratio of 3:1 (Figure 30a), according to the idealized net reaction equation $Li_3YCl_6 + 3Li \rightarrow 6LiCl + Y^0$. After 20 minutes of grinding, the reaction product turned out to be black powder, and the shiny lithium pieces became completely consumed (Figure 30b). The corresponding XRD patterns are shown in Figure 30c. Strong diffraction peaks attributed to LiCl were detected, as labeled. The signal of yttrium metal is not significant, mainly caused by the low volume fraction of Y^0 compared to LiCl. In addition, Y^0 can immediately react with other species to form Y_2O_3 or $Y_2(CO_3)_2$ species. Therefore, a fast-growing and mixed ion/electron conducting interface is formed one way or another. Similarly, the reaction products at the LPSCl/Li interface were investigated by mixing LPSCl powder and lithium pieces at a molar ratio 1:8 (Figure 30d), according to the net interfacial reaction $Li_6PS_5Cl + 8Li \rightarrow 5Li_2S + Li_3P + LiCl$. Lithium residues can still be observed from the grayish reaction products after 20 minutes (Figure 30e). The XRD pattern (Figure 30f) generally remains unchanged, with only one additional peak assigned to Li_2S, as labeled. The signal is rather weak, implying that the reaction is self-limited and the reaction layer is rather thin. The dominant decomposition product, Li_2S, is an ionic conductor with low electronic conductivity, leading to a formation of a resistive interfacial layer. Regarding the other two decomposition products, Li_3P is a fast LIC (~ 10^{-4} S cm^{-1}) and LiCl is less ionically conductive. Importantly, LiCl displays high interface energy against lithium, which can significantly suppress dendrite growth, the same role LiF played. Overall, a kinetically stable and ion-conducting interface can be expected between lithium and LPSCl, just as the SEI layer formed LEs.

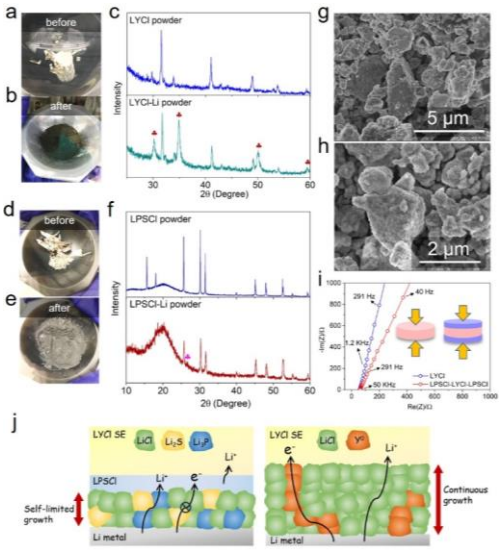

Figure 30. Pictures of Li-metal pieces and LYCl powder (a) before and (b) after hand grinding. (c) Corresponding X-ray diffraction (XRD) patterns of the reaction products. Pictures of Li-metal pieces and LPSCl powder (d) before and (e) after grinding. (f) Corresponding XRD patterns of the reaction products. Scanning electron microscopy images of (g) LPSCl and (h) LYCl powder. (i) Ionic conductivity measurement of LYCl pallet and LPSCl/LYCl/LPSCl composite pallet at room temperature. (j) Schematic illustration showing the Li/LPSCl/LYCl design (left) and Li/LYCl design (right).

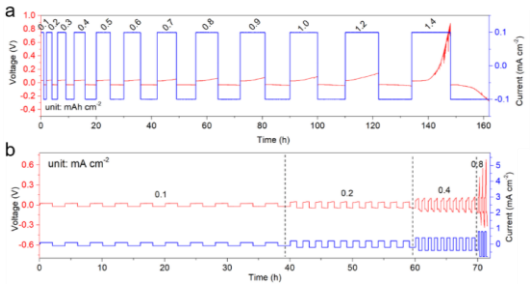

Figure 31. Voltage and current profiles of Li/LPSCl/LYCl/LPSCl/Li symmetric cell (a) at increased capacities with a constant current of 0.2 mA cm^{-2}, and (b) at increased current densities with a constant capacity of 0.2 mAh cm^{-2}.

As shown in Figure 31a, the Li/LPSCl/LYCl/LPSCl/Li symmetric cell was tested with an increased capacity, with the current fixing at 0.2 mA cm^{-2}. The maximum stripping capacity the cell can sustain is 1.4 mAh cm^{-2}, representing 16% utilization of the lithium electrode (theoretical capacity is 9 mAh cm^{-2}). Figure 31b displays voltage profiles of the symmetric cell tested with an increasing current density but fixing at a capacity of 0.2 mAh cm^{-2}. The critical current is determined to be 0.8 mA cm^{-2}. The critical current can be highly dependent on the external stack pressure. In this case, the threshold value of Li/LPSCl/LYCl/LPSCl/Li cell is 0.8 mA cm^{-2} at 4.4 MPa.

Patents/Publications/Presentations

Publication

- Ji, W., D. Zheng, X. Zhang, T. Ding, and D. Qu. "Kinetically Stable Anode Interface for Li_3YCl_6-based All-Solid-State Lithium Batteries." *Journal of Materials Chemistry A* 9 (2021): 15012–15018.

Task 1.10 – Molecular Ionic Composites: A New Class of Polymer Electrolytes to Enable All-Solid-State and High-Voltage Lithium Batteries (Louis Madsen, Virginia Polytechnic Institute and State University)

Project Objective. Based on a newly discovered class of solid PE materials, that is, molecular ionic composites (MICs), the overall objective is to develop solid-state lithium conductors targeted for use in transportation applications. MICs form a mechanically stiff, electrochemically stable, and thermally stable matrix. Specific objectives include the following: (1) development of robust MIC electrolyte thin films (~ 20 µm) to serve as simultaneous nonflammable separators and dendrite-blocking Li^+ conductors, (2) electrochemical quantification of key performance metrics including electrolyte stability, interfacial reactions, and suitability/compatibility with a range of electrode materials, and (3) comprehensive investigation of ion transport mechanisms and electrode-electrolyte interfacial reactivity under practical operating conditions using NMR and synchrotron X-ray analyses.

Project Impact. Commercialization of Li-metal SSBs is hampered by lack of a functional nonflammable SE that can provide high ionic conductivity, wide electrochemical window, favorable mechanical properties to inhibit lithium dendritic growth, and low interfacial resistance. The tunable MIC materials platform has potential to fulfill these requirements with relatively simple fabrication techniques, and thus shows promise for enabling nonflammable SSBs that can be optimized for low cost and high energy density.

Approach. MICs rely on a unique polymer that is similar to Kevlar® in its strength, stiffness, and thermal stability, but with densely spaced ionic groups that serve to form an electrostatic network that permeates mobile ions in the MIC. The team can tailor the ion concentrations and types to yield MIC electrolyte films that are electrochemically compatible with Li-metal anode as well as a range of high-voltage layered cathodes. They are searching the composition space of lithium salts, electrochemically compatible ionic liquids (ILs), and polymer [poly(2,2′-disulfonyl-4,4′-benzidine terephthalamide), or PBDT] molecular weight to determine best composition windows for MIC electrolytes. The team is also investigating best methods for casting thin films in terms of temperature, solvent/evaporation conditions, and control over the initial liquid crystalline gel formation point. Concurrently, they are testing MIC films in various electrochemical cells, quantifying transport and structural/morphology parameters with NMR and X-ray techniques, and measuring key mechanical (dynamic mechanical thermal analysis, stress-strain) and thermal [DSC, thermal gravimetric analysis (TGA)] properties.

Out-Year Goals. This year, the team will further optimize the film casting process to obtain thin MIC electrolyte films, but will focus primarily on detailed electrochemical quantification of key performance metrics including electrolyte stability, interfacial reactions, and suitability/compatibility with a range of electrode materials (with the focus on lithium metal and layered oxides). The team will understand and optimize the oxidative stability and interfacial impedance properties of MIC electrolytes. The team will develop and characterize working battery cells incorporating MIC electrolyte films with various cathode and anode materials, and will work to understand fundamental material compositions and interfacial compatibilities to choose favorable combinations for safe SSBs with high energy density.

Collaborations. The team is collaborating with T. J. Dingemans' group at University of North Carolina, Chapel Hill, in which they are forming composites based on PBDT polymer and carbon materials such as graphene oxide, and are beginning to develop charged rigid-rod polymers building on the PBDT structure. The team is exploring shear rheology and broadband dielectric spectroscopy collaboration with R. H. Colby at Pennsylvania State University (PSU). They are collaborating with D. Nordlund at SLAC National Accelerator Laboratory to conduct synchrotron X-ray studies on MIC films.

Milestones

1. Determine optimal synthetic conditions, Li-ion loading, and chemical composition. (Q4, FY 2020 / Q1, FY 2021; Completed, with ongoing improvements)
2. Determine parameter spaces for film formation, and develop design capable of meeting performance requirements for film casting process. (Q2, FY 2021; Completed, with ongoing improvements)
3. Optimize oxidative stability by using NMC/MIC/NMC and Li/MIC/NMC cell platforms to determine the upper limit of cycling voltage. (Q3, FY 2021; In progress)
4. Optimize electrolyte chemistry to achieve minimal interfacial impedance. (Q4, FY 2021; In progress)
5. Initial full cell integration and performance evaluation with Li/MIC/NMC and cycling under high current density. (Q1, FY 2022; In progress)

Progress Report

Electrolyte Composition Tuning for Enhanced Limiting Current Density

To improve the Li^+ transport dynamics, in this period the team has prepared solid MIC electrolytes with new compositions of lithium salts and ILs, including mixtures of different anions such as dicyanamide (DCA), bis(fluorosulfonyl)imide (FSI), and bis(TFSI). Most notably, a MIC composed of PBDT, LiTFSI, and $Pyr_{13}FSI$ with a mass ratio of 10:10:80 wt% demonstrates substantial improvement in ion diffusion and cycling capability (as compared to the team's previous benchmark material PBDT:LiTFSI:$Pyr_{14}TFSI$). Here, they present NMR diffusion data and lithium symmetric cell cycling test results for this new $Pyr_{13}FSI$-based MIC using LiTFSI as the salt additive.

Pulsed field gradient (PFG) NMR diffusometry experiments enable measurement of diffusion coefficients for the large mobile ions in the new MIC material and comparison with the previous MIC material. Figure 32a shows these diffusion coefficients as a function of temperature for the $Pyr_{13}FSI$-based MIC compared to the $Pyr_{14}TFSI$-based MIC. At room temperature, the cations and anions in the $Pyr_{13}FSI$-based MIC have a larger diffusion coefficient compared to the original $Pyr_{14}TFSI$-based MIC by a factor of 3 and 4, respectively. The activation energies of diffusion further complement this, where the cation (Pyr_{13}^+) and anions (FSI^- and $TFSI^-$) in the new $Pyr_{13}FSI$-based MIC were found to have a smaller activation energy of diffusion (both ≈ 25 kJ/mol) than the activation energy (≈ 37 kJ/mol) for the cation (Pyr_{14}^+) and anion ($TFSI^-$) in the original $Pyr_{14}TFSI$-based MIC. The team is undertaking diffusion measurements over a wider temperature range and attempting to measure Li^+ diffusion as well. These results support substantially faster Li^+ transport in these new compositions of the solid MIC electrolytes.

The current symmetric Li|Li cycling data for the new membranes incorporating $Pyr_{13}FSI$ (Figure 32b) further agree with the transport data observed (Figure 32a). As previously reported, the $Pyr_{14}TFSI$-based MIC was shown to have a limiting current density of between 0.15 mA/cm^2 and 0.20 mA/cm^2 at room temperature, with a charge and discharge time of 0.5 hours, respectively. Here, the new composition consistently shows a higher limiting current density under the same experimental conditions. Figure 32b shows a lithium symmetric cell cycled at various current densities using the $Pyr_{13}FSI$-based MIC with LiTFSI salt. The MIC electrolyte can reach a current density of at least 0.45 mA/cm^2.

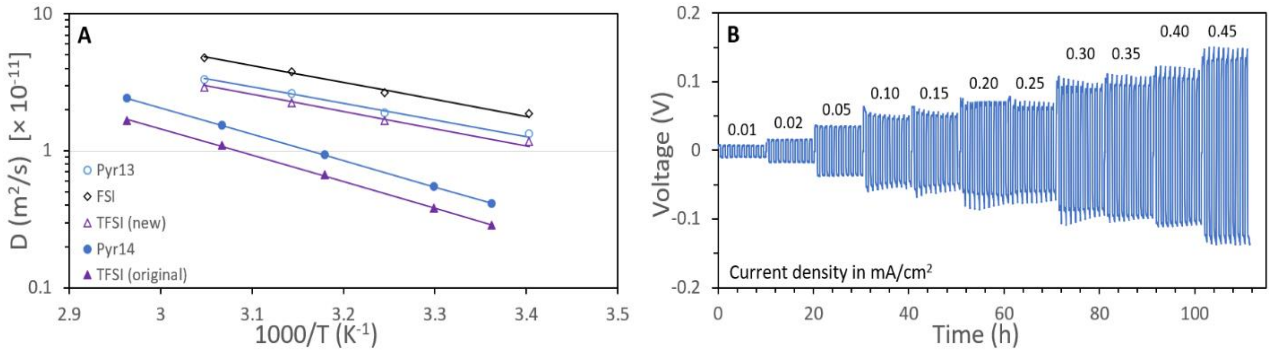

Figure 32. (a) Temperature-dependent diffusion coefficients (via nuclear magnetic resonance) for the cations and anions in the new $Pyr_{13}FSI$-based molecular ionic composite (MIC; hollow symbols) and original $Pyr_{14}TFSI$-based MIC (filled symbols). These new electrolytes are composed of 10:10:80 wt% PBDT:LiTFSI:IL. Activation energy of diffusion was derived using an Arrhenius fitting, where the measured ions in the $Pyr_{13}FSI$-based MIC have a substantially lower activation energy of diffusion compared to the measured ions in the $Pyr_{14}TFSI$-based MIC. These results are consistent with and support faster Li^+ transport in the $Pyr_{13}FSI$-based MIC. (b) Voltage profile of symmetric cell cycled at 23°C, with stepwise increases in current density every 10 cycles. Each cycle consisted of charge and discharge times of 0.5 hours, respectively. The electrolyte used is composed of a 10:10:80 wt% PBDT:LiTFSI:$Pyr_{13}FSI$ MIC membrane. Under these conditions, the limiting current density reaches 0.45 mA/cm². Multiple symmetric cells tested show consistent results. This is an improved limiting current density by at least a factor of 2 from the previous $Pyr_{14}TFSI$-based MIC, which showed a limiting current density below 0.2 mA/cm² under the same charge/discharge conditions. This cycling performance is consistent with the lower activation energy and faster diffusion coefficients of this MIC membrane as compared to the original composition.

Polymer Synthesis and Composite Cathode Formulation

This quarter, F. Lin's group has worked together with L. Madsen's group to establish in-house polymer synthesis capabilities. This will allow the team to make larger quantities of the rigid-rod PBDT polyanions for their future cell fabrication and systematic electrochemical measurements. The team also plans to use this as an avenue to explore optimal molecular weight by tailoring synthesis parameters, for example, degree of polymerization. This synthetic flexibility in-house can enable different molecular weight and polydispersity of the polymer (via both time and temperature). The resulting polymers will be used to investigate the mass production of ASSBs via an in-house-developed continuous process with an interface-less design. The team has also started optimization of the catholyte design. Specifically, they are tailoring the mass ratio and volume fraction of different cathode components, with the target of optimizing both ionic and electronic transport in the composite cathode. To date, the team has established different methods of formulating and processing composite cathodes, and will investigate how different processing conditions may influence the composite cathode performance.

PBDT Polymer Synthesis

The research team is now capable of synthesizing rigid-rod PBDT polymer, which is an essential component of the MICs. Figure 33 shows the reaction scheme for the synthesis. The team's recent synthetic abilities combined with their analytical expertise provided the avenue to tailor the properties of the PBDT polymer for development of ASSBs at the fundamental level. The synthesis of sulfonated aramids, Na-PBDT and Li-PBDT, are based on an interfacial polycondensation procedure. This recent progress on the synthesis of PBDT polymer is further accelerating research toward the mass production (laboratory scale) of ASSBs by more amply supplying PBDT polymer.

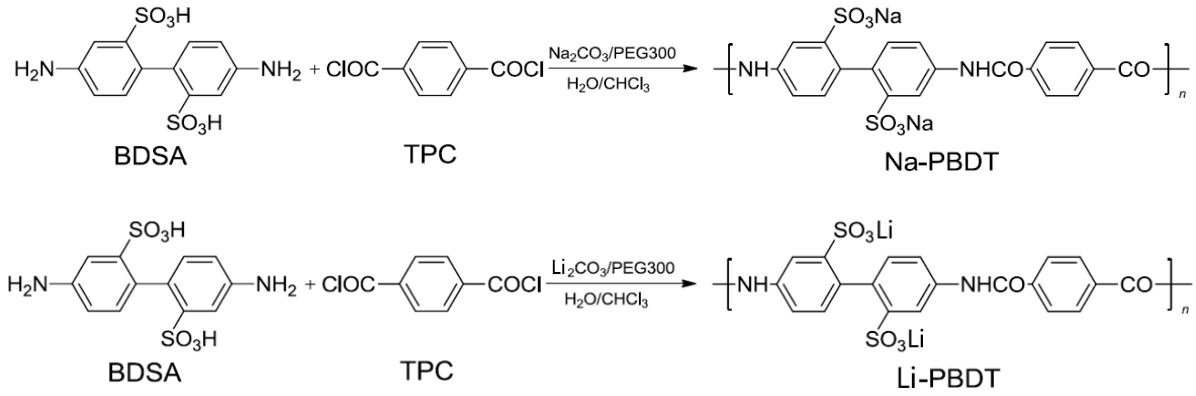

Figure 33. Synthetic routes to produce Na-PBDT and Li-PBDT from commonly available starting materials.

Composite Cathode Formulation

The poor contact of the electrode-electrolyte interface is a key factor that undermines the electrochemical performance of SSBs. To enhance the ionic conductivity and electronic conductivity in the system, microstructural engineering of composite electrodes is critical. Herein, with a solvent-assistant process, team members can introduce MIC solution on preparing the composite electrodes and develop a novel catholyte electrode. Figure 34 shows the flat and homogenized electrode morphology in both surface (a) and cross-section (b) without bare particles exposed to the ambient environment, which can potentially improve the solid-solid contact in the interfacial region and build a more uniform ionic percolation network. The team expects that the SSBs using such catholyte electrodes will have higher specific capacity and more stable cycle life. They are evaluating battery performance of these electrodes and have established research plans to further optimize the ratio between different cathode components.

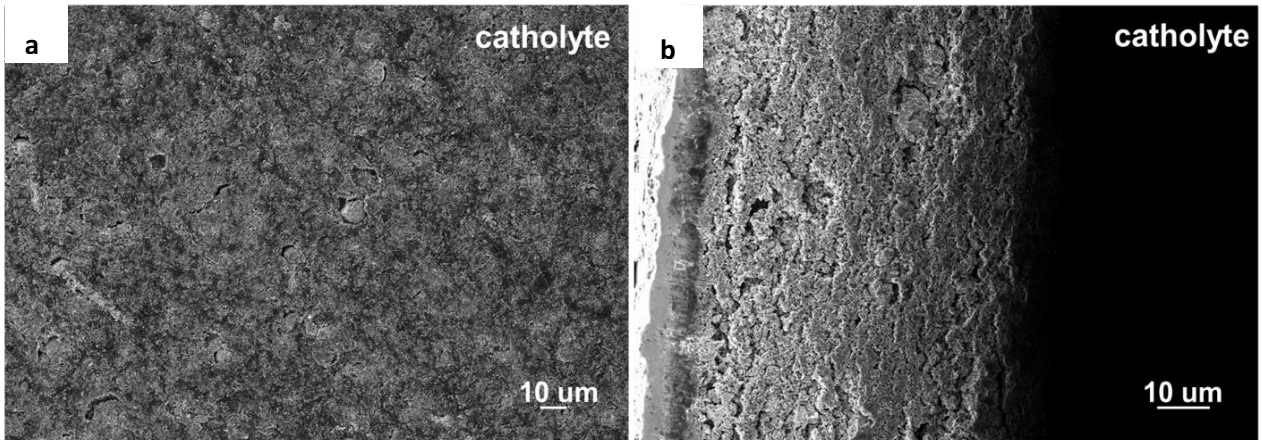

Figure 34. (a) Top surface and (b) cross-section of the as-prepared composite cathode with the molecular ionic composite solid electrolyte as the catholyte.

Patents/Publications/Presentations

Publication

- Yu, D., C. J. Zanelotti, R. J. Fox, T. J. Dingemans, and L. A. Madsen. "Solvent-Cast Solid Electrolyte Membranes Based on a Charged Rigid-Rod Polymer and Ionic Liquids." *ACS Applied Energy Materials* 4, No. 7 (2021): 6599–6605. doi: 10.1021/acsaem.0c03133.

Task 1.11 – All-Solid-State Batteries Enabled by Multifunctional Electrolyte Materials (Pu Zhang, Solid Power Inc.)

Project Objective. The project objective is to develop Li-metal SSBs enabled by multifunctional SSEs for EV application. The ultimate goal is scalable production of large-format ASSBs able to deliver ≥ 350 Wh/kg specific energy, ≥ 1000 cycle life, and ≤ $100/kWh cost.

Project Impact. The project is enabling scalable production of large-format ASSBs required by the vehicle market and is building domestic battery manufacturers as leaders in the global vehicle ASSB production. The proposed technology will address key limitations of state-of-the-art lithium batteries to meet DOE EV battery targets and accelerate their adoption as large-format EV batteries for sustainable transportation technology.

Approach. The project will develop a high-performance Li-metal solid-state cell enabled by a multifunctional SSE. The new SSE will (1) have high conductivity (up to 10 mS/cm), (2) be stable against lithium metal and high-voltage cathode (0-4.5 V), (3) promote uniform lithium plating (enabling > 2C charge rate), and (4) be compatible with large-scale manufacturing processes. The specific cell chemistry to be demonstrated will be the SSE with Li-metal anode and high-nickel-content Li-metal oxide cathode. The solid-state cell will be assembled by scalable roll-to-roll processes developed by Solid Power.

Out-Year Goals. In Year 1, multifunctional SSE will be developed with lithium ionic conductivity of ≥ 3 x 10^{-3} S/cm. A CCD of ≥ 6 mA/cm^2 will be achieved in a symmetric lithium cell. The SSE design concept will be proven by demonstrating cycle life of ≥ 200 in a full cell. In Year 2, SSE material will be optimized with lithium ionic conductivity of ≥ 5 x 10^{-3} S/cm. Scalable cell assembly processes will be developed. Cycle life of ≥ 500 will be demonstrated in a full cell. In Year 3, large-format solid-state cells (> 2Ah) will be assembled/tested to meet the final goal: ≥ 350 Wh/kg, ≥ 1000 cycles, and ≤ $100/kWh cost.

Collaborations. The proposed team consists of Solid Power and a subcontractor, University of California, San Diego (UCSD). Solid Power (PI: P. Zhang) will develop the multifunctional SSE and other cell components, assemble cells, and conduct cell tests. UCSD (PI: Y. S. Meng) will carry out material characterization by using advanced techniques such as XPS, cryogenic – scanning transmission electron microscopy (cryo-STEM) imaging, cryo-STEM energy dispersive X-ray spectroscopy (EDS), electron energy loss spectroscopy (EELS), and cryogenic – focused ion beam (cryo-FIB) milling. The UCSD team seeks to quantify the kinetics and evolution of each contributing factor and its impact on battery performance.

Milestones

1. Charge rate ≥ 0.5C. (Q1, FY 2021; Completed)
2. Pouch cell capacity ≥ 200 mAh. (Q2, FY 2021; Completed)
3. SSE CCD ≥ 18 mA/cm^2. (Q3, FY 2021; Completed)
4. SSE Li-ion conductivity ≥ 5 mS/cm. (Q4, FY 2021; Completed)
5. Cycle life ≥ 500. (Q4, FY 2021; In progress)

Progress Report

SSE Optimization

Solid Power is developing a class of halogenated LPS electrolyte materials with high conductivity and stability. This quarter, the electrolyte synthesis process has been optimized to improve material performance. The optimized electrolyte has shown a Li-ionic conductivity of 6 mS/cm at 25°C and a CCD of 20 mA/cm^2 at 70°C, which meets Milestone 3 and Milestone 4. The progress of the electrolyte development within the project is shown in Figure 35.

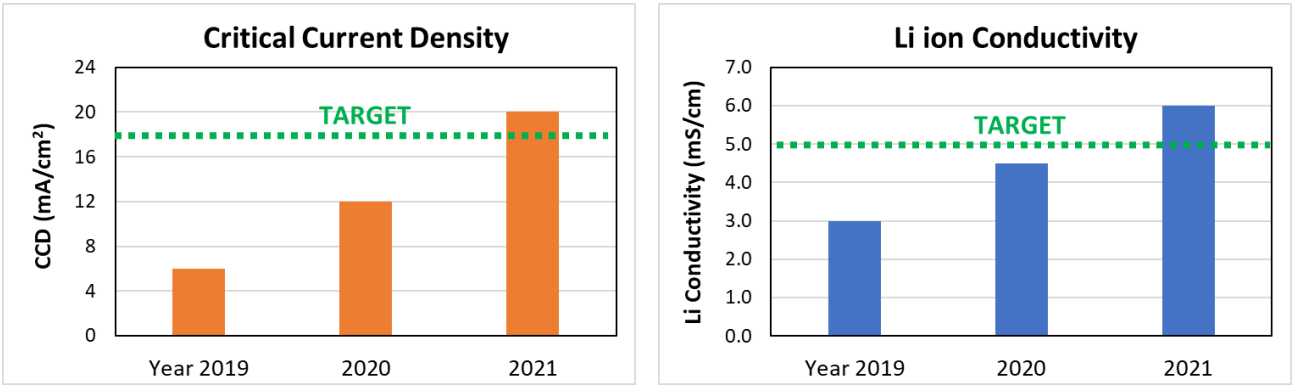

Figure 35. The electrolyte development progress: (left) critical current density at 70°C, and (right) Li-ion conductivity at 25°C.

Full-Cell Demonstration

The cycle life testing of a Li-NMC pouch cell was performed. When tested at 2.8-4.2 V, C/5-C/5, and ambient temperature (~ 25°C), the pouch cell showed 84% capacity retention after 400 cycles to date (Figure 36). The team is on track to meet the cycle life target of ≥ 500 by the end of the second budget period. It should be noted that the capacity fluctuation was due to ambient temperature change.

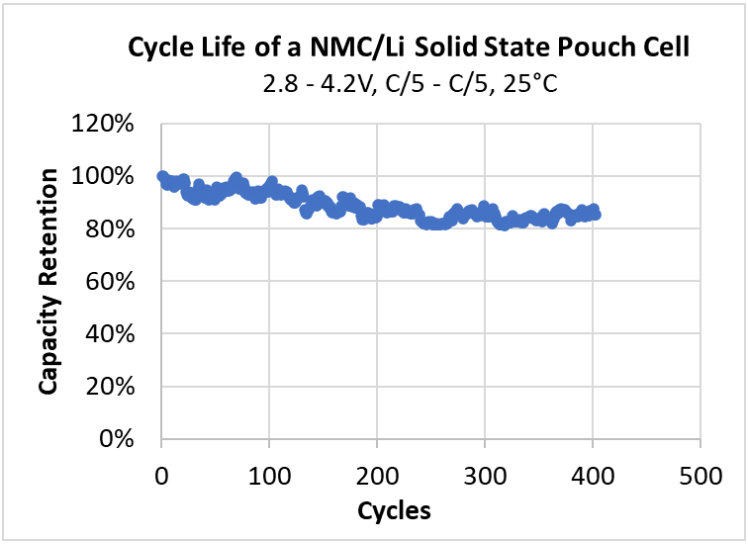

Figure 36. Cycle life of an NMC/Li-metal solid-state pouch cell with the multifunctional solid-state electrolyte at 25°C.

Patents/Publications/Presentations

The project has no patents, publications, or presentations to report this quarter.

Task 1.12 – Developing Materials for High-Energy-Density Solid-State Lithium-Sulfur Batteries (Donghai Wang, Pennsylvania State University)

Project Objective. The project objectives are to develop materials involving advanced S-C composite materials, solid additives, and sulfide-based SSEs, and to acquire knowledge for Li-S ASSBs. Li-S ASSBs with large areal sulfur loading (≥ 5 mg cm^{-2}) and high sulfur content (≥ 50 wt% in cathode), pairing with lithium or lithium alloy anode, will deliver a high initial specific capacity of over 1200 mAh g^{-1} at high charge/discharge rate (> 0.3 C) for 500 cycles with over 80% capacity retention.

Project Impact. This project aims to develop new materials to enable Li-S ASSBs with high energy density, excellent cycling stability, and good rate performance, and thus to build knowledge for fabrication of prototype Li-S ASSBs. Specifically, the developed new materials will greatly increase the specific capacity of sulfur and sulfur utilization at high areal sulfur loading, alleviate the interfacial problem between S-C composite and SSE within sulfur cathode, boost Li-ion conductivity, and improve moisture stability of glass and glass-ceramic sulfide-based SSE. Meeting the technical targets will potentially promote development of high-energy-density Li-S ASSBs and their practical application in EVs and plug-in hybrid EVs (PHEVs) and will also reduce petroleum consumption in the transportation sector by helping battery-powered vehicles become more accepted by consumers as a reliable source of transportation.

Approach. The project goal will be accomplished through developing new materials, together with in-depth characterization of sulfur cathode. Specifically, approaches to realize the project objectives include the following: (1) development of new carbon material with unique structure, high surface area, and large pore volume; (2) development of new S-C and S-C-M_xS_y materials (M = Li, Co, Ti, Mo, etc.) to facilitate electron/ion transport; (3) development of novel additives to tune interfacial behavior among components in the cathode; (4) development and optimization of new SSE through cation and anion doping with superior properties such as high ionic conductivity, good moisture, and stability; and (5) diagnostics, characterization, and cell tests on the developed new material or advanced sulfur cathode.

Out-Year Goals. The out-year goals are as follows: (1) develop new S-C-M_xS_y hybrid materials, new cathode additives, and anion-doped SEs (ionic conductivity above 3 mS cm^{-1} at room temperature), and (2) conduct characterization and performance tests on both material and electrode levels. The *Go/No-Go Decision* will be demonstration of all-solid-state sulfur cathode with over 1000 mAh g^{-1} discharge capacity at 0.1 C discharge rate and 50 wt% sulfur content for 100 cycles at room temperature.

Collaborations. There are no active collaborations.

Milestones

1. Demonstrate sulfur cathode with above 1000 mAh g^{-1} capacity at 0.2 C at 60°C. (Q1, FY 2021; Completed)
2. Demonstrate new anion-doped electrolyte with ionic conductivity > 2 mS cm^{-1} at 25°C, and sulfur cathode with > 1000 mAh g^{-1} using additives (≤ 3 wt%) at 0.3 C for 50 cycles. (Q2, FY 2021; Completed)
3. Demonstrate sulfur cathode with > 1000 mAh g^{-1} at 0.3 C for 50 cycles at 60°C using hybrid conductive materials. (Q3, FY 2021; Completed)
4. Demonstrate sulfur cathode with > 1000 mAh g^{-1} at 0.1 C for 100 cycles at room temperature, and anion-doped SEs with ionic conductivity > 3 mS cm^{-1} at 25°C. (Q4, FY 2021; In progress)

Progress Report

New SE for All-Solid-State Lithium-Sulfur Batteries (ASSLSBs)

This quarter, the team focused on designing and synthesizing specialized new SEs for ASSLSBs. A new SE was successfully synthesized and was evaluated in all-solid-state Li-In|S batteries. The sulfur cathode (carbon/sulfur/SE = 10/50/40, w/w/w) was prepared through a conventional ball-milling approach. The team employed $75Li_2S{\cdot}25P_2S_5$ (LPS) glass SE in the control sample. After optimizing the electrochemical window, the ASSLSBs were electrochemically tested between 0.8 V ~ 2.5 V (versus Li-In/Li^+) with a sulfur loading of 1.5 mg cm^{-2} ~ 2.0 mg cm^{-2} at 60°C. As shown in Figure 37a, a high discharge specific capacity of ~ 1282 mAh g^{-1} was achieved by using the new SE at 0.1 C (1 C = 1675 mAh g^{-1}), in contrast to the low discharge specific capacity of ~ 839 mAh g^{-1} in conventional sulfur cathode using LPS SE. The rate capability of sulfur cathodes was assessed at current rates from 0.1 C to 1 C (Figure 37b). The sulfur cathode using new SE demonstrated higher specific capacity at all current rates compared with the sulfur cathode using LPS. In detail, the sulfur cathode with new SE delivered high discharge specific capacities of 1430.3 mAh g^{-1}, 1275.1 mAh g^{-1}, 934.1 mAh g^{-1}, and 629.7 mAh g^{-1}, at 0.1 C, 0.2 C, 0.5 C, and 1 C, respectively.

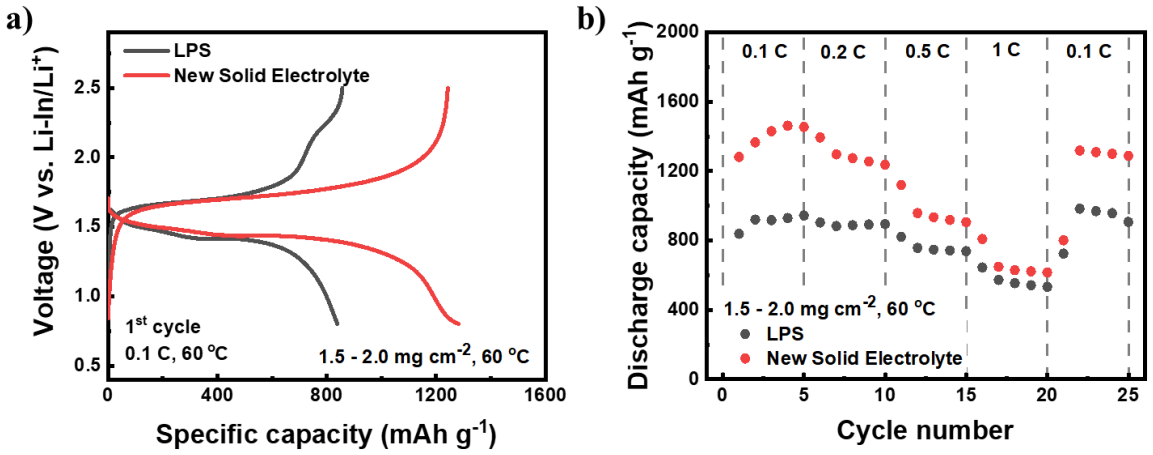

Figure 37. Electrochemical testing of Li-In|S batteries. (a) Galvanostatic discharge-charge curves at 1st cycle. (b) Rate performance at different current rates. The area sulfur loadings are between 1.5-2.0 mg cm^{-2}. The cells were tested between 0.8 V ~ 2.5 V at 60°C.

In addition to the rate performance, the team also evaluated cycling performance of sulfur cathode using new SE with a low sulfur loading of 1.5 mg cm^{-2} at 1 C under constant current / constant voltage (CCCV) mode (cutoff current rate is 0.1 C at 2.5 V). As shown in Figure 38, the cell delivered a high initial discharge specific capacity of ~ 1170 mAh g^{-1}. After 100 cycles, the discharge specific capacity remains at ~ 1198.6 mAh g^{-1}. The superior cycling performance meets the milestone for demonstrating sulfur cathode with > 1000 mAh g^{-1} at 0.3 C for 50 cycles at 60°C.

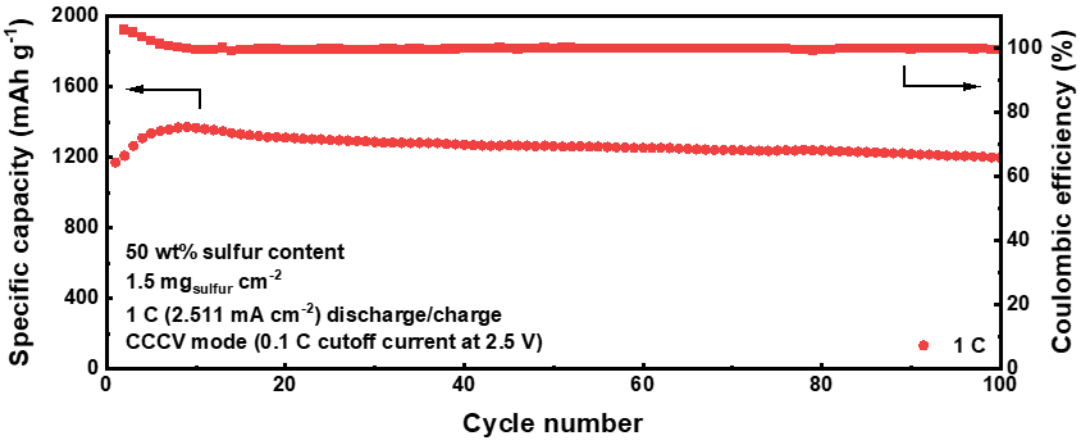

Figure 38. Cycling performance of the Li-In|S batteries using new solid electrolyte at 1 C (constant current / constant voltage mode; cutoff current rate of 0.1 C at 2.5 V). Sulfur loading: 1.5 mg cm^{-2}; cell tested between 0.8 V ~ 2.5 V at 60°C.

Patents/Publications/Presentations

The project has no patents, publications, or presentations to report this quarter.

Task 1.13 – Hot Pressing of Reinforced Lithium-NMC All-Solid-State Batteries with Sulfide Glass Electrolyte
(Thomas Yersak, General Motors LLC)

Project Objective. The objective of this project is to research, develop, and test Li-NMC ASSBs capable of achieving program performance metrics by implementing sulfide glass SSEs and hot-press processing in a dry-room environment. The performance of ASSBs with sulfide SSEs is limited because they are essentially green tapes with up to 20% porosity. In composite cathodes, the porosity limits energy density and power, while porosity in the separator acts as a conduit for Li-metal deposits if cycling conditions (that is, C-rate, operating temperature, and pressure) are not strictly controlled. The goal of the project is to demonstrate that the hot-pressing method and appropriately formulated sulfide glass SSEs can eliminate porosity to enable Li-NMC ASSBs with energy density of > 350 Wh/kg.

Project Impact. The hot-press processing method and appropriately formulated sulfide glass SSEs may enable Li-NMC ASSBs with improved energy density > 350 Wh/kg. The GM processing technology depends on heating a sulfide glass SSE above its glass transition temperature, Tg, at which point it can consolidate via viscoplastic flow. In the composite cathode, hot pressing provides liquid-like contact between the NMC cathode and SSE to increase energy density and power by enabling thick composite cathodes with high active material loading. Furthermore, cathode-supported sulfide glass separators can be made dense and thin by hot pressing. A dense separator enables the robust use of a Li-metal anode because lithium deposits may be more effectively blocked, preventing cell shorting.

Approach. The sulfide SSE used in the composite cathode, otherwise known as the catholyte, will dictate the processing specifications for ASSB hot pressing. Thermal stability can be achieved by NMC passivation and proper catholyte formulation. This project will systematically evaluate different NMC coatings, catholyte formulations, and hot-press processing specifications (that is, temperature, time, and pressure). The performance of hot-pressed ASSBs will be compared to green baseline ASSBs and hot-pressed control ASSBs consisting of the β-Li_3PS_4 and LPSCl model SSEs. Electron microscopy will be employed to understand interfacial phenomena and track composite cathode microstructure before and after hot pressing.

Out-Year Goals. In the second year of this project, a sulfide glass SSE will be formulated specifically for use as the separator. The separator glass SSE formulation will be designed to achieve full densification under the hot-press processing specifications determined for the catholyte. Separator glass formulation design will also consider cathodic stability, moisture stability, and ionic conductivity. Once a system of separator glass SSE and catholyte has been determined, the third year of the project will demonstrate hot-pressed full cells at the coin-cell and single-layer pouch-cell levels, which meets program target performance metrics.

Collaborations. GM will lead this project with no subrecipients.

Milestones

1. Establish protective coating on cathode: select best coating method and coating chemistry. Confirm conformality of coating using microscopy. (Q2, FY 2020; Completed)
2. Develop suitable baseline system with reversible capacity of ~ 120 mAh/g. (Q3, FY 2020; Completed)
3. Determine parameters required to prepare cathode samples via FIB/SEM lift-out and to analyze samples via high-resolution transmission electron microscopy (HRTEM). (Q2, FY 2021; Completed)
4. Demonstrate hot-pressed cathode with reversible capacity of 120 mAh/g. Analysis indicates technical approach capable of achieving performance targets. (Q3 FY 2021; Completed)

Progress Report

Last quarter, the team described the electrochemical performance of hot-pressed cathode composites with $LiNi_{0.85}Co_{0.10}Mn_{0.05}O_2$ (NCM-85105) and sulfide SSE catholytes. They reported that 1st-cycle reversibility of test cells made with these cathode composites was improved by adding a halide dopant to the baseline Li_3PS_4 catholyte, with the LiBr dopant yielding the best result. The buried NMC/SSE interface was then studied with CV, DSC, and XPS to determine if the halide dopant improved interfacial thermal stability. No substantial difference was found between cathode composites with β-Li_3PS_4 baseline catholyte and cathode composites with halide-doped catholytes. In this report, the team details why test cells with the Li_3PS_4 + ½LiBr catholyte delivered the best 1st-cycle reversibility. They conclude this report by detailing a compositional criterion for the selection of catholytes with good interfacial thermal stability to enable the hot-pressing of ASSBs.

The microstructure of cathode composites was quantified by digitally processing SEM images of cathode composite cross sections (Figure 39) using ImageJ software. The cross sections were prepared using a Xe^+ plasma FIB (PFIB, Helios G4 UXe, Thermo Fisher Scientific) at the University of Michigan (MC)^2 user facility. They observe that up to 30% of the NCM-85105 particles was damaged by microcracking. A pressure of ~ 370 MPa was used to consolidate cathode composites that damaged the NCM-85105 particles since high nickel content NCM secondary particles are susceptible to microcracking along primary particle GBs.[1] Microcracking leads to loss of NCM electrical contact and increases the NCM/SSE interfacial area. On hot-pressing, the NCM/SSE interface thermally degrades to increase cell impedance. Thermal degradation of the interface is analogous to the oxidation of SSE over long-term cycling.[2,3] To improve reversibility of hot-pressed ASSB, there are two strategies to compensate for the thermal degradation of the NCM/SSE interface. First, electronic and ionic transport of the cathode composite should be improved by utilizing carbon black and catholyte with high ionic conductivity, respectively. Second, microcracking of cathode active materials should be avoided to minimize the area of the NCM/SSE interface.

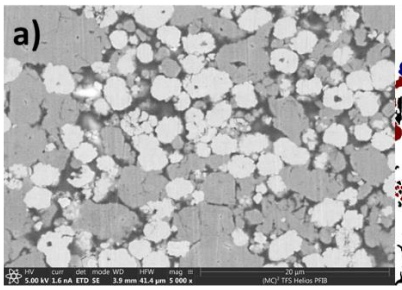

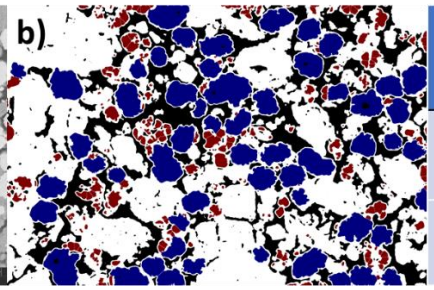

c)

		% of damaged particles	% of intact particles
NCM85105/ β-Li_3PS_4	CP	20.50%	79.50%
	HP	31.25%	68.75%
NCM85105/ Candidate B	CP	20.00%	80.00%
	HP	15.40%	84.60%

Figure 39. (a) Scanning electron microscopy image of a cold-pressed NCM-85105 cathode composite with β-Li_3PS_4 catholyte cross sectioned with plasma focused ion beam. (b) Processed image with white = solid-state electrolyte particle; black = pore, blue = intact NCM particles, and red = damaged NCM particles. (c) Table summarizing the extent of NCM damage for NCM-85105 cathode composites made with β-Li_3PS_4 baseline catholyte or Li_3PS_4 + ½LiBr (LPSB, Candidate B) catholyte. CP refers to cold-pressed and HP refers to hot-pressed.

Microcracking of NCM-85105 results in the disruption of electrical contact and poor electrochemical reversibility. The addition of 2 wt% carbon black improves the 1st-cycle reversibility of the hot-pressed β-Li_3PS_4 baseline cathode composite to 150 mAh/g (Figure 40) from 55 mAh/g without carbon black.[3] On the other hand, the addition of carbon black does not substantially improve the reversibility of cathode composites made with Li_3PS_4 + ½LiI (LPSI, Candidate A) or Li_3PS_4 + ½LiBr (LPSB, Candidate B) halide-doped glasses. Halide-doped catholytes promote good 1st-cycle reversibility because they have high ionic conductivity that compensates for thermal degradation of the NCM/SSE interface and NCM-85105 microcracking. The ionic conductivity of β-Li_3PS_4 is only 0.29 mS/cm, whereas hot-pressed LPSI has an ionic conductivity of 0.63 mS/cm and hot-pressed LPSB has an ionic conductivity of 1.77 mS/cm. Glassy LPSB has an ionic conductivity of only 0.54 mS/cm; however, the newly reported δ-Li_3PS_4 superionically conductive ceramic phase is precipitated from the glass during hot-pressing.[4] The XRD spectrum of the LPSB catholyte after

hot-pressing confirms the presence of the δ-Li_3PS_4 phase (Figure 40b). The team notes that ceramic phases do not always have higher ionic conductivity than that of the mother glass. Glassy LPSI has an ionic conductivity of 1.2 mS/cm; however, precipitation of the $Li_7P_2S_8I$ ceramic phase during hot-pressing lowers ionic conductivity. Nonetheless, the $Li_7P_2S_8I$ ionic conductivity of 0.63 mS/cm is sufficient for good electrochemical performance. Electrochemical performance of NCM/SSE composites was also improved by using $LiNi_{0.6}Co_{0.2}Mn_{0.2}O_2$ (NCM-622) because it is less susceptible to microcracking. Microstructural analysis of NCM-622 cathode composite cross sections found that only 8-15% of NCM-622 particles was damaged. When NCM-622 is used as the cathode active material, good electrochemical performance is obtained even for cathode composites made with baseline β-Li_3PS_4 catholyte (Figure 40c).

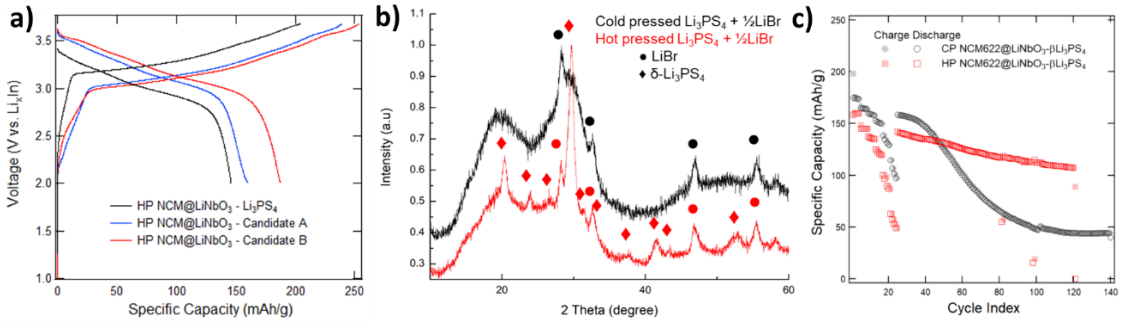

Figure 40. (a) 1st-cycle voltage profiles for NCM-85105 cathode composites with 2 wt% carbon black and hot-pressed at 200°C for 10 minutes. Conductive additive improves 1st-cycle reversibility. (b) X-ray diffraction spectra for cold-pressed (black) and hot-pressed (red) Li_3PS_4 + ½LiBr (LPSB, Candidate B) samples. Hot-pressing at 200°C for 10 minutes precipitates a newly described δ-Li_3PS_4 ceramic phase with high ionic conductivity.[4] High catholyte ionic conductivity improves 1st-cycle reversibility. (c) Cyclic stability for cold-pressed (black) and hot-pressed (red) cathode composites with NCM-622 and β-Li_3PS_4. The NCM-622 reduced microcracking improves electrochemical performance.

The interfacial thermal stability of a catholyte is dictated by local glass structure and not by the presence of a halide dopant. To prove this point, the team compared the properties of NCM-622 cathode composites with glass catholytes of $75Li_2S{\cdot}25P_2S_5$ (Li_3PS_4) or $70Li_2S{\cdot}30P_2S_5$ ($Li_7P_3S_{11}$) (Figure 41). NCM-622 cathode composites made with Li_3PS_4 had good 1st-cycle reversibility of 145 mAh/g, whereas NCM-622 cathode composites made with $Li_7P_3S_{11}$ have poor 1st- cycle reversibility of only 50 mAh/g (Figure 41a). DSC and CV scans show that NCM-622/$Li_7P_3S_{11}$ composites have higher peak responses than that of NCM-622/Li_3PS_4 composites (Figure 41b-c), which suggests that $Li_7P_3S_{11}$ glass has poor interfacial stability. The reduced stability of the $Li_7P_3S_{11}$ glass is explained by its local structure containing PS_4^{3-}, $P_2S_7^{4-}$, and $P_2S_6^{4-}$ structural units. The $P_2S_7^{4-}$ and $P_2S_6^{4-}$ are susceptible to oxidation due to labile bridging sulfur or P-P bonds. The Li_3PS_4 glass promotes good interfacial stability because it is composed predominantly of only stable PS_4^{3-} structural units.

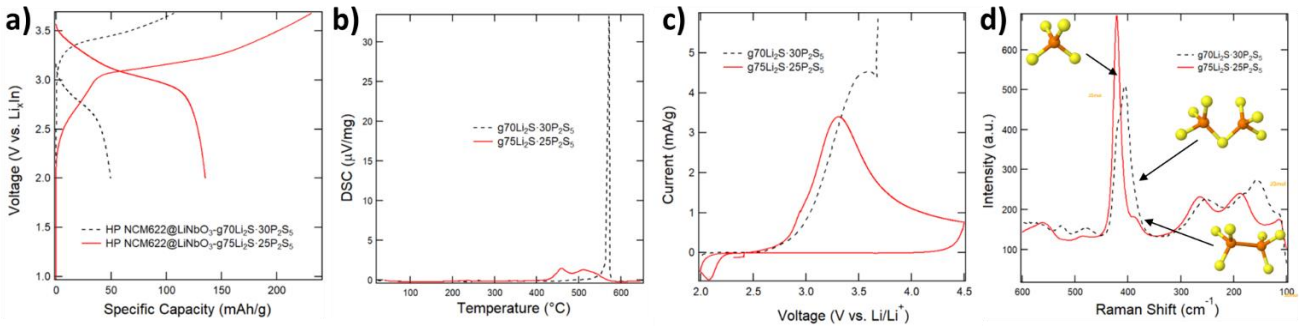

Figure 41. (a) 1st-cycle voltage profiles for hot-pressed NCM-622 cathode composites with either $70Li_2S{\cdot}30P_2S_5$ (dashed black) or $75Li_2S{\cdot}25P_2S_5$ (solid red) glassy catholytes. (b) Differential scanning calorimetry scans for NCM-622 cathode composites. (c) Cyclic voltammetry scans for NCM-622 cathode composites. (d) Raman spectroscopy of $70Li_2S{\cdot}30P_2S_5$ (dashed black) or $75Li_2S{\cdot}25P_2S_5$ (solid red) glassy catholytes.

References

[1] Nam, G. W., et al. *ACS Energy Letters* 4 (2019): 2995–3001.
[2] Tsukasaki, H., et al. *Journal of Power Sources* 367 (2017): 42–48.
[3] Yersak, T. A. *Q2 FY 2021 BMR Quarterly Report* (June 2021).
[4] Bui, A. D., et al. *ACS Applied Energy Materials* 4 (2021): 1–8.

Patents/Publications/Presentations

The project has no patents, publications, or presentations to report this quarter.

TASK 2 – DIAGNOSTICS

Team Lead: Guoying Chen, Lawrence Berkeley National Laboratory

Summary and Highlights

To meet the goals of the VTO programs on next-generation EVs, low-cost and abuse-tolerant batteries with higher energy density, higher power density, better safety, and longer lifetimes are needed. In pursuit of these goals, high cell operating voltages and demanding cycling conditions are used, which leads to unprecedented chemical and mechanical instabilities in cell components. Successful implementation of promising electrode materials (such as silicon anode and high-voltage cathodes) and new cell chemistry (such as high-energy Li-metal cells combined with SSEs) requires better understanding of fundamental processes, especially those at the interface/interphase of both anode and cathode. Identifying and understanding structure-property-electrochemical performance relationships in materials and various failure modes in cell chemistry are therefore more pressing than ever, not only in guiding battery development activities but also the scale-up efforts needed for commercialization.

Task 2 takes on these challenges by combining model systems, *ex situ*, *in situ*, and *operando* approaches, with an array of state-of-the-art analytical and computational tools. Numerous subtasks are tackling the chemical processes and reactions at the electrode/electrolyte interfaces in Li-metal batteries. Researchers at LBNL use surface- and bulk-sensitive techniques, including Fourier transform infrared (FTIR), attenuated total reflectance (ATR)-FTIR, near-field infrared (IR) and Raman spectroscopy/microscopy, and scanning probe microscopy (SPM) to characterize changes in materials and the physio-chemical phenomena occurring at the interface of Li-metal electrode. GM is developing *in situ* diagnostic techniques, including atomic force microscopy (AFM), nano-indentor, dilatometer, and stress-sensor, to be combined with atomic/continuum modeling schemes to investigate the coupled mechanical/chemical degradation of the SEI layer as well as the microstructural evolution at the interface/interphase of Li-metal anode. ANL aims to develop high-conductivity ceramic electrolytes through cation doping and to identify mechanistic barriers that limit chemical, mechanical, and electrochemical durability of solid/solid interfaces. University of Houston (UH) is developing multidimensional diagnostic tools, including FIB-SEM, TOF-SIMS, and in-SEM nanoindentation, to probe structural, chemical, and mechanical evolution at the interfaces of SSLBs. At LBNL, model systems of electrode, SSE, and their interfaces with well-defined physical attributes are being developed and used for advanced diagnostic and mechanistic studies at both bulk and single-particle levels. These controlled studies remove the ambiguity in correlating a material's physical properties and reaction mechanisms to its performance and stability, which is critical for further optimization. Subtasks at BNL and PNNL focus on the understanding of fading mechanisms in electrode materials, with the help of synchrotron-based X-ray techniques [diffraction and hard/soft X-ray absorption (XAS)] at BNL and HRTEM/STEM and related spectroscopy techniques at PNNL. The final subtask at Stanford/SLAC develops and utilizes an integrated X-ray characterization toolkit to investigate and generate insights on SSBs, by tracking the evolution of nanoscale chemistry as well as structure, microstructure, and transport properties. The diagnostics team not only produces a wealth of knowledge key to developing next-generation batteries, they also advance analytical techniques and instrumentation with a far-reaching effect on material and device development in various fields.

Highlights. The highlights for this quarter are as follows:

- The LBNL (G. Chen) group investigated the effect of component ratio in composite cathodes with Li_3YCl_6, revealing the importance of proper particle distribution in balancing ionic and electronic conduction and improving cycling performance of ASSBs.
- The Stanford/SLAC (Y. Cui / W. Chueh / M. Toney) team demonstrated successful use of multi-length-scale X-ray microscopy characterization. Manganese oxidation state maps at the primary particle, secondary particle, and electrode levels were obtained on a Li- and Mn-rich NMC (LMR-NMC) cathode.

Task 2.1 – Characterization and Modeling of Lithium-Metal Batteries: Model-System Synthesis and Advanced Characterization
(Guoying Chen, Lawrence Berkeley National Laboratory)

Project Objective. This project will use a rational, non-empirical approach to design and develop SSE materials and interfaces for next-generation Li-metal batteries. Combining a suite of advanced diagnostic techniques with carefully prepared model-system samples, the project will perform systematic studies to achieve the following goals: (1) obtain understanding on the role of SSE grain and GBs on ion conduction and dendrite formation, (2) obtain fundamental knowledge on rate- and stability-limiting properties and processes in SSEs when used in Li-metal batteries, (3) investigate the reactivities between SSE and electrodes, and gain insights on the dynamic evolution of the interfaces, and (4) design and synthesize improved SSE materials and interfaces for safer and more stable high-energy Li-metal batteries.

Impact. The project will focus on fundamental understanding of SSE and relevant interfaces to enable its use in Li-metal batteries. Knowledge gathered from model-system-based studies will guide the design and engineering of advanced materials and interfaces. The use of the non-empirical, rational-design approach will develop high-energy battery systems with improved commercial viability.

Approach. The project will combine model-system synthesis and advanced diagnostic studies to investigate ion conduction and interfacial chemistry of SSE in Li-metal batteries. Single crystalline, polycrystalline, and amorphous model SSE samples with various grain and GB properties will be synthesized. Model interfaces between the SSE and electrodes with controlled properties will also be developed. Both bulk-level and single-grain-level characterization will be performed. Global properties and performance of the samples will be established from the bulk analyses, while the single-grain-based studies will utilize time- and spatially-resolved analytical techniques to probe the intrinsic redox transformation processes and failure mechanisms under battery operating conditions.

Out-Year Goals. In the out-years, the project will deliver fundamental knowledge on the role of SSE microstructure in Li^+ conduction and lithium dendrite formation/propagation. Insights on performance-limiting physical properties and phase transition mechanisms as well as dynamic evolution of SSE/electrode interfaces will be obtained. Mitigating approaches, such as use of surface coating or "buffer layer" in stabilizing SSE/electrode interfaces, will be evaluated. Further, advanced SSE materials and interfaces for improved high-energy Li-metal batteries will be designed and synthesized.

Collaborations. This project collaborates with the following PIs: G. Ceder, K. Persson, M. Doeff, B. McCloskey, R. Kostecki, and R. Prasher (LBNL); W. Yang (Advanced Light Source, ALS); D. Nordlund and Y. Liu (Stanford Synchrotron Radiation Lightsource, SSRL); C. Wang (PNNL); and J. Nanda (Oak Ridge National Laboratory, ORNL).

`Milestones

1. Develop SSE/Li model interfaces for studying the reactivities and dendrite formation at the Li-metal anode interface. (Q1, FY 2021; Completed)
2. Synthesize SSE model samples and model interfaces for studying reactivities and dendrite formation at Li-metal anode. (Q2, FY 2021; Completed)
3. Advance the diagnostic studies of SSE/Li-metal anode interfaces. (Q3, FY 2021; Completed)
4. Obtain mechanistic understanding and deliver design strategies to mitigate reactivities at SSE/Li anode interface. (Q4, FY 2021; On schedule)

Progress Report

This quarter, the team continued to investigate the interfacial behavior between a halide SSE and Li-metal anode. ASSB cells were assembled with an NMC-811/Li_3YCl_6 (LYC) composite cathode, Li_3YCl_6 SSE separator, and Li-In alloy anode. To prepare the composite cathode, NMC-811 and LYC particles were mixed in various weight ratios and pressed into a pellet under external pressure. Figure 42a-c shows the effect of the ratio on voltage profiles as well as capacity of the ASSB full cell. All cycling was carried out at 0.1 C between 2.5 V and 4.4 V versus Li^+/Li. While a low NMC-811/LYC ratio of 70:30 delivered very small capacity, a high ratio of 90:10 also diminishes the cycling performance somewhat. This suggests that establishing effective conduction pathways through proper particle distribution in composite cathode is essential for ASSB cycling. The optimal ratio was found to be 85:15, where a reversible initial discharge capacity of ~ 140 mAh/g was obtained. The capacity increases during the first few cycles, but stabilizes after 4 cycles, reaching ~ 160 mAh/g. Stable cycling was achieved afterward, with the cell delivering performance near the level of what is typically obtained in a liquid cell (Figure 42d-e). Figure 42f-g shows the voltage profiles and rate capability of the same cell. Significant capacity loss was observed on increasing the rate from 0.1 C to 0.5 C, suggesting large cell impedance and the need to further optimize ionic and electronic conduction in the composite cathode as well as the interfaces. The team is investigating the effect of adding carbon as an electronic conductive additive and a third component into the composite electrode.

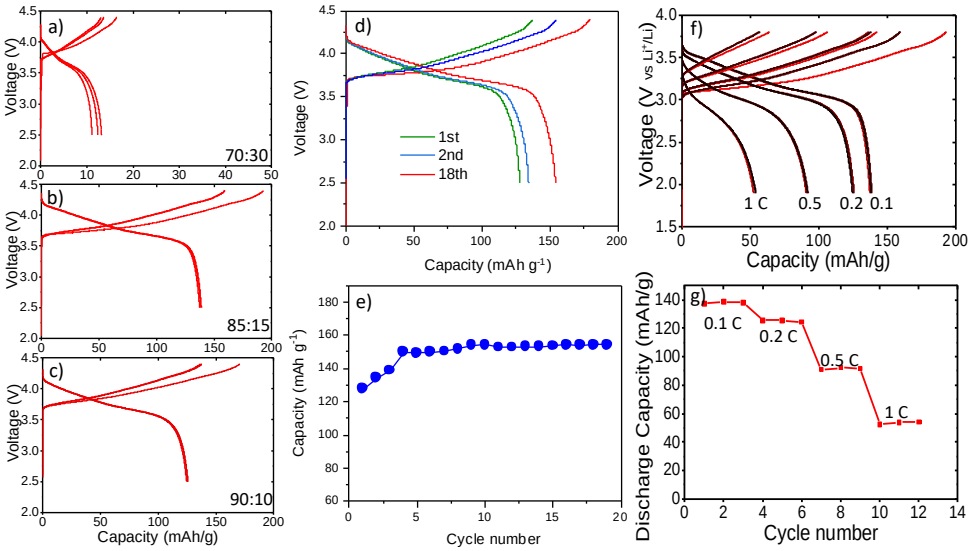

Figure 42. Charge/discharge voltage profiles of all-solid-state battery (ASSB) cells assembled with an NMC/LYC ratio of (a) 70:30, (b) 85:15, and (c) 90:10 in the composite cathode, respectively. (d-e) Charge/discharge voltage profiles and cycling stability of an ASSB cell assembled with an NMC/LYC ratio of 85:15. All cycling rate is 0.1 C. (f-g) Charge/discharge voltage profiles and rate capability of an ASSB cell assembled with an NMC/LYC ratio of 85:15.

The ASSB cell was disassembled after cycling, and the components were recovered for analysis. Figure 43a shows the cross-sectional SEM image collected at the interface between LYC and Li-In anode. While cracking was observed on the LYC separator, the physical contact at the interface was mostly maintained. The phase boundary between LYC and Li-In metal, however, became less even, with growth of additional small features clearly seen. Figure 43b-d shows the EDS elemental mapping for yttrium, chlorine, and indium, respectively. Indium was detected in the observed small features, suggesting that these are likely lithium dendrites with the inclusion of indium metal. The results show the dynamic nature of the anode interface, and further analysis is needed to gather fundamental understanding on cycling-induced changes.

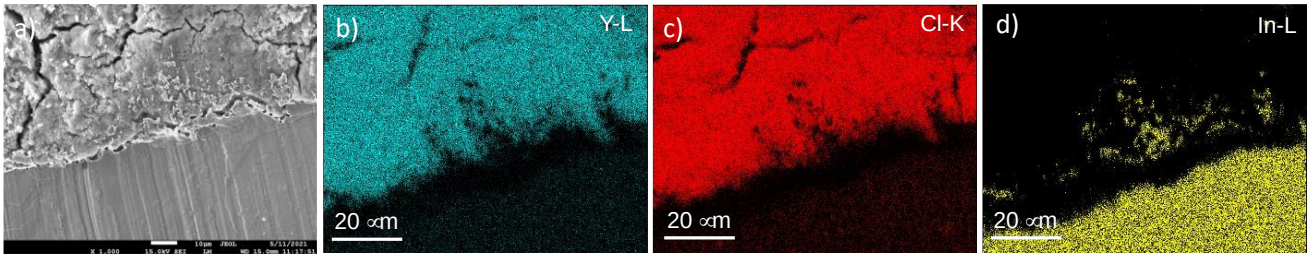

Figure 43. (a) Cross-sectional scanning electron microscopy image and (b-d) elemental mapping of Y-L, Cl-K, and In-L at the interface between LYC and In-Li anode recovered from the cell after 18 cycles at 0.1 C.

Patents/Publications/Presentations

Publication

- Li, L., Z. Lun, D. Chen, Y. Yue, W. Tong, G. Chen, G. Ceder, and C. Wang. "Fluorination-Enhanced Surface Stability of Cation-Disordered Rocksalt Cathodes for Li-Ion Batteries." *Advanced Functional Materials* 31, No. 25 (2021). doi: 10.1002/adfm.202101888.

Task 2.2 – Interfacial Processes – Diagnostics (Robert Kostecki, Lawrence Berkeley National Laboratory)

Project Objective. The objective of the proposed research is to establish specific design rules toward the next generation of low impedance Li-metal rechargeable batteries that are capable of performing 1000 deep discharge cycles at CE > 99.9% and suppressing lithium dendrite formation at high current densities (> 2 mA/cm^2). This project aims at the following: (1) establishing general rules between Li^+ transport properties in novel liquid/solid electrolytes, and (2) determining the mechanism of the SEI layer (re)formation. The other goal is development and application of far- and near-field optical probes and synchrotron-based advanced X-ray techniques to obtain insight into the mechanism of Li^+ transport and interfacial reactions in lithium/liquid model systems. Through an integrated synthesis, characterization, and electrochemistry effort, this project aims to develop a better understanding of lithium/LE interface so that rational decisions can be made as to their further development into commercially viable Li-metal cells.

Project Impact. Chemical instability and high impedance at the interface of Li-metal electrodes limits electrochemical performance of high-energy-density batteries. A better understanding of the underlying principles that govern these phenomena is inextricably linked with successful implementation of high-energy-density materials in Li-metal-based cells for PHEVs and EVs. New state-of-the-art techniques to identify, characterize, and monitor changes in materials structure and composition that take place during battery operation and/or storage will be developed and made available to the Program participants. The proposed work constitutes an integral part of the concerted effort within the BMR Program, and it supports development of new electrode materials for high-energy, Li-metal-based rechargeable cells.

Approach. The pristine and cycled composite electrode and model thin-film electrodes will be probed using various surface- and bulk-sensitive techniques, including FTIR, ATR-FTIR, near-field IR and Raman spectroscopy/microscopy, and SPM to identify and characterize changes in materials structure and composition. Novel *in situ / ex situ* far- and near-field optical multi-functional probes in combination with standard electrochemical and analytical techniques are developed to unveil the structure and reactivity at interfaces and interphases that determine materials electrochemical performance and failure modes.

Out-Year Goals. In the out-years, the project aims to achieve the following: (1) understand factors that control performance and degradation processes, (2) unveil structure and reactivity at hidden or buried interfaces and interphases that determine electrochemical performance and failure modes, and (3) propose effective remedies to address inadequate Li-metal-based battery calendar/cycle lifetimes for PHEV and EV applications.

Collaborations. The diagnostic studies will be carried out in sync with other diagnosticians (G. Chen, B. McCloskey, R. Prasher, and L-W. Wang) and theory and computational scientists (G. Ceder and K. Persson).

Milestones

1. Acquire near-field spectra from graphene/SEI. (Q1, FY 2021; Completed)
2. Determine composition of SEI on lithium via *in situ* near-field FTIR measurements. (Q2, FY 2021; Completed)
3. Complete preliminary near-field FTIR and XPS investigations of surface reactivity of lithium in LE and SE. (Q3, FY 2021; Completed)
4. Develop a valid mechanism for non-uniform current distribution on lithium/electrolyte interface. (Q4, FY 2021; In progress)

Progress Report

This quarter, the team has explored the ground for the *in situ* near-field FTIR nano-spectroscopy (nano-FTIR) and XPS characterization of interfaces of lithium and LEs. Their progress toward this quarter's milestone consists of both a better understanding of the nano-FTIR theory and experimental methodology, and also development of an *in situ* electrochemical cell compatible with nano-FTIR and XPS. As a reminder, for *in situ* characterization, the team assembled a cell, where a monolayer graphene sheet was used as a working electrode and optical window for nano-FTIR characterization. However, it is critical to understand how graphene shapes and affects the near-field FTIR signal. In particular, their work referred to two basic challenges: (1) how the near-(electric) field that drives dipole oscillations in nanoscopic spatial regions of interest decays in the subsurface, and (2) how near-field infrared nano spectroscopy absorption spectra of buried chemistries change as a function of subsurface depth.

To answer those questions, the team investigated the decay of the signal from the substrate depending on a different number of deposited graphene layers. They chose two substrates of interest: mica and polymethyl methacrylate (PMMA). Both offer a flat, clean surface that provides the nano-FTIR signal. They deposited the mono-layer to few-layer graphene via the scotch-tape method from highly oriented pyrolytic graphite (HOPG). This method provides a clean surface with the least contamination, which is essential for studying the interfaces. They observed the decay of the intensity of the nano-FTIR signal from both mica and PMMA substrates dependent on the number of graphene layers. To extract the correlation parameters, they collected hundreds of nano-FTIR spectra through one to four layers of graphene on both substrates and performed fitting of the decaying signal. For PMMA substrate, they investigated five vibrations (that is, 1155 cm^{-1}, 1196 cm^{-1}, 1242 cm^{-1}, 1267 cm^{-1}, and 1736 cm^{-1}); for mica, they investigated four vibrations (that is, 933 cm^{-1}, 998 cm^{-1}, 1042 cm^{-1}, and 1100 cm^{-1}).

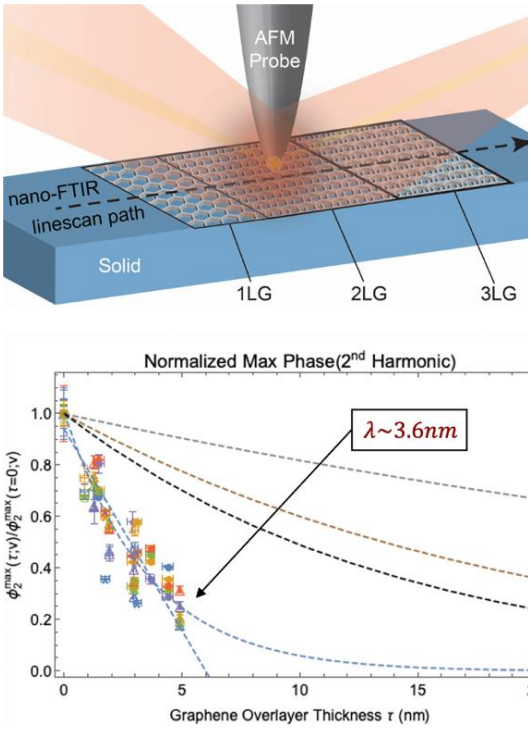

Figure 44. Graphene-subsurface nano Fourier transform infrared (nano-FTIR). (top) Schematic of the nano-FTIR experiment. Solid implies either PMMA or mica substrates (bottom) normalized phase of the 2nd harmonic (near field) FTIR signal. Exponential fitting yields a decay constant of ~ 3.6 nm.

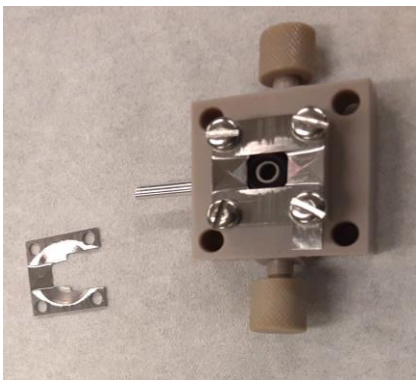

Figure 45. Photograph of a prototype *in situ* spectro-electrochemical nano Fourier transform infrared and X-ray photoelectron spectroscopy cell.

As a result, the team determined that nano-FTIR signals from known graphene-subsurface vibrational modes exponentially decay with increasing graphene thickness. The decay constant of λ~3.6 nm was obtained after performed fitting. This systematic study will allow better interpretation of results obtained from *in situ* measurements of Li/liquid and Li/solid interfaces.

Another challenge relevant to this quarter's milestone relates to designing and manufacturing an *in situ* spectro-electrochemical cell for nano-FTIR and XPS studies. The cell must include graphene window to analyze subsurface interfaces in rechargeable Li-based batteries, and at the same time, be compatible with the level of vacuum required to generate photoelectrons in XPS. The prototype cell is shown in Figure 45.

The two-electrode electrochemical cell is machined from PEEK and is compatible with both LEs and SEs. The current design allows the team to successfully perform nano-FTIR measurements through the graphene window. Next quarter, they will focus on electrochemical testing and preliminary measurements of model Li-based systems.

Patents/Publications/Presentations

The project has no patents, publications, or presentations to report this quarter.

Task 2.3 – Advanced *In Situ* Diagnostic Techniques for Battery Materials (Xiao-Qing Yang and Enyuan Hu, Brookhaven National Laboratory)

Project Objective. The primary objective of this project is to develop new advanced *in situ* material characterization techniques and to apply these techniques to support development of new cathode and anode materials with high energy and power density, low cost, good abuse tolerance, and long calendar and cycle life for beyond Li-ion battery systems to power PHEVs and battery electric vehicles (BEVs). The diagnostic studies will focus on issues relating to capacity retention, thermal stability, cycle life, and rate capability of beyond Li-ion battery systems.

Project Impact. The VTO Multi-Year Program Plan describes the goals for battery: "Specifically, lower-cost, abuse-tolerant batteries with higher energy density, higher power, better low-temperature operation, and longer lifetimes are needed for development of the next-generation of HEVs [hybrid electric vehicles], PHEVs, and EVs." The results of this project will be used for development of technologies that will significantly increase energy density and cycle life, and reduce cost. This will greatly accelerate deployment of EVs and reduce carbon emission associated with fossil fuel consumption.

Approach. This project will use a combination of synchrotron XRD and pair distribution function (x-PDF) and of neutron diffraction (ND) and pair distribution function (n-PDF); x-ray spectroscopies including hard/soft XAS, X-ray photon emission spectroscopy (PES); and imaging techniques including X-ray fluorescence (XRF) microscopy, transmission X-ray microscopy (TXM), and transmission electron microscopy (TEM).

Out-Year Goals. The out-year goals are to develop spectro-tomography, XRD, XAS, and PDF techniques and apply these techniques on Li-ion battery cathode, Na-ion battery cathode, and SSE.

Collaborations. The BNL team will work closely with material synthesis groups at ANL (Y. Shin and K. Amine) for the high-energy composite, at PNNL for the S-based cathode and Li-metal anode materials, and with ORNL on neutron scatterings. This project will also collaborate with industrial partners at GM and Johnson Controls, as well as with international collaborators.

Milestones

1. Complete three-dimensional (3D) spectro-tomography studies of Li-rich layered material $Li_{1.2}Ni_{0.13}Mn_{0.54}Co_{0.13}O_2$ at various states of charge (SOCs). (Q1, FY 2021; Completed)
2. Complete XRD, PDF analysis, and XAS studies of single-crystal sodium cathode material $Na_xNi_{0.76}Mn_{0.14}Co_{0.1}O_2$. (Q2, FY 2021; Completed)
3. Complete XRD/x-PDF/XAS studies of O3-type Na-cathode material $Na_xLi_{1.2-y}Mn_{0.54}Ni_{0.13}Co_{0.13}O_2$. (Q3, FY 2021; Completed)
4. Complete sulfur and phosphorus XAS studies of SSE $Li_{10}GeP_2S_{12}$ from various SOCs during the 1st cycle. (Q4, FY 2021; In progress)

Progress Report

This quarter, the team completed the third milestone and progressed on the fourth milestone. BNL has been focused on developing new diagnostic techniques to study and improve performance of high-energy-density Li-ion batteries and Na-ion batteries. Na-ion batteries, with gravimetric energy density potentially comparable to some Li-ion batteries and the raw materials widely available, have been pursued persistently for grid energy storage and low-speed vehicles. Mn-rich (manganese > 50%) layered oxide with high energy density and low cost have been explored extensively in Li-ion batteries and also in Na-ion battery cathode development. The large size of sodium ions affects the stacking of layers and hence further complicates the structure of these layered Na-ion materials. X-ray absorption near-edge structure (XANES) can clearly reveal the transition metal (TM) cation valence and is commonly used to study charge compensation mechanism for battery materials. In collaboration with X. Li at PNNL and X. Li at Harvard University, *ex situ* manganese, cobalt, nickel K-edge XANES studies were carried out on $Na_xLi_{1.2-y}Mn_{0.54}Ni_{0.13}Co_{0.13}O_2$ at fully sodiated, charged to 3 V and charged to 3.8 V states, along with some reference metal oxides, with results shown in Figure 46. The manganese K-edge XANES in Figure 46a reveals that manganese does not show obvious valence change on charging and stays at 4+ all the time. Cobalt K-edge XANES in Figure 46b shows that minor oxidation has taken place when charged to 3.8 V. The nickel K-edge XANES, however, displays very drastic change, as shown in Figure 46c. The fully sodiated $Na_xLi_{1.2-y}Mn_{0.54}Ni_{0.13}Co_{0.13}O_2$ has very close nickel valence to that of pristine $Na_xLi_{1.2-y}Mn_{0.54}Ni_{0.13}Co_{0.13}O_2$, which is between 2+ and 3+. When charged to 3.0 V, the valence becomes close to that of $LiNiO_2$ with 3+ valence state. Further charging to 3.8 V shows a continuous shift to a higher energy position located between $LiNiO_2$ (3+) and charged $LiNi_{1/3}Co_{1/3}Mn_{1/3}O_2$ (4+). The XANES results demonstrate that nickel is the major element that contributes to the capacity within the voltage range of 2 V to 3.8 V.

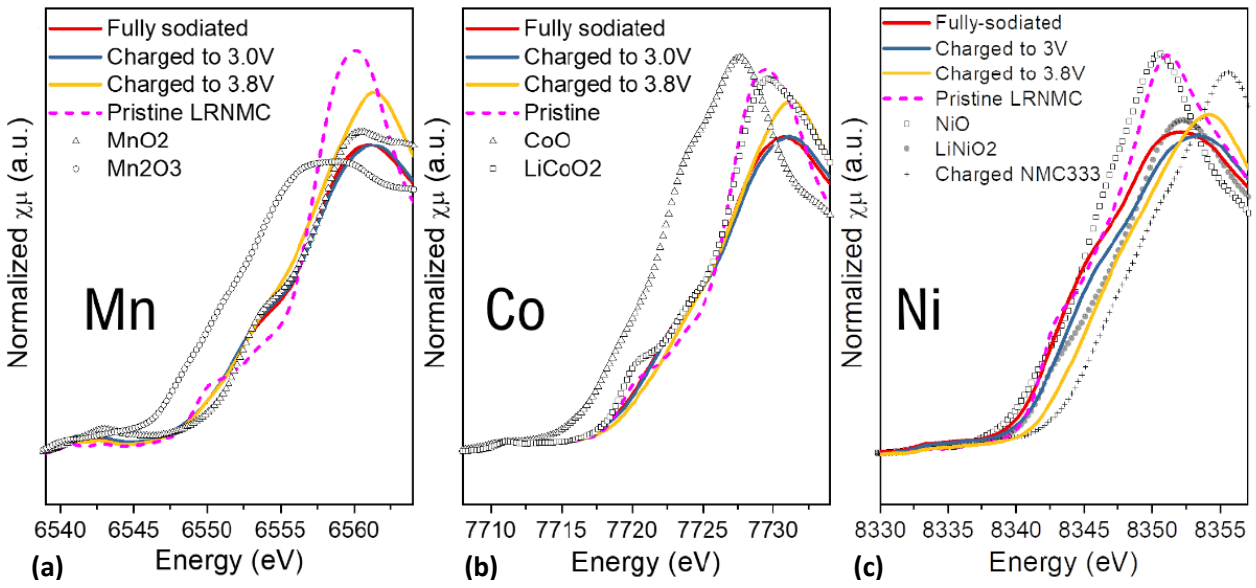

Figure 46. X-ray absorption near-edge structure data of $Na_xLi_{1.2-y}Mn_{0.54}Ni_{0.13}Co_{0.13}O_2$ cathode at K-edges of manganese (a), cobalt (b), and nickel (c) for the *ex situ* sample at different charged states. Spectra of reference oxides with known transition metal valences are also shown for comparison.

Patents/Publications/Presentations

Publications

- Cai, Z., Y. Ou, B. Zhang, J. Wang, L. Fu, M. Wan, G. Li, W. Wang, L. Wang, J. Jiang, Z. W. Seh, E. Hu, X-Q. Yang, Y. Cui,* and Y. Sun.* "A Replacement Reaction Enabled Interdigitated Metal/Solid Electrolyte Architecture for Battery Cycling at 20 mA cm^{-2} and 20 mAh cm^{-2}." *Journal of the American Chemical Society* 143, 8, (2021): 3143–3152. doi: 10.1021/jacs.0c11753; Publication Date (Web): February 17, 2021. Note: This paper was published in Q2 of FY 2021, but was not listed in that quarter's report.
- Lin, R., R. Zhang, C. Wang, X-Q. Yang, and H. L. Xin.* "TEMImageNet Training Library and AtomSegNet Deep-Learning Models for High-Precision Atom Segmentation, Localization, Denoising, and Deblurring of Atomic-Resolution Images." *Scientific Report* 11, Article No. 5386 (2021). doi: 10.1038/s41598-021-84499-w; Publication Date (Web): March 8, 2021. Note: This paper was published in Q2 of FY 2021, but was not listed in that quarter's report.
- Lin, R.,* S. Bak,* Y. Shin, R. Zhang, C. Wang, K. Kisslinger, M. Ge, X. Huang, Z. Shadike, A. Pattammattel, H. Yan, Y. Chu, J. Wu, W. Yang, M. S. Whittingham, H. L. Xin,* and X-Q. Yang.* "Hierarchical Nickel Valence Gradient Stabilizes High-Nickel Content Layered Cathode Materials." *Nature Communications* 12, Article No. 2350 (2021). doi: 10.1038/s41467-021-22635-w; Publication Date (Web): April 20, 2021.
- Li, S., Z. Shadike, G. Kwon, X-Q. Yang, J. H. Lee,* and S. Hwang.* "Asymmetric Reaction Pathways of Conversion-Type Electrodes for Lithium-Ion Batteries." *Chemistry of Material* 33 (2021): 3515−3523. doi: 10.1021/acs.chemmater.0c04466; Publication Date (Web): April 27, 2021.

Task 2.4 – Probing Interfacial Processes Controlled Electrode Stability in Rechargeable Batteries (Chongmin Wang, Pacific Northwest National Laboratory)

Project Objective. The main objective is to explore interfacial phenomena in rechargeable Li-ion batteries of both solid-state and LE configuration, to identify the critical parameters that control the stability of interface and electrodes as well as SE. The outcome will be establishing correlations between structural-chemical evolution of active components of batteries and their properties. These correlations will provide insight and guidance to battery materials development groups for developing high-performance battery materials.

Project Impact. The proposed characterization work focuses on atomic-level structural and chemical analysis and direct correlation with battery fading properties. The work can be directly used to guide design of electrode materials with tailored microstructure and chemistry for enhanced properties of increasing the energy density of Li-ion batteries and to accelerate market acceptance of EVs, especially for PHEVs as required by the EV Everywhere Grand Challenge.

Approach. The project will use integrated advanced microscopic and spectroscopic techniques, including *in situ* and *ex situ* STEM, environmental STEM, cryo-electron microscopy, and *in situ* liquid SIMS to directly probe the structural and chemical information during lithium deposition and stripping. Cryo-STEM with analytical tools, such as EDS and EELS, will be used to gain chemical and electronic structural information at the interface between lithium metal and electrolyte of both solid-state and liquid configuration, which will allow direct correlation between the morphology and chemistry. STEM – high-angle annular dark-field (HAADF) atomic-level imaging and EDS/EELS will be used to probe the interface and bulk lattice stability of cathode and SE in SSB. The work will be in close collaboration with the battery development group within the BMR and U. S.–Germany Collaboration on Energy Storage.

Out-Year-Goals. This project has the following out-year goals:

- Atomic-level multi-scale *ex situ* / *in situ* and *operando* STEM and cryo-STEM investigation on the fading mechanisms of energy-storage materials and devices in the system of both LE and SE; develop a fundamental understanding of electrochemical energy-storage processes and kinetics of electrodes.
- Develop new *in situ* and *ex situ* STEM capability for probing challenging questions related to energy storage technology for both solid-state and LE energy storage system.

Collaborations. This project collaborates with G. Chen (LBNL); J. Nanda (ORNL); Y. Yao (UH); K. Amine (ANL); D. Wang (PSU); A. Manthiram (University of Texas, or UT, Austin); W. Tong (LBNL); Y. Cui (Stanford); J. Zhang (PNNL); J. Liu (PNNL); W. Xu (PNNL); X. Jie (PNNL); D. Lu (PNNL); X. Xiao (GM); Y. S. Meng (UCSD); and M. S. Whittingham (State University of New York, Binghamton).

Milestones

1. Measure the electronic properties of SEI layer and identify their dependence on the electrolyte chemistry. (Q1, FY 2021; Completed)
2. Identify the structure and chemistry of surface layer formed on lithium metal when it contacts with LE. (Q2, FY 2021; Completed)
3. Reveal the nature of reaction product and the fading mechanism of NMC cathode when in contact with SE. (Q3, FY 2021; Completed)
4. Identify the structural and chemical difference of SEI on lithium dendrite and spherical particle to gain the correlation between SEI and lithium morphology. (Q4, FY 2021)

Progress Report

Lithium deposition morphology critically controls the performance of Li-metal batteries. One fundamental challenge for using lithium metal is the dendritic lithium deposition. Existing knowledge indicates that the morphologies of lithium deposits are affected by a range of factors, such as pressure, temperature, current density, electrolyte composition, and physical/chemical properties of the SEI. Although remarkable progress has been achieved in stabilizing lithium electrodeposition, an in-depth and comprehensive understanding of the underlying mechanisms of lithium dendrite growth still remains unclear.

This quarter, the team applied cryo-HRTEM, EDS, and EELS techniques to characterize the detailed structure and chemical distribution of SEI layers formed on the lithium particle and lithium whisker that are grown in the same coin cell by using carbonate-based electrolyte (1.2 M $LiPF_6$-EC-EMC). As they probe the SEI on the differing morphology of lithium within the same coin cell, the observation offers the opportunity for directly correlating the SEI features with the lithium morphology.

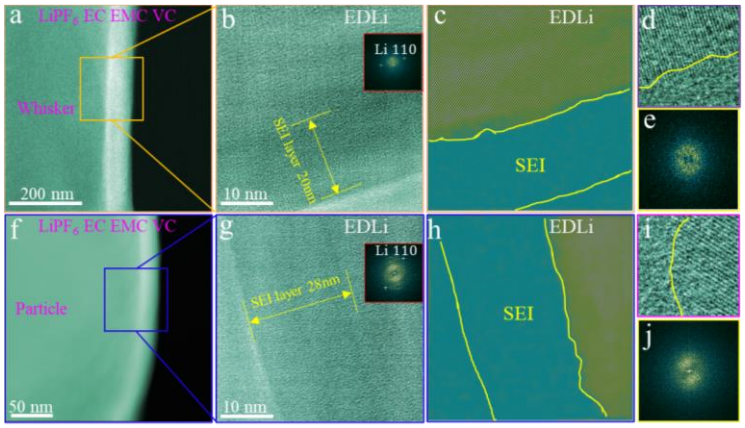

Figure 47. Structural features of SEI formed on lithium whisker and lithium particle that formed in the same coin cell using 1.2 M $LiPF_6$-EC–EMC with 5 wt% VC. (a/f) Cryo – high-angle annular dark-field scanning transmission electron microscopy image reveals SEI layer and lithium deposit. (b/g) Cryo – transmission electron microscopy (TEM) image shows the crystalline nature of lithium deposit and amorphous structure SEI layers (inset: fast Fourier transform, FFT). (c/h) Filtered image shows interface between Li-metal and SEI layer. (d/i) Cryo – high-resolution TEM (HRTEM) images reveal the interface between lithium and SEI. (e/j) FFT of the HRTEM image.

The team reveals that the SEI layer on the lithium whisker has a smooth surface (Figure 47a), with a thickness of ~ 20 nm, as shown in the atomically resolved cryo-TEM image in Figure 47b. The image (Figure 47b) and corresponding fast Fourier transform pattern (Figure 47e) indicate its amorphous structure. The interface between electrochemically deposited lithium (EDLi) and SEI is atomically sharp (Figure 47d). Similarly, the SEI layer on the lithium particle shows amorphous structure, which is thicker than that on the lithium whisker, as shown in Figure 47f-j.

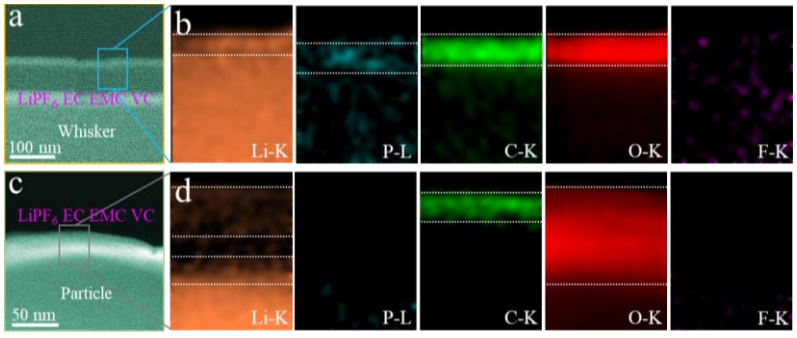

Figure 48. Cryo – electron energy loss spectroscopy map to reveal spatial distribution of different chemical species in the SEI layer. (a/c) Cryo – high-angle annular dark-field scanning transmission electron microscopy imaging reveals the SEI layer on lithium deposit. (b/d) Elemental distribution of lithium, phosphorus, carbon, oxygen, and fluorine in the SEI layer, indicating different spatial distribution for lithium particle and lithium whisker.

Cryo-EELS is used to reveal the fine structures of SEI layers on the lithium particle and lithium whisker. Figure 48 illustrates the EELS elemental maps, showing the spatial distribution of elements in SEI layers on the lithium whisker and lithium particle. As shown in Figure 48b, cobalt, oxygen, and lithium within the SEI on lithium whisker are uniformly distributed. For the lithium particle (Figure 48d), oxygen is distributed uniformly across the SEI, while carbon, phosphorus, and fluorine have a higher concentration in the outer layer of the SEI. Lithium shows non-uniform distribution across the SEI layer.

The present observation clearly indicates that lithium whisker and lithium particle could coexist in the same coin cell using carbonate-based electrolyte. The team then preserved and captured those beam-sensitive lithium deposits and SEI layers at atomic resolution, revealing detailed nanostructure and chemical features by using cryo-TEM, EDS, and EELS. By carefully comparing the nanostructure and chemical distribution of those different SEI layers, the team finds that the SEI layers on both lithium whisker and lithium particle have similarly monolithic amorphous structures, but differ in chemical composition. The SEI layer of lithium whisker has a high content of carbon, while the SEI layer on lithium particle has low concentration of carbon, but including fluorine. These results indicate the SEI on lithum particle is mostly derived from the salt of the electrolyte, while the SEI on lithium whisker is mostly derived from the solvent of the electrolyte. It appears that the SEI on the lithium whisker has a poor Li^+ ion conductivity, while the SEI on lithium particle has a high Li^+ ion conductivity.

The results provide correlation between the characteristics of SEI layer and the morphology of the lithium deposits within the same coin cell, offering insights regarding the possible root cause for development of whisker-shaped and particle-shaped lithium. Apparently, more work is needed to identify the factors that decisively control the growth of lithium from nuclei into either a lithium particle or a lithium whisker.

Patents/Publications/Presentations

Publications

- Zhang, X. H., L. F. Zou, Z. H. Cui, H. Jia, M. H. Engelhard, B. E. Matthews, X. Cao, Q. Xie, C. M. Wang, A. Manthiram, J-G. Zhang, and W. Xu. "Stabilizing Ultrahigh-Nickel Layered Oxide Cathodes for High-Voltage Lithium Metal Batteries." *Materials Today* 44 (2021): 15–24.
- Jia, H., Y. B. Xu, X. H. Zhang, S. D. Burton, P. Y. Gao, B. E. Matthews, M. H. Engelhard, K. S. Han, L. R. Zhong, C. M. Wang, and W. Xu. "Advanced Low-Flammable Electrolytes for Stable Operation of High-Voltage Lithium-Ion Batteries." *Angewandte Chemie International Edition* 133 (2021): 13109–13116.

Presentation

- 239th ECS Meeting / 18th International Meeting on Chemical Sensors, Digital Meeting (June 3, 2021): "Current Density Induced Microstructure Evolution on Li Dendrite and Solid Electrolyte Interphase Revealed by Cryogenic Transmission Electron Microscopy"; Y. B. Xu, H. P. Wu, H. Jia, J-G. Zhang, W. Xu, and C. M. Wang.

Task 2.5 – Integrated Atomic-, Meso-, and Micro-Scale Diagnostics of Solid-State Batteries (Yi Cui, William Chueh, and Michael Toney; Stanford University / SLAC National Accelerator Laboratory)

Project Objective. By developing a characterization toolkit that tackles length scales (Å to mm), cell pressure (1-100 bars), and dynamics (during synthesis, fabrication, and cycling), the project aims to generate insights to engineer SSBs for deployment in EVs. This interdisciplinary team aims to achieve this objective by merging a broad range of characterization approaches as well as modeling to track the evolution of nanoscale chemistry and structure, microstructure, and transport.

Project Impact. The project will have an impact in several areas: (1) accelerate rational design of coatings and artificial SEIs in SSBs; (2) inhibit the root causes leading to cell shorting, and enable high current cycling; (3) accelerate design of cathode coating and composite electrode architectures; and (4) reduce degradation and variability during SSB manufacturing via composition and surface engineering.

Approach. The project has a multi-fold approach that will encompass the following: (1) resolve nanoscale structure and chemistry of SEIs via cryo-TEM; (2) track SE and lithium microstructure evolution in 3D via X-ray micro and diffraction tomography; (3) visualize nanoscale ionic and electronic transport at GBs via conducting AFM; (4) map current distribution in cathodes via scanning transmission X-ray microscopy; and (5) monitor nanoscale SE evolution with gas impurity via *in situ* environmental TEM.

Out-Year Goals. The project will develop an integrated characterization toolkit to characterize SSBs within a single cycle and over hundreds of cycles, spanning a wide range of relevant length scales.

Collaborations. Project collaborations include work with SSRL, ALS, and Advanced Photon Source (APS) synchrotron light sources.

Milestones

1. Demonstrate *operando* X-ray microscopy to track lithium reactivity with LPS SE at open circuit as a function of pressure. (Q1, FY 2021; Completed)
2. Achieve 20-nm resolution for electrochemical impedance AFM for recording ionic and electronic conductivity. (Q2, FY 2021; Completed)
3. Determine composition of reacted phase between LPS and NMC cathodes after 10 cycles using various microscopy methods. (Q3, FY 2021; In progress)
4. Demonstrate *operando* SEM and FIB to record sub-surface microstructure in LLZO during lithium plating. (Q4, FY 2021)

Progress Report

The team's multi-length-scale characterization of cathodes from nanometer to microns was recently published in *Nature Energy* and is summarized here. The objective is to characterize chemistry and microstructure at the primary particle, secondary particle, and electrode length scales. The team selected LMR-NMC as a model system. The multi-length-scale characterization was achieved using synchrotron X-ray microscopy, performed both in conventional scanning transmission mode as well as in ptychography (coherent diffraction imaging) mode.

To preserve the electrode microstructure, the team employed dry ultramicrotome to obtain a ~ 300-nm-thick cross-section specimen of LMR-NMC electrode, a process that they also use to cross-section sulfide SSB. They successfully preserved the microstructure of the electrode along the thickness direction. Cross-sectioning was carried out in a glovebox to avoid air exposure. In contrast to FIB preparation, sample damage is non-existent. Figure 49 shows a typical manganese oxidation map of LMR-NMC in the discharged state. Variation in the oxidation state is clearly visible at the primary and secondary particle levels. In particular, the team observes that the manganese oxidation state, despite a long voltage hold, is heterogenous across the porous electrode. Generally speaking, the larger particle exhibited a higher manganese oxidation state than the smaller particles.

To investigate the manganese oxidation state heterogeneity more closely, the team performed X-ray ptychography at the primary particle length scale (while remaining intact in the secondary particle). Figure 50 shows these higher resolution maps. To understand the evolution of the manganese oxidation state, they first measured pristine and then electrodes after 1 cycle and after 125 cycles. The reduced manganese forms first at the surface of the primary particles, and diffuses inward. They attribute the manganese reduction to the formation of oxygen vacancies, which is consistent with a diffusion from the surface to the bulk of the primary particles.

This study demonstrates the capability to map the oxidation state at the primary particle, secondary particle, and electrode length scales using X-ray microscopy. This effort is being translated to SSB cathodes.

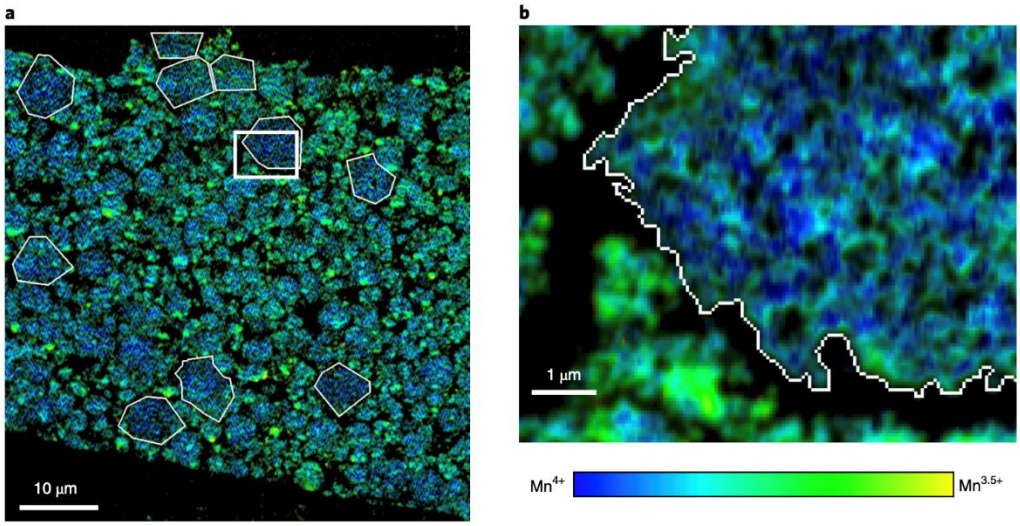

Figure 49. Scanning transmission X-ray microscopy images of cross-sectioned Li- and Mn-rich NMC in the discharged state. Color indicates manganese oxidation state.

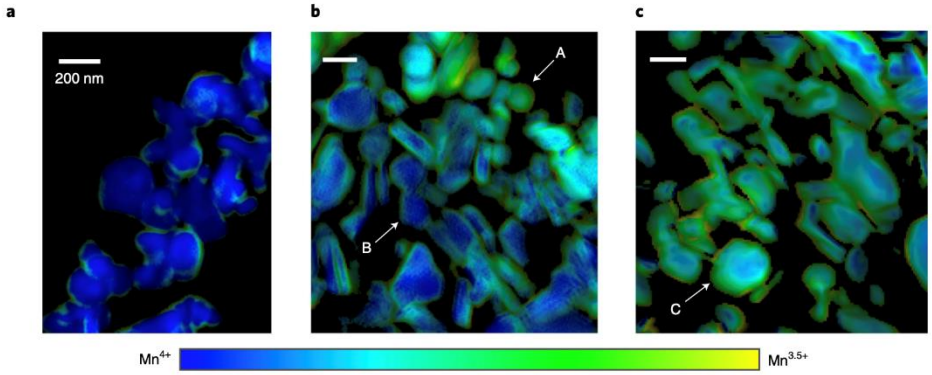

Figure 50. X-ray ptychography image of Li- and Mn-rich NMC: (a) pristine, (b) 1 cycle, and (c) 125 cycles. Color indicates manganese oxidation state.

Patents/Publications/Presentations

Publication

- Csernica, P., S. Kalirai, W. E. Gent, K. Lim, Y-S. Yu, S-J. Ahn, K. Stone, D. Shapiro, M. F. Toney, and W. C. Chueh. "Oxygen Diffusion and Release in Li-Rich Layered Oxides during Extended Cycling: Multi-Length-Scale Distribution and Structural Consequences." *Nature Energy* 6 (2021): 642.

Presentations

- 239th ECS Meeting, Digital Meeting (June 1, 2021); W. C. Chueh.
- MRS Meeting, Virtual (April 23, 2021); W. C. Chueh.
- Stanford, Nanoscale Prototyping Laboratory Seminar, Virtual (April 21, 2021); W. C. Chueh.

Task 2.6 – Investigating the Stability of Solid/Solid Interface (Zonghai Chen, Argonne National Laboratory)

Project Objective. The project objective is to characterize the physical/chemical properties of species at the solid/solid interfaces and to fundamentally understand the critical issues that limit the mechanical, chemical, and electrochemical stability of solid/solid interfaces at the cathode and the anode.

Project Impact. The project will lead to several areas of impact: (1) to generate knowledge that supports the rational design of materials and process development; (2) to establish structure-properties relationship of the interface; and (3) to understand the formation mechanism of lithium dendrite and to predict potential solutions.

Approach. The project approach is multi-fold: (1) understanding the physics behind the transformation between the low conductivity phase and the high conductivity phase; (2) investigating the bonding strength of the cathode electrolyte interface (CEI) using model systems; and (3) developing electrolytes with high ionic conductivity and good bonding to cathodes through cation doping.

Out-Year Goals. The project has the following out-year goals:

- Developing synchrotron-based diagnosis tools to investigate physical/chemical properties of solid/solid interface.
- Identifying mechanistic barriers that limit the chemical/mechanical/electrochemical durability of solid/solid interface.
- Developing model systems to validate the failure mechanism of solid/solid interface.

Collaborations. The project works with ANL collaborators A. Ngo, L. A. Curtiss, V. Srinivasan, Y. Ren, J. Libera, and Y. Z. Liu, and with BNL collaborators F. Wang and X. H. Xiao.

Milestones

1. *In situ* electron microscopic characterization of the dendrite formation on LLZO. (Q1, FY 2021; Completed)
2. Investigation of electronic conducting path in LLZO pellet. (Q2, FY 2021; Completed)
3. Investigation of the mechanical stability of cathode/LLZO interface using model system. (Q3, FY 2021; Completed)
4. Microscopic study of the mechanical stability of cathode/LLZO interface. (Q4, FY 2021; On schedule)

Progress Report

The team started to investigate the mechanical stability between NMC particles and LLZO electrolyte using electron microscopic approaches. During the experiment, a single NMC particle is welded to a tungsten tip using thermally evaporated amorphous carbon as an electrically conductive binder to "glue" the NMC particle to the tungsten tip. Then, the single particle is charged/discharged using lithium metal as the counter electrolyte. The morphologic changes on the particle are evaluated using scanning microscopy. Particularly, FIB is used to partially cut the particle apart to illustrate the morphology and connectivity between primary particles inside the secondary particle.

Figure 51 shows the SEM morphology of NMC-622 particle before and after complete charge/discharge cycling. The fresh surface created by FIB processing clearly shows close contact between primary particles; few gaps/voids are observed before cycling. However, just after the 1st cycle, the SEM image clearly shows that primary particles move away from each other, creating gaps/voids between adjunct primary particles. This morphological change inside secondary particle might not be an issue for batteries using LE because the LE can soak into the gaps/voids generated during cycling and maintain a functional Li^+ connectivity. The case could be different for liquid-free SSBs, in which there is no liquid to soak in, and the generated cracks/voids can lead significantly to the loss of active primary particles and the loss of electrochemical performance.

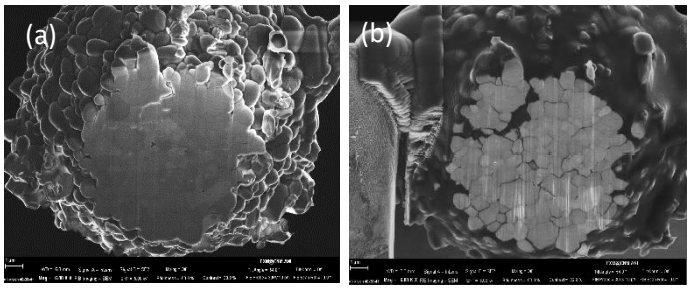

Figure 51. Scanning electron microscopy images of NMC-622 particle of (a) before and (b) after electrochemical cycling, showing the change of inter-connectivity among primary particles.

To confirm the team's observation on NMC-622 particle, LLZO is decorated on NMC-622 particle through a co-sintering process, during which the NMC-622 powder and LLZO powder are mixed and pressed into a pellet before sintering at 900°C. Figure 52 shows the SEM images and elemental mapping of both a co-sintered NMC-622/LLZO pellet and a single NMC particle taken from the co-sintered pellet. In Figure 52c-d, the particle has been partially removed using FIB. It can be seen that a compact contact between NMC-622 particles and LLZO particles can be created by co-sintering. However, the uniform distribution of NMC-622 and LLZO is not achieved. The evaluation on FIB cut particle shows that part of the LLZO electrolyte is able to soak into the crack/voids between primary particles during the co-sintering process, as shown in Figure 52d, which shows a small amount of LLZO inside the secondary particle.

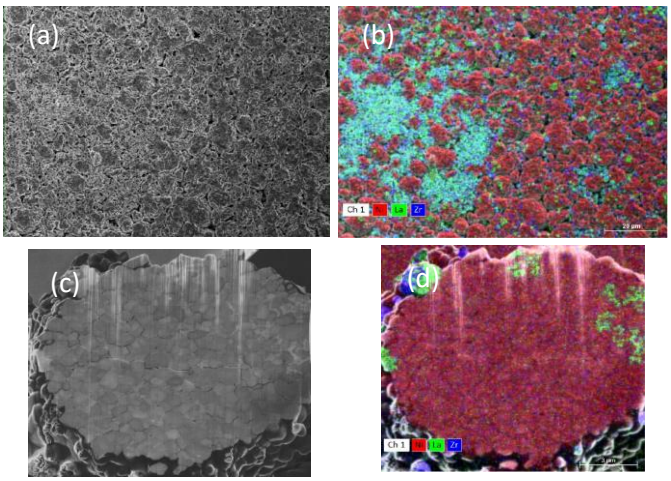

Figure 52. Scanning electron microscopy images (a/c) and elemental mapping (b/d) of co-sintered NMC-622/LLZO pellet (a/b) and a single LLZO-decorated NMC-622 particle (c/d).

In situ SEM experiment on the LLZO decorated NMC particles will be conducted next quarter to evaluate the mechanical stability between NMC particle and the decorated LLZO particle, as well as the primary particles. At the same, a single crystal cathode will also be investigated as a model system to mitigate the potential impact of cracking between primary particles.

Patents/Publications/Presentations

The project has no patents, publications, or presentations to report this quarter.

Task 2.7 – Fundamental Understanding of Interfacial Phenomena in Solid-State Batteries (Xingcheng Xiao, General Motors)

Project Objective. The project objective is to develop a comprehensive set of *in situ* diagnostic techniques combined with atomic/continuum modeling schemes to investigate and understand the coupled mechanical/chemical degradation associated with dynamic interfacial phenomena in SSBs. Specifically, *in situ* observations and characterizations of lithium plating-stripping processes, lithium dendrite formation, interphase formation, and the induced interfacial stresses, as well as the mechanical and electrochemical properties of interfaces and interphases, are paramount. The study will provide useful guidelines for optimizing cell structure design and engineering interfaces and interphases to enable SSBs.

Project Impact. The project will provide fundamental understanding of the dynamic interfacial phenomena and the coupled mechanical and chemical degradation. In addition, it will establish a critical guideline to design safe and durable SSBs with energy density > 500 wh/kg for EV applications.

Approach. The multi-scale *in situ* diagnostic tools, including AFM, nanoindentation, dilatometer, stress sensors, and pressure cells, will be used to investigate mechanical behavior and microstructure evolution at interface/interphase during lithium plating and stripping. The information (along with Li-ion transport properties and microstructure evolution obtained using the advanced spectroscopic ellipsometry, and *in situ* TEM) will be correlated with electrochemical performance toward high cycle efficiency and dendrite-free SSBs. The goal of this understanding is to develop strategies for surface and interface engineering, apply them to commercially available SEs (including powder, pellets, and foils), and assemble SSBs for further validation and optimization, eventually extending cycle life for EV application.

Out-Year Goals. The project seeks to develop SSB model systems to capture critical mechanical properties and probe the coupled mechanical-chemical degradation by further developing comprehensive *in situ* diagnostic tools. All results obtained from these *in situ* studies, combined with advanced *postmortem* analysis and modeling, will be correlated with the cycling stability of SSBs. The *in situ* tools developed will be applied to the following two periods to deeply understand the coupled mechanical and chemical degradation of interface/interphase.

Collaborations. The co-PIs involved in experiments and simulation will be as follows: B. W. Sheldon and Y. Qi (Brown University), Y-T. Cheng and A. Seo (University of Kentucky), and Q. Zhang (GM).

Milestones

1. Correlation between interfacial mechanical failure mechanisms and current density and pressure. (Q1, FY 2021; Completed)
2. Summary of the thickness, chemical bonding, and structural information of the interphases between anode and SE, and cathode and SE. (Q2, FY 2021; Completed)
3. Identified mechanisms of ionic transport through the interface/interphase. (Q3, FY 2021; Completed)
4. Multi-scale modeling framework to describe the coupled mechanical/chemical degradation. (Q4, FY 2021)

Progress Report

The developed DFT - kinetic Monte Carlo (KMC) multi-scale simulation scheme is employed to simulate the lithium vacancy evolution at two representative interfaces: Li/Li_2O (lithiophilic) and Li/LiF (lithiophobic), to understand how lithium ions transport through the interfaces. As the compressive stress is usually applied during battery operation, the stress-induced lithium creep effects are considered given the low melting point of lithium. Specifically, the DFT calculations are utilized to get the optimized atomic interface structures and to calculate the lithium vacancy formation energy and the lithium forward (toward the interface, E_f) and backward (toward the bulk, E_b) hopping barriers. The KMC simulation is then used to simulate the evolution of lithium vacancies near the interface by taking various lithium hopping rates based on the DFT as inputs.

The vacancy evolutions in lithiophilic Li/Li_2O and lithiophobic Li/LiF interfaces were simulated with and without the mechanical bias. Figure 53 shows the snapshots after 10^5 steps KMC simulations for Li/Li_2O and Li/LiF interfaces without (Figure 53a/c) and with (Figure 53b/d) the mechanical bias. For the Li/Li_2O interface, although vacancies are distributed quite uniformly in the lithium in both cases (Figure 53a/c), fewer vacancies are near the interface with the mechanical bias (Figure 53c). For the Li/LiF interface, large portions of vacancies migrate into the bulk and are widely distributed in the bulk with the mechanical bias (Figure 53d), while almost all the vacancies are trapped at the interface without the bias (Figure 53b). When analyzing the vacancy distribution (Figure 54a-b), the fractions of vacancies at different distances mostly fall between 1% and 10% in the Li/Li_2O and Li/LiF interfaces with the mechanical bias (red triangles), suggesting uniform distributions of vacancies. Figure 54c compares the average distances of vacancies from the interface in the two interfaces. Without the mechanical bias, the average distance of vacancies from the interface in Li/Li_2O (22 Å) is much larger than that in Li/LiF (4 Å). With the mechanical bias, the vacancies are pushed into deeper regions in the bulk in both interfaces. The average distance increases from 22 Å to 25 Å in Li/Li_2O, while a much larger increase of more than 15 Å is observed in Li/LiF. Hence, the interfacial properties (lithiophilic or lithiophobic) determine the vacancy hopping behavior with no creep effects, but have weaker influence on the vacancy evolution under compressive stress.

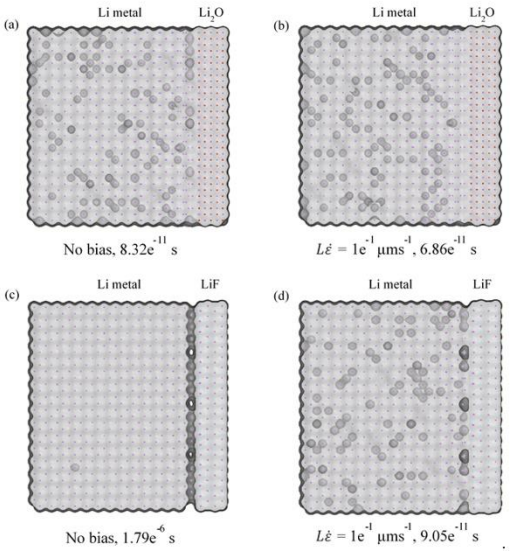

Figure 53. Snapshots after 10^5 steps of kinetic Monte Carlo simulations for Li/Li_2O (a-b) and Li/LiF (c-d) interfaces without (a/c) and with (b/d) the mechanical bias.

To understand the effects of compressive stress in maintaining a flat lithium surface, different $L\dot{\varepsilon}$ values ranging over 6 orders of magnitude, given the typical strain rates in Li-metal batteries, were imposed on the lithiophobic Li/LiF interface. Figure 55a compares the average distances of vacancies from the interface at different $L\dot{\varepsilon}$ values. Although $L\dot{\varepsilon}$ varies between 10^{-5} and 10^{-1} μms^{-1} (compressive stress in the range of 0.25-1 MPa), the average distances reach around 20 Å after 30 ps as long as the compressive stress is applied (Figure 55a). The vacancy distributions show a consistent trend that most vacancies submerge into the bulk and distribute uniformly regardless of the $L\dot{\varepsilon}$ value (Figure 55b-c), which helps maintain a flat lithium surface. This suggests that applying a compressive stress is important and beneficial during the stripping process.

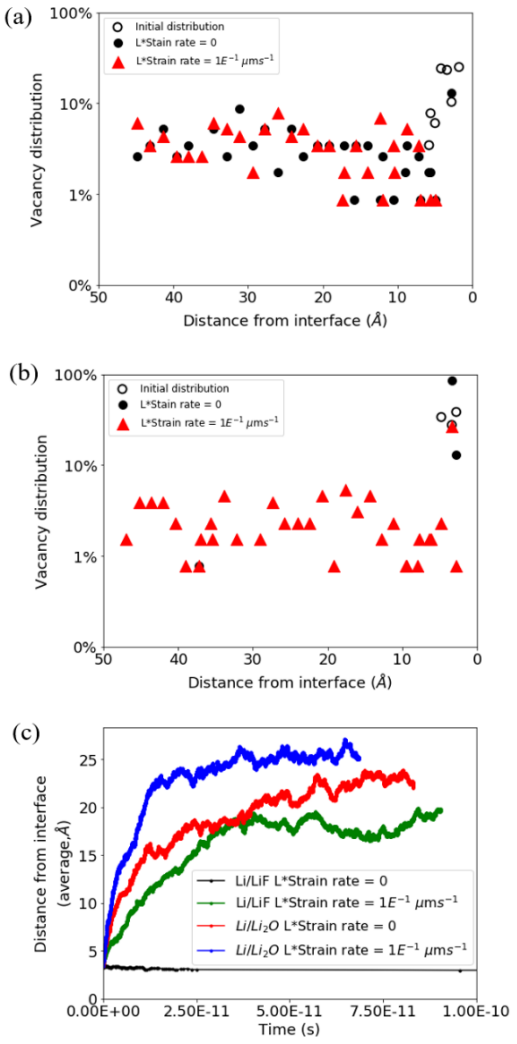

Figure 54. Vacancy distribution without (black dots) and with (red triangles) the mechanical bias after 10^5 steps of kinetic Monte Carlo simulation for Li/Li_2O (a) and Li/LiF (b). (c) Average distances of vacancies from the interface versus time (s).

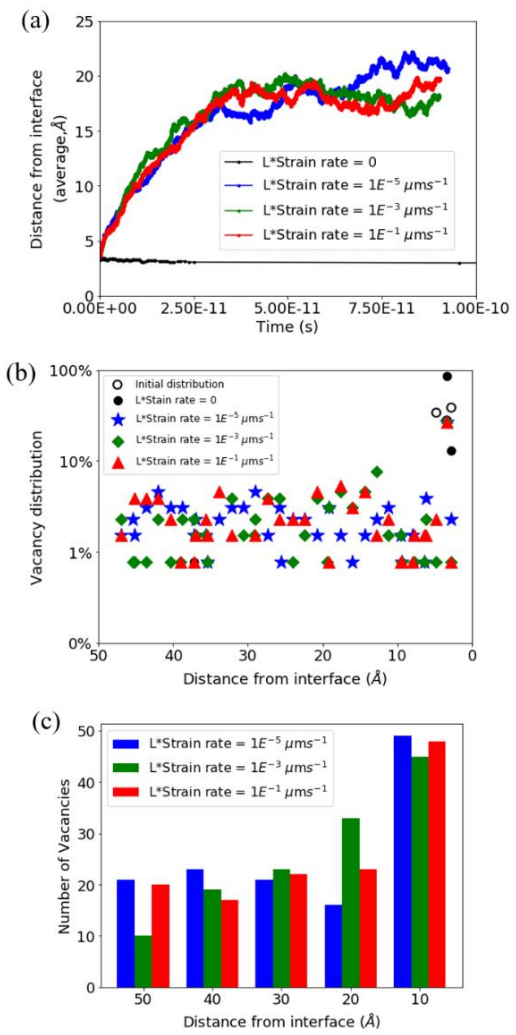

Figure 55. (a) Average distances of vacancies from the interface versus time (s) at different $L\dot{\varepsilon}$ values. Vacancy distributions at different $L\dot{\varepsilon}$ values in percentages (b) and in numbers (c).

Patents/Publications/Presentations

Presentation

- MRS Spring Meeting, Virtual (2021): "Understanding Electrochemical-Mechanical Degradation of Solid Electrolyte Interphases on Lithium Metal Electrode"; X. Xiao.

Task 2.8 – Multidimensional Diagnostics of the Interface Evolutions in Solid-State Lithium Batteries (Yan Yao, University of Houston)

Project Objective. The project objective is to develop a platform combining FIB-SEM tomography, TOF-SIMS, and in-SEM nanoindentation-based stiffness mapping for structural, chemical, and mechanical characterizations in SSLBs. Assessment of the influence of cell design and testing conditions (external pressure, current density, temperature) on the evolutions of interfaces will be performed.

Project Impact. The consolidated *in situ* structural–chemical–mechanical diagnostic platform established in this project will provide unprecedented insights into the failure mechanisms of SSLBs.

Approach. Space- and time-resolved structural, chemical, and mechanical characterizations of the cathode–electrolyte and anode–electrolyte interfaces will be performed on lithium ASSBs using FIB-SEM, TOF-SIMS, and in-SEM nanoindentation. Tasks include the following: (1) development of solid-state cell thin stacks and test-cell configurations that are suitable for *in situ* characterizations; (2) quantitative characterization and *in situ* tracking of interfacial voids formation within composite cathode and electrolyte layer; (3) identification and *in situ* tracking of the chemical composition, spatial distribution, and mechanical properties of electrolyte decomposition products at the lithium- and cathode-electrolyte interfaces; and (4) visualization, chemo-mechanical properties detection, and *in situ* tracking of lithium dendrites grown within the SE layer.

Out-Year Goals. In the out years, the project will develop thin-stack solid-state cells, micro-cells, in-SEM nanoindentation, and testing protocols. The correlation between structural evolution, electrolyte decomposition, and interfacial resistance increase will be investigated.

Collaborations. The UH team (Y. Yao, Z. Fan, and Y. Liang) works closely with the Rice University team (J. Lou and H. Guo).

Milestones

1. Nano-cell development. (Q4, FY 2021; Completed)
2. Cell optimization and electrochemical benchmarking. (Q2, FY 2021; Completed)
3. Multi-scale structural investigations. (Q1, FY 2022; In progress)
4. Composition and spatial distribution study. (Q2, FY 2022; In progress)
5. Selected region mechanical property probing. (Q3, FY 2022; In progress)

Progress Report

This quarter, the team applied the multidimensional diagnostic techniques to evaluate the cell components developed for thin solid-state NMC-Li cell fabrication. The many methods available today to prepare thin cathode and electrolyte layers can be categorized into (1) dry methods, which use insoluble binders such as PTFE, and (2) wet methods, where soluble binders like nitrile butadiene rubber (NBR) are used. Depending on the methods used and the degree of optimization, composites with apparently similar composition show major difference in performance. Structural and chemical characterization techniques at the suitable resolution and sensitivity will provide insights into the difference of the two processes, thus providing feedback and guidance on the fabrication process.

This quarter, the team compares two NMC-LPSCl-binder cathodes, one fabricated with a dry method using PTFE binder and the other with a wet method using NBR binder. Since the solvents used in the wet method are known to affect the conductivity of LPSCl, an additional control sample was fabricated with dry method using PTFE binder and LPSCl treated with the same solvents that are used in the wet method. SEM results show that the PTFE binder is fiber-like and distributes on the NMC and LPSCl particle surface (Figure 56a), while NBR is more homogenously blended with the particles with no individual binder domain (Figure 56b). Using TOF-SIMS offers the opportunity to visualize light elements with good resolution. Fragments F^- and $C_3H_5^+$, respectively representing PTFE and NBR binders, are mapped to quantify the distribution of each component in these electrode composites. The PTFE fibers are clearly visible in Figure 56c, as well as the homogeneous NBR in Figure 56f. The presence of PTFE does not correlate much with the NMC (Figure 56d) and

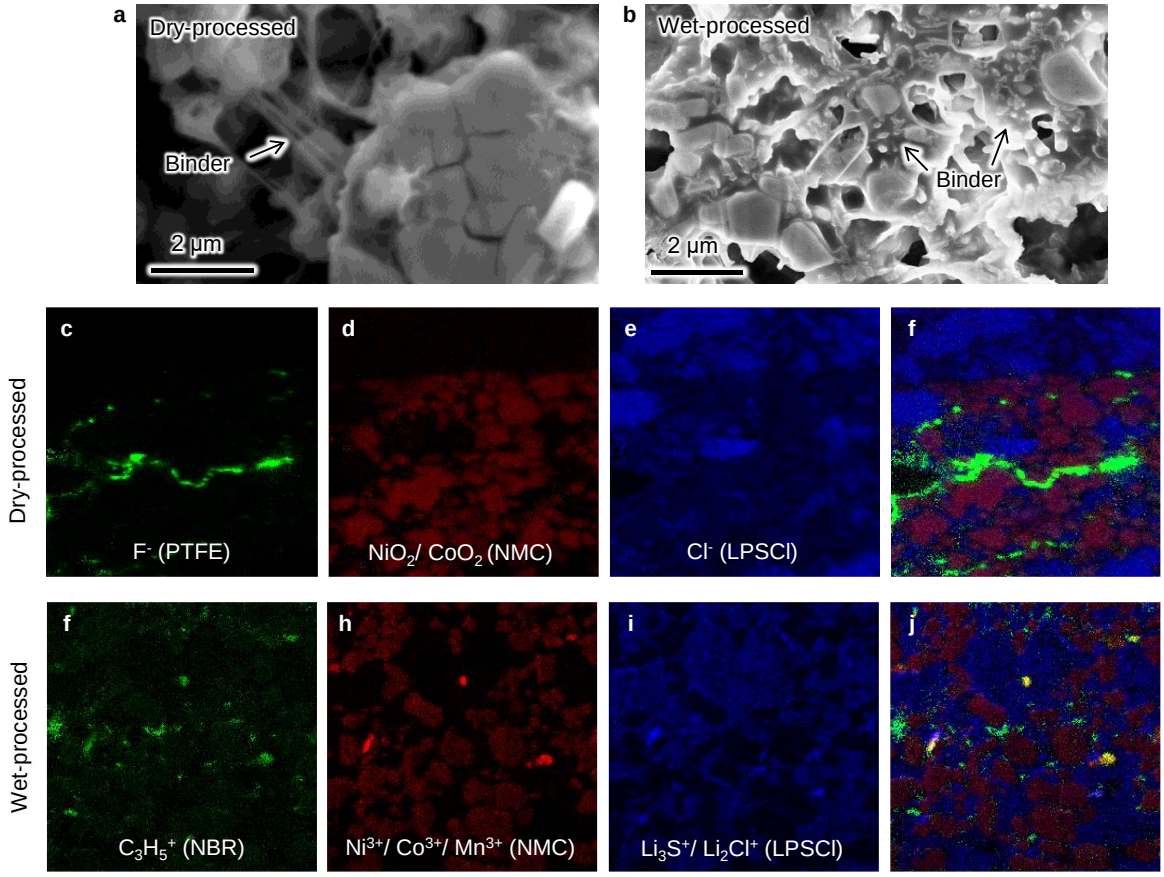

Figure 56. Characterization of NMC cathode composites processed with different methods. (a-b) Scanning electron microscopy images of cathodes containing PTFE (a) and NBR (b) binders processed with dry and wet methods, respectively. (c–j) Time-of-flight secondary ion mass spectroscopy mapping (30 µm by 30 µm) of fluorine (c/f), transition metals (d/h), chlorine (e/i), and the combined view of the three (f/j).

LPSCl (Figure 56e) particles. In contrast, the amount of NBR shows good alignment with NMC particle (Figure 56h) and slightly less so with LPSCl particles (Figure 56i), an indication of NBR enrichment on inorganic particle surface.

The electrochemical properties of the cathodes were then characterized both at the electrode level and cell level. The ionic conductivity of the cathode was measured with both alternating current (AC) and direct current (DC) methods, and the results are shown in Figure 57a. Both electrodes made with solvent-treated LPSCl show decreased ionic conductivity compared with the one made with pristine LPSCl (green circle). What is notable is the lower conductivity of the electrode containing NBR binder (blue up triangle) compared to that containing PTFE (magenta down triangle), which can be explained by the binder distribution revealed in the TOF-SIMS mapping: the NBR binder enriched on both the NMC and LPSCl surfaces could serve as an ionic (and possibly also electrical) insulator. While the soluble binder has the advantage of being uniformly dispersed in the composite, it also provides comprehensive passivation of active particles and induces undesirable performance reduction. Indeed, cells with dry-process cathode show greater rate capability in NMC-Li full cells (Figure 57b).

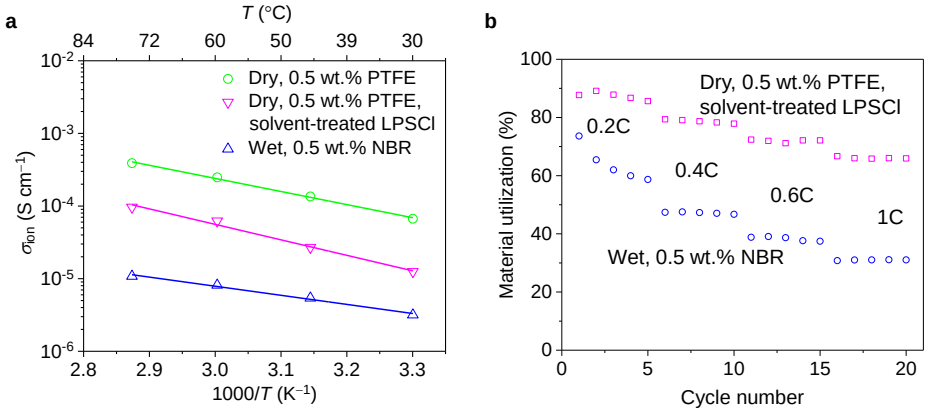

Figure 57. Electrochemical characterizations of NMC-Li cells containing composite cathodes prepared with different methods. (a) Dependence of ionic conductivity of cells on temperature. (b) Rate capability.

Patents/Publications/Presentations

Publications

- Wu, C., J. Lou, J. Zhang, Z. Chen, A. Kakar, B. Emley, Q. Ai, H. Guo, Y. Liang, J. Lou, Y. Yao,* and Z. Fan.* "Current Status and Future Directions of All-Solid-State Batteries with Lithium Metal Anodes, Sulfide Electrolytes, and Layered Ternary Oxide Cathodes." *Nano Energy* (2021): 106081.
- Zhang, J., Z. Chen, Q. Ai, T. Terlier, F. Hao, Y. Liang, H. Guo, J. Lou, and Y. Yao.* "Microstructure Engineering of Solid-State Composite Cathode via Solvent-Assisted Processing." *Joule* (2021). doi: 10.1016/j.joule.2021.05.017.

Presentations

- DOE VTO Annual Merit Review Meeting, Virtual (June 24, 2021): "Multidimensional Diagnostics of the Interface Evolutions in Solid-State Lithium Batteries." Invited.
- IUPAC-MACRO Conference, Virtual (May 19, 2021): "Quinone-Based Organic Materials for All-Solid-State Lithium Batteries." Invited.
- MRS Spring Meeting, Virtual (April 22, 2021): "High-Energy All-Solid-State Organic-Lithium Batteries." Invited.

TASK 3 – MODELING

Team Lead: Venkat Srinivasan, Argonne National Laboratory

Summary and Highlights

Achieving the performance, life, and cost targets outlined by VTO will require moving to next-generation chemistries, such as higher capacity Li-ion intercalation cathodes, silicon and other alloy-based anodes, Li-metal anode, and sulfur cathodes. However, numerous problems plague development of these systems, from material-level challenges in ensuring reversibility to electrode-level issues in accommodating volume changes, to cell-level challenges in preventing cross talk between the electrodes. In this task, a mathematical perspective is applied to these challenges to provide an understanding of the underlying phenomenon and to suggest solutions that can be implemented by the material synthesis and electrode architecture groups.

The effort spans multiple length scales, from *ab initio* methods to continuum-scale techniques. Models are combined with experiments, and extensive collaborations are established with experimental groups to ensure that the predictions match reality. Efforts also focus on obtaining parameters needed for the models, either from lower-length scale methods or from experiments. Projects also emphasize pushing the boundaries of the modeling techniques used to ensure that the task stays at the cutting edge.

A major focus of the effort is around Li-metal-based SSBs. While these chemistries hold promise, numerous challenges such as reactivity, conductivity, and mechanical stability prevent their commercialization. Mathematical models are ideal to provide the guidance and insights needed to solve these issues.

In the area of Li-metal anodes, the focus is on understanding how materials can be designed to prevent dendrite growth using continuum modeling approaches, combined with calculations on mobility in solid conductors. The results are used to guide materials development by providing the properties needed to prevent dendrites, while also achieving the energy and power goals. Models examine the role of the SEI on the morphology of the dendrite and describe the mechanical-electrochemical coupled effects that are critical for dendrite formation. Finally, efforts are focused on discovery of new solid ion conductors with properties that far exceed existing materials. The focus is on using these models as a guide before embarking on extensive experimentation.

Lithium metal with SEs will be paired with cathode materials, often intercalative in nature. Models are being developed to examine the solid-cathode interface in Li-metal based systems, where side reactions and interface debonding issues are known to limit cycling. These models are being used to understand how to prevent chemo-mechanical failure at the interface. Coatings, an effective strategy for high-voltage operation, are being explored with the aim of providing a rational design approach for new coating materials. In addition, focus is paid to porous electrodes with cathode particles to predict the impact of heterogeneities on electrode behavior.

Highlight. The highlight for this quarter is as follows:

- There has been much debate on the exact cause for dendrite formation in SEs. Recently, the impact of any electronic conductivity in the SE has become an area of interest to determine if such an effect can lead to dendrite formation. G. Ceder and colleagues have used a mathematical model to determine that electronic conductivity in SEs can lead to metal deposition in voids. This internal metal deposition not only leads to metal penetration in the SE, but also causes inhomogeneous plating at the electrode/SE interfaces. This effect is minimized if the voids are deep in the ceramic away from the anode. Modeling results suggest that coatings that are defect free can lead to minimization of this effect.

Task 3.1 – Characterization and Modeling of Lithium-Metal Batteries: First-Principles Modeling and Machine Learning
(Kristin Persson, Lawrence Berkeley National Laboratory)

Project Objective. This project supports VTO programmatic goals by developing next-generation, high-energy cathode materials and enabling stable cathode operation at high voltages through target particle morphology design, functional coatings, and rational design of electrolytes. The end-of-project goals include the following: (1) understanding of the factors that govern charge transport in nonaqueous, superconcentrated LEs, (2) critical surface and coating design and optimization strategies that will improve cycling of Li-ion battery cathodes by reducing cathode degradation from oxygen loss, and (3) simulation and machine learning (ML) of the early formation of the SEI on Li-metal electrodes.

Project Impact. This project is aimed at providing fundamental insights into the atomistic mechanisms underlying surface reactivity and performance of Li-ion cathode materials and electrolytes with the ultimate goal to suggest improvement strategies, such as coatings, surface protection, novel electrolyte formulations, and particle morphology design. Transport modes as a function of solvent and salt concentrations will be clarified, and a data-driven reaction network framework will be designed and implemented to predict early SEI formation on lithium metal.

Approach. First-principles calculations, both static and dynamic approaches, are used to model SSE material thermodynamics and kinetics. LEs are modeled through coupled classical molecular dynamics (CMD) and first-principles methods to accurately capture solvation structure as well as reactivity of the liquid system. The reaction network is built on large-scale first-principles data, using graph theory and ML models.

Out-Year Goals. Electrolyte work will be aimed toward understanding the atomistic interactions underlying performance of lithium electrolytes, specifically elucidating conductivity (as a function of salt concentration) and impact on the charge transport mechanisms at play. Amorphous coatings will be evaluated based on ionic transport metrics and thermodynamic stability. The reaction network will be tested against known interfacial species forming on lithium metal in $LiPF_6$/EC electrolytes.

Collaborations. This project is highly collaborative between BMR PIs G. Chen (LBNL), G. Ceder (University of California, Berkeley, UCB), and R. Kostecki (ANL). Improved coating formulations will be examined by Chen and Ceder, and interfacial reactivity insights will be corroborated by Kostecki.

Milestones

1. Preliminary insights into the SEI composition and reaction pathways for baseline electrolytes (BEs). First approximative reaction scheme proposed. (Q3, FY 2020; Completed)
2. Develop a valid model for amorphous structure as compared to experimental radial distribution function (RDF) data. (Q3, FY 2021; Completed)
3. Quantify the effect of co-solvents to at least one superconcentrated electrolyte. (Q4, FY 2021; In progress)
4. Correlation of electrolyte chemistry and Li/SEI compositional structure determined. (Q1, FY 2022; In progress)

Progress Report

This quarter, the team reports a computation scheme to evaluate Li^+ and O^{2-} ion transport in amorphous cathode coating. A cathode coating layer can increase the resistance and capacity loss at higher C-rates due to its large overpotentials at higher currents. Thus, they estimate the overpotential, ΔV, on the cathode surface because of coating. The relation between ΔV and Li^+ diffusivity D^{Li} is:

$$\Delta V = \frac{J l_c k_B T}{D^{Li} c^{Li} q^2} \quad (1)$$

where l_c is the coating thickness, k_B is the Boltzmann constant, T is the temperature, c^{Li} is the Li^+ concentration in the coating, q is the electron charge, and J is the electric current density through the cathode coating, which can be approximated as:

$$J = \frac{\rho V C}{S t} = \frac{\rho r C}{3t} \quad (2)$$

Where ρ is the cathode density, V is the particle volume, S is the particle surface area, r is the particle radius, C is the cathode capacity, and t is the charging/discharging time. Combining Equations (1) and (2), ΔV can be expressed as:

$$\Delta V = \frac{\rho r C}{3t} \frac{l_c k_B T}{D^{Li} c^{Li} q^2} \quad (3)$$

In this study, the team has chosen $LiNiO_2$ as the relevant cathode material, with $\rho = 4.78\ \mathrm{g/cm^3}$. To avoid detrimental phase transitions and oxygen evolution, they consider that $LiNiO_2$ can only be charged to 65% of its theoretical capacity with $C = 180\ \mathrm{mAh/g}$. Equation 3 shows that a smaller ΔV can be realized by reducing cathode particle size and coating thickness, and selecting a coating with high Li^+ diffusivity D^{Li} and concentration c^{Li}. By assuming an $r = 1\ \mu m$ $LiNiO_2$ primary particle and a 1C rate current density through the coating, J is estimated to be $0.03\ mA/cm^2$. In the team's previous work, they estimated that Li^+ diffusivity in amorphous Al_2O_3 is $10^{-16} cm^2/s$; therefore, they estimate $\Delta V = 0.17\ V$ for a 1-nm thick coating.

To evaluate the effectiveness of the amorphous cathode coating in blocking O^{2-} transport, they estimate the O^{2-} flux J^O and the time t required for O^{2-} to diffuse through the coating. They assume the oxygen-loss-induced surface rocksalt layer mainly consists of NiO phase, which is densified from the layered NiO_2. Let c^O_{max} denote the upper value of the O^{2-} concentration in NiO_2, and t can be expressed as:

$$t = \frac{0.5 V c^O_{max}}{A J^O} \quad (4)$$

where V and A are the shell volume of the surface rocksalt phase and surface area of the coated $LiNiO_2$, respectively. To estimate J^O under the driving force of the chemical potential gradient across the coating layer, the team applied the Onsager transport equation:

$$J^O = -L^{OO} \nabla \mu^O \quad (5)$$

where L^{OO} and $\nabla \mu^O$ are the Onsager transport coefficient, and oxygen chemical potential gradient, respectively. Assuming steady-state conditions, they can reasonably approximate the chemical potential gradient $\nabla \mu^O$ to be a constant throughout the coating, which renders the above equation as

$$J^O = L^{OO} \frac{\mu^O_c - \mu^O_e}{l_c} \quad (6)$$

where μ_c^O and μ_e^O are the chemical potentials at the cathode and electrolyte sides, respectively. Combining Equations (4) and (6), t can be expressed as:

$$t = \frac{r^3 - (r - l_s)^3}{6(r + l_c)^2} \frac{c_{max}^O l_c}{L^{OO}(\mu_c^O - \mu_e^O)} \quad (7)$$

μ_c^O can be estimated from the cathode densification reaction consistent with the phase diagram. For example, at 4.3 V, layered NiO_2 would densify to rocksalt NiO, with oxygen being released at μ_c^O=−4.95 eV. μ_e^O can be estimated using the condition where oxygen loses electrons to the carbon network and is released as O_2 (at μ_e^O=−5.24 eV at room temperature and $P_e^{O_2}$=0.21 atm). The team set the thickness of the surface rocksalt phase to be $l_s = 2\ nm$. Therefore, the time t required for the surface NiO_2 to lose 50% of its oxygen is estimated to be 1.6 hours.

Patents/Publications/Presentations

Presentation

DOE VTO Annual Merit Review Meeting, Virtual (2021): "Predicting and Understanding Novel Electrode Materials from First-Principles"; K. A. Persson. Poster.

Task 3.2 – Electrode Materials Design and Failure Prediction (Venkat Srinivasan, Argonne National Laboratory)

Project Objective. The main project objective is to develop computational models for understanding the various degradation mechanisms for next-generation Li-ion batteries. This year's goal is to use the continuum-based mathematical model to investigate interfacial stability between Li-metal electrodes and SEs during deposition and dissolution of lithium under externally applied currents. Both soft polymer and hard ceramic type electrolytes will be investigated. The team also aims to develop a computational model for understanding the interdiffusion of ions and its impact on other degradation mechanisms at the CEI. Ceramic-based SEs are expected to enable high-energy-density and liquid-free, safe, next-generation Li-ion batteries. Li-metal anodes should be incorporated due to their substantially larger volumetric and specific capacity, as compared to present day graphite-based anodes. During charge, lithium dendrites are observed through the SEs, which are supposed to occur because of the non-uniform current distribution at the Li/electrolyte interface. Interfacial detachment between the lithium electrode and SE has been observed during electrochemical dissolution of lithium (or, the stripping process), which can lead to nonhomogeneous contact and substantially higher charge transfer resistance between the electrode and electrolytes. Similar issues have also been observed at the Li/PE interface during lithium stripping, which will be investigated thoroughly. On the cathode side, diffusion of TMs into the SEs, along with delamination between cathode and SE, leads to increased interfacial resistance. The side reaction between cathodes and SEs is a bigger issue for the sulfides as compared to the oxide-based ceramics, whereas the delamination is supposed to be more dominant within the oxides. The developed computational model will be used to investigate the impact of physicochemical and transport properties of the SE on the overall interfacial degradation observed at both the cathode and anode sides. The main focus will be to elucidate interfacial issues and devise strategies to enable successful implementation of SE in next-generation Li-ion batteries.

Project Impact. Findings from this research will give a better understanding of the factors, at the electrode/SE interface, limiting the cycle life of SE-based Li-ion batteries. These results will help to enable all-solid-state Li-ion batteries.

Project Approach. The approach used here is to develop mesoscale models based on governing principles at the continuum level to describe the critical processes occurring in the materials. Electrochemical, microscopic, and spectroscopic data from experiments are combined with theories for parameter estimation and model validation. The model is then used to provide insights and guidance for design of new materials.

Out-Year Goals. At the end of this project, a computational framework will be presented that is capable of estimating lithium stripping and interdiffusion of ions at electrode/electrolyte interface.

Collaborations. This project collaborates with L. A. Curtiss, A. T. Ngo, and C. M. Phatak at ANL.

Milestones

1. Develop a mesoscale model to capture the void formation at the Li/LLZO interface during dissolution. (Q1, FY 2021; Completed)

2. Compare the lithium dissolution results as predicted by the mesoscale computations (conducted at ANL) with the experimental results obtained from the German group (J. Janek at Justus Liebig University, Giessen). (Q2, FY 2021; Completed)

3. Understand current distribution around a dendritic protrusion during lithium dissolution. (Q3, FY 2021; Completed)

Progress Report

Understand Current Distribution around a Dendritic Protrusion during Lithium Dissolution. Li-metal electrodes are necessary for next-generation batteries because of the possibility of enhancement in energy density. Dendrite growth during the charge, or lithium deposition process, is a major bottleneck preventing widespread implementation of Li-metal anodes. SEs are being actively considered for their capability to prevent growth of dendritic protrusions. Due to the generation of mechanical stress field at the tip of the protrusion, the shape and size of the lithium dendrites observed within SEs are very different than that in LEs. Evolution of the globular morphology of lithium deposits within SEO SEs are attributed to the current focusing associated with concentration and potential gradients within the SE, and influence of stress-induced electrochemical potential on the BV reaction current density. Generation of compressive stress is expected to slow down the lithium deposition process at the tip of the protrusion, but not prevent it completely. Dissolution of dendritic protrusions is also an interesting aspect. Experimentally, it has been observed that during discharge, or electrochemical dissolution of lithium, the dendritic protrusions tend to dissolve quickly.[1] It is indeed true that the dendritic protrusion is closer to the counter electrode and thus should experience larger magnitudes of anodic current, which should lead to its early dissolution. Whether the mechanical stress field around the globule demonstrates any impact needs to be studied. Accordingly, this quarter the team simulated the dissolution of a lithium dendritic protrusion within SEO electrolyte with dimensions the same as that reported in the experimental article.[1] Change in protrusion dimension during the dissolution process is shown in Figure 58a-b. Evolution of stress within the SE adjacent to the bottom electrode is shown in Figure 58c as a function of the distance from the tip of the protrusion. Compressive stress prevails within the SE.

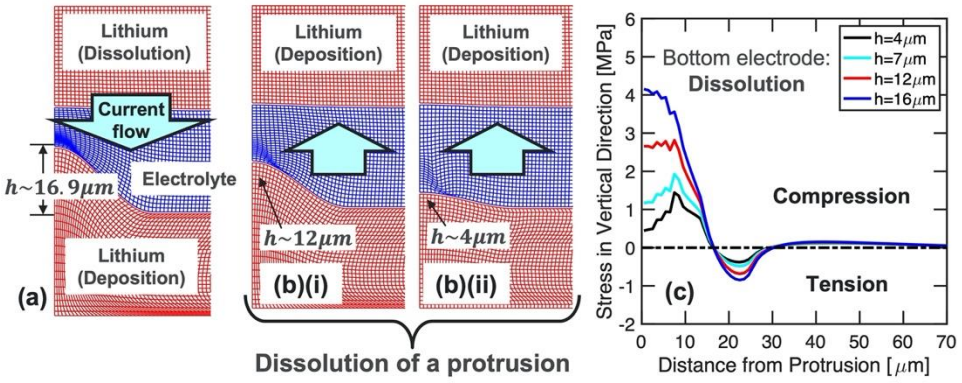

Figure 58. (a) Evolution of a dendritic protrusion during deposition at the bottom electrode. (b) Electrochemical lithium dissolution from the bottom electrode shows preferential dissolution of the protrusion. (c) Stress evolution within the polymer electrolyte adjacent to the bottom electrode along the vertical direction.

Compressive stress helps to increase the anodic component of reaction current, which leads to faster dissolution of lithium in regions under higher compression. Dissolution current density at the tip for different heights of the dendritic protrusions is shown in Figure 59a. The ratio of excess current at the tip of the protrusion over the applied current density is shown in Figure 59b for different heights of the globule and compared with experiments, showing good qualitative correlation. This completes the milestone for the third quarter.

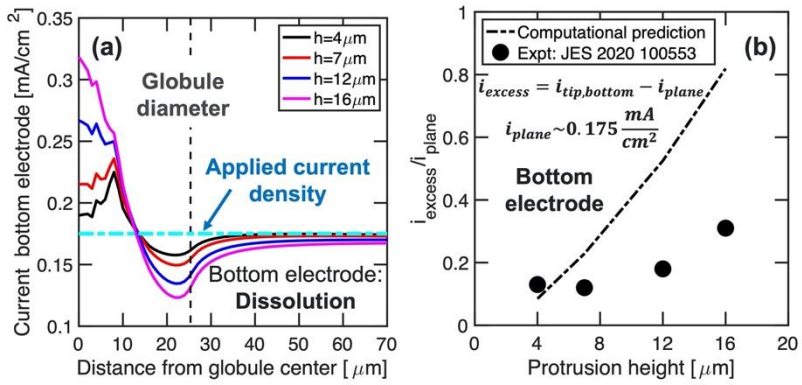

Figure 59. (a) Current distribution at the bottom electrode around the dendritic protrusion during the dissolution process. It is evident that current on top of the protrusion is higher than the applied current density, which indicates preferential dissolution of the dendritic protrusion. (b) Ratio of excess current at the tip of the protrusion over the applied (or planar) current observed far away from the protrusion. The computational predictions are compared with experimental observation.[1]

Reference

[1] Maslyn, et al. "Preferential Stripping of a Lithium Protrusion Resulting in Recovery of a Planar Electrode." *Journal of the Electrochemical Society* 167 (2020): 100553.

Patents/Publications/Presentations

Publication

- Barai, P., T. Rojas, B. Narayanan, A. T. Ngo, L. A. Curtiss, and V. Srinivasan. "Investigation of Delamination Induced Performance Decay at the Cathode/LLZO Interface." *Chemistry of Materials* (2021). doi: 10.1021/acs.chemmater.0c04656.

Task 3.3 – Modeling of Amorphous Solid-State Conductors (Gerbrand Ceder, University of California, Berkeley)

Project Objective. SSBs are promising to achieve high energy density. The project objective is to determine the design principles needed to create SSEs with high Li-ion conductivity, while also achieving stability against common Li-ion cathodes and Li-metal anodes.

Project Impact. The project will lead to understanding the factors that control Li-ion motion in crystalline and amorphous solids and will develop strategies to create stable interfaces against lithium metal and high-voltage cathode materials. The understanding of such processes is necessary to determine design principles to develop reliable ASSBs.

Approach. HT computation is used to screen suitable SE with high electrochemical stability and high ionic conductivity, by incorporating nudged elastic band (NEB) and an AIMD method. Meanwhile, DFT is used to calculate bulk elastic constants of materials, surface energies, and interface decohesion energies of GBs. Thermodynamic interface stability is assessed from *ab initio* computed grand potential phase diagrams in which the lithium voltage can be controlled. Kinetic limits for SE decomposition are assessed by topotactic lithium insertion and removal from the SE.

Out-Year Goals. Future goals include the following: (1) gain insight into what creates high Li-ion conduction in sulfide and oxide solids, and (2) develop stable, processable solid-state conductors that can be applied in ASSBs.

Collaborations. There are no collaborative activities this quarter.

Milestones

1. Finite T phase diagram of L-P-S system. (Q1, FY 2021; Completed)
2. Develop model for electronic conductivity in SEs. (Q2, FY 2021; Completed)
3. Evaluate effect of ionic and electronic conductivity on lithium plating in SE. (Q3, FY 2021; Completed)
4. Develop a valid model for amorphous structure, and compare to spectroscopy data. (Q4, FY 2021)

Progress Report

Shadowing Effect at the Flat Anode/SE Interface due to Internal Deposition in the SE

The existence of electronic conductivity in SEs can cause metal deposition inside voids in the SEs. This internal metal deposition not only leads to metal penetration in the SE, but also causes inhomogeneous plating at electrode/SE interfaces ("shadowing effect"). The result shown in Figure 60 reflects the shadowing effect due to the presence of metal deposition in the void. The vertical coordinate shows the magnitude of the total current density going into the anode. In this graph, the point ($y = z = 0$) is the projection of the void center in the anode plane. Shadowing by the void reduces the current by 0.5% at the point ($x = y = z = 0$), but the total current converges to the applied value (i_0) far enough from the center. The shadowing effect rapidly increases as the void approaches the interface. For example, the current inhomogeneity increases from 0.5% to 4% when the void is moved from $0.001L$ to $0.0001L$ from the anode (L is the SE thickness). Therefore, the total current distribution is not only affected by the electrode/SE interface, but also by internal deposition within the SE.

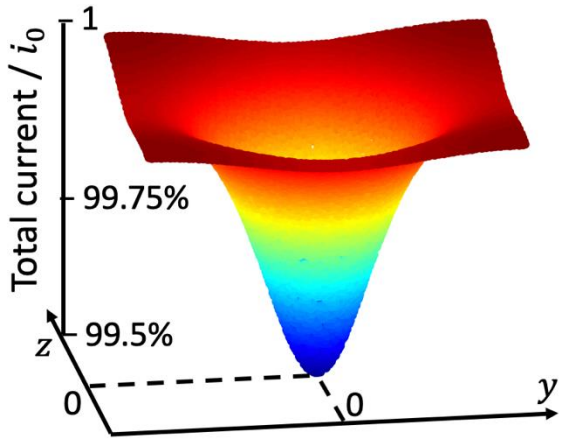

Figure 60. Total current density at the anode / solid electrolyte interface. Both the vertical coordinate and the contour plot represent the magnitude of the deposition current. All the length units in the figures are in μm.

Internal Metal Deposition Decreases Rapidly as Voids are Deeper within the SE

Figure 61 shows the average deposition current ($\bar{i}_V$) of the voids in the SE under an applied current i_0. The deposition current decreases rapidly as voids are positioned deeper within the SE. This is because both the electrochemical potential of electrons ($\tilde{\mu}_{e^-}$) and the deposition overpotential ($-e\eta_V = \tilde{\mu}_{M^+} + \tilde{\mu}_{e^-}$) decrease rapidly. For SE materials with higher electronic conductivities (σ_{e^-}), the average deposition current is larger and decays much slower. However, the value still decays to a negligibly small value for voids located deeper than $0.02L$ (L is the SE thickness). Therefore, preparing a sufficiently dense or void-free surface of the SE at the anode side can be an efficient strategy to prevent M metal deposition in the voids of the SE. An ideal void-free coating layer can be synthesized with the same SE material, but under well-controlled conditions. Different materials can also be used with required void-free thickness determined by different ionic/electronic conductivities.

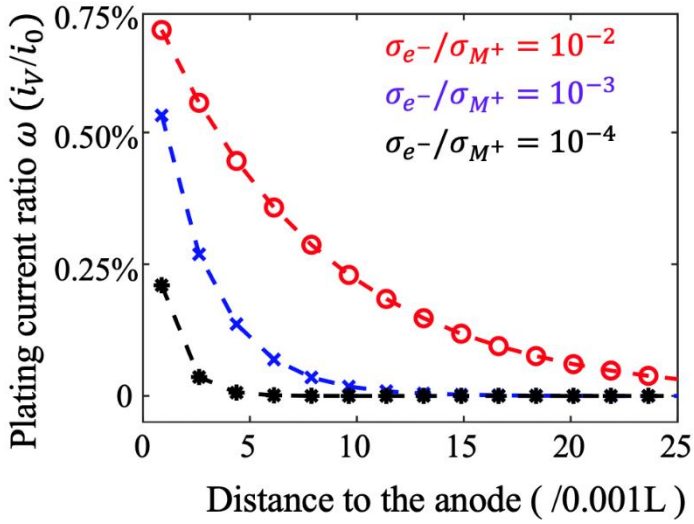

Figure 61. Distribution of deposition current i_V under applied current i_0 at three different solid electrolyte electronic conductivities. The ionic conductivity σ_{M^+} is fixed 0.1 mS/cm, while the electronic conductivity σ_{e^-} varies.

Patents/Publications/Presentations

Publication

- Yang, J. H., H. Kim, and G. Ceder. "Insights into Layered Oxide Cathodes for Rechargeable Batteries." *Molecules* 26, No. 11 (2021): 3173.

Task 3.4 – Characterization and Modeling of Li-Metal Batteries: Force Field Theory and Lithium-Sulfur Battery Simulations (Lin-Wang Wang, Lawrence Berkeley National Laboratory)

Project Objective. The project objective is to develop force field (FF) based on *ab initio* calculations to study Li-S cathode and lithium LE. It also includes designs for Li-S cathode systems for high gravimetric and volumetric capacities. Lithium diffusion in both LE in a confined space and in Li-S cathode systems is a main focus of this project. To enable calculation of large systems, ML-FF trained on *ab initio* calculation data will also be developed. The success of this new approach will greatly expand the capability of theoretical simulation for battery systems. ML-FF can also be used in combination with traditional classical FF to deal with the nonreactive parts of the system.

Project Impact. Making the Li-S battery a commercial reality will have a major impact on society and also help to realize the VTO goal of 500 km per charge for EV. However, the nature of chemical reaction makes it different from the traditional intercalation-based Li-ion battery. The molecular nature of Li_2S_n also allows solvation in the electrolyte. To address these problems, it is essential to have fundamental studies and understandings of the underlying mechanisms. Theoretical simulations can play an important role in discovering and designing new cathode materials. However, traditional *ab initio* calculations are limited by their computational size, while the classical FF simulations are limited by their accuracy and the lack of adequate FF. The development of ML-FF can overcome these problems by bridging the size gap between the *ab initio* simulation and the real systems that need to be studied.

Approach. ML-FF will be developed by first running *ab initio* simulations, which can generate hundreds of thousands of datasets. The project has a unique capability of decomposing the total energy of a DFT calculation into the energy of each atom. Compared to conventional DFT calculations, this increases the number of data by hundreds of times, an important requirement for ML model training. The dependence of the atomic energy to the local atomic bonding environment will be captured using ML methods. Three ML approaches will be: linear fitting; neural network (NN) model; and Gaussian process regression model. The team will compare the efficacies of these models. Meanwhile, they will also deal with the long-range Coulomb interactions existing in the electrolyte system and the ionic species in LE. The idea is to first fit the charge density of the system and also remove the long-range electrostatic energy before the fitting of the local energy on each atom. The team will design new Li-S and Na-S cathode materials. In particular, they will design an amorphous Li-S mixture, with other materials such as carbon nanotube (CNT), black carbon, or electric conductive two-dimensional (2D) materials.

Out-Year Goals. In outgoing years, the project will further develop computational methods for more accurate entropy and interaction energy calculations for the electrolyte, as well as for Li-S cathode systems.

Collaborations. The project will collaborate with G. Liu and Y. Cui for cathode design. It has also collaborated with F. Pan of Beijing University for lithium battery research in general.

Milestones

1. Lithium charge density fitting in electrolyte, to fit long-range Coulomb interaction. (Q1, FY 2021; Initiated)
2. Study of electrolyte behaviors, including their stability problems. (Q2, FY 2021; In progress)
3. Incorporation of Coulomb interaction in local energy calculation; ML-FF fitting. (Q3, FY 2021; In progress)
4. Further study of Li-S cathode with polymer, to study electric conductivity in such a system. (Q4, FY 2021; In progress)

Progress Report

This quarter, the team realized the decomposition of EC on the lithium anode in the molecular dynamics (MD) calculation under a fixed potential method. In the fixed-potential method, the total number of electrons in the system was floated to match the given electrode Fermi energy automatically to mimic the realistic experimental processes. As seen in Figure 62, the EC is decomposed into carbonates and C_2H_2. The carbonates are bonded on the surface firmly, while the C_2H_2 is released. Carbonate is an important composite in the SEI. In the following, the team will compare their results with those obtained in the normal MD and real-time, time-dependent DFT calculations. By doing that, they can identify the mechanism underneath the decomposition and the role of electron transfer in the reaction.

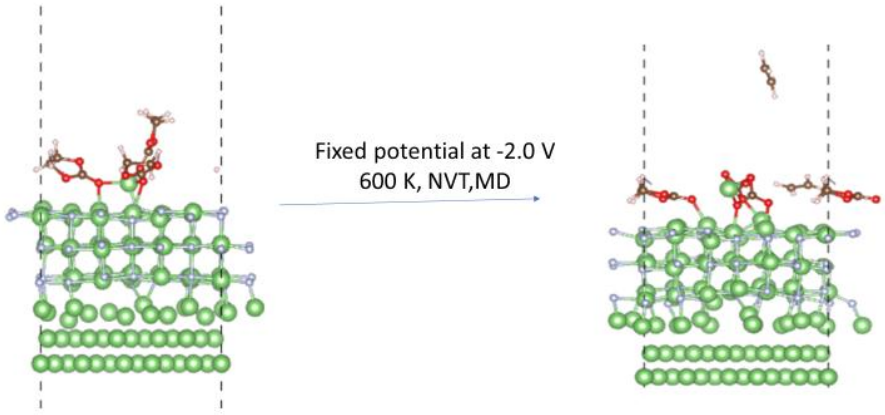

Figure 62. The decomposition of ethylene carbonate on the lithium anode.

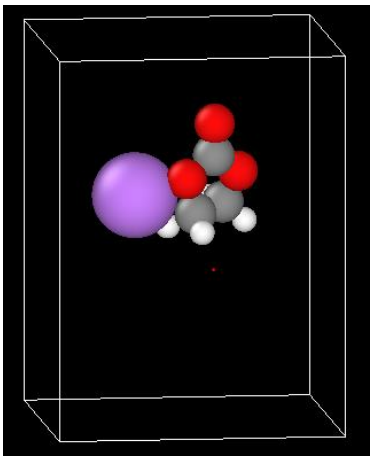

Figure 63. The Li^+ ion interacting with an ethylene carbonate molecule during a molecular dynamics simulation.

The team has also developed the polarization model in their charge-density-based ML-FF. This allows them to carry out simulation for organic electrolyte with Li^+ ions. The interaction between the Li^+ ion to the electolyte molecule is mostly through the polarization interactions. In their previous work, only the electrostatic interaction and exchange interaction are included without polarization. To develop the polarization, they have used many point charges at different positions to the molecule to carry out DFT calculations. The resulting polarization energy is fitted with a polarization model. They have finished the code development for MD simulations under the new FF. One such simulation is shown in Figure 63. Next quarter, they plan to fit the ML-FF for different molecules and systems, and carry out bench mark simulations for different system.

Patents/Publications/Presentations

The project has no patents, publications, or presentations to report this quarter.

Task 3.5 – *In Situ* and *Operando* Thermal Diagnostics of Buried Interfaces in Beyond Lithium-Ion Cells
(Ravi Prasher, Lawrence Berkeley National Laboratory)

Project Objective. Transport at various interfaces in *beyond lithium ion* cells will play a major role in electrochemical performance and reliability. It has not yet been possible to thermally profile a Li-metal cell during operation to provide a spatially resolved map of thermal transport properties throughout the cell. The objective of this research is to create a metrology capable of spatially resolved *in operando* thermal property profiling, and then to relate thermal property to the quality of electrodes and interfaces, and to use the developed thermal metrology to understand electrochemical processes in Li-metal batteries, such as dendrite growth, interface kinetics, and ionic transport.

Project Impact. Characterizing electrochemical processes in Li-metal cells such as lithium deposition and dendrite growth at interfaces is of great significance for understanding and enhancing their electrochemical performance and reliability. *In situ* and *operando* micro electrothermal sensors can provide significant information regarding the impact of buried interfaces as a function of time, material, voltage, current, temperature, etc. Therefore, it is important to develop *operando* micro electrothermal sensors and develop models relating those signals to electrochemical performance for *beyond lithium ion* cells. The physics-based model relating thermal and electrochemical properties based on these measurements can facilitate future design of Li-metal batteries.

Approach. To accomplish project goals, the team will utilize an in-house adapted 3-omega (3ω) technique to probe thermal properties of a Li-metal cell while it is in operation, without affecting the operation of the cell. The 3ω sensors will be deposited and fabricated on Li-metal cells based on previous learning on 3ω sensor fabrication. The characteristic depth of the thermally probed region is defined by the wave's "thermal penetration depth," $\delta_p = \sqrt{D/2\omega}$, where D is the sample's thermal diffusivity, and 2ω is the heating frequency of the thermal wave. By depositing the project's 3ω sensors on the battery's outer surface and adjusting ω, the team controls δ_p to span the full range from the top to the bottom layer, thereby noninvasively probing the thermal transport in subsurface layers and interfaces within the bulk of the battery. Thermal transport can be related to quality of the interfaces. By doing concurrent thermal transport and electrochemical performance measurements, the team plans to relate thermal transport to electrochemical performance. As frequency-based thermal measurement techniques provide excellent spatial resolution within the cell, the team also plans to study heat generation at the electrolyte – Li-metal interface and to relate the thermal signals to the interface kinetics and ionic transport. The frequency dependence of heat generated due to transport resistance is different from that due to kinetic resistance. The team plans to utilize this difference to separate the contributions of kinetic and transport resistance at the interface, which will enable understanding of interface kinetics and transport at the Li-metal – SSE interface.

Out-Year Goals. The project will design, build, and implement the adapted 3ω metrology to examine thermal properties and a general frequency-dependent thermal metrology to examine heat generation. This will involve developing and testing the metrology itself along with accompanying theory, designing compatible battery samples, and applying the technique to live cells. The team will measure thermal transport properties of battery materials provided by collaborators. Combined with the electrochemical performance measurement, this will provide significant information relating the thermal signal to the electrochemical process.

Collaborations. This project collaborates with two LBNL groups: V. Battaglia's for cell assembly for 3ω studies, and R. Kostecki's for pristine battery active material growths for studies of thermal signals related to electrochemical process.

Milestones

1. Completed iteration of electrothermal sensor design. (Q1, FY 2021; Completed)
2. Fabrication of Li-symmetric test cells with incorporated electrothermal sensors. (Q2, FY 2021; Completed)
3. Sensitivity analysis and sample design optimization to maximize measurement sensitivity to target electrochemical properties. (Q3, FY 2021; In progress)
4. Baseline impedance spectroscopy of cells for ion and electron mobility. (Q4, FY 2021)

Progress Report

This quarter, the team performed the sensitivity analysis to extract the electrochemical parameters, namely the exchange current density, interface transport resistance, electrolyte transport resistance, and entropic coefficient. They are using their in-house method: multi-harmonic electrothermal spectroscopy (METS) to sense the thermal signature of the electrochemical processes. This quarter, they also worked on determining the appropriate method for microKelvin temperature sensing needed for the thermal signal measurement.

Figure 64 shows the schematic of the cell used in the analysis. The cell consists of a 50-µm-thick copper current collector on which the thermal sensor is deposited. They use a symmetric cell with 1.2-mm-thick LLZO SSE and 200-µm-thick lithium foil on both sides of the electrolyte. The sensors on the two sides are labeled as Sensor 1 and Sensor 2, and the Li-LLZO interfaces on the corresponding sides are labeled as Interface 1 and Interface 2.

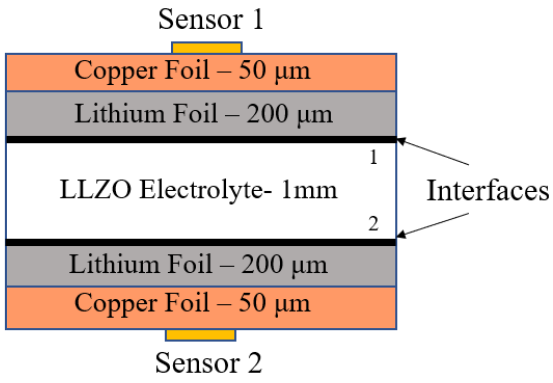

Figure 64. Schematic of lithium symmetric cell with multi-harmonic electrothermal spectroscopy (METS) sensors.

Figure 65 shows the result of the sensitivity analysis at different harmonics of the AC frequency of the current passed through the cell, and Figure 66 shows the temperature rise as a function of frequency at the different harmonics. In the first harmonic (1ω), the signal is the most sensitive to the reaction entropy for all the frequencies of interest. Similarly, the second harmonic (2ω) thermal signature, which relates to the transport losses, is the most sensitive to the electrolyte transport resistance. Similarly, the fourth harmonic (4ω) thermal signature is the most sensitive to the exchange current density, a measure of the reaction kinetics at the interface.

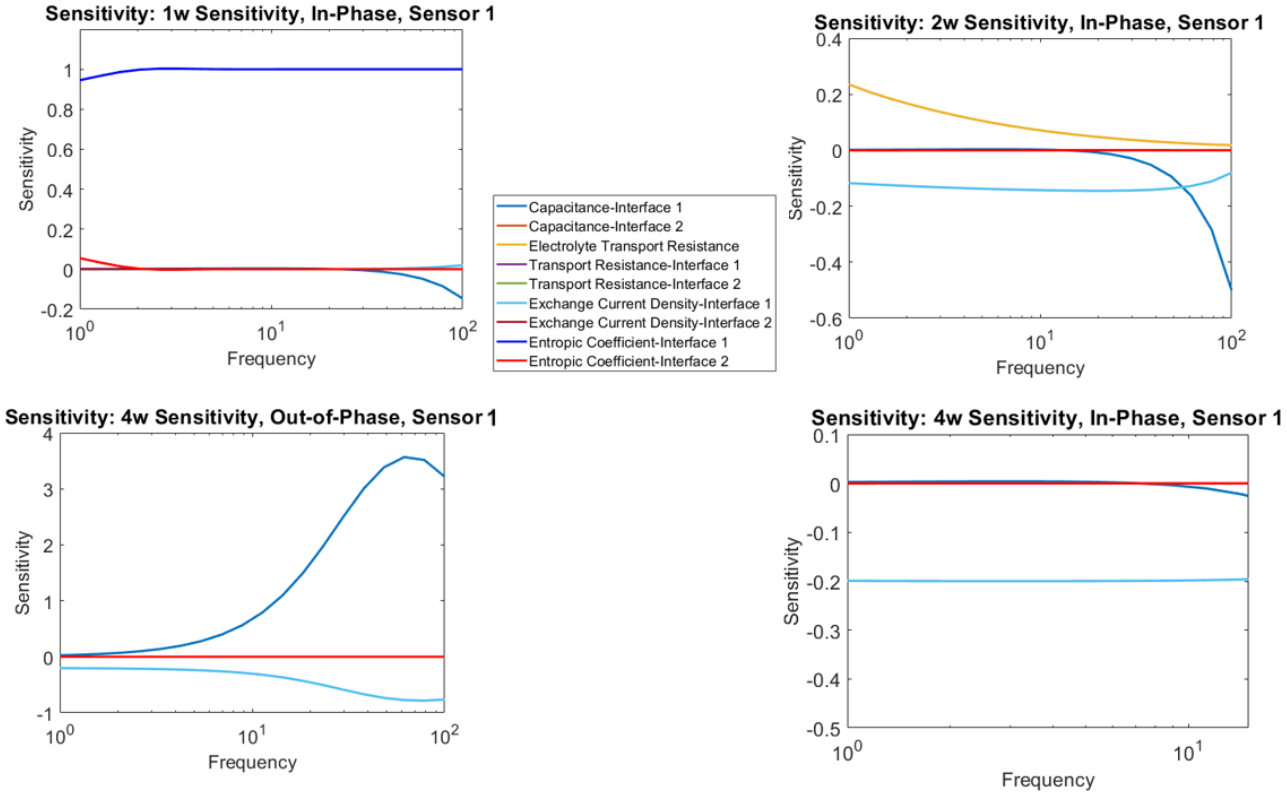

Figure 65. Schematic of the lithium symmetric cell with multi-harmonic electrothermal spectroscopy (METS) sensors.

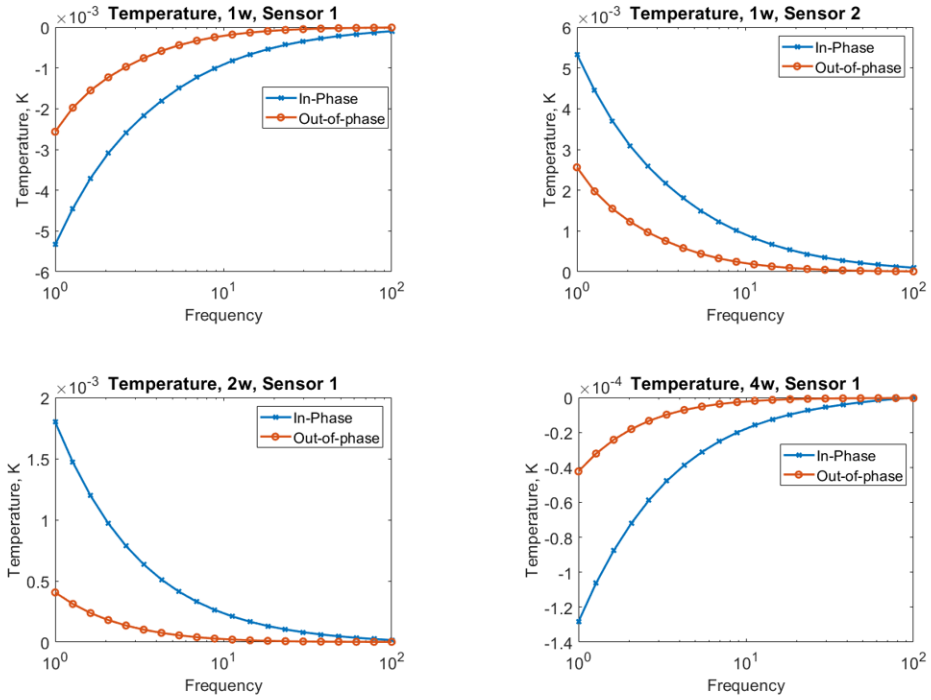

Figure 66. Temperature rise at different harmonics measured by the multi-harmonic electrothermal spectroscopy (METS) sensors.

As seen in Figure 66, the temperature rise in each harmonic is in the order of milliKelvins. Therefore, the team needs a temperature-sensing technique that can resolve such small temperature oscillations. They have identified a scheme developed by Chen et al. [*Review of Scientific Instruments* 84 (2013): 114901] to be the appropriate technique for the temperature detection for their purposes. In addition to the lock-in temperature sensing commonly employed in 3-omega measurements, this method will also employ a Wheatstone bridge scheme to cancel the effects of the ambient temperature fluctuations. Additionally, the team will also use a Keithley 6221 current source, which is capable of shot noise suppression, to minimize the noise due to current fluctuations in the sensor. By adopting this scheme, they should theoretically be able to achieve a temperature resolution within microKelvins, which is sensitive enough for the temperature rise they expect to measure.

Patents/Publications/Presentations

The project has no patents, publications, or presentations to report this quarter.

Task 3.6 – Multi-Scale Modeling of Solid-State Electrolytes for Next-Generation Lithium Batteries (Anh Ngo, Larry A. Curtiss, and Venkat Srinivasan, Argonne National Laboratory)

Project Objective. This project is part of a multi-scale modeling effort to obtain an in-depth understanding of the interaction of the electrode and the SE aimed at developing highly efficient SSE batteries for vehicle applications. Input parameters needed for mesoscale (continuum) level calculations are being obtained from atomistic calculations including DFT and CMD simulations. This atomistic input will enable a multi-scale computational procedure for SSEs that is capable of successfully capturing the physicochemical aspects during charge and discharge process, including lithium transport mechanisms, interfacial phenomena during the insertion and extraction of lithium ions, and mechanical deformation of SSE.

Project Impact. A major safety concern experienced with commercially available Li-ion batteries under some scenarios is leakage of the LE, which can potentially catch fire. Replacement of the LE is necessary to decrease the fire hazard and improve safety associated with present-day Li-ion batteries. In addition, use of SEs provides a path to prevent dendrites in Li-metal anodes, thereby leading to batteries with significantly higher energy density. The impact of this project will be to help in development of good SSEs as a replacement for the commercially used organic LEs to improve safety and energy density in Li-ion batteries.

Approach. Parameters needed for mesoscale modeling of grain interior, GB, and electrode-electrolyte interface will be calculated by DFT-based calculations along with Monte Carlo (MC) and MD simulations. The calculations will be used to determine properties of the electrode with the SE as well as in GB regions of the SE. This will include calculations of structure, stability, ionic conductivity, Young's modulus, fracture toughness, exchange current density, and other properties.

Out-Year Goals. The out-year goals of this work are to calculate other properties such as fracture toughness and include other SSEs and coatings in the multi-scale modeling.

Collaborations. This project collaborates with Y. Cui at Stanford.

Milestones

1. Determine stable surface of the LPSCl SSE and the NMC-811/LPSCl interface. (Q1, FY 2021; Completed)
2. Conduct AIMD study of electrochemical interface between NMC-811/LPSCl. (Q2, FY 2021; Completed)
3. Investigate Li-ion transport of the NMC-811/LPSCl interface, and calculate exchange current density. (Q3, FY 2021; Completed)
4. Incorporate information obtained from the atomistic calculations into the mesoscale model, and predict the impact of performance. (Q4, FY 2021; Initiated)

Progress Report

SEs are expected to stabilize the Li-metal anodes due to higher stiffness than lithium, which can effectively suppress propagation of dendrites. A combination of SEs with Li-metal anodes can also improve the volumetric energy density of commercially used Li-ion batteries, as well as improve the safety issues associated with them. Oxide SEs with garnet (LLZO) or NASICON (LATP) structure show extremely high elastic modulus (~150 GPa), which makes these solid ionic conductors non-conformable and decreases the electrochemically active surface area associated with the non-uniform Li-metal anode. On the other hand, sulfide-based SEs (LGPS, LPS) are mechanically softer (~ 20 GPa) and can potentially maintain better contact with the metal anode. These sulfide electrolytes also demonstrate better ionic conductivities (~ 1mS/cm or higher) than the oxides (~ 0.1 mS/cm). In the present research, the team will investigate the sulfide-based SE LPSCl, which has an argyrodite type crystal structure. Being a sulfide, it shows significantly enhanced ionic conductivities (~ 2.5 mS/cm) under room-temperature conditions, and the elastic modulus of this material is ~ 22 GPa. The inherent softness of LPSCl enables the cold sintering of these materials with layered oxide cathodes, which effectively avoids many cathode/electrolyte side reactions. During processing, cathode/electrolyte side reactions at elevated temperatures are a major issue for several oxide-based SEs, such as NMC/LLZO.

In spite of these advantages, sulfide SEs demonstrate poor interfacial stability with both Li-metal anode and layered oxide cathodes, which leads to continuous capacity fade and performance decay with cycles. The major problems faced by the LPSCl electrolyte located adjacent to the cathode active materials are as follows:

- Interdiffusion of TM (nickel, cobalt, manganese), phosphorus and sulfur ions, and formation of a highly resistive CEI layer. Some experimental studies reveal the possible formation of phosphates (PO_4^{3-}) and sulfates (SO_4^{2-}), which can potentially increase interfacial resistance.
- Formation of a space charge near the CEI due to strong attraction between lithium from electrolytes and oxygens from the cathode materials. Such a space charge layer can effectively increase interfacial resistance at the CEI.
- Oxidation and reduction of LPSCl itself during charge and discharge processes can substantially minimize the effectiveness of the SE. For example, during charge, the SE can oxidize to LiCl, P_2S_5, and elemental sulfur. These side reactions can occur wherever there is a flow of electron.

$$2Li_6PS_5Cl \rightarrow 2LiCl + P_2S_5 + 5S + 10Li^+ + 10e^- \qquad (1)$$

  Such side reactions are usually irreversible in nature because the conventional cathode cells are never operated at potentials where reduction of these side products occur (sulfur and phosphorus reduce at 2 V and 1 V, respectively). Such undesired side reactions may lead to very high 1st-charge capacities with LPSCl SEs, but never achieved later, not even the 1st discharge.

The first two phenomena mentioned above work to enhance the interfacial charge transfer resistance, which in turn aggravates the delamination-induced capacity fade. The third phenomena alters the bulk structure of the LPSCl electrolyte, which can substantially minimize the bulk conductivity of the SE. The influence of these side reactions at the cathode/SE interface, on the overall cell performance is investigated in this study. Strategies to mitigate these issues through the application of interphase layers, will be studied using multi-scale modeling. Multi-scale modeling can provide insight into the mechanism for dendrite growth and other instabilities for guidance into how to prevent them. Mesoscale (continuum) modeling requires atomistic-level input from theory or experiment to accurately capture physicochemical aspects during charge and discharge processes.

This quarter, the team focused on lithium transport across the NMC/LPSCl interface. They have studied the dynamics of the NMC/LPSCl interface by carrying out AIMD simulations at different temperatures. From these simulations, they calculated the lithium mean square displacements (MSD), as well as the corresponding diffusion coefficients (D) of lithium atoms. The results of the simulations reveal that the thermodynamic energy barrier (obtained from AIMD), ΔG, is 0.62 eV; the energy barrier obtained from the climbing image NEB (cNEB) analysis indicates the higher magnitude of ΔG (0.69 eV).

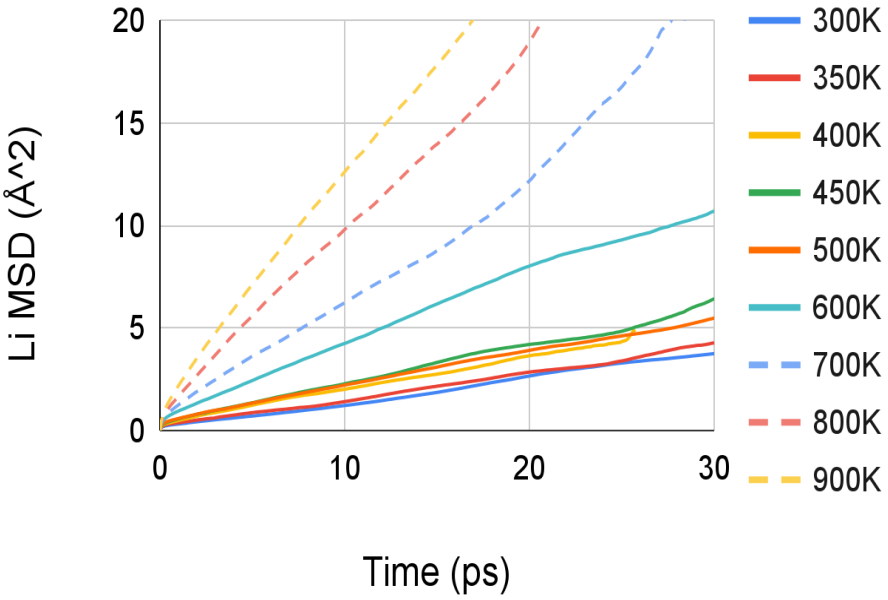

Figure 67. Lithium mean squared displacement (MSD) obtained from *ab initio* molecular dynamics simulations for the NMC/LPSCl interface at different temperatures.

For an electrode and SSE interface, the magnitude of exchange current density (i_0) can be given as:

$$i_0 = F k_{ref} \cdot \left(\bar{k}_c \cdot c_{Li^+} \cdot \left(c_{Li,max} - c_{Li}\right)\right)^{\alpha_a} \cdot \left(\bar{k}_a \cdot c_{Li}\right)^{\alpha_c}$$
$$\text{where, } \bar{k}_a = \nu \exp\left(-\frac{\Delta G}{k_B T}\right), \text{ and } \bar{k}_c = \nu \exp\left(-\frac{\Delta G}{k_B T}\right) / c_{Li,max} \qquad (1)$$

Here, F indicates Faraday's constant, c_{Li^+} stands for Li-ion concentration within the electrolyte, α_a is the cathodic component of transfer coefficient (assumed to be 0.5 in the present research), ν is the reaction rate pre-factor, ΔG indicates thermodynamic energy barrier at equilibrium, k_B is the Boltzmann's constant, and T denotes temperature in Kelvin scale. Among all the parameters and constants mentioned here, ΔG *and* ν can be computed directly from the AIMD calculations, and Li-ion concentration within the electrolyte can be estimated from lower length scale analysis.

The exchange current densities obtained from these first-principles calculations will be used as input for continuum-level modeling of the LPSCl/NMC-811 interface. The continuum-level modeling will provide insight into the interfacial resistance at the CEI.

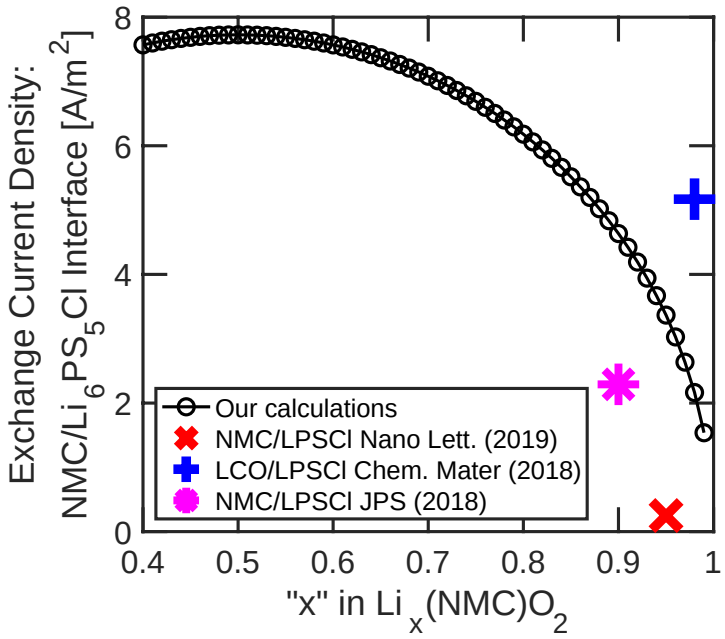

Figure 68. The magnitude of NMC/LiPSCl exchange current density as a function of the NMC Li-ion concentration. ΔG *and* ν can be obtained directly from *ab initio* molecular dynamics (AIMD) calculations.

Patents/Publications/Presentations

Publication

- Barai, P., T. Rojas, B. Narayanan, A. Ngo, L. A. Curtiss, and V. Srinivasan. "Investigation of Delamination Induced Performance Decay at the Cathode/LLZO Interface." *Chemistry of Materials* 33, No. 14 (2021): 5527–5541. doi: 10.1021/acs.chemmater.0c04656.

Task 3.7 – Integrated Multi-Scale Modeling for Design of Robust 3D Solid-State Lithium Batteries (Brandon Wood, Lawence Livermore National Laboratory)

Project Objective. This project will develop a multi-scale, multi-physics modeling framework for probing the effects of materials microstructure and device architecture on ion transport within 3D ceramic SSB materials, with the goal of enhancing performance and reliability. The project has three primary objectives: (1) integrate multi-physics and multi-scale model components; (2) understand interface- and microstructure-derived limitations on ion transport; and (3) derive key structure-performance relations for enabling future optimization.

Project Impact. This project will lead to understanding interfacial losses and instabilities that impede performance and promote failure of SSBs. The multi-scale and multi-physics modeling framework developed in this work will address shortcomings of existing modeling strategies that either lack coupling of the multi-physics nature of various processes active in 3D batteries or fail to incorporate processes at different length scales to understand function. Ultimately, the tools and understanding generated by this project can be utilized to realize optimization of interface-dominated 3D batteries.

Approach. The project approach integrates simulations at three scales to predict ion transport limitations within the ceramic SSE LLZO, as well as across the interface between LLZO and $LiCoO_2$ (LCO) cathodes. A particular focus is on understanding the effects of microstructures and architectures resulting from processing of 3D SSBs as well as their mechanical and chemical evolution at different stages of cycling. First-principles and CMD simulations are used to compute fundamental Li-ion diffusion within bulk SE and cathode materials, along/across GBs of the electrolyte, and along/across electrolyte/cathode interfaces. Next, phase-field simulations are used to generate digital representation of realistic microstructures of the materials, which are combined with the atomistic simulation results to parameterize mesoscale effective property calculations and to establish microstructure-property relationships for ion transport. Finally, these relationships inform a cell-level macroscopic electro-chemo-mechanical modeling framework, which can be used to optimize performance of ceramic 3D SSLBs based on LLZO SEs.

Out-Year Goals. Future activities will focus on computing properties capable of scaling the atomistic interface diffusion models to longer timescales. The team will also work with collaboration partners to reconstruct microstructures of 3D-printed materials and apply them to determine effective stresses and ion transport through the polycrystalline materials. Development and validation of the EIS models will continue, but these activities will be scoped down due to recent staffing shortages. Instead, the team will pivot to understanding transport in composite structures using their multi-scale approach.

Collaborations. This project collaborates with N. Adelstein from San Francisco State University on atomistic diffusion modeling, and J. Ye from Lawrence Livermore National Laboratory (LLNL) on 3D printing of SSB materials. They also partner with T. Danner and A. Latz from Deutsches Zentrum für Luft- und Raumfaurt (DLR) on impedance modeling and electro-chemo-mechanical interface models, with P. Zapol from ANL on modeling of interfaces in LLZO, and with D. Fattakhova-Rohlfing from Forschungszentrum Jülich (FZJ) and E. Wachsman from UMD on properties of LLZO with varying densities and microstructures as part of the U. S.–Germany partnership on SSB research.

Milestones

1. Demonstrate microstructural model of stress effect on ion transport. (Q1, FY 2021; Completed)
2. Compute barriers for ion transport across LCO/LLZO interface. (Q2, FY 2021; Completed)
3. Integrate polycrystalline diffusion model with EIS simulations. (Q3, FY 2021; Delayed by staffing issues)
4. Demonstrate full multi-scale EIS model using ion transport simulations of CEIs. (Q4, FY 2021; Delayed by staffing issues)

Progress Report

ML Interatomic Potentials for Accelerated Atomistic Simulations of Interfaces. This quarter, the team continued development of the ML potential that can simulate larger, more complex pristine and doped LLZO internal interfaces for much longer times. Specifically, the ML potential was improved to simulate both crystalline and amorphous LLZO systems, the latter of which is a proxy for high-angle GBs. As a major milestone, the team successfully achieved their goal by training an artificial neural network (ANN) with total energies of structures and also force components of all atoms, using 20-20 hidden-layer ANN architecture and local atomic environmental features with symmetry functions. The developed ML potential presents quantum level of accuracy for energies and forces for both crystalline and amorphous LLZO (Figure 69a), as benchmarked against DFT calculations. The energy and force root mean square errors (RMSEs) are < 10 meV/atom and 0.2 eV/Å for both crystalline and amorphous LLZO, remaining uniform throughout the entire simulation time. This implies that the ML potential can perform stable MD simulations for long times and at high temperatures. Figure 69b compares the calculated RDFs for atomic pairs using the ML potential with an AIMD result at 3000 K. Again, the project's ML potential is able to reproduce the RDF features found in the AIMD simulation. The ML potential also predicts a bulk modulus of LLZO (117.2 GPa) close to that by DFT (114.4 GPa), as well as a predicted activation energy of 0.20 eV for lithium diffusion in crystalline LLZO, similar to that calculated from AIMD (0.22 eV). This confirms that the ML potential MD simulations can be performed with quantum accuracy. Note that the predicted activation energy for amorphous LLZO is 0.44 eV, consistent with literature results for GBs. Using a similar approach, the team is training another ML potential that can handle aluminum, barium, or tantalum doping of LLZO. This will be the primary atomistic effort next quarter.

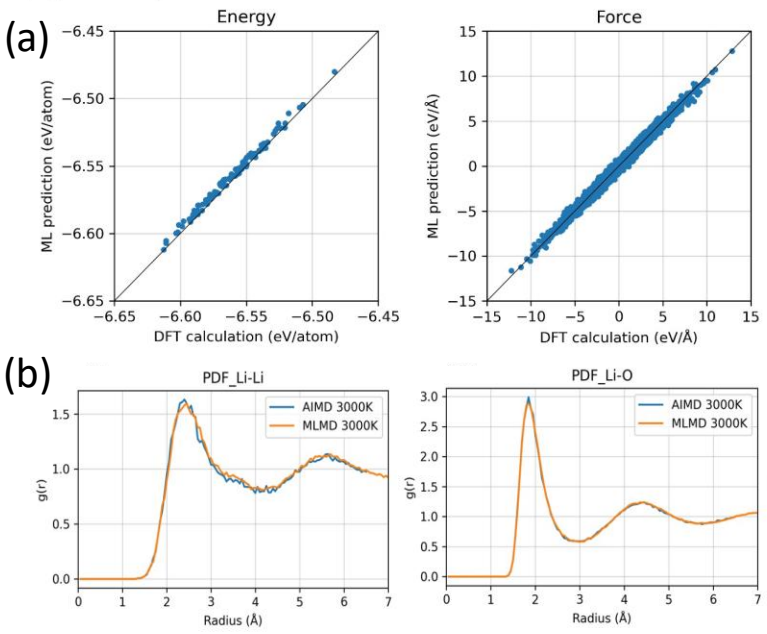

Figure 69. Performance test of the machine-learning potential in a molecular dynamics simulation of amorphous LLZO at 3000 K, showing the ability to replicate (a) energy/forces, and (b) key radial distribution functions.

Mesoscale Modeling of Microstructural Effects on Lithium Transport in Polycrystalline LLZO under Stress. This quarter, the team further refined the integration of two mesoscale models for predicting microstructural impacts on both Li-ion transport and local stress concentrations in LLZO. Within the LLNL *MesoMicro* code framework, the team successfully combined two numerical schemes for solving the mechanical equilibrium and steady-state diffusion equations in the presence of complex SE microstructures. This framework is now capable of naturally incorporating microstructure-aware stress effects on the local lithium concentration profile within any polycrystalline microstructure. The team applied the framework to a digital representation of polycrystalline LLZO (Figure 70a) with a microstructure generated by a phase-field simulation. They first verified the ability to predict a nonuniform internal stress profile under applied loading. As shown in Figure 70b, the local von Mises stress profile is affected by local microstructural features, as previously reported. Next, the lithium composition profile was analyzed at steady state in the presence of the local stress profile. Figure 70c shows the computed lithium composition profile for that scenario. For comparison, the computed lithium composition profile without the stress effect is shown in Figure 70d. The simulations confirm that stress concentration can perturb the lithium composition profile, inducing segregation or depletion near GBs and junctions. The team is analyzing the correlation between local lithium composition and the microstructure-dependent stress profile to quantify how stress affects the net ionic conductivity under various operation conditions.

Mesoscale Modeling of Lithium Transport and Micromechanical Response in a Polymer/LLZO Composite. The team also extended their mesoscale models and MesoMicro code framework to compute properties of composites. A polymer/LLZO composite was chosen to demonstrate the general applicability of the approach to new classes of SEs. Figure 71a shows an example 3D digital representation of a realistic porous LLZO microstructure filled with a polymer. Mesoscale modeling approaches were applied to compute the following: (1) local mechanical responses within the microstructure; (2) effective elastic modulus; and (3) effective ionic conductivities of both cations (Li^+) and anions ($TFSI^-$). For input materials parameters, the team incorporated DFT-derived LLZO elastic modulus reported in previous quarters, a reasonable polymer elastic modulus, and experimental ionic conductivities of LLZO and PEs. It should be noted that the employed materials parameters (that is, elastic moduli and ionic conductivities) for LLZO and polymer result in strongly inhomogeneous elasticity and conductivity within the composite microstructure. The team verified that their mesoscale modeling approaches can be applied successfully to strongly inhomogeneous composite electrolytes. Figure 71b shows the preliminary simulation result of the local mechanical response (represented by the von Mises stress) within the employed composite microstructure. The simulation verifies the presence of concentrated mechanical stress near the polymer/LLZO interfaces. As shown in the Figure, the level of stress concentration is sensitive to local topological features such as interface curvature. More detailed analysis for relating stress concentration and microstructural features is in progress. Additionally, by applying loads along various normal and shear directions, the team extracted the effective elastic modulus of the composite (Figure 71c), which is expected to be highly sensitive to microstructure and LLZO/polymer phase fraction. More quantitative analysis is forthcoming as the team applies the method to new composite microstructures in the next quarter.

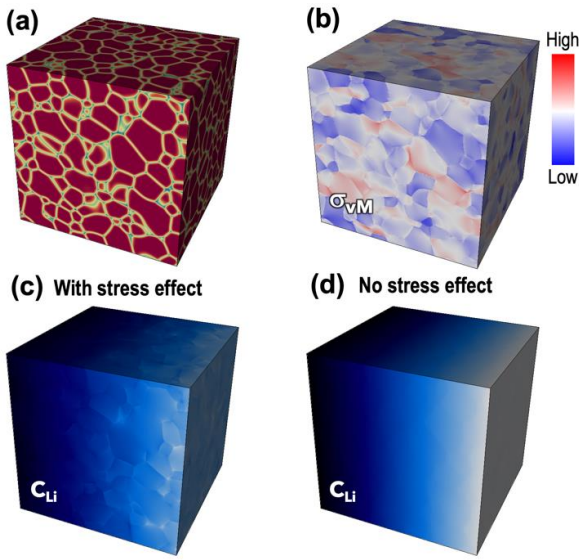

Figure 70. (a) Digital representation of polycrystalline LLZO microstructure. (b) Computed von Mises stress profile. (c-d) Lithium composition profile (c) with and (d) without mechanical stress.

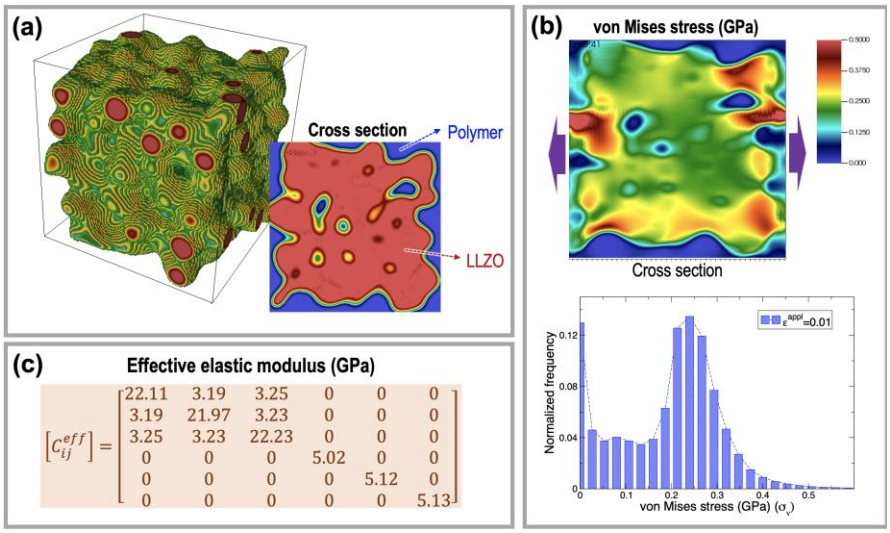

Figure 71. (a) 3D porous LLZO microstructure and cross-section of LLZO/polymer composite microstructure. (b) Computed von Mises stress (top: spatial distribution; bottom: statistics) in the composite microstructure under applied loading. (c) Computed effective elastic modulus of the composite microstructure.

Patents/Publications/Presentations

Presentation

- MRS Spring Meeting, Virtual (2021): Elucidating Interfacial Instability in All-Solid-State Lithium Batteries from First-Principles Simulations"; L. Wan, A. M. Dive, M. Wood, K. Kim, T. Li, and B. C. Wood.

Task 3.8 – First-Principles Modeling of Cluster-Based Solid Electrolytes (Puru Jena, Virginia Commonwealth University)

Project Objective. The objective of the project is to use cluster-ions, which are stable atomic clusters that mimic the chemistry of individual atoms, as the building blocks of new SEs for Li-ion batteries and the corresponding battery system. The advantages of using cluster-ions to replace elemental ions is that the size, shape, and composition of the former can be tailored to achieve higher superionic conductivity, electrochemical stability, and charge transfer across the solid-state ions (SSIs) than the conventional materials. More specifically, the goal is to develop superior SEs based on cluster-ions and to model these SEs and their interfaces with electrodes, especially with the Li-metal anode, for successful integration into high-performance SSBs for EVs. The team will model and screen cluster-based SEs that, compared to conventional SEs, have low activation energies, practical room-temperature ionic conductivities, wide electrochemical stability windows, and desired mechanical properties that, for example, can inhibit the Li-metal anode dendrite growth. They will provide a fundamental understanding of the ionic conduction mechanism in the newly developed, cluster-based SEs and identify means to further improve property metrics via chemical and defect engineering. The team will model the interfacial properties, such as the structural, chemical, electrochemical, and ion/charge transfer properties, between the cluster-based SEs and electrodes at the atomic level, as well as find the interfacial coating materials with desired properties. Based on accumulated data from modeling, they will establish links between the basic parameters of the cluster-ions and the bulk/interface properties, which can directly guide experiments. Meanwhile, the team will work closely with experimentalists in the BMR Program to complement the project's theoretical efforts and to guide them in focused development of the predicted cluster-based SEs and the interfaces.

Project Impact. The proposed project will open a new avenue for guiding experiments in the synthesis of SSBs equipped with cluster-based SEs and capable of operating over a wide temperature range. Modeling and understanding of the ionic conduction of cluster-based electrolytes and their interfacial properties with electrodes, especially with Li-metal anode, will enrich current battery science and also train the future workforce in SSB development for next-generation EVs by supporting postdoctoral fellows.

Approach. This project will employ multi-scale theoretical methods and computational techniques.

Out-Year Goals. The out-year goals involve modeling development of new cluster-based SE materials and database.

Collaborations. The team is working with J. Nanda of ORNL, Y. Wu of Ohio State University (OSU), and D. Mitlin of UT, Austin, on SEs.

Milestones

1. Complete development of new cluster-based SE materials with a database. (Q4, FY 2021; Completed)
2. Structural studies of the chemically mixed systems containing both cluster-ions and elemental ions. (Q2, FY 2021; Completed)
3. Characterizations of the chemically mixed systems. (Q3, FY 2021; Completed)
4. Cation doping in the cluster-based SE systems. (Q4, FY 2021; In progress)

Progress Report

Research toward the Q3 milestone is completed as planned. Based on the ground-state configurations obtained in the last period, study of different concentrations of chemically mixed systems, ionic conductivities, and activation energies of 35 new SEs have been studied and characterized.

Figure 72 shows two typical cases of the studied SEs. For a specified cluster-based system, the diffusivities at different temperatures for each halogen (for example, chlorine) concentration (in the range of 0 to 100% with a step of 12.5%) are calculated and fitted using Arrhenius relation (left panels). The ionic conductivity at room temperature and the activation energy at each concentration are extracted.

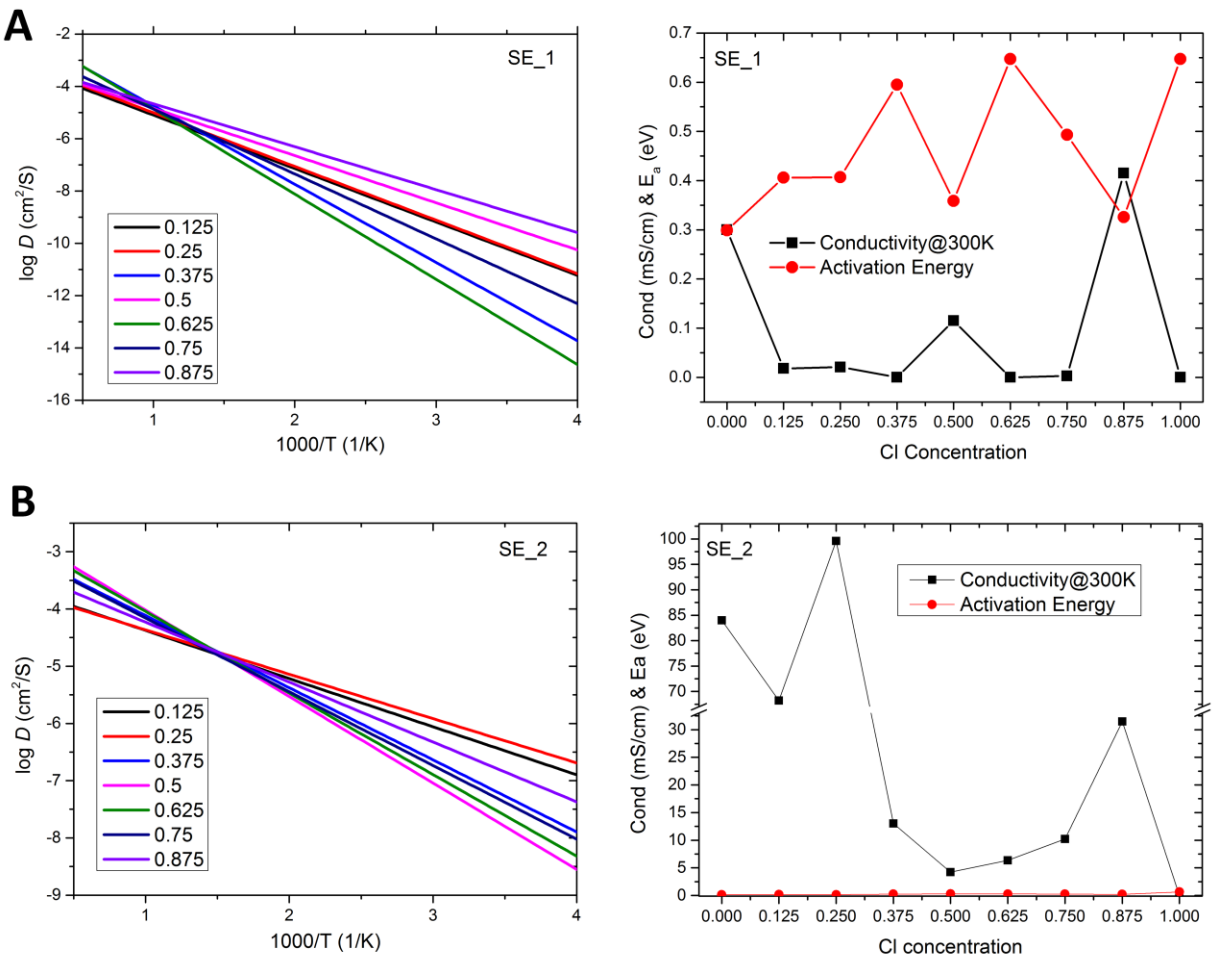

Figure 72. Two typical cases of the studied chemically mixed systems. (a) Calculated diffusivities at different temperatures (left) for different halogen concentrations (in the range of 0% to 100% with a 12.5% step). The extracted room-temperature ionic conductivities and activation energies at different halogen concentrations are drawn to find the optimal concentration (right) for the cluster-based solid electrolyte 1 (SE_1). (b) Calculated diffusivities at different temperatures (left) for different halogen concentrations (in the range of 0% to 100% with a 12.5% step) for the cluster-based solid electrolyte 2 (SE_2). The extracted room-temperature ionic conductivities and activation energies at different halogen concentrations (right) show that the optimal mixing concentration is 25% at which the room-temperature ionic conductivity reaches 100 mS/cm and activation energy is 0.154 eV.

The team presents three major findings:

- The ionic conductivity (for example, at room temperature) and activation energy of the chemically mixed system do not change monotonically with the increasing halogen concentration.
- There exists one mixing concentration that can enable the optimized ionic diffusion properties based on a specific cluster-based system. For example, as shown in Figure 72a (right), the optimized halogen concentration is 87.5% at which the room-temperature ionic conductivity is increased to over 0.4 mS/cm compared to the original 0.3 mS/cm of the cluster-based SE (SE_1). In another case, as shown in Figure 72b (right), the optimized halogen concentration is 25% at which the room-temperature ionic conductivity is the highest (100 mS/cm) and the activation energy is the lowest (0.154 eV) throughout the whole range.
- In general, the calculated ionic conductivity and activation energy are in the same order of those of the original cluster-based system, as shown in Figure 72a-b (right). More details and the updated database of the cluster-based SE materials will be given in the research performance progress report.

For each studied SE (with certain halogen concentration), AIMD simulations are carried out using a large supercell containing hundreds of atoms. In each case, AIMDs are performed at 4 to 5 different temperatures. A typical AIMD lasts ~ 100 ps with a 2-fs time step, where 5-10 ps is allowed for the system to reach thermal equilibrium before the data are collected to calculate the MSD for all the atomic species in the system. Those data that show phase transition or melting are not considered in the analysis. The diffusivity at each temperature is then calculated from the MSD. The calculated diffusivities at a few temperature points are fitted to the Arrhenius relation and extrapolated to other temperatures, especially room temperature. The activation energy is extracted from the fitting. The room-temperature ionic conductivity and activation energy for each cluster-based SE are then drawn against the halogen concentration to find the optimal chemically mixed system that enables the best properties.

Patents/Publications/Presentations

Presentation

- DOE VTO Annual Merit Review Meeting, Virtual (June 24, 2021).

Task 3.9 – Predictive Engineering of Interfaces and Cathodes for High-Performance All-Solid-State Lithium-Sulfur Batteries
(Badri Narayanan, University of Louisville)

Project Objective. The primary goal of this project is to leverage data-driven methods and ML strategies to develop accurate multi-physics models for ASSLSB materials that can capture electrochemical and transport phenomena over atomic-to-mesoscopic length/timescales; these models will be rigorously validated by synthesis and advanced characterization experiments. The team will leverage the predictive power of these models, alongside synthesis/characterization experiments and battery fabrication to address longstanding issues at the electrode/electrolyte interfaces in all-solid-state Li-S batteries. The project's proposed technology involves the following: (1) halide-doped solid sulfide electrolytes that can concurrently provide high Li^+ ion conductivity and suppress dendrite growth; (2) novel mesoporous cathode composed of interconnected carbon nano-cages co-infiltrated with sulfur and sulfide electrolyte, which hold potential to allow high sulfur loading and optimal ion/electron pathways; and (3) functionalization of sulfide electrolyte with ILs to improve physical contact and minimize impedance at the CEI.

Project Impact. ASSLSBs remain far from commercialization due to poor understanding of fundamental electrochemical/chemical and transport processes that occur at the interfaces, especially at atomic to mesoscopic scales. Successful development of proposed predictive models (at multiple scales) will bridge this knowledge gap and will advance fundamental understanding of reaction chemistry, kinetics, charge transfer, and dendrite growth at electrified SSIs. This will enable predictive design of effective strategies to mitigate interfacial problems in ASSLSBs, including poor interfacial contact, interfacial impedance to Li^+ ion transport, and poor electron/ion conduction within cathodes. Ultimately, the fundamental knowledge gained will lead to development of high-performance ASSLSBs that meet DOE targets of specific energy (350 Wh/kg @C/3), sulfur loading (> 6 mg/cm^2), and high cycle life (1000).

Approach. The project brings together innovative solutions in multi-scale materials modeling, electrolyte synthesis, fabrication of cathode architecture, and electrolyte functionalization to overcome the issues at electrode/electrolyte interfaces in ASSLSBs. The central idea is to employ a data-driven and ML-based approach to develop accurate multi-physics battery models at atomic-to-mesoscopic scales. This approach overcomes critical problems with existing model development methods by foregoing the need for pre-defined functional forms, introducing deep-learning technique to describe reactivity, and employing optimization methods that do not require human intuition. Multi-scale simulations based on the newly developed models will provide insights into electrochemical phenomena at electrode/electrolyte interfaces.

Out-Year Goals. In Year 2, the goal is to gain atomic-scale understanding of interfacial reactions in ASSLSBs, and to assess the effectiveness of functionalizing CEIs with ILs.

Collaborations. The team collaborates with the groups under A. Ngo and L. A. Curtiss at ANL for quantum simulations of battery systems; they plan to collaborate with J. Nanda at ORNL for advanced spectroscopic *in situ* characterization of interfaces.

Milestones

1. Extend reactive interatomic potential models to include interfaces. (Q1, FY 2021; Completed)
2. Advance characterization of CEIs to understand their reactivity, stability, and structure; validate predictions of reactive interatomic potentials. (Q2, FY 2021; Completed)
3. Utilize reactive MD to gain insights into interfacial processes, and predictively design stable interface with good ion transport. (Q3, FY 2021; Completed)
4. Fabricate batteries that meet interim performance metrics. (Q4, FY 2021; In progress)

Progress Report

This quarter, the team made good progress on (a) gaining fundamental understanding of interfacial reactions that occur between cathode and solid sulfide electrolyte, (b) improving the classical reactive force field (ReaxFF) for Li-P-S system to enhance its predictive power for interfaces, and (c) synthesis of cathodes with high sulfur loading, alongside battery fabrication/testing.

Atomic-Scale Understanding of Interfacial Reactions at CEI. Solid sulfide electrolyte materials comprise networks of several P-S anion motifs surrounded by lithium ions. For example, Li_7PS_6, $Li_4P_2S_6$, Li_2PS_3, and $Li_7P_3S_{11}$ electrolyte systems comprise PS_4^{3-}, $P_2S_6^{2-}$, PS_3^-, and $P_2S_7^{4-}$ motifs, respectively. This quarter, the team employed AIMD simulations to understand the effect of P-S motifs on the reactivity of CEIs. They considered cathodes at two extreme states of charging, namely (a) fully charged: a-S_8 (cubic, *Fddd*), and (b) fully discharged: Li_2S (face-centered cubic). They chose three solid sulfide electrolyte compositions for this study: Li_7PS_6, $Li_4P_2S_6$, and Li_2PS_3 containing PS_4^{3-}, $P_2S_6^{2-}$, and PS_3^- motifs, respectively.

For all cases, they investigated the interface between the cathode (Li_2S and S_8) and solid sulfide electrolyte oriented such that their crystallographic [001] directions are aligned normal to the interface, as shown in Figure 73. The computational supercell was designed based on the following criteria: (a) minimize the lattice mismatch between the solid sulfide electrolytes and cathodes, (b) balance the computational resources. In all cases, typical supercell sizes were ~ 1 nm × ~ 1 nm × ~ 3-5 nm (~ 300 atoms). Considering all cases, the team finds four distinct atomic processes: (a) breaking of PS_4^{3-} and $P_2S_6^{2-}$ structural units, (b) breaking of sulfur (S_8) rings, (c) polymerization of PS_3^- to form $P_2S_6^{2-}$ structural units, and (d) formation of new Li-S bonds at the interface. Detailed analysis of the project's AIMD trajectories shows that regardless of the type of motifs, solid sulfide electrolytes react more with the fully discharged state of cathode (Li_2S) as compared to the fully charged state (that is, S_8). However, the motifs strongly govern the extent and type of interfacial reactions.

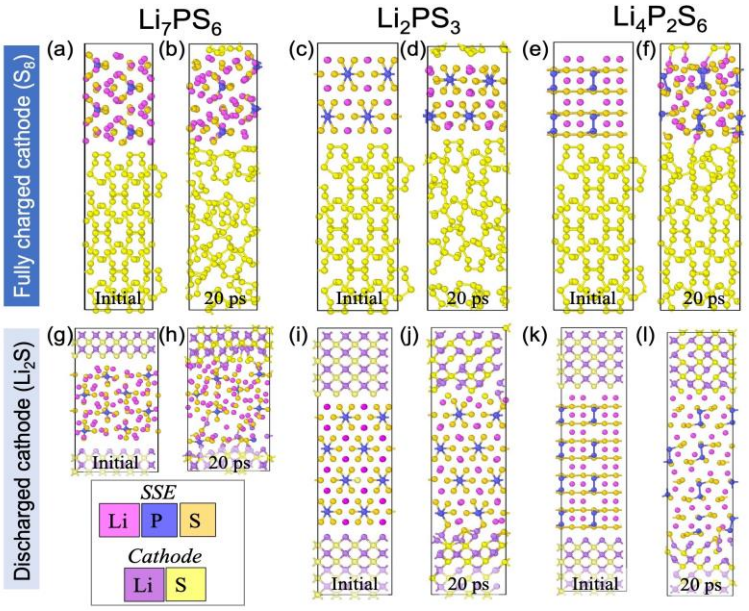

Figure 73. Structural evolution of cathode/electrolyte interface obtained from *ab initio* molecular dynamics simulations under ambient conditions. The atomic-scale structure of interface between S_8(001) (that is, fully charged cathode) and electrolytes with varying P-S motifs (a-b) Li_7PS_6 (001) (PS_4^{3-}), (c-d) Li_2PS_3 (001) (PS_3^-), and (e-f) $Li_4P_2S_6$ (001) ($P_2S_6^{2-}$). Corresponding interfaces with Li_2S (001) (that is, fully discharged cathode) are shown for (g-h) Li_7PS_6 (001), (i-j) Li_2PS_3 (001), and (k-l) $Li_4P_2S_6$ (001). In all panels, lithium, phosphorus, and sulfur atoms belonging to solid sulfide electrolyte are depicted as magenta, blue, and tan spheres respectively; the lithum and sulfur in cathode are shown in dark purple and yellow colors.

The AIMD trajectories show that Li_7PS_6 and Li_2PS_3 do not decompose via interaction with the cathode at the fully charged state of cathode, that is, S_8 (Figure 73a-d). Note, the PS_3- motifs in Li_2PS_3 polymerize to form a new $P_2S_6^{2-}$ motifs system (Figure 73c-d). On the other hand, $Li_4P_2S_6$ exhibits decomposition reactions involving (a) ring opening of S_8 rings in the cathode via lithium of solid sulfide electrolyte, and (b) conversion of $P_2S_6^{2-}$ to form P_2S_5 (Figure 73e-f). Interfaces of the solid sulfide electrolytes with Li_2S are found to be more reactive than that with S_8, due to the presence of lithium atoms in Li_2S. For the interface of Li_7PS_6 with Li_2S, the team found that PS_4^{3-} motifs in the SSEs decompose to form reduced species, namely, PS_3^-, PS_2,

and PS. During the 20 ps of AIMD, ~ 25% of PS_4^{3-} gets decomposed (~ 12.5% forms PS_3^- and the remaining 12.5% forms PS), as shown in Figure 73g-h. Similarly, for the interface of $Li_4P_2S_6$ with Li_2S, ~ 12.5% $P_2S_6^{2-}$ motifs are broken to form P_2S_5 (Figure 73k-l). In both the above cases, motifs exposed to lithium side of Li_2S cathode undergoes decomposition. For the interface of Li_2PS_3 with Li_2S, initially polymerization reaction takes place due to which all the PS_3^- motifs are converted to $P_2S_6^{2-}$motifs. During 20 ps of AIMD, ~ 37.5% of $P_2S_6^{2-}$ motifs break into P_2S_5. In this case, the $P_2S_6^{2-}$ motif exposed to both sulfur and lithium side of Li_2S undergoes decomposition (Figure 73i-j). In all three cases, the sulfur atoms released from decomposition of PS_4^{3-} and $P_2S_6^{2-}$ motifs move toward the cathode to form new $Li_{(cathode)}$-$S_{(solid\ sulfide\ electrolyte)}$ bonds.

Reactive MD to Understand Interfacial Processes. In the first quarter, the team had extended their Tersoff+Qeq interatomic potential to account for electrode/electrolyte interfaces with reasonable success. This classical potential was found to perform well for Li | solid sulfide electrolyte, and Li_2S | solid sulfide electrolyte interfaces. Note that Tersoff+Qeq predicted these interfaces to be more reactive than accurate AIMD simulations; this raises concerns on its suitability for investigating long-time dynamics associated with these interfaces. More importantly, CMD simulations with Tersoff+Qeq on the S_8(001)/LiPS(001) interface exhibit an anomalous behavior—most of the S_8 rings in the cathode open, in stark contrast to previous AIMD reports, wherein the S_8 structure remains largely unperturbed. Careful analysis of the CMD trajectories indicates that this spurious behavior is an artifact of the inherent inability of the Tersoff+Qeq potential in treating the dihedral interactions within S_8 rings, and long-range dispersive forces between S_8 rings. To address this issue, the team added dihedral terms to their Tersoff+Qeq potential; the overall potential has the same formalism as the ReaxFF developed by Adri van Duin. The team employed their in-house ML-based FF development framework to optimize the ReaxFF parameters by employing the large first-principles dataset (constructed over the last year), including atomic structures, energies, atomic charges for numerous configuration, equation of state of various condensed phases, elastic properties, surface properties, and interfacial structure/energy/charges. The Tersoff+Qeq potential was used as a starting point for the fitting process. The newly developed ReaxFF potential can accurately predict (a) lattice parameters (within ~ 1% of DFT), (b) heat of formation (~ within 15 meV/atom of DFT), and (c) elastic constants (within ~ 20% of DFT) (Figure 74). Additionally, the predicted interfacial energies for various Li | solid sulfide electrolyte, S_8 | solid sulfide electrolyte, and Li_2S | solid sulfide electrolyte are within 0.2 J/m^2 of DFT values; the atomic charges in the interface are close to Bader charges predicted by DFT calculations.

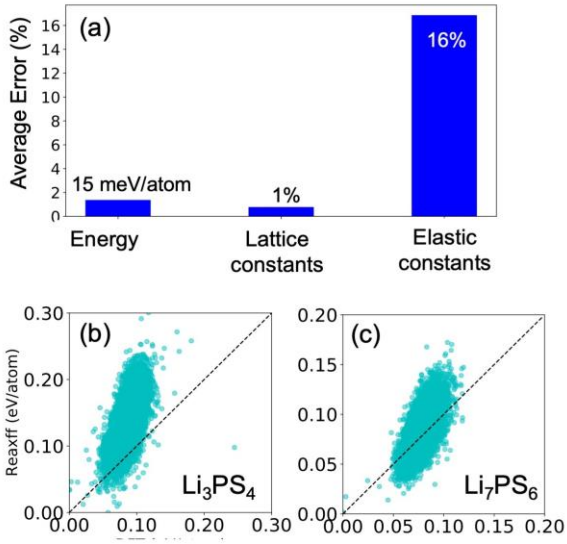

Figure 74. Predictive power of newly developed reactive force field (ReaxFF) for Li-P-S. (a) Average deviation in ReaxFF predictions from density functional theory (DFT) calculated values for energy of given configuration, lattice parameters, and elastic properties. As a representative example, ReaxFF predicted energy for 10,000 different configurations for (b) Li_3PS_4 and (c) Li_7PS_6 are compared with energy values obtained from DFT calculations. The configurations employed in panels (b) and (c) are sampled using *ab initio* molecular dynamics simulations. Furthermore, the energies in panels (b) and (c) are shown relative to equilibrium

To assess the performance of the newly developed set of ReaxFF parameters in describing interfacial processes, the team conducted ReaxFF-CMD simulations for three interfaces containing Li_7PS_6 SE, namely: Li(001)/LiPS(001), S(001)/LiPS(001), and Li_2S(001)/LiPS(001). The team's computational supercell for Li(001)/LiPS(001) interface is composed of 16,000 atoms in lithium anode and 15,680 atoms in the solid sulfide electrolyte. Similarly, in S_8(001)/LiPS(001), the cathode is composed of 7,680 sulfur atoms, and the solid sulfide electrolyte is built with 19,712 atoms. Finally, the Li_2S(001)/LiPS(001) consists of 9,360 atoms in

Li_2S electrode and 8,960 atoms in solid sulfide electrolyte. All interfaces are constructed such that the epitaxial strain is < 1%. Before performing MD simulations, the interface structures are optimized using the conjugate gradient algorithm. After minimization, they performed the equilibration run within a canonical ensemble (NVT) under ambient conditions for 0.1 nanosecond (ns) with a timestep of 1 femtosecond (fs). Figure 75 shows the equilibrated structure of all three interfaces obtained from the ReaxFF-CMD simulations.

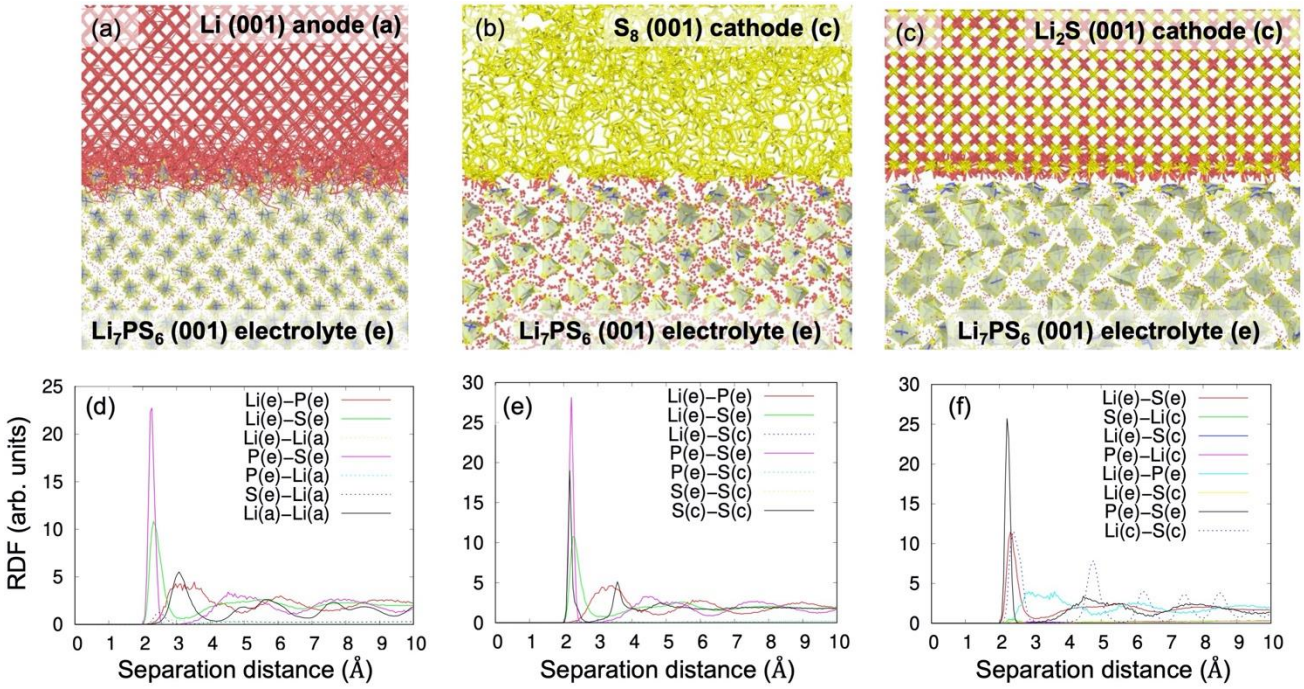

Figure 75. Equilibrated interface structures obtained from reactive force field (ReaxFF) – classical molecular dynamics simulations under ambient conditions. (a) Li(001)/LiPS(001), (b) S_8(001)/LiPS(001), and (c) Li_2S(001)/LiPS(001) interfaces. The lithium, sulfur, and phosphorus atoms are shown in red, yellow, and green colors. The PS_4^{3-} tetrahedra are shown in green. Radial distribution functions (RDF) g(r) for selected atom pair types for each interface are shown in the bottom row. The labels (e), (c), and (a) identify the atoms that belong to electrolyte, cathode, and anode.

Direct visualization of the CMD-ReaxFF simulations shows that PS_4^{3-} motifs in the LiPS solid sulfide electrolyte undergo reductive decomposition against lithium metal to form $LiPS_x$ compounds at the anode / solid sulfide electrolyte interface, as indicated by formation of new bonds between lithium of the anode and P/S atoms of solid sulfide electrolyte (Figure 75a). The formation of these new Li-P and Li-S bonds is evidenced by appearance of new peaks in the RDF for Li(a)-P(e) at ~ 2.6 Å, and Li(a)-S(e) at ~ 2.1 Å. Such reductive decomposition of solid sulfide electrolyte against lithium metal is consistent with previous AIMD simulations. On the other hand, no new peaks are observed in the RDF for S(c) – Li (e) pairs in the equilibrated S_8 | LiPS, and the S_8 rings remain largely intact. This suggests that no reactions occur at the S_8 | LiPS interface, consistent with the AIMD simulations (Figure 73a-b). Notably, the newly developed ReaxFF completely eliminates spurious opening of S_8 rings and their polymerization—the artifacts of the Tersoff+Qeq potential reported in the first quarter. Similarly, few Li-S bonds form across the interface between Li_2S and LiPS, as shown by a small peak in the Li(c)-S(e) RDF at ~ 2.1 Å, consistent with the AIMD trajectory (Figure 73g-h). Clearly, the newly developed ReaxFF is capable of treating the electrode/electrolyte interfaces in the Li-P-S system accurately. The team is employing ReaxFF-CMD simulations to understand the effect of GBs and extended defects on Li-ion conduction in solid sulfide electrolytes. Such an understanding promises to unravel new pathways to engineer morphology of solid sulfide electrolytes to control Li-ion conduction.

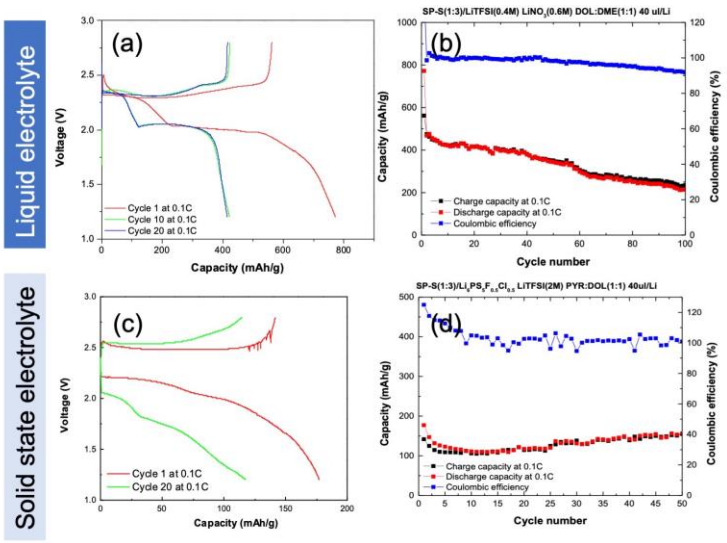

Figure 76. Performance of battery with super-P cathode at high S-loading (4.6 mg/cm²) using (a-b) liquid electrolyte [0.4 M LiTFSI with 0.6 M $LiNO_3$ in DOL/DME (1:1)], and (c-d) solid electrolyte ($Li_6PS_5F_{0.5}Cl_{0.5}$). Charge-discharge curves at selected cycles are shown in panels (a) and (c). In panels (b) and (d), capacity (left axis) and Coulombic efficiency are plotted as a function of cycles as the batteries are cycled at C/10 rate.

Synthesis of Cathodes with High Sulfur Loading and Battery Testing. This quarter, the team modified the binder chemistry and employed porous aluminum collectors to prepare stable cathodes with high sulfur loading. Cathode consisted of Super P-S (1:3) 88 wt%, CNT 8 wt%, and carboxymethyl cellulose (CMC) 4 wt%. First, to optimize cathode with high sulfur loading, the cathode with high sulfur loading was tested with LEs. Figure 76a-b shows the performance of a battery with C-S cathode (Super-P based) with 4.6 mg/cm^2 sulfur loading and lithium anode with LE [0.4 M LiTFSI with 0.6 M $LiNO_3$ in DOL/DME (1:1)] at C/10 rate. It shows initial discharge capacity of ~ 800 mAh/g, but drops to ~ 500 mAh/g after the first cycle and retains its capacity at ~ 230 mAh/g after 100 cycles. Further increase of sulfur loading to 5.2 mg/cm^2 resulted in lower capacity (< 400 mAh/g) and unstable cycling performance, even with the LE. On using a solid sulfide electrolyte ($Li_6PS_5F_{0.5}Cl_{0.5}$), the performance of a battery with C-S cathode (Super-P based) with 4.6 mg/cm^2 sulfur loading, lithium anode, and CEI functionalized with 2 M LiTFSI in 40 µL PYR:DOL (1:1) IL, an initial discharge capacity of ~ 175 mAh/g is observed at 60°C; this battery retains capacity at ~ 150 mAh/g after 50 cycles at C/10 rate. When the sulfur loading was increased to 5.0 mg/cm^2, the performance diminished with the initial capacity of 100 mAh/g and a retention of 75 mAh/g after 35 cycles. Although these results show promise, further engineering of electronic conductivity of cathode is essential to improve the battery performance. Currently, the team is exploring several strategies including (a) adding more CNT to improve electronic conductivity of cathode, (b) engineering porosity of the cathode, (c) adding SSE into cathode to improve its ionic conductivity, and (d) optimizing the functionalizing IL.

Patents/Publications/Presentations

Presentations

- MRS Spring Meeting, Virtual (April 2021): "Understanding Ion Transport and Interfacial Stability in Fluorine Containing Lithium Argyrodite Electrolytes for Solid-State Lithium-Sulfur Batteries"; V. Shreyas, S. Gupta, W. Arnold, G. Sumanasekera, J. Jasinski, H. Wang, and B. Narayanan.*
- American Chemical Society (ACS) Spring Meeting, Energy and Fuels Division, Virtual (April 2021): "Liquid Synthesis of Halide Doped Lithium Argyrodites with Precise Composition Control"; W. Arnold, V. Shreyas, Y. Li, B. Narayanan, and H. Wang.

Task 3.10 – Predicting the Nucleation and Evolution of Interphases in All-Solid-State Lithium Batteries
(Sabrina (Liwen) Wan, Lawrence Livermore National Laboratory)

Project Objective. The goal of this project is to develop and apply a suite of new computational tools to predict early-stage formation of metastable interphases in SSBs. To achieve this goal, this project focuses on meeting three primary objectives corresponding to different regimes within the early-stage interphase formation: (1) identify chemical motifs for pre-nucleation; (2) predict possible interphase structures; and (3) model the kinetics of interphase formation.

Project Impact. Degradation of SSE and formation of undesired secondary interphases at the solid electrolyte/electrode interfaces are some of the key issues that limit SSB technology from practical applications. The computational tools developed in this project will allow modeling of nucleation and formation of interphases with quantum-level accuracy and significantly improved efficiency compared to currently available methods. Completion of this project will also provide valuable insights into the correlation between local chemistry and interphase formation, which can be used to inform design of interfacial structures to lower interfacial resistance and to extend cycling life of SSBs.

Approach. The project approach centers on close integration of *ab initio* simulations, ML, and stochastic methods to probe chemistry and nucleation across broad ranges of time and length scales. First, the team will identify chemical motif, which acts as chemical precursor for pre-nucleation based on ML and large-scale AIMD simulations. Second, they will predict possible interphase structures based on stochastic minimizations of population-weighted chemical motifs identified from the MD simulations. Third, they will model the kinetics of interphase formation and evolution using KMC. To test the general applicability of the proposed computational methods, the team considers a variety of commercially viable SE and cathode materials, including cubic LLZO and LiPON SEs, and LCO and LFP cathodes. These materials also represent a range of degrees of stability arising from their intrinsic properties—in particular, LiPON|LCO, LLZO|LCO, and LLZO|LFP are expected to form stable, less stable, and reactive interfaces, respectively.

Out-Year Goals. The future goal is to predict practical strategies either to facilitate formation of the desired interphase that allows for fast Li^+ diffusion and is stable on cycling or to suppress the formation of undesired interphase to reduce interfacial impedance of ASSBs.

Collaborations. There are no collaborative activities this quarter.

Milestones

1. Identify chemical precursors for interphase formation. (Q1 FY 2021; Completed)
2. Construct initial interphase structures. (Q2, FY 2021; Completed)
3. Identify proper constraints for global optimization. (Q3, FY 2021; In progress)
4. Obtain possible interphase structures and compositions. (Q4, FY 2021; In progress)

Progress Report

Global Optimization to Identify Formation of Secondary Phases at the Solid Electrolyte/Cathode Interface. This quarter, the team continued efforts to characterize distinct interphase structures for LLZO|LCO interfaces. From the last quarters, they identified different interphase nuclei based on the continued high-temperature AIMD simulations. These interphase nuclei comprise a highly intermixed region of different ions, as shown in Figure 77a. To accelerate the search of potential interphase formation from such complex interfacial regions, the team identified unique clusters based on the local coordination populations analysis. It is found that cobalt atoms prefer tetrahedral coordination with oxygen, as shown in Figure 77b. Based on the population analysis, they identified nine distinct clusters with varying compositions of lanthanum, cobalt, lithium, zirconium, and oxygen. Figure 78a-d shows the relaxed structures at 0 K for some of these clusters. To summarize, as the interface continues to evolve, these unique clusters would act as seed nuclei for forming possible interphases at the LLZO|LCO interface. The team is performing global energy minimization to obtain stable structures of these clusters using the Basin Hopping algorithm. They have performed several test runs to identify optimal parameter/ constraints in Basin Hopping to speed up the search for local minima on the potential energy surface. Figure 79 presents the flowchart to identify energy-minimum structures using Basin Hopping. The team will create a library of local minima structures from the potential energy surface generated using Basin Hopping, based on which they will perform further relaxations to ensure convergency to the lowest energy states. An example of the initial 200 steps in the Basin Hopping runs for a La-Co-O cluster is given in the right-hand panel of Figure 79. For one local minimum (highlighted as a star in Figure 79), they identified from the potential surface energy obtained during the Basin

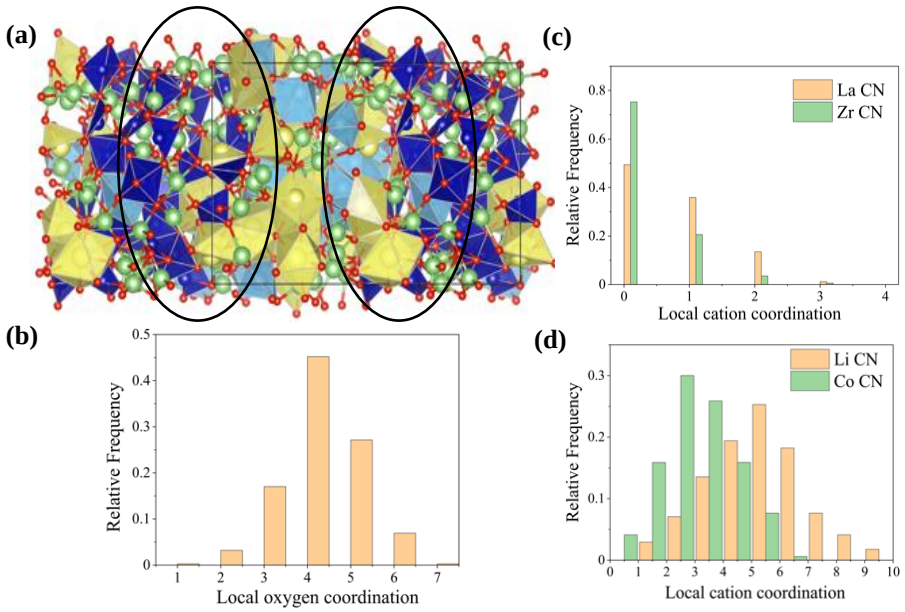

Figure 77. (a) Structure representation of LLZO/LCO interface obtained from high-temperature *ab initio* molecular dynamics (AIMD) simulations (b) Population analysis of Co-O local coordination showing preferred tetrahedral coordination for Co-O. For the Co-O tetrahedral coordination environment, population analysis is performed for other cations around cobalt, and the results are shown in (c) for lanthanum and zirconium, and in (d) for lithium and cobalt. In the structure representation, lanthanum, cobalt, zirconium, lithium, and oxygen ions are represented by yellow, blue, light blue, green, and red spheres, respectively; the coordination environment is shown as polyhedra, except lithium.

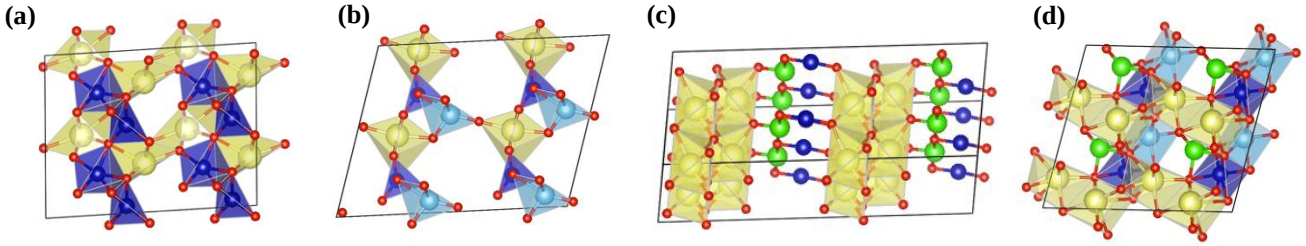

Figure 78. The relaxed structures of distinct unique clusters observed at the LLZO|LCO interface: (a) $LaCoO_3$, (b) $CoLaZrO_5$, (c) $CoLa_2LiO_5$, and (d) $CoLa_2LiZrO_7$.

Hopping runs at 750 k_B that further relaxation reveals a completely different crystal structure (on the right) compared to the initial one (on the left); this proves the effectiveness of Basin Hopping algorithm to identify new crystal structures. Continued Basin Hopping runs would generate additional structures corresponding to the local minima on the potential energy surface and allow the team to obtain possible stable structures as secondary phases for the compositions identified as the solid electrolyte/cathode interfaces.

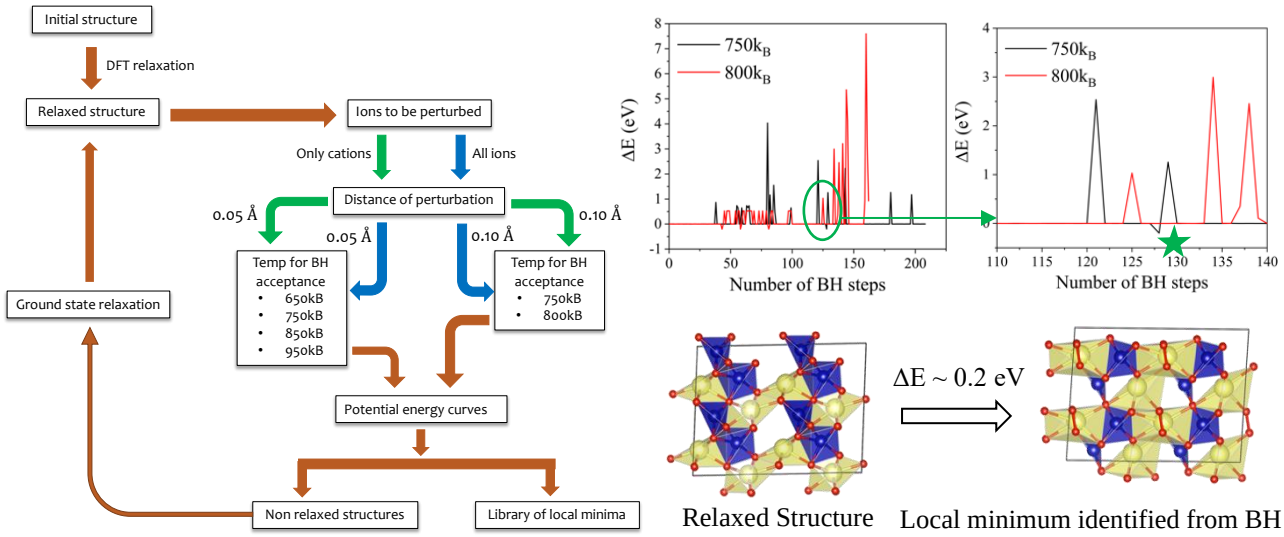

Figure 79. Illustration of workflow (left) to generate a library of local minima using the Basin Hopping energy minimization algorithm. An example of a Basin Hopping run for a $LaCoO_3$ cluster is shown on the top right, with 0.1Å perturbation distance at 750k_B and 800 k_B. Zoomed in plot shows a local minimum identified during the Basin Hopping minimization. The corresponding relaxed structure for this local energy minimum is shown on the bottom with comparison to its original structure.

ML Interatomic Potentials for Accelerated Atomistic Simulations of Interfaces. This quarter, the team developed a new ML potential for LLZO|LCO interface. It was achieved by training an ANN with total energies of structures and also force components of all atoms, using 20-20 hidden-layer ANN architecture and local atomic environmental features with symmetry functions. The training data consist of structures for bulk LLZO, bulk LCO, and LLZO|LCO interface systems, which had been collected from AIMD simulations at various temperatures. To evaluate the performance of the ML-FF, they performed MD simulations for bulk and interfacial systems and compared the results with DFT calculations. Figure 80 demonstrates the ability of the developed ML potential to perform atomic simulations with quantum (DFT) level of accuracy for energies and forces. The energy and force RMSE are at most 5.6 meV/atom and 0.27 eV/Å for bulk systems at high temperatures, as shown in Figure 80a-c. For an LLZO|LCO interfacial system with 744 atoms, the energy and force RMSE are at most 3.0 meV/atom and 0.30 eV/Å at 2100 K (Figure 80d). Figure 81 compares the atomic configurations of an interfacial model from MD simulation using the ML-FF with those obtained from AIMD simulation. The team's ML potential has shown the ability to capture key phenomena such as cobalt atoms occupying lithium sites in bulk LCO and the diffusion of cobalt, lanthanum, and zirconium atoms across the interface, as have been observed from AIMD simulations. These preliminary results imply that the ML potential can perform stable MD simulations for a long time and at high temperatures for bulk and interfacial systems with quantum accuracy. The team will perform additional performance tests by evaluating additional energy/force errors for the interfacial systems and by predicting properties of interfaces. Once the ML-FF is fully validated, they will use it to probe cation interdiffusion and accelerate the search for potential degradation products or secondary phase formation at the interfaces.

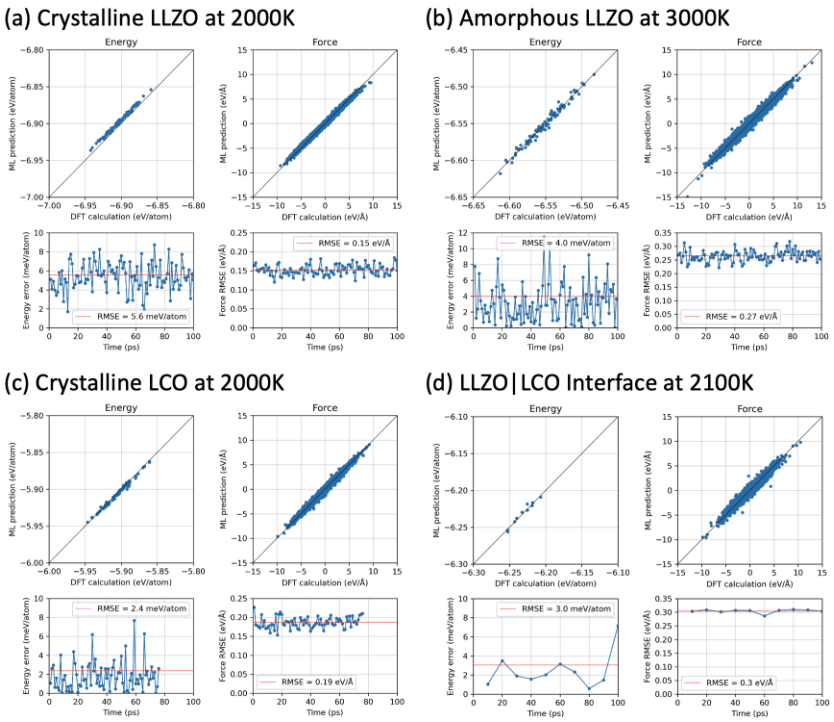

Figure 80. Performance test of the machine learning (ML) potential developed for the LLZO|LCO interface. NVT molecular dynamics simulations with the ML potential were performed for (a) crystalline LLZO at 2000 K, (b) amorphous LLZO at 3000 K, (c) crystalline LCO at 2000 K, and (d) LLZO|LCO interface at 2100 K; the results are compared to DFT calculations using snapshots obtained every 1 ps (10 ps for LLZ|LCO interface) to evaluate energy and force errors. Simulation cells with 192 atoms were used for LLZO and LCO, and a structure model with 744 atoms was used for LLZO|LCO interface.

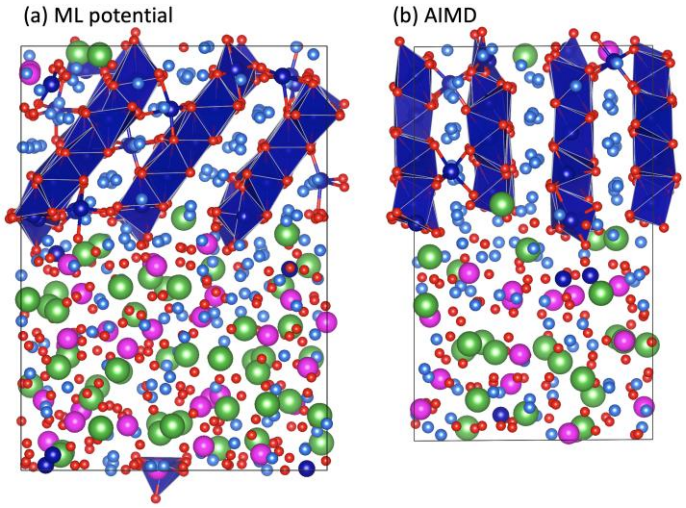

Figure 81. Snapshot of the atomic structure of LLZO|LCO interface from (a) NVT molecular dynamics simulation with the machine learning potential at 2100 K after 100 ps using a 744-atom interfacial model with the (104) LCO orientation and (b) NVT *ab initio* molecular dynamics simulation at 2000 K using a 432-atom interface system with the (100) LCO orientation. The lithium, lanthanum, zirconium, cobalt, and oxygen atoms are represented as light blue, green, magenta, navy, and red spheres; the navy polyhedra represent CoO_6, and Co-O bonds indicate cobalt atoms at lithium sites in bulk LCO.

Patents/Publications/Presentations

Presentation

- MRS Spring Meeting, Virtual (2021): "Elucidating Interfacial Instability in All-Solid-State Lithium Batteries from First-Principles Simulations"; L. Wan, A. M. Dive, M. Wood, K. Kim, T. Li, and B. C. Wood. Visual.

Task 3.11 – Design of Strain Free Cathode – Solid-State Electrolyte Interfaces Using Chemistry-Informed Deep Learning
(Hakim Iddir, Argonne National Laboratory)

Project Objective. The main objective of this project is to use state-of-the-art ML techniques and high-performance computing (HPC) to model complex oxide materials that will allow the team to develop cathode – SE interfaces that exhibit minimal or no strain as well as provide chemical stability at the interface between the cathode material and the SSE. A deep understanding and control of the cathode/SSE interface (including its chemical and mechanical stability) is needed to develop an effective SSB. The active cathode material changes volume during cycling, particularly at high task SOC. This volume change leads to strained interfaces triggering loss of contact and delamination, and hence reduction/elimination of electron and ion transport pathways. The increased strain could also generate cracks within the SSE, creating new paths for lithium dendrite growth channels. These structural changes degrade the electrochemical performance of the battery. Several strategies have had limited success in alleviating these drawbacks, including mixed SSE, buffer layers between the cathode and the SSE, and dopants to improve chemical stability of the interface. These approaches, although promising, could not solve both the chemical and mechanical stability of the interface. In this project, the team proposes a new approach that takes advantage of well-established ML techniques and HPC to screen for candidate dopants of high-Ni-content NMC cathodes that would both reduce the volume expansion and the chemical reactivity (mixing) at the interface, with minimum impact on electrochemical performance and energy density of the cathode.

Project Impact. Structure-property relationships are at the heart of most fundamental scientific approaches. However, the link between structure and property remains a challenge in the materials science of complex systems, such as the oxides that form battery components. In particular, the chemical and mechanical stability of the cathode-SSE interface presents a challenge to development of SSBs. High-performance DFT calculations provide the necessary framework to understand such systems. Unfortunately, given the limited number of atoms and time scales accessible by the method, along with the myriad calculations required to achieve satisfactory results, the computational cost of simulating all the possible configurations of a multicomponent oxide is prohibitive. In this work, the team augments the DFT data with ML (especially deep learning) techniques that allow them to access the large system sizes and longer time scales necessary to build thermodynamic models. They focus on understanding the nature of benchmark $Li_{1-\alpha}Ni_{1-x-y-z}Mn_xCo_yM_zO_2$ structures (M dopant, α, x, y, z < 1), their volume change with lithium content, the nature and concentration of the dopants, and chemical stability of the SSE-cathode interface. The DFT and ML approach will provide new cathode compositions that will reduce the strain of the SSE-cathode interface and hence improve its mechanical and chemical stabilities.

In this project, the team aims at developing a methodology that will allow them to explore and expand the configurational space using HPC approaches in a systematic and efficient way. The methodology will encompass DFT, AIMD, MD, and ML. The methodology will also take advantage of various software already developed at ANL and at other DOE laboratories (for example, Balsam) to automate, manage, and control the large number of calculations needed to achieve the project goal.

Approach. All calculations will be performed by spin-polarized DFT as implemented in the Vienna *ab initio* simulation package (VASP). After geometry optimization within the DFT+U framework, electronic relaxation will be performed using a single-point calculation with the hybrid functional HSE06. For production calculations, they will use the message-passing interface (MPI) parallelized version of VASP.

Exploration of the potential energy surface is needed to predict the structure of solid materials and interfaces. Such calculations are infeasible using MD or DFT calculations alone. Thankfully, the potential energy surface of a system can be represented by the sum of the energies of the local neighborhoods surrounding each atom. This enables the use of ML surrogate models trained with DFT calculations to capture the energies in local neighborhoods. The input to the ML surrogate must be a unique representation of the system under study.

Consequently, the local environment of each ion is described using a local environment descriptor that renders the atomic configuration invariant to rotations, translations, and permutations of the atoms. In recent years, several different descriptors have come to prominence with advantages and disadvantages. Once the ML surrogate is trained, the total energy and forces over all the ions of any structural configuration can be determined. Such information can be used for atomistic simulations, namely, MD and MC.

In this project, the team proposes to use the open-source DeepMDkit python/C++ package to construct the ML potential energy surface and FFs. The promise of DeepMDkit in this work is to provide near-DFT accuracy at orders-of-magnitude lower computational expense, comparable to traditional MD simulations. Efficiency in training is facilitated through integration with TensorFlow and MPI / graphics processing unit support.

One of the challenges of developing ML potential energy surface is achieving accurate predicted forces and energies across the entire configurational space, while minimizing the total number of calculations required for training. In recent years, active learning has been highlighted for its ability to target training examples most likely to improve the model quality or to achieve some other objective (that is, maximizing a predicted material property). DP-GEN, an open source python package based on DeepMDkit, implements a similar active learning scheme with HPC support, and has been employed to construct ML potential energy surface with accuracy approaching DFT and sometimes exceeding embedded atom potential for experimentally measured properties of interest. In this work, the team proposes to leverage DeepMDkit and DP-GEN to efficiently generate ML-PESs for cathode-electrolyte systems including a variety of dopants.

Out-Year Goals. One out-year goal involves developing a DFT-trained ML model on NMC/LLZO interface, ready to use for large screening of new cathodes, SSE compositions, and cathodes/SSE interfaces. A second is to provide fundamental understanding on critical parameters limiting performance and stability of the cathode/SSE interface and hence of the SSB.

Collaborations. Project collaborators include J. Croy, C. Johnson, and E. Lee from ANL Chemical Sciences and Engineering Division for the synthesis phase of the project.

Milestones

1. Determine volume changes and phase transformation during charging for $LiNiO_2$ using the developed DFT-trained ML model. (Q1, FY 2021; Completed)
2. Determine elemental segregation, volume changes, and phase transformation during charging of $Li(Ni_{0.8}Mn_{0.1}Co_{0.1})O_2$ using the developed DFT-trained ML model. (Q2, FY 2021; Data generation completed, with fine tuning of trained ML model in progress)
3. Extend solid bulk models to include surfaces and dopants. (Q3, FY 2021; Completed for NMC-811-LLZO, and dopants in progress)
4. Apply ML model to understand mechanical and chemical interactions on CEIs. (Q4, FY 2021; In progress)

Progress Report

The team finished work on the extreme Ni-rich composition $LiNiO_2$, used as the base to build the rest of their models and analysis. Based on previous *ab initio* results, they determined the phase stability in terms of Gibbs free energy for Li_xNiO_2 (x = 0.04, 0.08, 0.12, and 0.17). With the ML-FF developed last quarter, the Gibbs free energy of each phase modeled by the hybrid computational cells (O1-rich and O3-rich) and composition were each computed with respect to the reference Gibbs free energy of an Einstein solid using the adiabatic switching method. An Einstein solid was chosen as the reference because of the temperature range of interest (T = 300 K to 350 K). Further, a linear enthalpy model was assumed to capture the variation of enthalpy in this temperature range for each phase and composition. Shown in Figure 82 are the linear model enthalpies for each phase and composition in Li_xNiO_2. Uncertainty intervals represent the 95th confidence interval by fitting a Student's t-distribution to the computed enthalpy from MD NPT (constant number of atoms, pressure, and temperature) trajectories derived from an ensemble of four interatomic potentials.

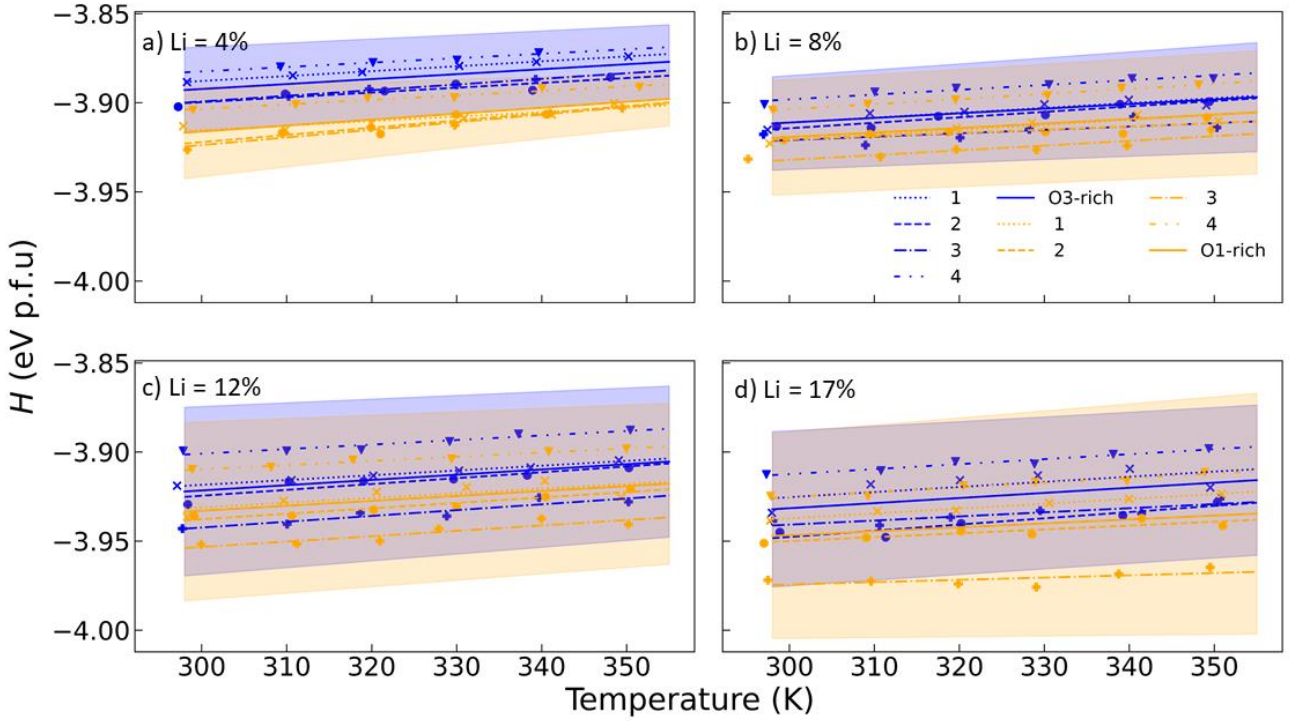

Figure 82. Enthalpies from molecular dynamics using the developed machine learning interatomic potential for the H3 (O3-rich) (blue) and H3/H4 (O1-rich) (orange) phases for lithum compositions (a) 4%, (b) 8%, (c) 12%, and (d) 17%, each over the temperature interval of 298.15 K to 350 K. Enthalpies determined for each potential are shown as 6 points in the temperature interval, with symbols with the linear fits shown as dashed or dotted lines (Potential 1: crosses, dotted lines; Potential 2: circles, dashed lines; Potential 3: pluses, dashed-dotted lines; and Potential 4: inverted triangles, doubly dotted dashed lines). The mean prediction is shown as a solid line, with the shaded region indicating the 95th confidence interval.

The Gibbs free energy of each phase and composition is obtained by thermodynamic integration of the enthalpies. This linear enthalpy corresponds to the following Gibbs free energy function, referenced to the reference Gibbs free energy at the reference temperature ($G_{ref}\ at\ T_{ref}$) for each phase and composition.

$$H\ (T) = aT + b$$

$$G_{phase,\ \ w.r.t\ G_{ref}\ at\ T_{ref}}(T) = \frac{TG_{ref}}{T_{ref}} + a\left(1 - \frac{T}{T_{ref}}\right) - bTln\left(\frac{T}{T_{ref}}\right)$$

A reference state for the Gibbs free energy for each phase and composition is required to make a consistent comparison of the Gibbs free energy between the phases and compositions considered in this study. The reference Gibbs free energy is computed at a temperature of 330 K for each of the phases following an adiabatic switching method previously applied to alloys.[1-2]

Shown in Figure 83 are the mean Gibbs free energies with their 95th confidence interval each. The uncertainty on the mean prediction (half-width of the 95th confidence interval) for the Gibbs free energy ranges from 25 meV/f.u. to 40 meV/f.u. Further bootstrap samples would reduce this uncertainty, but this was not pursued owing to computational cost associated with fitting and calculating properties for a single interatomic potential. Nonetheless, compared pair-wise, the energy differences between the same potentials for each composition and phase is also of the order of 25 meV/f.u. or less. These results show that there is uncertainty in whether O1-rich or O3-rich stacking is thermodynamically preferred. Moreover, the magnitude of the energy and associated uncertainty, 25 meV/f.u. to 40 meV/f.u., is comparable to the amount of thermal energy available through lattice vibrations per dimension over the operating temperature of 298.15 K to 350 K (k_BT = 25 to 30 meV/f.u.). Further, the team performs a Student's t-test on these Gibbs free energies. The obtained p-values indicate that the Gibbs free energies are statistically indistinguishable for the compositions x = 0.08, 0.12, and 0.17, and only distinguishable for x = 0.04, over the temperature interval of 298.15 K to 350 K. This indicates that the O1-rich stacking would be preferred for the x = 0.04 composition, while neither stacking is preferred for the compositions x = 0.08, 0.12, and 0.17.

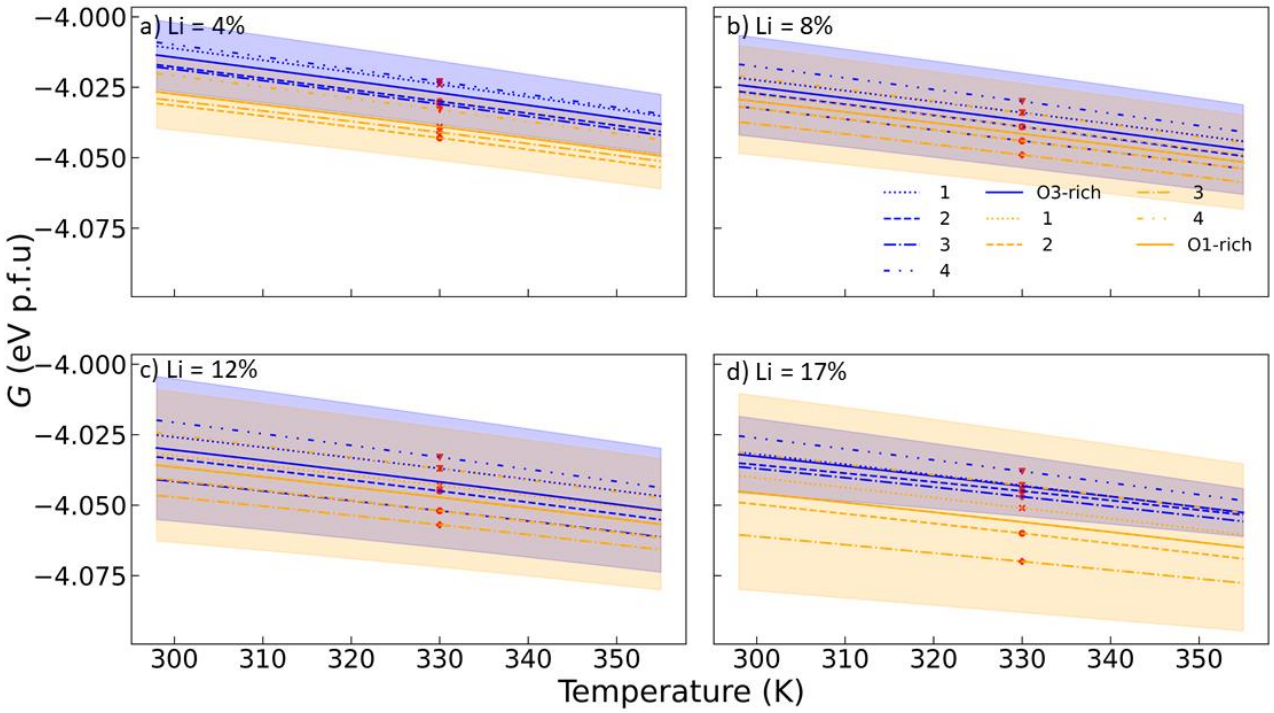

Figure 83. Gibbs free energies for the H3 (O3-rich, in blue) and H3/H4 (O1-rich, in orange) phases for (a) 4% lithium, (b) 8% lithium, (c) 12% lithium, and (d) 17% lithium for 4 potentials from the ensemble. 95th confidence intervals are indicated by the shaded region and were determined from a Student's t-distribution fit.

Additionally, the team has extended the ML model to different cathode compositions and SOCs (lithium content). The model training is being performed simultaneously in parallel simulations. The largest error is indicated currently for NMC-811. Improvement to the model is in progress. The original lithium configurations and volume of the system have been taken from DFT simulations. For instance, Figure 84 shows the energy of formation of NMC-811 as a function of the lithium content. For each composition, several lithium configurations have been found. Based on these configurations ML potentials are being fit. After the fitting the

lithium distribution for each composition will be explored further. For each calculation, they will get a volume change that will lead the search for a composition that minimizes strains at the interface.

The potential has also been extended to cathode-LLZO interfaces. The interface potential will inform about any effect of the chemical interaction that could affect the mechanical behavior of the system—in a positive or negative manner. Figure 85 shows a sample simulation cell of the LNO-LLZO interface. This cell contains a whole LLZO unit cell forming an interface between the low energy LLZO (001) facet and LNO (104) facet oriented to minimize the interfacial strain. This interface is suitable for potential training purposes. A ML-FF was fit to a training set comprising 20 fs AIMD trajectories of the 432 atom NMC-811 bulk configurations, 496 atom fully lithiated computational cells of LNO-LLZO with the La-termination, and 467 atom 40% lithium computational cells of LNO-LLZO. The potential was fit using a cutoff radius of 7 Å for local atomic environment interactions. Parity plots of the forces are shown below in Figure 85. Stable NVE (constant number, volume, and energy) MD (conserving total energy) for a supercell of the interface (1988 atoms in Figure 84) could be performed for 30 fs. The goal is to perform stable MD with such models including dopants to determine Gibbs free energies for assessing phase stability and volumetric strain on delithiation. An active learning framework will be deployed to improve this potential to this end.

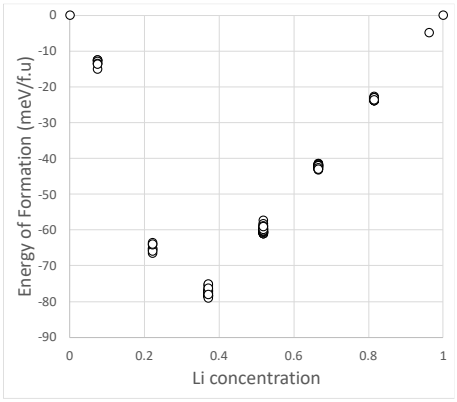

Figure 84. NMC-811 energy of formation as a function of the lithium content.

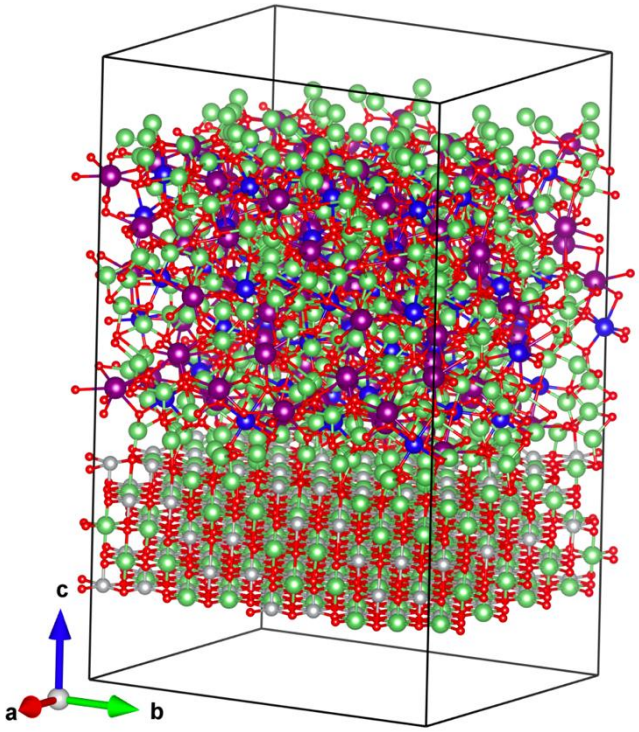

Figure 85. Example size of LLZO-LNO interface to be studied in this work, currently showing stable molecular dynamics (conserving total energy) for 30 fs. Green, gray, purple, blue, and red spheres represent lithium, nickel, lanthanum, zirconium, and oxygen, respectively.

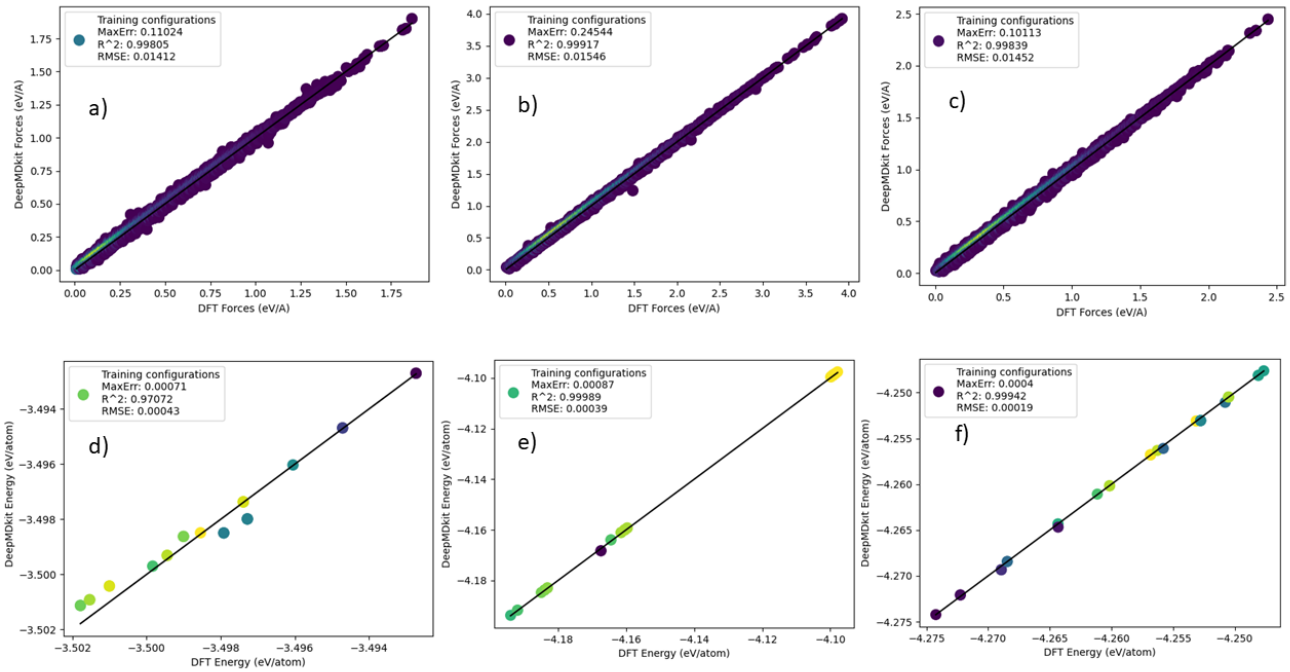

Figure 86. Parity plots of machine learning force field for forces and energies for (a/d) NMC-811, (b/e) LLZO-LNO interface fully lithiated, and (c/f) LLZO-LNO interface delithiated down to 40% lithium.

References

[1] Kirkwood, J. G. "Statistical Mechanics of Fluid Mixtures." *Journal of Chemical Physic* 3, No. 5 (1935): 300–313. doi: 10.1063/1.1749657.

[2] Baskes, M. I., K. Muralidharan, M. Stan, S. M. Valone, and F. J. Cherne. "Using the Modified Embedded-Atom Method to Calculate the Properties of Pu-Ga Alloys." *Journal of The Minerals, Metals & Materials Society* 55, No. 9 (2003): 41–50. doi: 10.1007/s11837-003-0029-7.

Patents/Publications/Presentations

The project has no patents, publications, or presentations to report this quarter.

Task 3.12 – Tackling Solid-State Electrochemical Interfaces from Structure to Function Utilizing High-Performance Computing and Machine-Learning Tools

(Shinjae Yoo, Feng Wang, and Deyu Lu, Brookhaven National Laboratory; Nongnuch Artrith and Alexander Urban, Columbia University)

Project Objective. This project aims at elucidating the structural evolution and other dynamic properties of the interphases at the SSIs in SSBs under processing and electrochemical cycling conditions that strongly impact cell performance. By leveraging synergies of first-principles theory, HPC, ML, and computational/experimental spectroscopy, this project involves a comprehensive investigation of SE systems and SSIs that may enable the practical use of lithium anodes and high-nickel NMC cathodes in SSBs. Specific project objectives are as follows: (1) develop realistic atomic-scale structure models of the heterostructural SSIs, (2) determine the impact of structural evolution on the stability and transport properties of the SSIs, and (3) identify the coating/doping chemistry that may stabilize SSIs during formation and electrochemical cycling.

Project Impact. Interfacial properties and the dynamical evolution of interphase structures are crucial for the stability and performance of SSBs. This project will lead to fundamental understanding of current materials limits and will identify key materials parameters for optimizing the performance of SSBs. By corroborating atomic-scale theory with experiment, the project will identify structure–property relationships of the heterostructural SSIs in SSB systems that are relevant for EVs. The outcomes of this project will therefore accelerate development of high-energy-density, safe SSBs for EVs.

Approach. Accurate ML potentials will be trained on an extensive database from DFT calculations to simulate the structure evolution and electrochemical properties of the SSIs. Using a second ML model, key physical descriptors will be extracted from EELS and XAS measurements. This spectral fingerprinting will enable the automated interpretation of spectroscopy measurements, thereby bridging between atomistic modeling and experiment. An experimental platform will be developed to integrate experimental/computational spectroscopy and modeling of SSIs. In combination, the two ML models and the spectroscopic data will facilitate the construction of a physics-based model to unravel the structure-property relationships of the SSIs.

Out-Year Goals. The project will progress toward establishing dynamic composition-structure-property relationships for interface stability and transport within and across the electrochemical SSIs in SSBs. The ML approach will be further developed to a general model for thermodynamic and transport properties of dynamic heterostructural electrochemical interfaces and will eventually be applied to the practical SSB systems.

Collaborations. The project is collaborating with Y. Du at BNL.

Milestones

1. Complete mapping of the phase diagram and structure-stability-conductivity relationships in the glass/ceramic (*gc*) Li_2S–P_2S_5 (LPS) system. (Q1, FY 2021; Completed)
2. Characterize initial stages of the interfacial reaction of *gc*-LPS with lithium metal using ML-augmented DFT and XAS spectroscopy. (Q2, FY 2021; Completed)
3. Correlate characteristic structural motifs of *gc*-LPS and the *gc*-LPS/Li interface with XAS spectral features using ML. (Q3, FY 2021; Completed).
4. Determine formation and evolution mechanisms of *gc*-LPS/Li interphases using XAS measurements and ML models. (Q4, FY 2021; In progress)

Progress Report

In previous quarters, atomic structure (Q1) and sulfur K-edge XANES spectral (Q2) databases were developed for *gc* $(Li_2S)_x(P_2S_5)_{1-x}$ (*gc*-LPS) materials. The structure and spectral databases consist of ~ 2.5 k symmetrically inequivalent sulfur absorbers sampled from 18 crystalline and 47 amorphous structures. This quarter, those established atomic structure models and the corresponding simulated XANES spectra were used to develop ML models for correlating characteristic structural motifs of the sulfur sites with their XANES spectral features in *gc*-LPS. The progress this quarter lays the groundwork for investigating the formation and dynamic evolution of the *gc*-LPS/Li interface through a combination of experimental measurements, data analysis, and ML modeling.

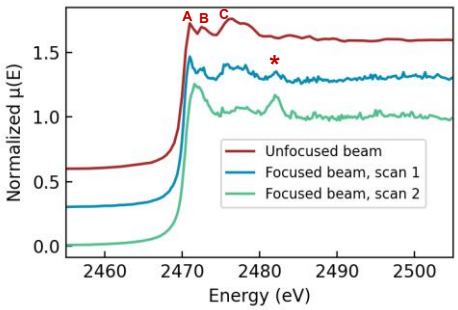

Figure 87. X-ray absorption spectra of β-LPS. From top to bottom: data taken from a pellet with an unfocused beam (red), data from a powder sample with a focused beam (blue), and the 2nd scan from the same sample (green).

Tender XAS Spectroscopy of *gc*-LPS. XAS measurements were taken from pristine β-phase Li_3PS_4 (β-LPS) at the NSLS-II TES (8-BM) beamline. Since the attenuation length of LPS is only about 10 μm near the sulfur K-edge (~ 2.47 keV), XAS spectra were measured in fluorescence mode. With optimization of the sample preparation and beam focus, reliable spectra of the sulfur K-edge with high statistics were recently measured. One representative spectrum is presented in Figure 87 (top; in red), showing three characteristic peaks associated with the sulfur K-edge XAS of β-LPS (labeled with A, B, and C). Specifically, LPS electrolyte was pressed into a pellet to increase the loading density of the sample. An unfocused beam (2.5 mm in diameter) was used to sample a larger area with relatively smaller area illumination. Under these conditions, identical spectra were obtained from consecutive scans, without observable radiation damage. In previous experiments, a focused X-ray beam was found to induce oxidation of LPS, as shown by a characteristic peak at ~ 2482 eV (indicated by *) present from the 1st scan and becoming more pronounced in the 2nd scan (Figure 87, lower two curves). The focused beam also caused rapid damage, as evidenced by the increased peak intensities at ~2472 eV and ~2482 eV between the 1st and 2nd scans. With the optimized experimental setup that avoids beam damage-related issues, high-quality sulfur K-edge XAS spectra were obtained from pristine LPS with an unfocused tender X-ray beam, giving the team confidence in using them for benchmarking DFT calculations and ML models, as presented here.

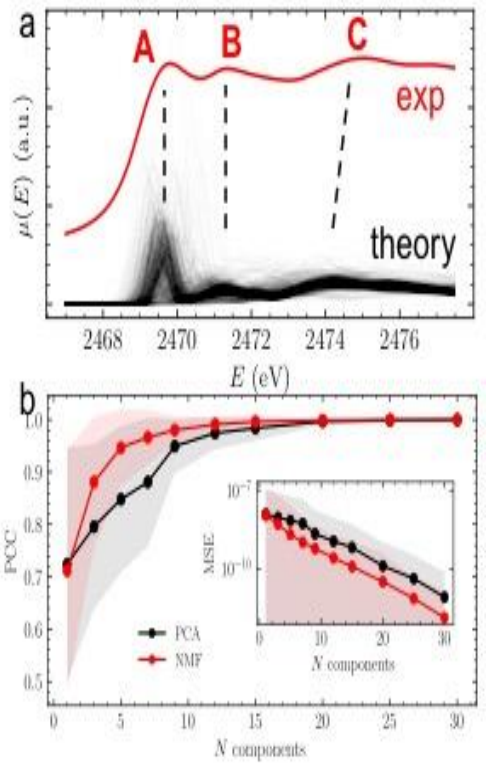

Figure 88. (a) Experimental β-LPS spectrum from the unfocused beam (only the X-ray absorption near-edge spectroscopy, or XANES, region and smoothed) and 1000 randomly chosen simulated sulfur K-edge XANES spectra. (b) Pearson correlation coefficient (PCC) and pointwise mean squared error (MSE) spectrum reconstruction errors plotted for entire dataset for both principal component analysis and nonnegative matrix factorization decompositions. The error bar corresponds to ± 1 standard.

Spectral Data Analysis. As shown in Figure 88a, the simulated sulfur K-edge XANES spectra overall also contains three key features: a main edge (A) at about 2469.5 eV, a lower peak (B) about 2471.5 eV, and a broad peak (C) around 2474 eV. These three peaks align well with those in the project's experimental β-*ex situ* LPS spectrum (Figure 87; in red). It is well-known that XANES is highly dependent on the local environment surrounding the absorbing atom. For example, the main K-edge absorption feature in *gc*-LPS compounds is known to correspond with a core-to-3p σ^* excitation,[1] which is sensitive to the electron

density surrounding the absorbing sulfur atom, and therefore to the particular local environment of that absorber.[2] Before proceeding with more complicated data analysis techniques, the team examined the databases in terms of the structural descriptors and the degree of the spectral complexity.

Structural Descriptors. They analyzed the atom-resolved coordination number of all symmetrically inequivalent absorbing sulfur atoms in the structural database, using Pymatgen with an empirical 3 Å for nearest neighbor distance cutoff.[3] The vast majority of relevant sulfur sites in *gc*-LPS are characterized by sulfur atoms with exactly one phosphorous neighbor (96.8%), and by sulfur atoms without sulfur neighbors (98.1%). The distribution of lithium neighbors exhibits a larger variation. Next, they correlate statistically relevant structural motifs with spectral intensity profiles. In particular, they have developed ML models to predict S-P bond lengths from the sulfur K-edge XANES spectra. In the future, they plan to further study the spectral signatures correlated to, for example, the lithium CN and local sulfur polyhedral arrangement. The ML models developed for local structure inference will be used in later studies for interpreting experimental sulfur K-edge spectra from sulfide electrolytes.

Dimensionality Reduction. The team examined the number of distinct features in the spectral database using linear analysis methods, including principal component analysis (PCA) and nonnegative matrix factorization (NMF). PCA involves diagonalizing the covariance matrix of the spectral data and using the eigenvectors as kernels for projecting each spectrum into a reduced-dimensional space. NMF is an iterative method that can decompose a collection of spectra into nonnegative weights and components (or kernels). The team plots the average Pearson correlation coefficient (PCC) and pointwise mean squared error (MSE) in Figure 88b, demonstrating that only roughly 15-20 components are required to sufficiently capture the variance in the spectral database.

ML S-P Bond Lengths from XANES Spectra. The distribution of bond lengths in the database is shown in Figure 89, which confirms sufficient sample diversity for statistically relevant analysis. Each data point is "labeled" by its S-P bond length. The team chose random forests (RFs), which are ensembles of decision trees, as a boilerplate modeling paradigm to test whether a non-linear model can successfully map XAS to S-P bond lengths, due to their speed, ease of implementation, and ability to easily interpret feature importance. They use scikit-learn for all model implementations and an 80/20 train/test split.[4] Only the results on the testing set are reported. Based on the distribution in Figure 89, they aim for a threshold of 0.02 Å accuracy in their predictions to achieve sufficient resolution for the variance in the dataset. Using a trained RF regressor with 100 decision trees at maximum depth 10, they achieve 0.87 accuracy with respect to the threshold of 0.02 Å on the pointwise dataset. A breakdown of these testing set results with respect to binned bond length and spectrum featurization is shown in Table 4. The results highlight that the RF models perform well in most cases, regardless of the S-P bond length, except for the ranges $[2, 2.02)$ and > 2.1 where the database only has a small amount of data.

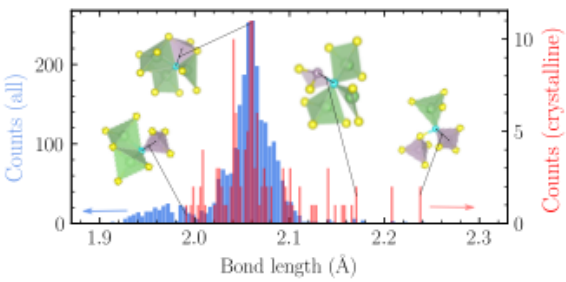

Figure 89. Distribution of S-P bond lengths in both the full and the crystalline-only dataset with exemplary S-P bonds (and their local environments) shown. Sulfur is yellow (absorbers are cyan), lithium is green, and phosphorous is purple.

Table 4. Overall accuracy of random forests (RF) models trained and tested on pointwise data (full spectrum as input), and nonnegative matrix factorization (NMF) and principal component analysis (PCA) coefficients. Overall accuracy represents percentage of bond lengths classified under the 0.02 Å threshold. Values in parentheses indicate bond length-resolved mean absolute error and uncertainty (standard error) in the last digit (with poor results greater than the threshold highlighted in red).

Model	Accuracy	$[0, 1.95)$	$[1.95, 2)$	$[2, 2.02)$	$[2.02, 2.04$	$[2.04, 2.06)$	$[2.06, 2.08)$	$[2.08, 2.1)$	$[2.1, \infty)$
RF Pointwise	0.87	0.011(5)	0.016(4)	0.029(4)	0.013(1)	0.007(1)	0.006(0)	0.011(2)	0.041(6)
RF NMF	0.87	0.026(6)	0.014(3)	0.028(5)	0.014(1)	0.007(0)	0.007(0)	0.013(2)	0.051(9)
RF PCA	0.85	0.024(8)	0.022(4)	0.026(4)	0.011(1)	0.007(0)	0.008(1)	0.013(2)	0.046(7)

Finally, the team analyzed the importance of each feature (that is, each location on the energy grid) via random feature permutation. This is achieved by training the RF on the training set, and then scrambling each feature in the testing set and observing its impact on baseline performance. Results of this analysis indicate that almost all important features of the spectrum are located in a single eV region, between 2470 eV and 2472 eV, as shown in Figure 90. Because this energy range overlaps with the second peak in the sulfur K-edge XANES, the feature importance analysis suggests the intensity of the second peak can be used as a spectral signature of long S-P bond length.

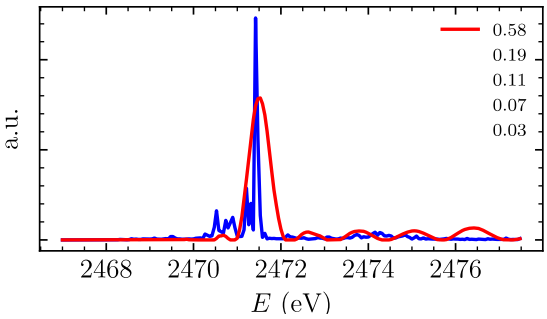

Figure 90. Feature importance as ranked by the pointwise (blue) and nonnegative matrix factorization (NMF, red) random forests models overlaid on the 100 randomly selected sulfur K-edge X-ay absorption near-edge spectra (black). The blue line shows the relative pointwise feature importance, and the red lines show the five most important NMF kernels, with their relative importance shown in the legend.

In summary, high-quality sulfur K-edge XAS spectra were measured from β-LPS under optimized experimental conditions. With the new spectral data, along with previously established structure and spectral databases, ML models were developed for correlating characteristic structural motifs of the sulfur sites with their XANES spectral features in *gc*-LPS. The identified spectrum-structure correlation will be used for investigating the formation and dynamic evolution of the *gc*-LPS/Li interface through *in situ* / *ex situ* tender XAS spectroscopy, as to be reported next quarter.

References

[1] Fleet, M. E. "XANES Spectroscopy of Sulfur in Earth Materials." *The Canadian Mineralogist* 43, No. 6 (2005): 1811–1838.

[2] Dietrich, C., R. Koerver, M. W. Gaultois, G. Kieslich, G. Cibin, J. Janek, and W. G. Zeier. "Spectroscopic Characterization of Lithium Thiophosphates by XPS and XAS–A Model to Help Monitor Interfacial Reactions in All-Solid-State Batteries." *Physical Chemistry Chemical Phy*sics 20, No. 30 (2018): 20088–20095.

[3] Ong, S. P., W. D. Richards, A. Jain, G. Hautier, M. Kocher, S. Cholia, D. Gunter, V. L. Chevrier, K. A. Persson, and G. Ceder. "Python Materials Genomics (Pymatgen): A Robust, Open-Source Python Library for Materials Analysis." *Computational Materials Science* 68 (2013): 314–319.

[4] Pedregosa, F., G. Varoquaux, A. Gramfort, V. Michel, B. Thirion, O. Grisel, M. Blondel, P. Prettenhofer, R. Weiss, and V. Dubourg. "Scikit-Learn: Machine Learning in Python." *Journal of Machine Learning Research* 12 (2011): 2825–2830.

Patents/Publications/Presentations

The project has no patents, publications, or presentations to report this quarter.

TASK 4 – METALLIC LITHIUM

Team Lead: Jagjit Nanda, Oak Ridge National Laboratory

Summary and Highlights

The use of a metallic lithium anode is required for advanced battery chemistries like Li-ion, Li-air, and Li-S to realize dramatic improvements in energy density, vehicle range, cost requirements, and safety. However, use of metallic lithium with liquid and solid polymer or ceramic electrolytes has so far been limited due to parasitic SEI reactions and dendrite formation that eventually short circuit the battery. Adding excess lithium to compensate for such losses negates the high-energy-density advantage of a Li-metal anode and leads to further concern for battery safety. For a long lifetime and safe anode, it is essential that no lithium capacity is lost either (1) to physical isolation by roughening, dendrites, or delamination processes, or (2) to chemical isolation from side reactions. The key risk, and current limitation, for this technology is the gradual loss of lithium over the cycle life of the battery.

BMR, Battery500, and other DOE programs are addressing this challenge with many innovative and diverse approaches. Key to all is the need for a much deeper analysis of the degradation processes and new strategies to maintain a dense, fully connected lithium and a dendrite-free electrolyte so that materials can be engineered to fulfill the target performance metrics for EV application, namely 1000 cycles and a 15-year lifetime, with adequate pulse power. Projecting the performance required in terms of just the lithium anode, this requires a high rate of lithium deposition and stripping reactions, specifically about 30 µm of lithium per cycle, with pulse rates up to 10 and 20 nm/s (15 mA/cm^2) charge and discharge, respectively, with little or no excess lithium inventory. This is daunting in the total mass and rate of material transport that must be achieved without failures.

The efficient and safe use of metallic lithium for rechargeable batteries is then a great challenge, and one that has eluded R&D efforts for years. This project takes a broad look at this challenge for both SSBs and batteries continuing to use LEs. Electrolytes reported here include nonflammable liquid solutions, gel type polymer-in-a-salt, composites of ceramic polymer phases, common and novel PEs, and both oxide and sulfide ceramic electrolytes. In most studies, the electrolyte phases were modified by addition of plasticizers or interface coatings to improve transport, stability, and ease of manufacturing. Researchers are typically working toward cycling of full cells with relevant and balanced capacities for the lithium anode and cathode using measures of CE, interface resistance, and post-cycling observation of the disassembled cell components to assess stability of the Li-metal anode and chosen electrolyte.

Highlights

The highlights for this quarter are as follows:

- The ORNL team (X. C. Chen and N. Dudney) has fabricated thin 3D interconnected Ohara LICGC™ ceramic electrolyte network backfilled with crosslinked PEO (xPEO) PE. SSB full cell was fabricated and tested integrating with NMC cathodes and thin Li-metal.
- The ANL team (S. Tepavcevick and L. A. Curtiss) reports using Li_3BO_3 (LBO) as a sintering aid to improve densification and reduce the GB resistance of garnet SE-LLZO. EIS and microstructural characterization were performed to determine how LBO impacts overall conductivity of the electrolyte.
- The LLNL team (J. Yi) fabricated and tested an ASSB by filling a CPE ink with 30 wt% Li-La-Zr-Ta-O (LLZTO) in 1:8:1 PEG diacrylate (PEGDA) / PEG methacrylate (PEGMA) / PEO in a 3D-printed LFP cathode. ASSB showed reasonable capacity retention for few cycles at 1C rate.

Task 4.1 – Lithium Dendrite Prevention for Lithium Batteries (Wu Xu and Ji-Guang Zhang, Pacific Northwest National Laboratory)

Project Objective. The objective of this project is to enable lithium metal to be used as an effective anode in rechargeable Li-metal batteries with good stability and high safety. The investigation this fiscal year will focus on two aspects. First, develop nonflammable polymer composite electrolytes (NPCEs) and investigate effects of various flame-retardant solvents and polymers on ionic conductivity, lithium CE, lithium anode morphology, flammability, and battery performances in terms of long-term cycling stability and rate capability at various temperatures. Second, establish correlation of morphologies of SEI layer and deposited lithium with electrolyte formulation, current density, and lithium deposition/stripping cycling.

Project Impact. Lithium metal is an ideal anode material for high-energy-density rechargeable batteries; however, the application of Li-metal anode is hindered by safety concerns and short cycle life. The safety concerns of Li-metal batteries mainly arise from lithium dendrite growth and electrolyte flammability, while the short cycle life is related to low lithium CE. Although much progress has been achieved in suppressing lithium dendrites and increasing lithium CE in LEs, most LEs are flammable and may pose safety hazards in case of extreme conditions. Therefore, development of electrolytes with improved safety for advanced battery chemistry is imperative. An ideal electrolyte for Li-metal anode should not only suppress lithium dendrite growth and have high CE, but also be intrinsically nonflammable. This fiscal year, the team will develop NPCEs that have high lithium CE, suppress lithium dendrites, and are stable with high-voltage cathodes. The success of this project will increase safety of Li-metal and Li-ion batteries and accelerate market acceptance of EVs, as required by the EV Everywhere Grand Challenge.

Approach. The approach will encompass several areas: (1) develop NPCEs that can enable long-term cycling with significantly improved safety features of Li-metal batteries, (2) develop current collectors with 3D structure for Li-metal anode to suppress lithium dendrite growth, increase lithium utilization, and extend cycle life of Li-metal batteries, and (3) conduct mechanistic studies on lithium deposition behavior to lay groundwork for future improvement of electrolytes (salts, solvents, and additives) for Li-metal batteries.

Out-Year Goals. The long-term goal of the proposed work is to enable Li-metal and Li-ion batteries with a specific energy of > 350 Wh/kg (in cell level), 1000 deep-discharge cycles, 15-year calendar life, and less than 20% capacity fade over a 10-year span to meet the goal of EV Everywhere Grand Challenge.

Collaborations. This project collaborates with C. Wang of PNNL on characterization by TEM/SEM; K. Xu and M. Ding of U. S. Army Research Laboratory (ARL) on DSC measurements; and B. Polzin at ANL on coated electrode sampling.

Milestones

1. Evaluate properties of NPCEs and cycling performance of Li||NMC cells using the NPCE. (Q1, FY 2021; Completed, December 31, 2020)
2. Elucidate influencing factors on lithium deposition behavior by *in situ* AFM. (Q2, FY 2021; Completed)
3. Fabricate 3D-structured current collectors and characterize their physical properties. (Q3, FY 2021; Completed)
4. Evaluate influence of 3D-structured current collector on Li-metal deposition behavior and cycling performance of Li||NMC cells. (Q4, FY 2021)

Progress Report

Last quarter, the 3D porous polyimide membrane was prepared via a template/etching approach. The polyimide membrane (11-μm thick) was combined with a layer of thin PE separator (7 μm) to form a dual-layer membrane and used in Li||NMC-622 cells, where the polyimide layer exhibits a highly uniform pore size distribution to regulate the Li^+ flow. The cells with two different orientations of the dual-layer separator were investigated. In one configuration, the polyimide layer was in direct contact with the Li-metal electrode. In a reversed configuration, the polyimide layer was in direct contact with NMC-622 electrode. The long-term cycling performances of the Li||NMC-622 cells using the forward composite (polyimide/PE) and the reversed composite (PE/polyimide) separators were investigated. As a reference, the cells with a single-layer PE (20 μm) separator were also evaluated.

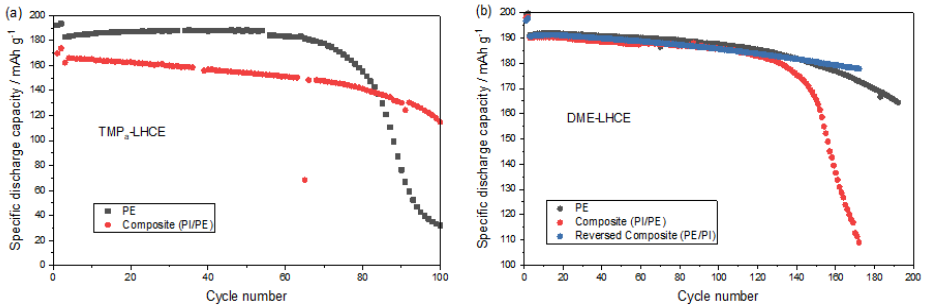

Figure 91. (a) Cycling performance of Li||NMC-622 cells using the combinations of TMP_a-based localized high concentration electrolyte [LHCE (LiFSI:TMP_a:TTE = 1:1.4:3 by mol.)] and two different separators. (b) Cycling performance of Li||NMC-622 cells using the combinations of DME-based LHCE (LiFSI:TMP_a:TTE = 1:1.1:3 by mol.) and three different separators. Voltage range: 2.5-4.4 V; rates: C/10 for charging and C/5 for discharging, where 1C = 4.2 mA cm^{-2}.

The influence of the separators was first evaluated with the TMP_a-based localized high concentration electrolytes (LHCE). As shown in Figure 91a, although the cell with the composite separator (polyimide/PE) exhibits a lower specific capacity than the cell using the single-layer PE separator, it shows higher capacity than the single-layer PE cell after 85 cycles since the cell using the single-layer PE suffers rapid capacity loss starting at about the 70^{th} cycle. However, both cells exhibit relatively fast capacity fading, which could be due to the intrinsic incompatibility between the TMP_a-LHCE and the Li||NMC-622 cell chemistry. Therefore, the influence of the separators on the cycling performance of Li||NMC-622 cells was further evaluated with the DME-based LHCE. As shown in Figure 91b, cells using the composite separator exhibit an inferior cycling performance to the single-layer PE cells. It could be probably assigned to the chemical incompatibility between polyimide and lithium. However, when the composite separator is reversed in the cells, the capacity decay is significantly alleviated. After ~ 160 cycles, cells using the reversed composite separator outperform the single-layer PE cells. The mechanism behind this phenomenon will be studied in the next work.

In addition, the lithium growth behaviors in different electrolytes were evaluated with *in situ* AFM in the previous report. Based on the *in situ* AFM results, the growth kinetics can be obtained. As shown in Figure 92a, the introduction of different additives has a substantial influence over the nucleation density in the early stage of lithium deposition. Figure 92b shows the voltammetry of the *in situ* AFM cells during the lithium deposition process, from which the overpotential, η, can be obtained. The dependence of particle size over η^{-1} and the natural logarithm of surface energy over η^{-2} can also be obtained (Figure 92c-d, respectively). The interpretations of these dependences will be further analyzed

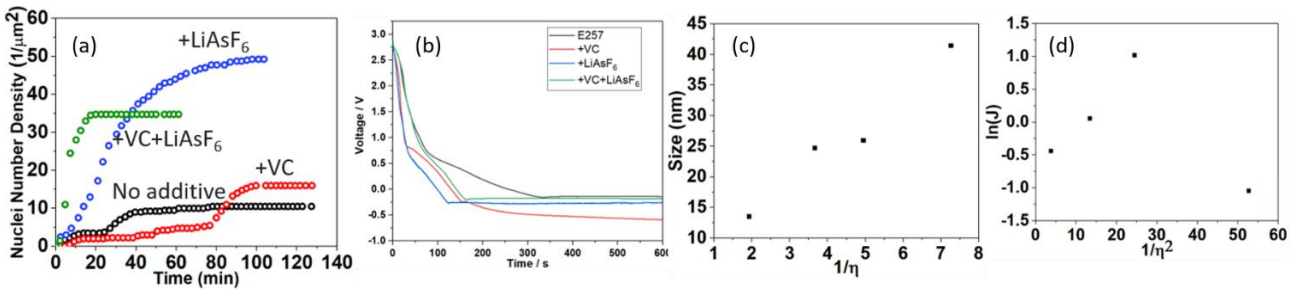

Figure 92. (a) Lithium nuclei density on copper electrodes as a function of deposition time in 1 mol L^{-1} $LiPF_6$ in EC:EMC = 3:7 (by wt) with different additives. (b) Voltammetry of the *in situ* atomic force microscopy cells using studied electrolytes. (c) Dependence of nuclei size on η^{-1} and (d) dependence of ln(surface energy) on η^{-2}.

Patents/Publications/Presentations

Publications

- Jia, H., and W. Xu.* "Nonflammable Nonaqueous Electrolytes for Lithium Batteries." *Current Opinion in Electrochemistry* 30 (2021): 100781. doi: 10.1016/j.coelec.2021.100781.
- Wu, H., P. Gao, H. Jia, L. Zou, L. Zhang, X. Cao, M. H. Engelhard, M. E. Bowden, M. S. Ding, D. Hu, S. D. Burton, K. Xu, C. Wang, J-G. Zhang,* and W. Xu.* "A Polymer-in-Salt Electrolyte with Enhanced Oxidative Stability for Lithium Metal Polymer Batteries." *ACS Applied Materials & Interfaces* 13, No. 27 (2021): 31583–31593. doi: 10.1021/acsami.1c04637.
- Gao, P., H. Wu, X. Zhang, H. Jia, J-M. Kim, M. H. Engelhard, C. Niu, Z. Xu, J-G. Zhang, and W. Xu.* "Optimization of Magnesium-Doped Lithium Metal Anode for High Performance Lithium Metal Batteries through Modeling and Experiment." *Angewandte Chemie International Edition* 133, No. 30 (2021): 16642–16649. doi: 10.1002/anie.202103344.

Presentations

- DOE VTO Annual Merit Review Meeting, Virtual (June 21–24, 2021): "Lithium Dendrite Prevention for Lithium Batteries"; W. Xu and J-G. Zhang. Poster.
- 239th ECS Meeting, Digital Meeting (May 30 – June 3, 2021): "Optimization of Magnesium-Doped Lithium Metal Anode for Lithium Metal Batteries: Simulation and Experiment"; P. Gao, H. Wu, X. Zhang, H. Jia, J-M. Kim, M. H. Engelhard, C. Niu, Z. Xu, J-G. Zhang, and W. Xu.

Task 4.2 – Composite Electrolytes to Stabilize Metallic Lithium Anodes (Nancy Dudney and X. Chelsea Chen, Oak Ridge National Laboratory)

Project Objective. The project has several objectives: (1) prepare novel polymer and ceramic electrolyte materials that can work together to achieve thin membranes that have the unique combination of electrochemical and mechanical properties required for practical manufacturing and to stabilize the metallic lithium anode for good power performance and long cycle life, (2) identify key features of the composite composition, architecture, and fabrication that optimize performance, and (3) fabricate thin electrolyte membranes to use with a thin metallic lithium anode that provides good power performance and long cycle life.

Project Impact. A stable lithium anode is critical to achieve high energy density with excellent safety, lifetime, and cycling efficiency. This study will identify key design strategies that should be used to prepare composite electrolytes to meet the challenging combination of physical, chemical, and manufacturing requirements to protect and stabilize the Li-metal anode for advanced batteries. By utilizing well characterized and controlled component phases, design rules developed for composite structures will be generally applicable toward substitution of alternative and improved SE component phases as they become available. Success will enable DOE technical targets: 500-700 Wh/kg, 3000-5000 deep discharge cycles, and robust operation.

Approach. This project seeks to develop practical SEs to provide stable, long-lived protection for Li-metal anode. Current electrolytes have serious challenges when used alone: oxide ceramics are brittle, sulfide ceramics are air-sensitive, polymers are too resistive and soft, and many electrolytes react with lithium. Composites provide a clear route to address these issues. While work continues to emphasize study of ceramic electrolyte / PE interfaces, this effort has expanded to address the following: (1) practical processing routes to fabricate full batteries using better composite electrolytes with a composite cathode and thin Li-metal anode, and (2) introduction of alternative polymer and ceramic phases to replace well-known model materials and develop improved composite electrolytes. In addition to solid-state devices, hybrid batteries are investigated using a fluid or gel catholyte within the porous cathode. Coatings have also been employed to stabilize electrode interfaces. These directions increase complexity of the studies, but are needed to improve cycling stability and rate performance and to advance practical implementation of the SE and Li-anode technology.

Out-Year Goal. The goal is to use advanced manufacturing processes where the architecture of the composite membrane can be developed and tailored to maximize performance and cost-effective manufacturing.

Collaborations. Work is conducted by B. Armstrong, S. Kalnaus, A. Ullman, and X. C. Chen. Ceramic electrolyte powders (LICGC™) are obtained from Ohara Corporation. J. Libera from ANL provided a large quantity of LLZO powders.

Milestones

1. Sinter and characterize porous LLZO network by different processes. (Q1, FY 2021; 80% completed)
2. Compare polymer-LLZO ceramic composites with four different ceramic loadings. (Q2, FY 2021; 60% completed)
3. Elucidate the Li-ion path through at least two distinct polymer-ceramic composites. (Q3, FY 2021, Completed)
4. Measure Li^+ transference number with at least two different anion receptors. (Q4, FY 2021; 80% completed)

Progress Report

Fabrication and Cell Integration of Self-Standing 3D Interconnected Composite Electrolyte

This quarter, the team explored the fabrication and cell-integration of self-standing composite polymer electrolyte sheets composed of porous, 3D interconnected Ohara LICGC™ ceramic electrolyte network that is backfilled with xPEO PE. Two unsupported LICGC™ tapes were cast using two starting averaging particle sizes (D50 of 0.4 and 1 µm), while solids loadings and wet coating thickness (doctor blade height) were held constant at 22 vol% and 20 mils (508 µm), respectively. These were fabricated using a non-aqueous solvent-based tape-casting method using a poly(vinyl butyral) binder system. Some agglomeration of the LICGC™ particles was evident in the final, dried tapes. The agglomeration was worse in the tape containing the 0.4 µm particles. An attempt at tape-casting LLZO was also made, but it was unsuccessful. Gelation occurred during the slurry making process. Further optimization of the binder composition and milling processes to eliminate the agglomeration and gelation is under way. For the rest of the study, the tape containing 1 µm size LICGC™ particles was used.

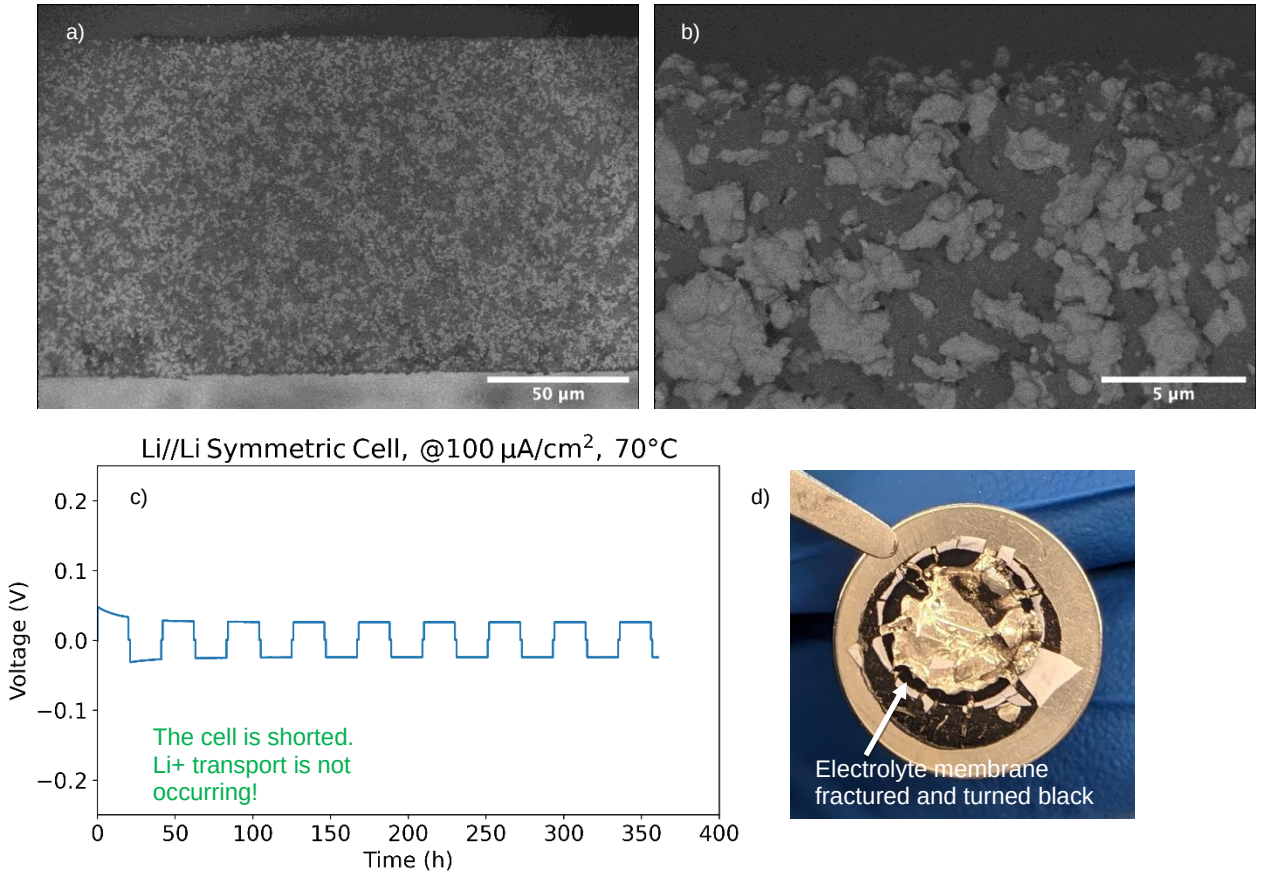

Figure 93. Characterization and cycling performance of a ~ 140-µm-thick *unplasticized* xPEO-Ohara (3D interconnected) composite electrolyte. (a-b) Cross-section scanning electron microscopy of the 3D interconnected Ohara ceramic tape, backfilled with *unplasticized* xPEO-based polymer electrolyte. Absence of a polymer layer on the surface of the composite-electrolyte membrane can be seen in the zoomed-in image. (c) Li//Li symmetric cell cycling of this electrolyte, where the extremely flat and unchanged voltage profile indicated the cell to be shorted. (d) Photograph of another symmetric cell with the same electrolyte that was shorted.

The effect of the presence or absence of liquid plasticizer on electrochemical performance and handleability was also studied. Figure 93a shows cross-section SEM images of such a typical composite electrolyte tape in "dry" form, that is, without any plasticizer. The brighter phase is the ceramic, whereas the gray-colored phase is the polymer. Complete infiltration of the ceramic backbone with polymer can be observed. Based on weight

calculations before and after infiltration, ~ 78% of the porosity has been filled by the polymer. A close-up of the surface reveals no apparent surface film of excessive/non-infiltrated polymer (Figure 93b). This is not completely desired, as the surface polymer layer can help improve contact with the Li-metal electrode as well as prevent reaction of the ceramic phase with lithium metal, which is known be a self-propagating reaction. Several Li//Li symmetric cells were fabricated with this electrolyte; however, poor mechanical strength (brittleness) of the film as well as lack of a protective polymeric surface layer caused all cells to fail due to shorting. A hard short occurred if fracture of the composite electrolyte membrane occurred during cell crimping; a soft short occurred if the fracture did not occur, but reaction of ceramic phase with the lithium metal caused the formation of electronically conductive phase. Figure 93c shows the voltage profile of a symmetric cell with a soft short, where extremely flat voltage profile during cycling was observed. Figure 93d shows another symmetric cell after de-crimping, where the composite electrolyte can be seen to have been fractured and turned black due to reaction with lithium.

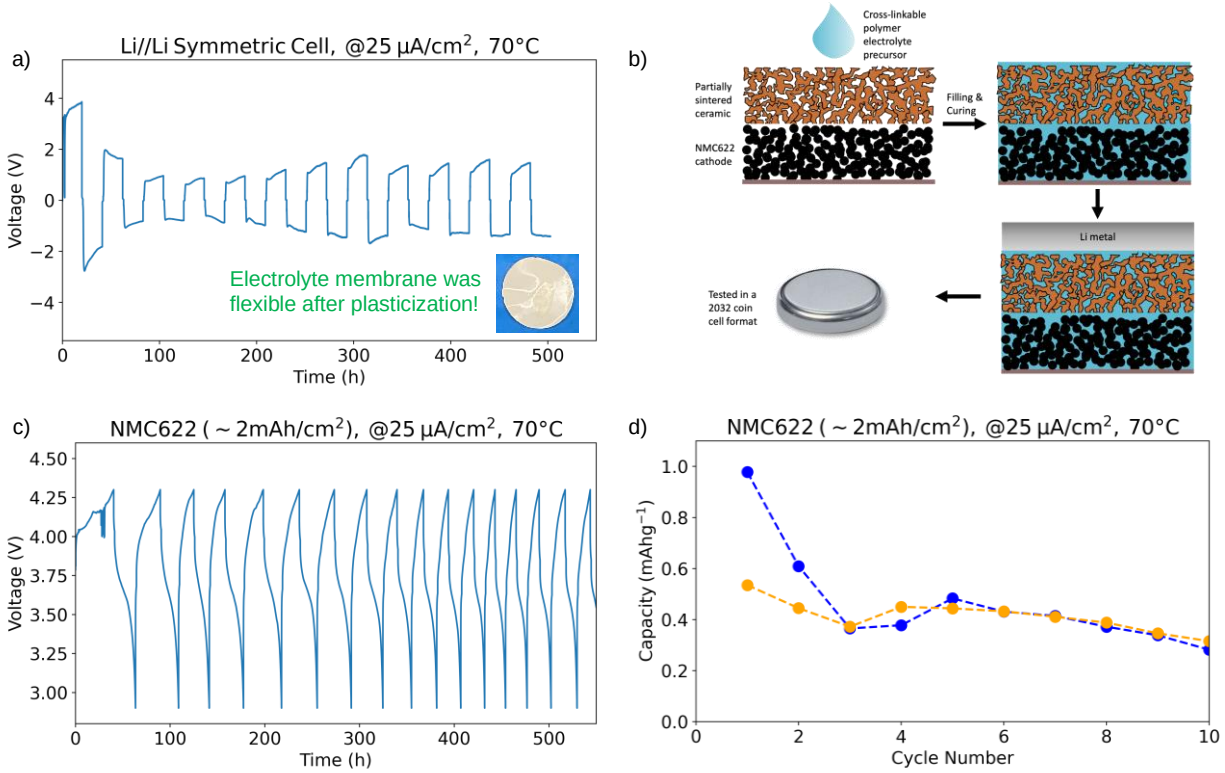

Figure 94. Cycling performance of a ~ 140-μm-thick *plasticized* xPEO-Ohara (3D interconnected) composite electrolyte. (a) Li//Li symmetric cell with the *plasticized* composite tape at 25 μA/cm² and 70°C. (b) Schematic illustrating the half-cell assembly procedure with a conventional PVDF-binder based NMC-622 cathode and a 3D interconnected Ohara ceramic electrolyte porous tape, *plasticized* with liquid TEGDME plasticizer. (c) Cycling performance of the illustrated half-cell at 25 μA/cm² and 70°C. (d) Absolute cell charge and discharge capacity (mAh) of the cell versus cycle number. The cathode loading was ~ 2 mAh/cm².

The composite electrolyte demonstrated much improved mechanical properties and lithium metal stability after it was soaked in tetraethylene glycol dimethyl ether (TEGDME) liquid plasticizer for about 30 minutes. Figure 94a shows stripping/plating voltage profile of Li//Li symmetric cell containing this membrane, where a constant current of 25 μA/cm² was applied for a period of 20 hours during each half cycle (to pass a capacity of 1 mAh/cm²). The 'non-flat' nature of strip/plate plateaus and also the high overpotentials suggest that the cell was not shorted. The plasticizer also seems to have helped stop any reaction between the lithium metal and the ceramic phase, likely by decomposing to form a conductive interphase layer. The inset photograph shows the composite electrolyte membrane after plasticization, where its flexible nature can be observed in its folds (before plasticization, the membrane was flat and brittle). Figure 94b illustrates 'in-essence' the half-cell assembly procedure, where the porous ceramic tape was placed on top of a conventional PVDF-based

NMC-622 cathode and then infiltrated with the xPEO liquid precursor. This layered stack was cured together and used in the cell assembly. Plasticizer was again used to soften the membrane and prevent any reaction at the Li//PE interface (not shown in schematic). Figure 94c shows the charge/discharge voltage profile as the cell was cycled galvanostatically at 25 μA/cm^2 and 70°C. The corresponding charge and discharge capacity in mAh is plotted in Figure 94d.

Elucidation of Ion Transport Path in 3D Interconnected Composite Electrolyte

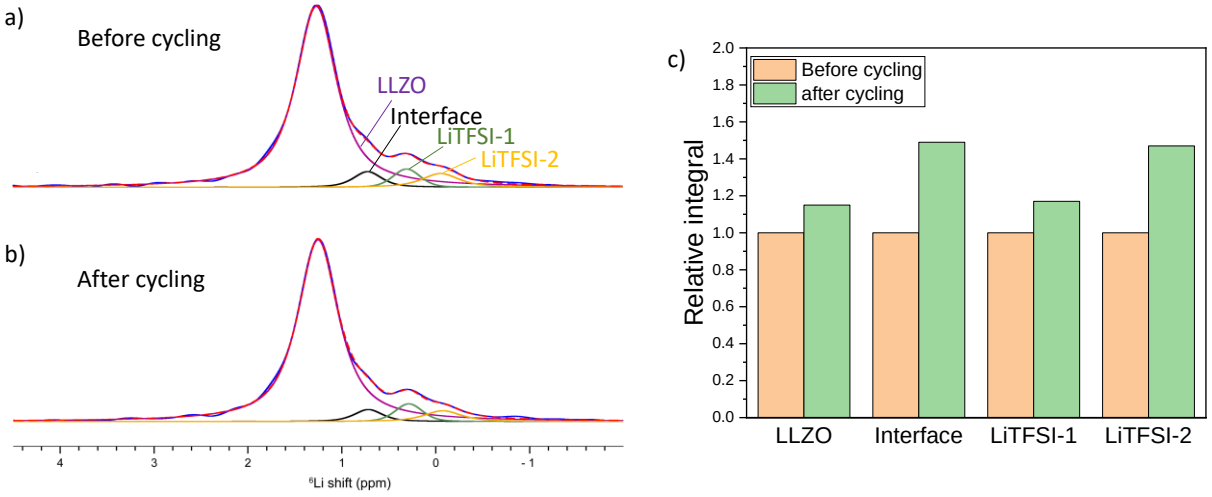

Figure 95. Tracer exchange ^{6}Li nuclear magnetic resonance results on xPEO-LLZO (3D interconnected) composite electrolyte. (a-b) ^{6}Li NMR spectra of the composite electrolyte before (a) and after (b) cycling. (c) Relative integral ratio of the ^{6}Li amount in LLZO, at the polymer/LLZO interface, and LiTFSI in the PEO/TEGDME complex, respectively.

To mechanistically elucidate the ion transport path in the interconnected composite electrolyte, the team conducted tracer exchange ^{6}Li NMR experiments. These experiments were done through the collaboration with the Y. Hu group at Florida State University. LLZO powder was provided by J. Libera from the Materials Engineering Research Facility at ANL. The LLZO/xPEO composite was chosen because the lithium chemical shift in LICGC™ was much closer to that of lithium salt compared to LLZO, which makes it harder to deconvolute different lithium species. The LLZO/xPEO (plasticized with TEGDME) sample was prepared by pressing a 1-mm-thick LLZO pellet, partially sintering it at 900°C for 3 hours, and then following with backfilling the partially sintered ceramic with xPEO and LiTFSI precursors and curing at 100°C. The polymer phase was plasticized with TEGDME in this composite. Symmetric cells using ^{6}Li as the electrodes were prepared by sandwiching the composite electrolyte with two pieces of ^{6}Li disks followed by two stainless-steel rods. The cell was sealed in two layers of heat shrink tubing and cycled at 70°C at 10 μA/cm^2 in a AA battery holder. ^{6}Li NMR spectra before and after cycling are shown in Figure 95a-b. Four peaks can be identified through peak deconvolution, representing lithium species in LLZO, LLZO/xPEO interface, LiTFSI-1, and LiTFSI-2. It appears that Li^+ in LiTFSI experiences two different environments, coded as LiTFSI-1 and LiTFSI-2. While still under investigation, the current interpretation for the two peaks is that LiTFSI-1 is mainly associated with the xPEO matrix, and LiTFSI-2 is mainly associated with TEGDME.[1] The relative integral ratio of each species before and after cycling is shown in Figure 95c. The amount of ^{6}Li increased in all four species, indicating that ion transporting occurred in the LLZO ceramic, the plasticized polymer, and the ceramic/polymer interface. The largest change in the relative integral ratio is seen at the LLZO/xPEO interface and in LiTFSI-2. More data analysis is under way.

Novel Polymer Electrolyte with Anion Acceptor Motifs

The team continued investigating novel PEs that contain motifs to allow for dynamic bonds between polymer chains (denoted as dPEO). The effects of the motifs on ionic conductivity, Li^+ transference number, and mechanical properties of dPEO were examined this quarter. Compared to linear PEO with the same lithium

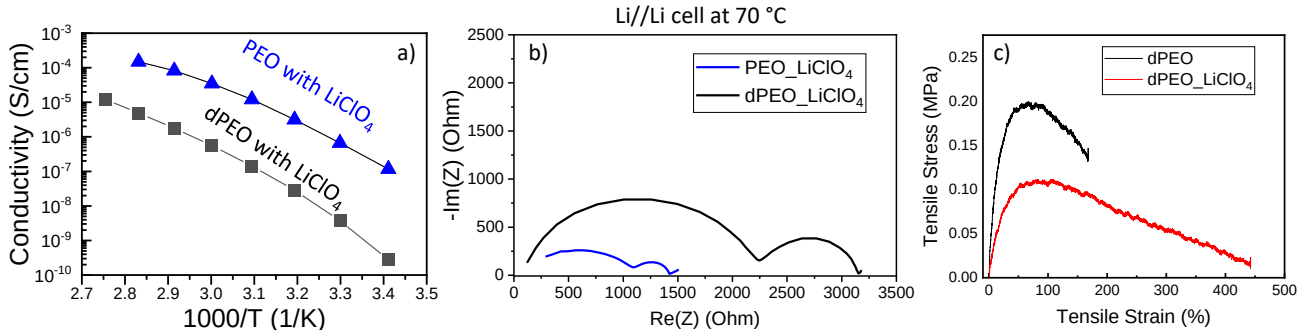

Figure 96. Transport and mechanical properties of dPEO with $LiClO_4$ salt. (a) The ionic conductivity as a function of inverse temperature; the ionic conductivity of linear PEO with the same salt concentration was also plotted. (b) Nyquist plot of Li//Li symmetric cells at 70°C. (c) Tensile stress-strain curves of dPEO and dPEO with $LiClO_4$ salt.

salt ($LiClO_4$) and salt concentration, the ionic conductivity of dPEO electrolyte is more than one order of magnitude smaller (Figure 96a). The Li^+ transference number increased slightly compared to linear PEO (Table 5). The impedance spectra of the lithium symmetric cells before polarization are shown in Figure 96b. The area of the cells was 1 cm^2. Lithium disks with 0.6-mm thickness were used as the lithium electrodes without further treatment. The interfacial resistance with lithium for linear PEO electrolyte was 340 $\Omega \cdot cm^2$, whereas that of dPEO was 910 $\Omega \cdot cm^2$, almost a three-fold increase. The motifs in dPEO did enhance the transference number of the electrolyte, but they also decreased ionic conductivity dramatically and increased interfacial resistance with lithium. Therefore, the transport properties of dPEO are less satisfying. On the other hand, dPEO exhibits very high ductility, especially after mixing in the lithium salt (Figure 96c). The elongation at break for dPEO with $LiClO_4$ salt was 450%. Next quarter, the team will fill the interconnected ceramic with dPEO electrolyte and assess the mechanical properties of the composite. They will take advantage of high ductility of dPEO to enhance the flexural strength of the composite. Meanwhile, they will adjust the composition of dPEO to improve its transport properties.

Table 5. Li^+ transference number, t_+, of dPEO and PEO with $LiClO_4$ salt at 70°C.

Sample	t_+ at 70°C
dPEO_$LiClO_4$	0.37
PEO_$LiClO_4$	0.27

Modeling of Li-Ion Concentration Gradients in Composite Electrolytes

The team continues to utilize numerical modeling and simulations to study the influence of introducing a SIC to a polymer binary electrolyte. This quarter, they finalized 3D simulations based on the LATP-PEO(LiTFSI) system with the material constants presented in the last report. They include the interface between the SIC and PE as a thin film with prescribed resistance. The 3D form of Nernst-Planck equations is solved to obtain concentration of ions at each time step. The three arrangements are shown in Figure 97. To model the particulate composite, the LATP particles were approximated as spheres with the size following the distribution measured in-house by the laser diffraction particle size analyzer. A random seed (50% by volume) of a cube with 40-μm side was performed, from which a 10-μm subdomain was obtained. The plots in Figure 97 show the concentration of lithium cations in PE normalized to the initial concentration, with the interface conductivity equal to 10^{-7} S/cm. It can be seen that, similar to the 2D case, the placement of SIC particles increases the concentration gradient in the binary polymer electrolyte, while the placement of SIC membrane (impenetrable to the anions) leads to lower concentration gradient in steady state.

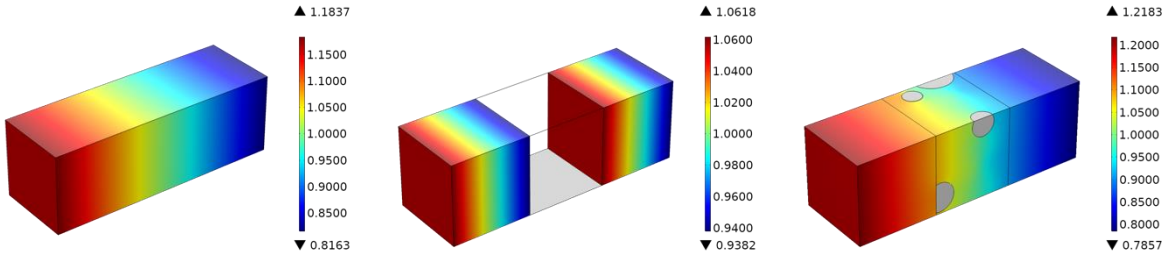

(a) (b) (c)

Figure 97. Lithium cation concentration in: (a) polymer membrane, (b) polymer membrane with LATP layer in the middle, and (c) polymer membrane with composite polymer electrolyte in the middle.

Reference

[1] Zheng, J., H. Dang, X. Feng, P-H. Chien, and Y-Y. Hu. "Li-Ion Transport in a Representative Ceramic–Polymer–Plasticizer Composite Electrolyte: $Li_7La_3Zr_2O_{12}$–Polyethylene Oxide–Tetraethylene Glycol Dimethyl Ether." *Journal of Materials Chemistry A* 5, No. 35 (2017): 18457–18463.

Patents/Publications/Presentations

Publication

- Kalnaus, S., L. E. Asp, J. Li, G. M. Veith, J. Nanda, C. Daniel, X. C. Chen, A. Westover, and N. J. Dudney. "Multifunctional Approaches for Safe Structural Batteries." *Journal of Energy Storage* 40 (2021): 102747.

Presentation

- DOE VTO Annual Merit Review Meeting, Virtual (June 2021): "Composite Electrolyte to Stabilize Metallic Lithium Anodes"; X. C. Chen, et al. Poster.

Task 4.3 – Enabling Solid-State Batteries through Characterization and Modeling (Sanja Tepavcevic and Larry A. Curtiss, Argonne National Laboratory)

Project Objective. The project objectives are multi-faceted, including development of a new mechanically and chemically stable and Li-ion conductive ($\geq 2 \times 10^{-4}$ S/cm at 298 K) crystalline/amorphous SE for SSB. The anode and cathode are composed of lithium metal and a Li-based oxide, respectively, allowing operation at cathode potentials > 5 V (denoted as a S_{Li}-S_{EL}-S_C system).

Project Impact. Protective organic and inorganic compounds can enhance stability of the interface, improve Li-ion interfacial transport, minimize dendrite formation, and increase safety in Li-ion batteries.

Approach. The project proposes to develop and use interdisciplinary, atomic-/molecular-level insight obtained from integrating both experimental- and computational-based methodologies to define the landscape of parameters that control interfacial properties for a new generation of the Li-ion solid-solid battery systems. The strategy will involve transferring knowledge gained from well-characterized thin-film materials to real-world materials. This strategy forms a closed loop wherein the knowledge gained from model systems is used to design more complex, real-world materials, and vice versa. The work will focus on utilizing existing in-house synthesis and characterization methods to enable rapid transition from fundamental science to realistic cells.

Out-Year Goals. The out-year goals are to use and develop the physical and chemical synthesis methods for design of SSI with unique chemical/mechanical/conductivity properties. The proposed work will develop and exploit a variety of *ex situ* and *in situ* experimental optical and surface sensitive techniques and electrochemical methods to explore and explain bulk and interfacial properties of the selected materials. The results will serve to unravel many puzzling bulk and interfacial properties of S_{Li}-S_{EL}-S_C systems, including various types of ceramic and glass materials.

Collaborations. This project funds work at ANL and collaboration with J. Sakamoto at UM.

Milestones

1. Evaluating chemical stability and correlating with interfacial reactivity for vacuum-deposited Li/Al -doped LLZO interfaces. (Q1, FY 2021; Completed)
2. Understanding impact of different dopants in LLZO (aluminum versus gallium) on chemical and electrochemical reactivity with metallic lithium by surface and bulk sensitive techniques and computational tools. (Q2, FY 2021; Completed)
3. Modifying energy barrier for Li^+ transport in Al-doped LLZO by controlling the chemistry of the GBs via additives. (Q3, FY 2021; Completed)
4. Optimizing nanoLLZO+PEO composite and characterizing chemical and electrochemical reactivity with metallic lithium by surface and bulk sensitive techniques. (Q4, FY 2021)

Progress Report

LLZO garnet-based oxides are a promising class of SEs used as the separator in ASSBs. Cubic LLZO generally densifies at temperatures above 1200°C via solid-state sintering, but this rather high sintering temperature can cause volatilization of lithium and can lead to a phase transition back to the less conductive tetragonal phase. Presence of pores left from an unsatisfactory sintering procedure can reduce ionic transport as well as degrade mechanical properties of the SE. GBs between crystals in the electrolyte can limit performance through the following: (1) adding more resistance to the overall cell by presenting a barrier to Li^+ transport, and (2) generally having higher electrical conductivity, thus generating favorable pathways for lithium dendrite formation. This second point can be worsened by dopant (for example, aluminum, niobium, gallium) segregation to the GBs. It is important, therefore, to control GB chemistry to prevent these issues and increase the ionic conductivity and CCD of the SE.

One potentially useful and straightforward route to optimization of the densification procedure is GB engineering. Sintering aids such as LBO are used during the annealing and sintering procedures to lower the temperature needed for LLZO grain growth. During sintering, LBO forms a liquid phase at temperatures below 1000°C and enhances the densification of LLZO grains via liquid-phase sintering. LBO is excluded to the outside of growing grains, and, in theory, is incorporated into GBs due to phase segregation. Since LBO itself is a moderate Li^+ conductor (~10^{-6} S/cm at room temperature), it should still allow high conductivity in the electrolyte. As a result, this improved densification procedure can lower sintering temperature and minimize the negative impacts of GBs.

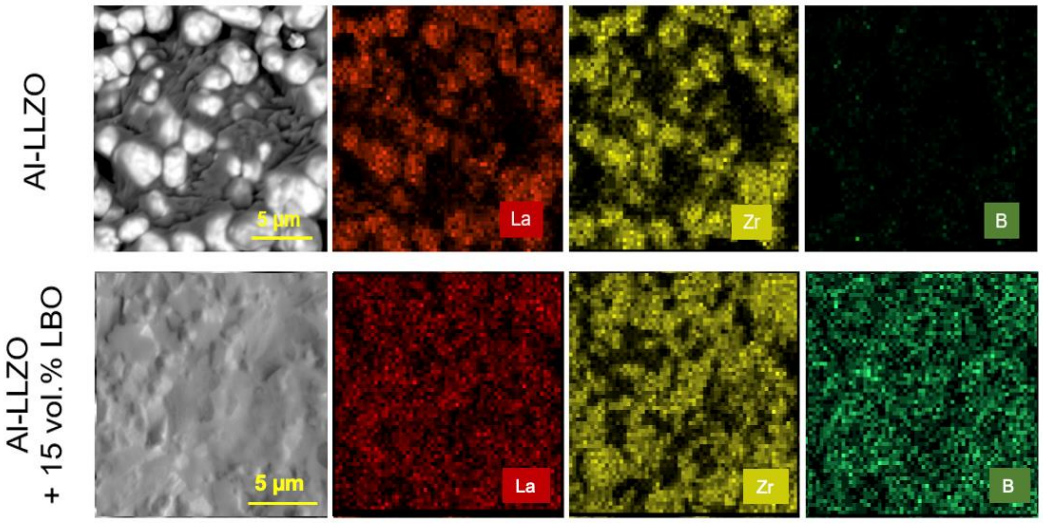

Figure 98. Scanning electron microscopy and energy dispersive X-ray spectroscopy elemental mapping of Al-doped LLZO with and without Li_3BO_3 (LBO). Inclusion of LBO during sintering significantly increases grain size and electrolyte density.

Figure 98 shows SEM and EDS analysis of the top surface of sintered Al-doped LLZO and of sintered Al-doped LLZO with 15 vol% LBO. Both samples show misstructures with fairly straight GBs, reflecting the rather late stage of sintering. Importantly, pellets including 15 vol% LBO were not only sintered at lower temperatures, they were also denser. Furthermore, EDS elemental mapping of sintered Al-doped LLZO shows the distribution of lanthanum and zirconium across the top surface of the sample, together with negligible counts of boron. On the other hand, EDS elemental mapping of the sample including LBO shows that the overall LLZO grain size is slightly larger (refer to lanthanum and zirconium maps) together with B-rich GBs and coatings. This analysis provides direct evidence that LBO not only decreases the temperature required for sintering, but it also shows

that LBO segregates to GBs and surfaces of the primary grains/particles. This microstructural feature is expected to influence the electrochemical properties of the electrolyte and its ability to cycle with high-capacity anodes such as lithium metal.

To modify the GBs of LLZO with LBO, two sets of precursors needed to be synthesized: cubic Al-doped LLZO ($Li_{6.25}Al_{0.25}La_3Zr_2O_{12}$) and lithium borate (LBO). Cubic Al-doped LLZO was synthesized by mixing stoichiometric amounts of LiOH, $La(OH)_3$, ZrO_2, and $Al(NO_3)_3$ in isopropanol at 82.5°C with stirring at > 300 rpm. Once all isopropanol evaporated, the powder was collected, pressed into green bodies, placed in a MgO crucible, and calcined/annealed at 900°C under a flow of dry O_2 for 12 hours with a ramp rate of 10°C/minute. Lithium garnet pellets were then collected, powdered, and stored in an Ar-filled glovebox for further use. Lithium borate (Li_3BO_3) was synthesized by mixing stoichiometric amounts of LiOH and H_3BO_3 in methanol. This mixture was then heated to >80°C with mixing at > 300 rpm; once all methanol was removed, the resulting powder was transferred to an alumina crucible and heated to 450°C in a muffle furnace for 4 hours with a ramp rate of 10°C/minute. The LBO was then collected, powdered, and stored in an Ar-filled glovebox for further use. Next, two sets of samples were synthesized: sintered Al-doped LLZO, and sintered Al-doped LLZO with 15 vol% LBO. For sintered Al-doped LLZO, as-obtained calcined/annealed lithium garnet powder was pressed into a green body, placed into a MgO crucible, and sintered at 1100°C under a flow of dry O_2 for 10 hours. For Al-doped LLZO with 15 vol% LBO, stoichiometric ratios of LBO and lithium garnet were ground with an agate mortar and pestle in an argon-filled glovebox, pressed into a green body, placed into a MgO crucible, and sintered at 1000°C under a flow of dry O_2 for 10 hours. Note that inclusion of LBO decreases the temperature required for sintering. The phase of each pellet was confirmed with XRD.

To confirm the spatial distribution of LBO in the LLZO electrolyte, the team used Raman microscopy. Mapping of LBO on the pellet surface shows clear segregation of LBO outside of large 5-10 µm LLZO grains (Figure 99). LBO is found between grains in GBs and triple junctions. Discrete crystals of LBO are also present, either embedded in the electrolyte or as surface particles. This suggests that GB modification with LBO is possible by simple inclusion as sintering aid.

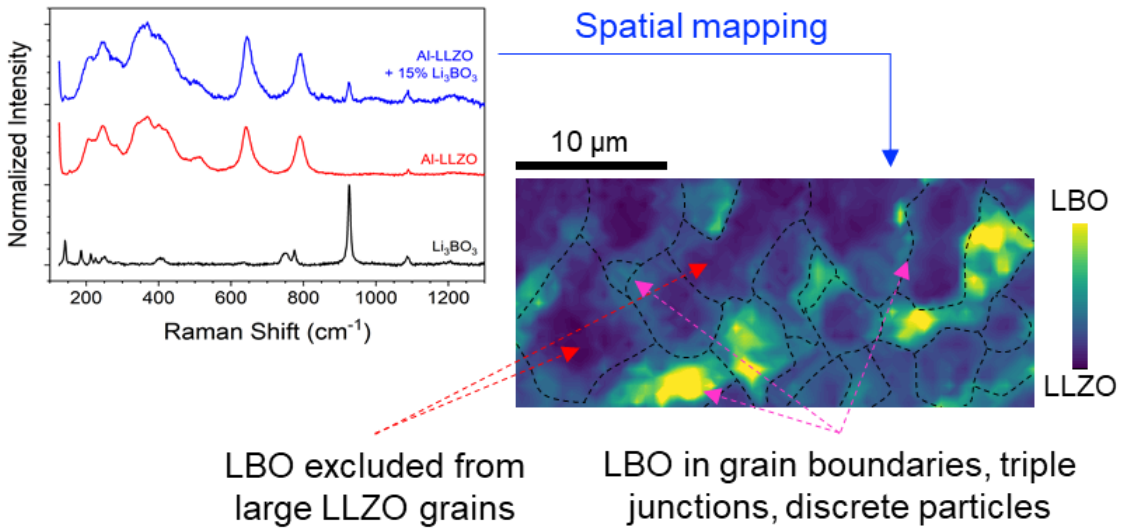

Figure 99. Raman spectra and spatial mapping of Li_3BO_3 (LBO) content within an Al-LLZO pellet synthesized with 15 vol% LBO. Mapping of the pellet surface shows LBO in grain boundaries (GBs), in triple junctions, and as discrete particles. Dotted lines in the image are drawn to guide the eye around LBO in GBs.

The team used EIS to determine how LBO impacts overall conductivity in the electrolyte. Figure 100 shows Nyquist plots of Al-doped LLZO with and without 15 vol% LBO doping. Quantitative fits show that combined bulk and GB impedance (10 MHz-10 kHz) increases for the doped sample (19.9 kΩ cm^2) compared to the

undoped sample (15.8 kΩ cm^2). This agrees with expectations that adding a poorer conductor in between grains will increase resistance, although it appears in this case only by ~ 25%. More apparent is the change in interfacial/charge transfer resistance (10 kHz-100 Hz), which is almost two orders of magnitude higher for the undoped sample (2.4 MΩ cm^2 versus 45 kΩ cm^2). This result may be due to the surface impurities present on each sample—Li_2CO_3 is known to form on LLZO in air and cause significant resistance, while Li_3BO_3 would protect LLZO to an extent and has moderate Li^+ conductivity itself. This demonstrates the benefits of using LBO as a sintering aid and GB modifier in LLZO processing.

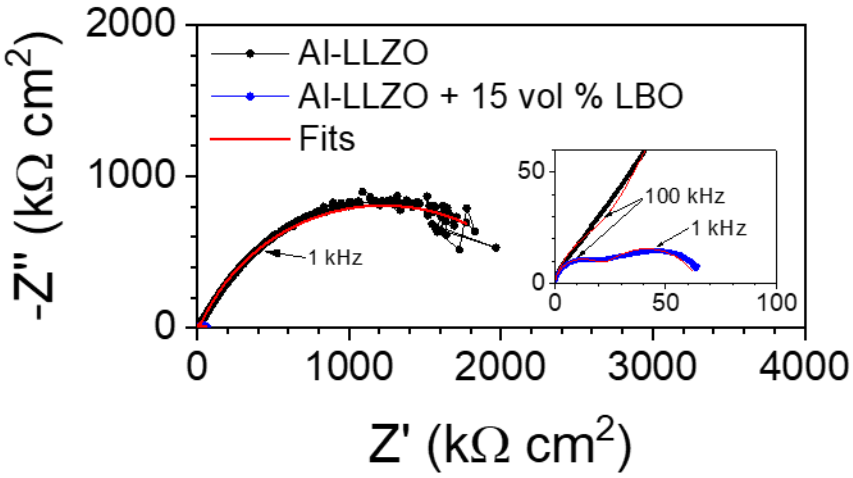

Figure 100. Electrochemical impedance spectra of Al-LLZO pellets sintered without and with 15 vol% Li_3BO_3 (LBO). The undoped pellet shows slightly lower bulk and grain boundary resistance, but overall higher resistance due to interfacial and charge transfer impedance compared to the doped sample. A symmetric Li|Li cell at room temperature with frequency range 10 MHz-100 Hz was used in each case.

Patents/Publications/Presentations

The project has no patents, publications, or presentations to report this quarter.

Task 4.4 – 3D Printing of All-Solid-State Lithium Batteries (Jianchao Ye, Lawrence Livermore National Laboratory)

Project Objective. This project has three objectives: (1) tuning microstructures of 3D-printed SSE separators, (2) determining material and processing compatibilities with cathode printing, and (3) 3D printing of sintering-free SSE separators.

Project Impact. ASSLBs are difficult to process due to the brittleness of ceramic materials, poor solid-solid contact, and electrolyte-electrode stability issues. As a result, the energy and power density and also cycling stability are far from satisfying. This project will address fabrication difficulties by using state-of-the-art 3D-printing techniques that can introduce 3D interfaces and architectures to enhance solid-solid contact and reduce charge transfer resistance. Success will benefit the DOE by establishing the best manufacturing methods for ASSBs to achieve VTO goals on the performance of beyond Li-ion batteries.

Approach. The project employs 3D-printing techniques to manufacture SSEs and related components for ASSBs. The team starts with direct ink writing (DIW) to develop ink recipes with desired rheological properties and to explore post-sintering approaches to achieve high densification. In parallel with DIW 3D printing, the team also explores other 3D printing options, such as projection microstereolithography. Both sintering and sintering-free approaches can gain benefit from 3D printing and therefore will be investigated.

Out-Year Goals. The team will determine the co-sintering stability of printed NMC/LLZTO films and compare with that of hydraulic-pressed NMC/LLZTO pellets. They will print SSE/cathode bilayer structures with controlled interfaces and determine their electrochemical performance with or without post sintering process.

Collaborations. Microstructures, ionic conductivities, and mechanical properties will be provided to the LLNL simulation team, led by the PI, B. Wood, for establishing and validating phase-field modeling methods.

Milestones

1. Evaluate new commercial LLZTO powder sources. (Q1, FY 2021; Completed)
2. Determine performance of ASSBs based on 3D-architected LLZTO structure. (Q2, FY 2021; Completed)
3. Determine performance of ASSBs based on composite PE. (Q3, FY 2021; Completed)
4. Evaluate ASSBs based on co-sintering approach. (Q4, FY 2021; In progress)

Progress Report

Solid Polymer Electrolyte (SPE)

Fifteen different PEGDA-/PEGMA-/PEO- based SPEs were prepared to screen the optimized composition for best conductivity. Figure 101 shows a map of the ionic conductivity in the PEGMA rich region. Note, the LiTFSI is constant, 25 wt%. PEGMA-only SPE shows the highest ionic conductivity, 6.5×10^{-5} S/cm. With the increase of PEO600K and PEGDA concentration, the conductivity decreases, which is likely due to the increase of Tg and the crosslink-induced "slowing" of polymer chain segmental motion. While the PEGMA SPE is a "gel-like" sticky semi-solid, replacing PEGMA with 10 wt% PEGDA and 10 wt% PEO600K makes a freestanding solid film. The ionic conductivity decreases to 1.55×10^{-5} S/cm. The value is lower than the team previously found with a similar PEGDA/PEGMA/PEO ratio (1:9:1) that gave 1.06×10^{-4} S/cm, which may be attributed to the degree of polymerization and PEGMA content.

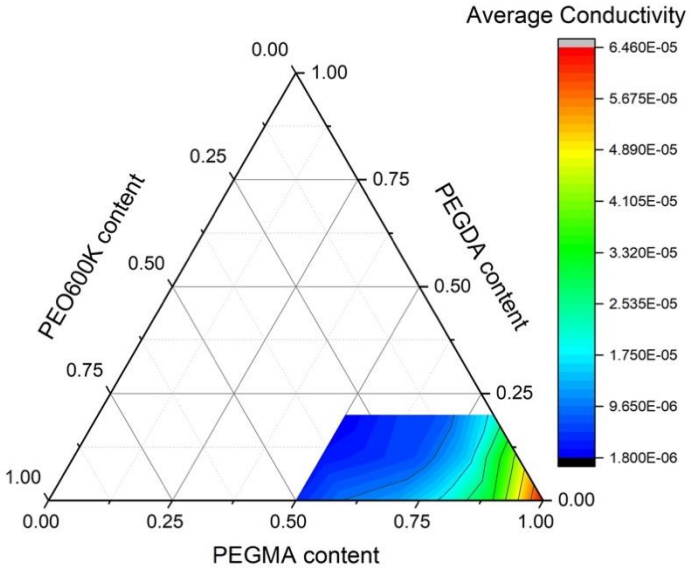

Figure 101. Ionic conductivity at room temperature.

CPE

To improve ionic conductivity and mechanical properties, CPEs were further developed by adding ball-milled LLZTO nano powders. In the preparation of LLZTO-based CPEs, the team found that sometimes the ink could not be crosslinked, or the crosslinked membrane lost mechanical properties after thermal treatment in an 80°C oven. The reason might be attributed to the side reactions catalyzed by LLZTO with trace water in the mixture, breaking the ester bond between acrylate and PEG repeat units. In Figure 102, the red curve is the NMR result of PEG-acrylate monomers after ball-milling with LLZTO. The heat generated from ball milling accelerated the degradation reaction, which was evidenced by the decreased NMR peak intensity of Ha and Hb [Figure 102; red (after ball milling), blue (before ball milling)]. When mild mixing condition was applied, such as stirring with more solvent, the mixture was not heated up. Consequently, the degradation reaction was greatly slowed down (green curve). It is likely that H_2O reacts with LLZTO to form LiOH base, which catalyzes the ester hydrolysis. To prove this hypothesis, the team modified their sample preparation procedure to minimize moisture exposure. Indeed, they found that ultraviolet (UV) crosslinking works much better for the samples than the those exposed to air or stored too long.

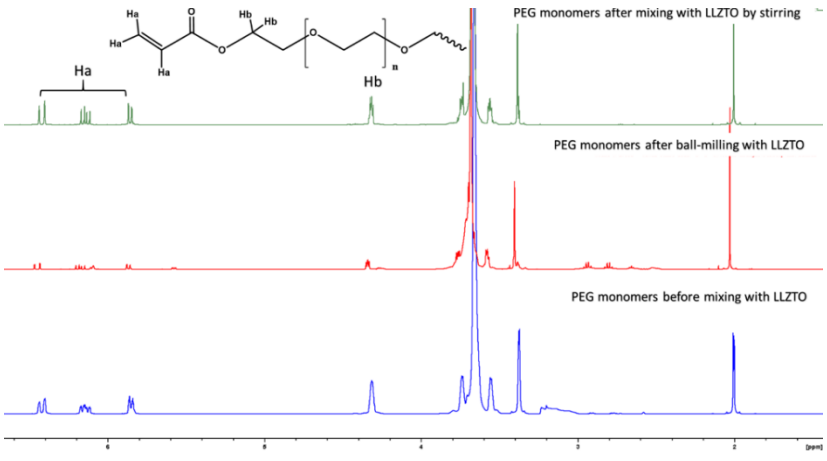

Figure 102. Nuclear magnetic resonance spectra of PEG-acrylate monomers.

Further improvement of ionic conductivity was found by adding 13-18 wt% LLZTO; see examples in Figure 103. A 13 wt% LLZTO in 1:8:1 PEGDA/PEGMA/PEO CPE shows 5.6×10^{-5} S/cm ionic conductivity, about 3.7 times that of SPE without LLZTO.

Further increasing LLZTO content to 18 wt% seems to show less improvement (3.2×10^{-5} S/cm), which is consistent with the trend found in much of the literature. However, the degree of improvement may also be related to the composition of the polymer blend. For example, a 23 wt% LLZTO in 1:7:2 PEGDA/PEGMA/PEO CPE shows 3.2×10^{-5} S/cm, about 4.5 times that of the corresponding SPE without LLZTO (7.2×10^{-6} S/cm). More data will be collected to make a contour map similar to that shown in Figure 101.

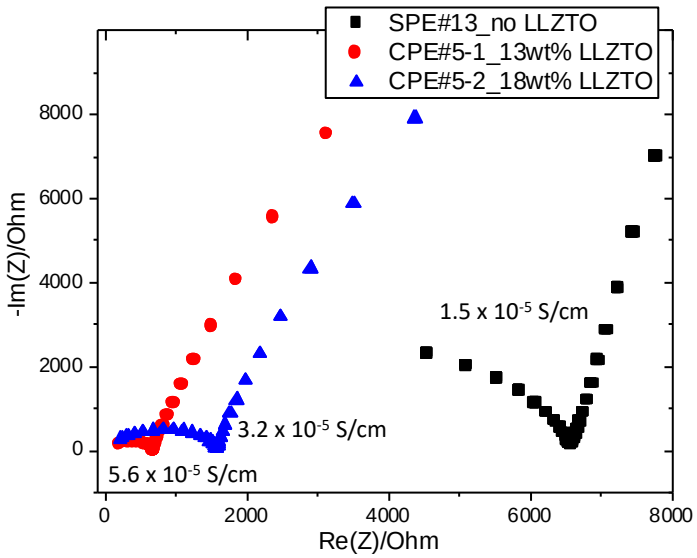

Figure 103. Electrochemical impedance spectroscopy plots of composite polymer electrolytes (CPEs) in SS|CPE|SS symmetric cells. All three samples have the same PEGDA/PEGMA/PEO/LiTFSI ratios. SPE#13 has no LLZTO added. CPE#5-1 and #5-2 have 13 wt% and 18 wt% LLZTO added, respectively. All tests were measured at room temperature without external pressure.

Full Battery Test

To evaluate a full battery performance based on the developed CPEs, 3D LFP cathodes were printed on aluminum foil (Figure 104a). A CPE ink with 30 wt% LLZTO in 1:8:1 PEGDA/PEGMA/PEO compositions was infilled into the LFP structure. After vacuum drying and UV plus thermal curing, a CPE/LFP composite bilayer structure was obtained. A lithium chip was directly attached against the CPE/LFP bilayer, and a coin cell was assembled in an Ar-filled glovebox. Figure 104b shows the impedance of the cell at 60°C. The overall interfacial plus bulk resistance is ~ 320 Ω before cycling for an 8-mm-in-diameter sample area. After 25 cycles at varying C-rates, resistance increased to 480 Ω, mainly contributed from the second semicircle that represents an interfacial impedance between CPE and electrode (the team still needs to determine whether it is from the anode or cathode side). Figure 104c shows the first five cycles of galvanostatic charge/discharge at relatively high C-rate, 0.8C, at 60°C. The 1st charge capacity reaches 163 mAh/g, which is surprisingly high.

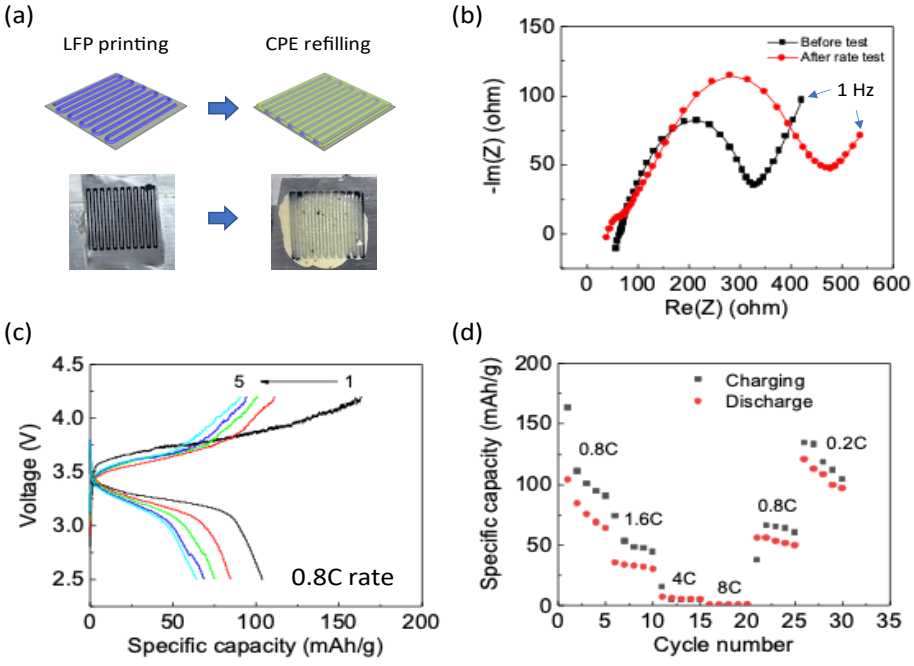

Figure 104. Battery assembly and testing for a composite polymer electrolyte (CPE) based all-solid-state lithium battery (ASSLB). (a) ASSLB made from infilling of CPE into a 3D-printed cathode. (b) Electrochemical impedance spectroscopy before and after testing. (c) Charge/discharge curves at 0.8C rate. (d) Rate performance. All tests were conducted at 60°C in coin-cell setup.

The curve is, however, noisy. The charging "noise" might be an indicator of micro shorts, suggesting the CPE is not resistive enough to block the lithium dendrites. The discharge curve is smooth, with a capacity of 104 mAh/g. The capacity decay is significant, after 5 cycles, the discharge capacity is only 64 mAh/g. The rate test (Figure 104d) shows that almost no capacity can be extracted at 4C rate. When the cell was cycled at slower rate of 0.2C, the discharge capacity started from 134 mAh/g and dropped to 104 mAh/g after 5 cycles. Long-term cycling is still ongoing, and more cells for repeatability are under way.

Overall, the ASSLMB based on the 3D-printed cathode and infilled CPE can be cycled and showed reasonable performance. The main problems to be solved in the future studies include the low CE and fast capacity decay. Symmetric cell testing may reveal the origin of the stability problem, whether from the contact with lithium anode or the LFP cathode. Thickness and stiffness control may mitigate/solve the micro short issue. Galvanostatic charging or potentiodynamic linear sweep voltammetry may reveal the cathode stability. Applying external pressure may also benefit cycling stability. More tests will be conducted on other CPEs with different PEGDA/PEGMA/PEO/LLZTO mixing ratios for comprehensive studies.

Patents/Publications/Presentations

The project has no patents, publications, or presentations to report this quarter.

Task 4.5 – Interfacial Studies on Lithium Thiophosphate Based Solid Electrolytes and Cathodes (Jagjit Nanda, Oak Ridge National Laboratory)

Project Objective. Capacity fading and the underlying interfacial side reactions between thiophosphate SEs and cathode active materials are not well understood. A key project deliverable is to combine EIS measurements with complementary *in situ* and *ex situ* spectroscopy and microscopy to identify decomposition reaction products at the CEI. Ultimately, this work will enable a mechanistic understanding of factors that limit the rate performance and capacity loss of SSBs. The goal here is to combine the information from these techniques to provide a unified overview of the interfacial layer's composition, structure, and morphology. In this multi-year work, the team will investigate a number of SEs [LPS, LGPS, and $Li_{9.54}Si_{1.74}P_{1.44}S_{11.7}Cl_{0.3}$ (LSiPCl)] and cathode compositions belonging to different structural families [LFP (olivine), FeS_2 (sulfide-based conversion cathode), and $LiNi_{0.6}Mn_{0.2}Co_{0.2}O_2$ (NMC-622, layered oxide)].

Project Impact. SSBs are poised to be the next-generation battery technology for meeting EV goals in terms of energy density, cycle life, and safety. Among other technical barriers, the success of this technology relies on design of stable electrode/electrolyte interfaces. Sulfide-based SEs have high ionic conductivity ($> 10^{-4}$ S/cm) and are mechanically soft, which simplifies processing compared to their oxide counterparts. Furthermore, sulfide SEs are comprised of earth abundant materials (for example, sulfur and phosphorus) and can be easily synthesized using scalable, low-temperature, solution-based routes.

Approach. A low-temperature (< 350°C) solution-based synthesis method will be used to synthesize the LPS family of SEs. The structure of these materials is characterized using XRD, Raman spectroscopy, and neutron scattering. Standard AC/DC electrochemical methods are used to characterize ionic conductivity, electrochemical stability, and CCD. The work scope includes using various *in situ* and *ex situ* electrochemical, microscopic, and spectroscopic tools for characterizing the structure, morphology, and kinetics of the interfacial reaction layer formed between thiophosphate SEs and cathodes.

Out-Year Goals. Develop thiophosphate SEs – sulfide cathode interfaces with low ASR for ASSBs.

Collaborations. This project will collaborate with G. Ceder (UCB) and P. Jena (Virginia Commonwealth University) on modeling and synthesis guideline, as well as with S. Greenbaum on solid-state NMR to measure ion-diffusivity and local bonding.

Milestones

1. Demonstrate and test hot-sintering method to fabricate composite thiophosphate SE-NMC cathodes. (Q1, FY 2021; Completed)
2. Optimize synthesis and processing conditions (for example, interfacial coatings and stack pressure) to minimize the ASR between argyrodite SEs and NMC cathodes. (Q2, FY 2021; Completed)
3. Perform Raman microscopy, NMR, and electron microscopy to characterize bulk argyrodite SE and cathode SE interfaces to investigate capacity loss and degradation mechanisms. (Q3, FY 2021; In progress)
4. Select and optimize a few solid-state cathode compositions to demonstrate room-temperature cycling with LPS and/or argyrodite SEs. Stretch Goal: 50 cycles with < 20% capacity fade. (Q4, FY 2021; In progress)

Progress Report

Last quarter, the team showed that pellet-type SSBs containing a thin lithium anode (~ 45 µm on copper foil), ß-Li_3PS_4 separator (LPS, ~ 0.9 mm thick), and composite cathode (NMC-811+C+LPS) exhibited high initial charge capacity (~ 200 mAh/g), but suffered from poor reversibility (~ 50% initial CE) and capacity/voltage fade during cycling. To determine whether these issues are primarily related to the lithium anode or NMC cathode, this quarter the team performed analogous experiments using a Li_xIn anode. As reported in literature, alloying anodes are commonly used in the SSB to avoid lithium dendrite formation; direct comparisons with cells containing lithium metal are rarely reported. In the present study, the following two methods were investigated to prepare the Li_xIn alloy: (1) combining lithium and indium foils via isostatic pressing at room temperature, and (2) Coulombically titrating indium metal in SSB containing a lithium anode and LPS separator. The first method did not yield the desired LiIn phase (determined via XRD, results not shown); thus, this approach was not further explored. In contrast, Figure 105a shows that the Li_xIn alloy prepared using the second method had a constant open-circuit potential (E^{oc}) of 0.622 V versus Li/Li^+ throughout the 2-phase In/LiIn region. The titration was stopped at x = 0.169, at which point the $Li_{0.169}In$ alloy was harvested from the cell for use in a full cell. Notably, this endpoint was selected to ensure the Li_xIn alloy could cycle moderate lithium inventories (± 2 mAh) while remaining in the desired 2-phase region with a well-known electrochemical potential.

Figure 105b-c shows galvanostatic cycling data for NMC-811-based SSBs containing either a lithium metal or $Li_{0.169}In$ anode prepared using standard protocols developed in this program. These cells exhibited nearly identical voltage profiles and cycling performance with initial reversible capacities of ~ 110 mAh/g, which gradually faded during cycling. Notably, the slightly higher capacity of the Li_xIn cell is within experimental error for the measured cathode loading (6.6 ± 0.8 mg_{NMC}/cm^2). After 50 cycles, the Li_xIn cell retained only 25% of its initial capacity, which is attributed to formation of a resistive CEI and/or degradation of solid-solid contacts in the cathode. Overall, these results demonstrate that replacing lithium metal with a Li_xIn alloy had negligible impact on SSB performance, which provides very strong evidence that cathode design is the major bottleneck for Li|LPS|NMC cells. To address this issue, studies next quarter will replace LPS with new SE compositions (for example, LPSCl) in the composite cathode and/or separator. New cathode compositions and mixing methodologies will also be explored to optimize SSB performance.

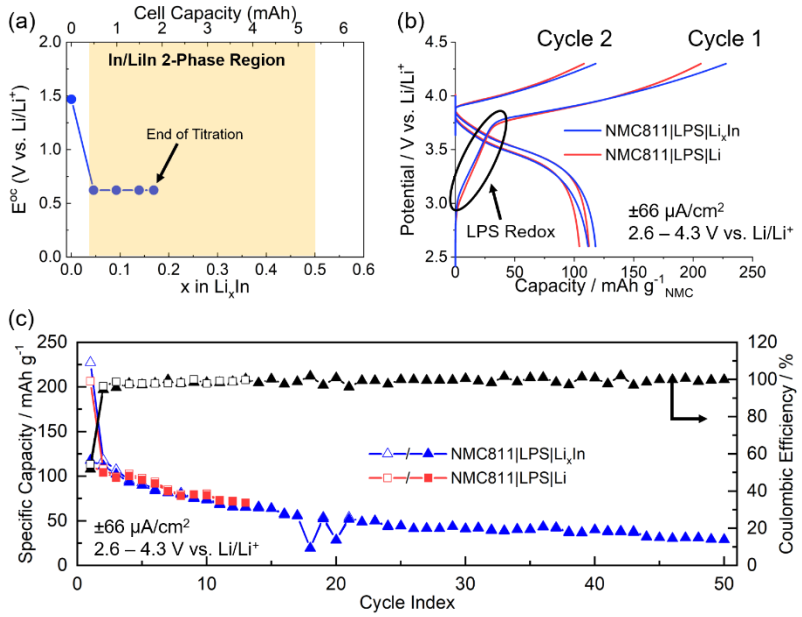

Figure 105. (a) Open-circuit potential (E^{oc}) of a Li_xIn alloy prepared by Coulombically titrating indium metal in a Li|LPS|In solid-state battery (SSB) at -79 µA/cm² at room temperature. (b-c) Electrochemical characterization of SSBs containing an NMC-811 cathode, LPS separator, and either a Li-metal or $Li_{0.169}In$ anode tested at room temperature with a stack pressure of 5 MPa. (b) Galvanostatic charge/discharge curves for the first 2 cycles and (c) cycling performance. In panels (b-c), the cathode potential in the Li_xIn-containing SSB was referenced versus Li/Li^+ by adding 0.622 V to the measured cell potential. Spurious data points at cycles 18 and 20 are due to a potentiostat glitch.

Patents/Publications/Presentations

Publication

- Self, E. C., P-H. Chien, L. F. O'Donnell, D. Morales, J. Lieu, T. Brahmbhatt, S. Greenbaum, and J. Nanda. "Investigation of Glass-Ceramic Lithium Thiophosphate Solid Electrolytes Using NMR and Neutron Scattering." *Materials Today Physics* 21 (2021): 100478. doi: 10.1016/j.mtphys.2021.100478.

Task 4.6 – Prelithiation of Silicon Anode for High-Energy Lithium-Ion Batteries (Yi Cui, Stanford University)

Project Objective. Prelithiation of high-capacity electrode materials is an important means to enable those materials in high-energy batteries. This study pursues three main directions: (1) development of facile and practical methods to increase 1st-cycle CE of anodes, (2) synthesis of fully lithiated anode to pair with high-capacity, Li-free cathode materials, and (3) prelithiation from the cathode side.

Project Impact. Prelithiation of high-capacity electrode materials will enable those materials in the next generation of high-energy-density Li-ion batteries. This project's success will make high-energy-density Li-ion batteries for EVs.

Approach. Silicon electrode film will be prepared by coating the slurry of silicon nanoparticles, carbon black, and binder mixture on copper foil through a doctor-blading method. The silicon electrode film will be prelithiated by pressing a Li-metal foil on top of it and heating it in an argon glovebox for a certain time. Then, Li_xSi electrode film can be obtained by removing the redundant lithium foil through a peeling-off approach. The redundant lithium foil is reusable for the next prelithiation. The structure, morphology, and other properties can be analyzed by SEM, TEM, XPS, Raman spectroscopy, XRD, etc. In the first year, the team aims to fabricate Li_xSi freestanding electrode film and improve its air stability. In the second year, the team aims to improve the electrochemical stability in full cells.

Out-Year Goals. Materials containing a large quantity of lithium will be synthesized for pre-storing lithium ions inside batteries. Materials and processes will be developed to be compatible with battery electrode and cell fabrication. First-cycle CE of anodes will be improved and optimized by prelithiation materials. Develop materials for prelithiation from the cathode side.

Collaborations. This project engages in collaboration with the following: BMR PIs; SLAC: M. Toney *(in situ* X-ray); and Stanford: W. Nix (mechanics).

Milestones

1. Produce ultra-thin lithium foil as a new dry prelithiation reagent. Produce lithium foil of different thickness to match the varied anode capacity. (Q1, FY 2021; Completed)
2. Demonstrate controllable initial CE improvement by prelithiation with ultra-thin lithium foil of different thickness. (Q2, FY 2021; Completed)
3. Demonstrate the microstructural and chemical evolution of silicon anode during ultra-thin lithium foil prelithiation. (Q3, FY 2021; Completed)
4. Demonstrate the role of ultra-thin lithium foil prelithiation to improve good cycle capacity retention in full battery. (Q4, FY 2021; In progress)

Progress Report

Substantial improvements on energy density of Li-ion batteries require development of high-capacity electrodes. Silicon anodes—which have high theoretical capacities (3579 mAh/g) that are ten times higher than the conventional graphite anodes (372 mAh/g)—hold great potential for application in high-energy Li-ion batteries. However, silicon anodes exhibit a low initial CE of 50-80%, which means 20-50% of battery capacity will be lost after 1st cycle due to side reactions. Therefore, a strategy to compensate for the initial active lithium loss and improve initial CE is urgently needed to prevent battery capacity degradation.

Last quarter, the team presented fabrication of reduced Gr oxide (rGO) hosted ultra-thin lithium (Li@eGF) foils as a new prelithiation reagent. Through a tunable calendering process and an edge-contacting molten lithium infusion, Li@eGF foils with varied thickness of 0.5 to 20 μm were fabricated, corresponding to 0.1 mAh cm^{-2} to 4 mAh cm^{-2} capacity, respectively. The team has further applied Li@eGF foils for silicon anode prelithiation, and has achieved controllable initial CE improvement from ~ 80% to ~ 100%. Here, they report on continued investigation of the chemical and morphological evolution of silicon anode with Li@eGF prelithiation.

They first investigated chemical evolution of silicon anode after Li@eGF prelithiation through XPS. High-resolution silicon 2p spectra (Figure 106a) can be differentiated into three peaks: Li_xSiO_y at ~ 102 eV, silicon peak at ~ 99.2 eV, and Li_xSi peak at ~ 98.2 eV. The appearance of Li_xSiO_y peak and Li_xSi peak indicates prelithiated status of silicon, where Li_xSiO_y comes from lithiated surface oxides on silicon particles. Interestingly, silicon peak remains after prelithiation, indicating partial lithiation of silicon particles. This phenomenon raises the assumption that in the 100-nm silicon particles used in this project, the outer surface of the particles is lithiated, while the core of the particles remains in pristine state. The slow prelithiation of silicon core can be possibly explained by the low diffusion coefficient of lithium ions in silicon (~ 10^{-12} cm^2/s) and the limited prelithiation time of 10 hours. Figure 106b further shows the appearance of lithium 1s peak after prelithiation, confirming the prelithiated status of silicon. LiF and ROLi signals possibly come from the reduction product of electrolyte. Besides chemical evolution of silicon anode after Li@eGF prelithiation, the team further explores the morphological evolution of silicon anode with and without Li@eGF prelithiation after cycling. A unique advantage of Li@eGF in prelithiation is that it leaves a conductive layer of reduced graphene (exfoliated graphene fluoride, eGF) film above silicon anode after prelithiation. This eGF film acts both as a secondary current collector to enhance the conductivity between silicon particles, and as a protective layer to tightly hold the silicon particles together to reduce cracks. As shown in the SEM images, silicon anode cycled without Li@eGF prelithiation is not protected by eGF film during cycling, thus leading to amounts of cracks after cycling (Figure 106c). In comparison, silicon anode cycled with Li@eGF prelithiaion shows a smooth surface without obvious cracks (Figure 106d), which has benefited from the condensation role of eGF film. These results well support that Li@eGF provides strong protection of silicon anode during cycling.

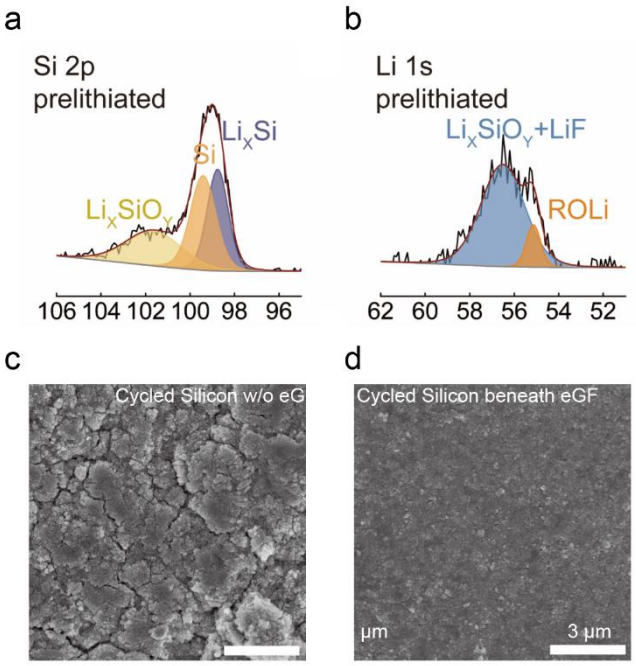

Figure 106. (a-b) X-ray photoelectron spectra of the silicon anode after Li@eGF prelithiation. (a) Silicon 2p spectra. (b) Lithium 1s spectra. (c-d) Top-view scanning electron microscopy images of cycled silicon anode without (c) and with (d) Li@eGF prelithiation.

Patents/Publications/Presentations

Publication

- Chen, H., Y. Yang, D. T. Boyle, Y. K. Jeong, R. Xu, L. S. de Vasconcelos, and Y. Cui. "Free-Standing Ultrathin Lithium Metal–Graphene Oxide Host Foils with Controllable Thickness for Lithium Batteries." *Nature Energy* 6 (2021): 790–798.

TASK 5 – SULFUR ELECTRODES

Team Lead: Prashant Kumta, University of Pittsburgh

Summary

The collected work of the projects in this Task encompasses the following areas:

- Conducting focused fundamental research on the mechanism of "shuttle effect" inhibition for rechargeable Li-S batteries.
- Developing electrode and electrolyte systems that can mitigate the "shuttle effect" so the low self-discharge and long cycle life can be achieved.
- Synthesizing sulfur composite materials with an emphasis on polymer sulfur composite materials.
- Developing creative electrode-making processes to improve processability and aerial capacity; for example, polymeric sulfur composites may not be suitable for the traditional slurry casting process.
- Developing a novel S_xSe_y cathode material for rechargeable lithium batteries with high energy density and long life, as well as low cost and high safety.
- Delivering an electrochemically responsive self-formed hybrid LIC as a protective layer for Li-metal anodes, enabling Li-metal anodes to cycle with a high efficiency.
- Developing high-energy, low-cost Li-S batteries with long lifespan.

Highlights. The highlights for this quarter are as follows:

- The ANL team (K. Amine) focused on investigating the electrochemical performance of sulfur / 3D ordered microporous sulfur host (OMSH) / ZnS,Co-N-C composite. This composite structure exhibits double-end binding (DEB) sites that serve to immobilize while also enabling the catalysis of the polysulfides. They showed that these novel composite systems exhibited a higher capacity retention rate of 93.86% and a CE of 100% after cycling at 0.2C rates for 100 cycles, compared to the standard Ketjenblack (KB) / sulfur composite that exhibits only 60.25% capacity retention and a CE of 97%. They also showed that the novel 3D-OMSH/ZnS,Co-N-C composite presents the highest specific capacity of ~ 750-1400 mA h g^{-1} when tested at 5.0C to 0.15C rates. They state that this outstanding performance is due to the DEB sites serving to physically bind and catalyze the polysulfides over that of the single-end binding (SEB) sites prevalent in C/S systems. They have also demonstrated that the system is able to deliver areal sulfur capacities of 4.9 mA h cm^{-2} and 6.5 mA h cm^{-2} for sulfur loadings of 6 mg cm^{-2} and 9 mg cm^{-2}, respectively, when cycled at 0.6C for 100 cycles. The team plans to conduct detailed characterization and modeling to reveal the underlying mechanisms. The results demonstrate the efficacy of these novel 3D-OMSH/ZnS,Co-N-S DEB site composite structures for attaining promising Li-S battery performance.
- The PNNL group (D. Lu and J. Liu) further studied the effect of particle size of carbon and inclusion of Li-ion conducting polymeric or inorganic additives on the electrolyte infiltration and porosity on overall electrochemical performance. They have demonstrated realization of extremely low porosity of 25% in high sulfur loaded electrodes of 4 mg cm^{-2} under lean electrolyte conditions of electrolyte/sulfur (E/S) = 2.5 ml mg^{-1} S, resulting in the electrode delivering a capacity > 1000 mA h g^{-1}. Decreasing electrode porosity not only increases cell energy density, but also extends cell cycling under lean electrolyte conditions. Accordingly, they have demonstrated that electrodes with 35% porosity and 25% porosity both having high sulfur loadings of 4 mg cm^{-2} can be cycled at lean electrolyte conditions of 3 ml mg^{-1} and 2.5 ml mg^{-1}, exhibiting capacities > 1000 mA h g^{-1} for 25 cycles and 15 cycles, respectively, albeit in coin cells. These

results demonstrate the influence of reduced electrode porosity and electrolyte uptake with the use of an effective LIC. The team plans to understand the mechanism of the improved cell performance while identifying methods to minimize electrolyte permeation during cell assembly.

- The Stanford group (Y. Cui) report continuing results demonstrating the efficacy of use of an effective catalyst to lower the over-potential for removal of lithium in Li_2S in their quest to overcome the polysulfide dissolution problem in SPEs in fabricating an ASSLSBs. They have correspondingly showed that by coating TiS_2 on Li_2S, the activation energy barrier is reduced to below 2.5 V, as opposed to 3.3 V. Furthermore, the coating is successful in lowering the impedance and thereby reducing the charge transfer resistance compared to uncoated bare Li_2S. CV also confirms the lower oxidation potential and higher reduction potential of the TiS_2-coated Li_2S compared to the bare uncoated Li_2S electrodes. Similarly, the peak CV current versus the square root of the scan rates, although showing a linear relationship, exhibits a higher slope for the TiS_2 coated Li_2S compared to uncoated Li_2S, reflecting a faster Li-ion diffusion within the coated Li_2S electrode. They further affirmed their observation by first-principles calculation, showing that the TiS_2 coating indeed modulates the Li_2S oxidation energetics, making it more favorable. Their results clearly demonstrate the influence of an effective catalyst for harnessing useful electrochemical response of Li_2S as the cathode likely facilitating the generation of ASSLSBs.
- The BNL / University of Wisconsin, Milwaukee, group (E. Hu and D. Qu) have conducted a thorough characterization of sulfur organic polymers to evaluate their efficacy toward reduced polysulfide dissolution and exhibiting high capacity. They conducted XRD and DSC analyses to illustrate that the sulfur ceases to exist as a crystalline phase and that the thermal signature also does not showcase the characteristic phase transition, melting, and liquid sulfur phase transitions. They also extracted sulfur in the polymer via solvent extraction and observed that although elemental sulfur was seen in the extractant following high-performance liquid chromatography, but only to less than 2 wt% of sulfur, indicating that most of the sulfur remained in the stable polymer. The initial constant current cycling results of the polymers showed performance signatures very similar to that of Li-S polymer batteries in ether-based electrolytes exhibiting capacities as high as 800 mA h gm^{-1}. These results thus attest to the benefits of vulcanization of sulfur in an organic backbone polymer for confining the sulfur and preventing polysulfide migration in Li-S batteries.
- The UCB group (G. Liu) studied the influence of $LiNO_3$ to stabilize the Li-metal surface and the combined effect on the performance characteristic of a dissolved polysulfide solution in a traditional sulfur electrode design. The team has correspondingly studied Li-S cells with high LiTFSI concentration electrolytes such as 0.6 M and 0.8 M LiTFSI, exhibiting low specific capacity of 300 mA g^{-1} and 400 mA g^{-1}, respectively. They confirm that the 0.4 M LiTFSI with 0.6 M $LiNO_3$ electrolyte exhibits low capacity of ~ 500 mA g^{-1} in early cycles increasing to higher values of 800 mA g^{-1} compared to the commercial electrolyte of 1 M LiTFSI with 1% $LiNO_3$ (~ 0.15 M) after 30 cycles. However, the cells begin to fade after 70 cycles, likely due to consumption of the $LiNO_3$. They also confirm that although 0.6 M and 0.8 M LiTFSI electrolytes with fixed amounts of 0.6 M $LiNO_3$ showed low capacity, they nevertheless exhibit high CEs of ~ 100% for 100 cycles. These results essentially demonstrate the effect of additives in stabilizing the Li-metal anode; however, continued consumption of these additives could ultimately lead to decreased cell performance, thereby emphasizing the need for polysulfide dissolution resistant electrolytes for improved Li-S battery performance.

Task 5.1 – Novel Chemistry: Lithium Selenium and Selenium Sulfur Couple (Khalil Amine, Argonne National Laboratory)

Project Objective. The project objective is to develop a novel S_xSe_y cathode material for rechargeable lithium batteries with high energy density and long life, as well as low cost and high safety.

Project Impact. Development of a new battery chemistry is promising to support the goal of PHEV and EV applications.

Approach. The dissolution of lithium polysulfides in nonaqueous electrolytes has been the major contribution to the low energy efficiency and short life of Li-S batteries. In addition, insulating characteristics of both end members during charge/discharge (sulfur and Li_2S) limit their rate capacity. To overcome this problem, sulfur or Li_2S is generally impregnated in a carbon-conducting matrix for better electronic conductivity. However, this makes it difficult to increase the loading density of practical electrodes. It is proposed to solve these barriers using the following approaches: (1) partially replace sulfur with selenium, (2) nano-confine the S_xSe_y in a nanoporous conductive matrix, and (3) explore advanced electrolytes with suppressed shuttle effect.

Out-Year Goals. This new cathode will be optimized with the following goals:

- A cell with nominal voltage of 2 V and energy density of 600 Wh/kg.
- A battery capable of operating for 500 cycles with low capacity fade.

Collaborations. This project engages in collaboration with the following: Y. Ren and C. Sun of APS at ANL, and L. A. Curtiss and L. Cheng at ANL.

Milestones

1. Build in-house Li-S pouch cell fabrication line, and demonstrate > 100 mAh pouch cell performance using Se-doped sulfur cathode and fluorinated ether-based electrolytes. (Q1, FY 2021; Completed)
2. Design and characterize novel cathode host for Li-S and Li-Se/S batteries. (Q2, FY 2021; Completed)
3. Validate electrochemical performance of new cathode host. (Q3, FY 2021; In progress)
4. Conduct *operando* and *ex situ* characterization on developed cathodes during charge/discharge. (Q4, FY 2021; In progress)

Progress Report

This quarter, the team has investigated the electrochemical performance of sulfur/3D-OMSH/ZnS,Co-N-C composite. The electrolyte is conventional ether-based electrolytes (1 M LiTFSI/DOL + DME (1/1,v/v) + 0.1 M $LiNO_3$). The E/S ratio for all the cells was controlled at ~ 10 µL mg^{-1}. To demonstrate the effectiveness of the team's DEB sites concept in immobilizing and catalyzing polysulfides, the team prepared and tested the following sulfur cathode materials for comparison: KB/S, 3D-OMSH without ZnS/Co-N-C DEB sites (denoted as 3D-OMSH/pure-carbon/S), 3D-OMSH with only ZnS polar sites (denoted as 3D-OMSH/ZnS/S) and 3D-OMSH with only Co-N-C single-atom catalyst sites.

As shown in Figure 107a, the 3D-OMSH / ZnS,Co-N-C/S cathode exhibited a higher capacity retention rate (93.86%) and CE (100%) after cycling at 0.2 C (1.0 C= 1.675 mA g^{-1}) for 100 cycles, as compared with KB/S (60.25% and 97%, respectively), 3D-OMSH/pure-carbon/S (54.7% and 94%), 3D-OMSH/ZnS/S (69.22% and 97%), and 3D-OMOSH/Co-N-C/S (83.15% and 98%). These findings demonstrate that the DEB sites can effectively immobilize the dissolved LiPSs to eliminate the capacity decay caused by the shuttle effect. At a higher charge/discharge rate of 1.0 C, the 3D-OMSH/ZnS,Co-N-C/S cathode still demonstrated the best performance among the five samples (Figure 107b). The rate capability test (Figure 107c) further showed that the 3D-OMSH/ZnS,Co-N-C/S cathode presents the highest specific capacity among the five samples under all testing rates (0.15 C to 5.0 C). These results clearly demonstrate the significant advantages of DEB sites over SEB sites in suppressing the LiPS shuttle effect and boosting the reaction kinetics (Figure 108). For bare carbon, there is very weak physical binding strength and poor catalyzing effect on the polysulfides, resulting in severe polysulfide dissolution into the electrolytes, hence leading to rapid capacity degradation. For SEB sites, either the binding strength or the catalyzing effect is not optimal. In sharp contrast, the DEB sites can provide both high binding strength and good catalyzing effect. This is because the interfacial redox kinetics of Li-S batteries is dominated by the following: (1) a large binding energy, allowing adsorption with sufficient surface coverage, and (2) fast charge transfer at the triple-phase boundaries during the redox reaction of the adsorbates, requiring an optimal 'polysulfides confinement-catalysis' process.

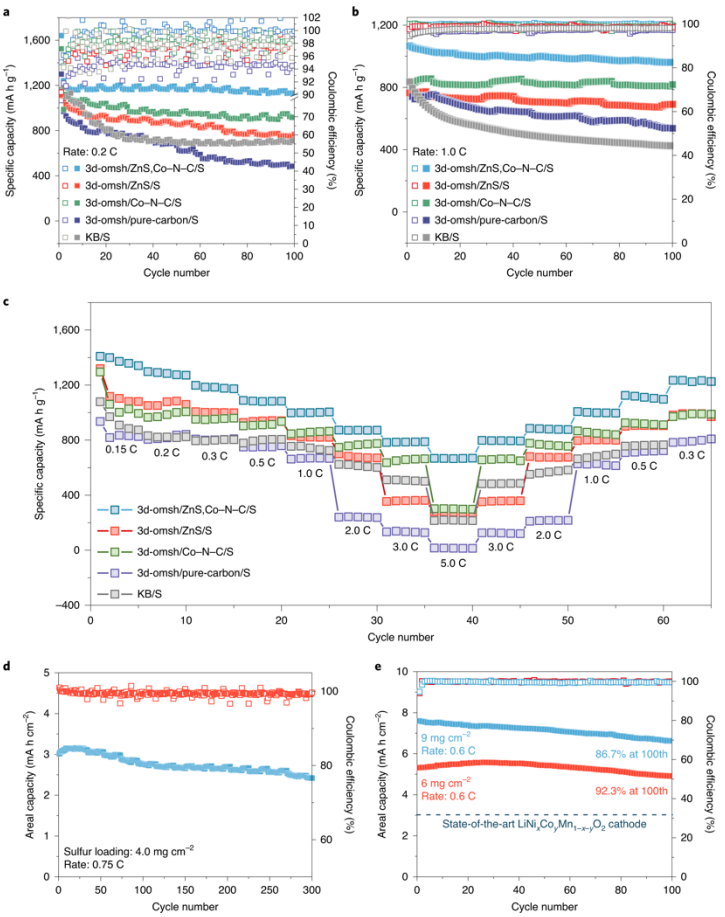

Figure 107. (a-b) Cycling performance of various sulfur cathodes at a charge/discharge rate of 0.2 C (a) and 1.0 C (b). (c) Rate capability of various sulfur cathodes. (d-e) Cycling performance of the 3D-OMSH/ZnS,Co-N-C/S cathode with high areal sulfur loading: 4 mg cm^{-2} for 300 cycles at 0.75 C (d) and 6 mg cm^{-2} and 9 mg cm^{-2} for 100 cycles at 0.6 C (e).

The team further evaluated electrochemical performance of the sulfur/3D-OMSH/ZnS,Co-N-C composite at a high areal sulfur loading. Under a higher areal sulfur loading to 4.0 mg cm^{-2} (Figure 107d), the 3D-OMSH/ZnS,Co-N-C/S exhibits an initial areal capacity of 3.07 mA h cm^{-2} and can maintain a reasonable

areal capacity of 2.41 mA h cm^{-2} with minimal voltage polarization after 300 cycles at 0.75 C, demonstrating good cycling stability. Moreover, the CE is all maintained at ~ 100%, indicating low shuttle effect. The team further increased the areal sulfur loading to extreme high areal sulfur loading of 6 mg cm^{-2} and 9 mg cm^{-2} (Figure 107e). After cycling at 0.6 C for 100 cycles, these cathodes can still deliver 4.9 mA h cm^{-2} and 6.5 mA h cm^{-2}, respectively. Such results have outperformed many reported results based on SEB sites.

Therefore, the key to achieving excellent electrochemical performance of Li/S batteries is to balance the binding strength and catalyzing effect. The team will conduct detailed characterization and modeling to reveal the underlying mechanisms. These findings have also inspired the team to create better structural designs to achieve even better electrochemical performance.

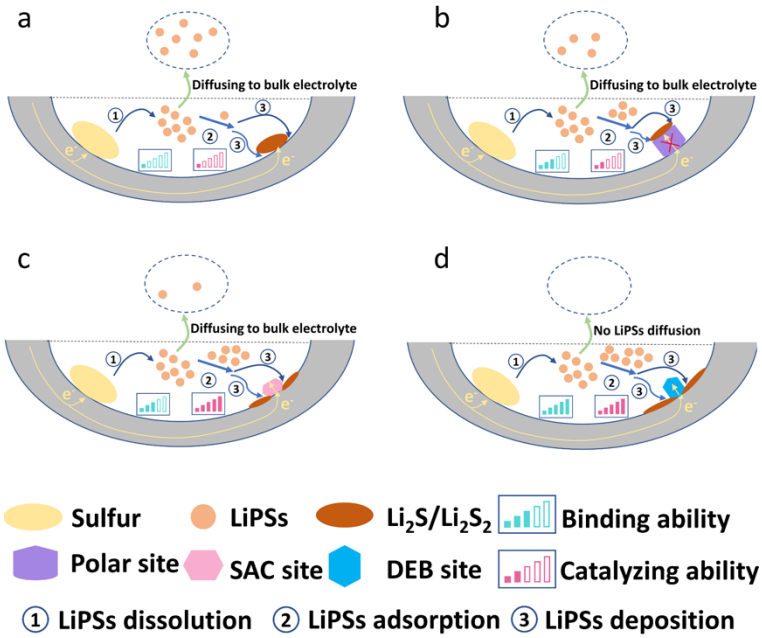

Figure 108. Scheme for demonstrating the effectiveness of different hosts in immobilizing and catalyzing lithium polysulfides: (a) bare carbon, (b) carbon+polar site, (c) carbon+SAC, and (d) carbon+SAC+polar site. DEB: double-end binding; LiPSs: lithium polysulfides; and SAC: single-atom catalyst.

Patents/Publications/Presentations

Presentations

- 239th ECS Meeting, Digital Meeting (May 31, 2021): "New Cathode and Electrolytes Strategies to Enable High-Energy Li-S Batteries"; G-L. Xu and K. Amine.
- Battery & Electrification Summit (June 16, 2021): "Stabilization of Advanced Cathode and Anode to Make Better Batteries"; G-L. Xu. Invited.

Task 5.2 – Development of High-Energy Lithium-Sulfur Batteries (Dongping Lu and Jun Liu, Pacific Northwest National Laboratory)

Project Objective. The project objective is to develop high-energy, low-cost Li-S batteries with long lifespan. All proposed work will employ thick sulfur cathode (≥ 4 mg/cm^2 of sulfur) at a relevant scale for practical applications. The diffusion process of soluble polysulfide out of thick cathode will be revisited to investigate cell failure mechanism at different cycling. The fundamental reaction mechanism of polysulfide under the electrical field will be explored by applying advanced characterization techniques to accelerate development of Li-S battery technology.

Project Impact. The theoretical specific energy of Li-S batteries is ~ 2300 Wh/kg, which is almost three times higher than that of state-of-the-art Li-ion batteries. The proposed work will design novel approaches to enable Li-S battery technology and accelerate market acceptance of long-range EVs required by the EV Everywhere Grand Challenge.

Approach. The project proposes the following approach: (1) to identify and address key issues of applying high-energy sulfur cathodes including materials, binders, electrode architectures, and functional electrode additives, (2) to advance the mechanism study of sulfur cathode and electrolyte by using *in situ* / *ex situ* techniques and custom-designed hybrid cell setup, and (3) to verify effectiveness of the new approaches with coin/pouch cells by using high-loading electrodes (> 4 mg/cm^2), limited lithium (< 200% lithium excess), and lean electrolyte (E/S < 4 µL/mg).

Out-Year Goals. This project has the following out-year goals:

- Fabricate Li-S pouch cells with thick electrodes to understand sulfur chemistry/electrochemistry in environments similar to those witnessed in real application.
- Leverage the Li-metal protection project funded by the DOE and PNNL advanced characterization facilities to accelerate development of Li-S battery technology.
- Develop Li-S batteries with a specific energy of 400 Wh/kg at cell level, 1000 deep-discharge cycles, improved abuse tolerance, and less than 20% capacity fade over a 10-year period to accelerate commercialization of EVs.

Collaborations. This project engages in collaboration with the following: X-Q. Yang (BNL), J. Bao (PNNL), P. Khalifah (BNL), and J. Tao (PNNL).

Milestones

1. Optimize electrode architecture to realize sulfur utilization of > 1000 mAh/g in high loading sulfur electrode (> 4 mg S/cm^2) at very low porosity (< 40%). (Q1, FY 2021; Completed)
2. Build an electrode model to understand the effects of electrode porosity and tortuosity on the electrolyte transport and sulfur reaction kinetics. (Q2, FY 2021; Completed)
3. Enable a quasi-SE network by introducing PEs and/or SEs into the low porosity electrodes, and realize cell operation at an extremely low E/S. (Q3, FY 2021; Completed)
4. Identify compatible binder and solvent combinations to enable the scale-up preparation of the quasi-SE. (Q4, FY 2021; In progress)

Progress Report

This quarter, an extremely low porosity (25%) was realized in high sulfur-loaded electrodes while maintaining a high sulfur utilization rate > 1000 mAh/g; effects of polymers on the performance of dense sulfur electrodes were studied at various porosities and electrolyte conditions. The task focus is to minimize pore-filling electrolyte by reducing the electrode porosity and conserving more electrolyte available for cell cycling. When compared to dense NMC cathodes of the same areal capacity, sulfur cathodes are much thicker and more porous (> 65%) due to use of low density and porous S/C materials that severely diminish the cell energy and require more electrolyte to fill the pores. In practice, reducing porosity of high-loading electrodes is hindered by poor electrode wetting and low sulfur utilization rate. Electrodes featuring low porosity have slow electrolyte diffusivity, limiting reaction kinetics and sulfur utilization rate. Therefore, approaches that can promote electrolyte infiltration and distribution in a dense cathode are critical to increase the effective electrolyte supply, particularly at a low E/S ratio.

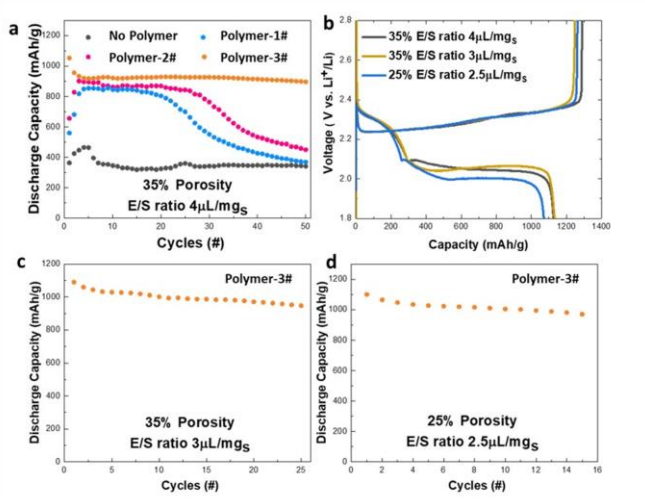

Figure 109. Electrochemical performances of low-porosity sulfur electrodes with polymer/liquid electrolyte design. (a) Effects of polymer on sulfur utilization rate and cycling stability with electrode porosity of 35% and E/S ratio = 4 μL/mg. (b) Charge/discharge curves of polymer integrated electrodes at various porosities and E/S ratios. (c) Cycling performance of 35% porosity electrode and E/S ratio = 3 μL/mg. (d) Cycling performance of 25% porosity electrode at E/S = 2.5 μL/mg. Note: 4 mg S/cm² and 0.1C for both charge and discharge.

The team strategy is to build up a hybrid Li-ion conduction network in dense electrodes by introducing an appropriate solid polymer or inorganic Li^+ conductors. Results presented here are based on polymer/liquid hybrid electrolytes. The selected polymer can be introduced into the electrodes either through pre-coating of cathode materials or during the slurry making. After electrode drying and calendering, the polymeric components will stay between the electrode particles or in the electrode voids. One important selection criterion for the polymer is high affinity with LEs. This helps to address electrode wetting issues in low-porosity electrodes by facilitating uniform electrolyte infiltration through the polymeric networks. After electrode wetting, interactions between the PEs and LEs cause partial solidification or gelation of the LEs, which in turn confines the LE inside the electrode and suppresses free shuttling of soluble lithium polysulfides. The team studied effects of polymer property and content on cell performance by using high-sulfur loaded electrodes (4 mg/cm^2) under lean electrolyte conditions. The presence of a polymer component improves sulfur utilization in low-porosity electrodes, with the effectiveness dependent on the polymer properties. For the electrode at a porosity of 35% without polymer, high polarization and very limited capacity were observed at lean electrolyte conditions (E/S=4 μL/mg) due to blocked electrode wetting (Figure 109a). Introducing polymer into the electrodes significantly improved the sulfur utilization rate, particularly for polymer-3#. The electrode delivered a high initial specific capacity of > 1000 mAh/g and maintained stable cycling for over 50 cycles. To validate the effectiveness of the approach, electrode porosity was further decreased to 25%, and the E/S was lowered to 2.5 μL/mg S. As shown in Figure 109b, the 35% electrodes have almost identical discharge capacities at E/S of 4 μL/mg and 3 μL/mg. Even at harsh conditions of 25% porosity and E/S of 2.5 μL/mg, the electrode is still able to deliver a capacity > 1000 mAh/g. Benefits of decreasing electrode porosity not only include an increase in cell energy density, but also extending the cell cycling under lean electrolyte conditions. As shown in Figure 109c-d, the electrode can be cycled at E/S ratios of 3 μL/mg and 2.5 μL/mg in coin cells, while the cells using porous electrodes always fail under similar conditions. This strategy is transferrable to practical Li-S pouch cell fabrication. Continuing research is focused on understanding the mechanism behind the improved cell performance and identifying measures to facilitate utilization of the electrolyte that is permeated out of the electrodes during the cell assembling process.

Patents/Publications/Presentations

Patent

- Lu, D., Z. Yu, J. Xiao, and J. Liu. "Stable and Highly Conductive Sulfide Based Solid-State Electrolytes." U. S. Pat. App. No. 63/145,063.

Presentations

- MRS Spring Meeting, Virtual (April 17–23, 2021): "Rational Design of Sulfur Cathode for High-Energy Lithium-Sulfur Batteries"; S. Feng, L. Shi, C. Anderson, Y. Lin, J. Xiao, J. Liu, and D. Lu.
- MRS Spring Meeting, Virtual (April 17–23, 2021): "Enabling Highly Conductive and Flexible Solid-State Electrolyte Film for All-Solid-State Lithium-Sulfur Batteries"; Z. Yu, K. Ahn, J. Xiao, J. Liu, and D. Lu.
- MRS Spring Meeting, Virtual (April 17–23, 2021): "Reaction Heterogeneity in High-Energy Lithium-Sulfur Pouch Cells"; L. Shi, C. Niu, C. Anderson, S. Feng, D. Liu, D. Lu, J. Xiao, and J. Liu.

Task 5.3 – Nanostructured Design of Sulfur Cathodes for High-Energy Lithium-Sulfur Batteries (Yi Cui, Stanford University)

Project Objective. The charge capacity limitations of conventional TM oxide cathodes are overcome by designing optimized nano-architectured sulfur cathodes. This study aims to enable sulfur cathodes with high capacity and long cycle life by developing sulfur cathodes from the perspective of nanostructured materials design, which will be used to combine with Li-metal anodes to generate high-energy Li-S batteries. Novel sulfur nanostructures as well as multi-functional coatings will be designed and fabricated to overcome issues related to volume expansion, polysulfide dissolution, and the insulating nature of sulfur.

Project Impact. The capacity and cycling stability of sulfur cathode will be dramatically increased. This project's success will make Li-S batteries to power EVs and decrease the high cost of batteries.

Approach. The approach involves three main efforts:

- Advanced nanostructured sulfur cathodes design and synthesis, including (1) engineer empty space into sulfur cathode to solve problem of electrode volume expansion, (2) develop novel sulfur nanostructures with multi-functional coatings for confinement of S/Li polysulfides to address issues of active materials loss and low conductivity, (3) develop/discover optimal nanostructured materials that can capture the polysulfide dissolved in the electrolyte, (4) develop space-efficiently-packed nanostructured sulfur cathode to increase volumetric energy density and rate capability, and (5) identify interaction mechanism between sulfur species and different types of oxides/sulfides, and find optimal material to improve capacity and cycling of sulfur cathode.
- Structure and property characterization, including *ex situ* SEM, XPS analysis, and *in operando* XRD and optical microscopy.
- Electrochemical testing including coin cells and pouch cells as well as a set of electrochemical techniques.

Out-Year Goals. The cycle life, capacity retention, and capacity loading of sulfur cathodes will be greatly improved (200 cycles with 80% capacity retention, > 0.3 mAh/cm^2 capacity loading) by optimizing material design, synthesis, and electrode assembly.

Collaborations. This project collaborates with the following: BMR PIs; SLAC: M. Toney *(in situ* X-ray); and Stanford: W. Nix (mechanics) and Z. Bao (materials).

Milestones

1. Understanding polysulfides dissolution behavior in polymer-based ASSLSBs. (Q1, FY 2021; Completed)
2. Demonstrating nanoscale encapsulation concept from liquid to ASSLSBs. (Q2, FY 2021; Completed)
3. Exploring mechanism of nanoscale encapsulation in improving ASSLSBs experimentally and theoretically. (Q3, FY 2021; Completed)
4. Enabling ASSLSBs with high energy density, long-term cycling stability, and high safety. (Q4, FY 2021; Ongoing)

Progress Report

Last quarter, to solve the polysulfide dissolution in SPEs, the team incorporated a nanoscale encapsulation concept from liquid to ASSLSBs. This quarter, the team further studied the catalytic effect of TiS_2 coating in ASSLSBs. Coin cells (type 2032) are assembled using Li_2S composite cathodes, SPEs, and Li-metal anodes. Due to the large charge transfer resistance and intrinsic poor electronic conductivity of Li_2S, the as-assembled unencapsulated Li_2S cells show a high energy barrier of 3.3 V at the initial charge cycle for activation (Figure 110a) and a large charge transfer resistance at open-circuit voltage (Figure 110b). This indicates that the oxidation reaction may only occur at the localized regions of the active particles directly interfacing electron and ion transfer channels, thus resulting in a much lower specific capacity than the theoretical value. After TiS_2 coating, the initial activation energy barrier significantly decreases below 2.5 V (Figure 110a). This is direct evidence that TiS_2 coating facilitates the Li_2S oxidation reaction. Moreover, owing to the high conductivity of TiS_2, the impedance spectrum of the as-assembled $Li_2S@TiS_2$ cells also shows a smaller semicircle in the high-frequency region compared with bare Li_2S cells, indicating a reduced charge-transfer resistance (Figure 110b). The charge transfer resistance is comparable with that in the liquid system and further decreases after 10 cycles, which indicates formation of a stable TiS_2 interface allowing fast charge transfer during cycling.

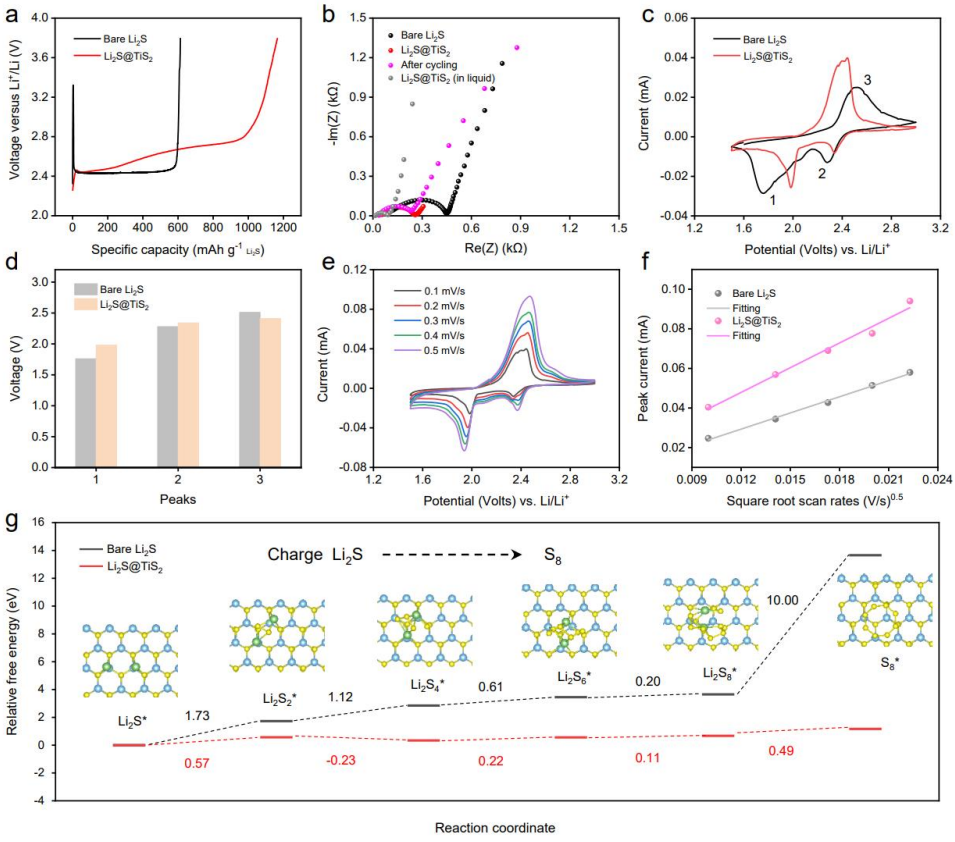

Figure 110. TiS_2 enhanced Li_2S oxidation reaction kinetics in all-solid-state Li-S batteries (ASSLSBs). (a) 1st-cycle charge voltage profiles of $Li_2S@TiS_2$ and bare Li_2S cathodes. (b) Electrochemical impedance spectra of ASSLSBs using bare Li_2S and $Li_2S@TiS_2$ cathodes, and the liquid system data adapted from *Nature Communications* 5 (2014): 5017. (c) Cyclic voltammetry (CV) curves and (d) corresponding peak potentials of $Li_2S@TiS_2$ and bare Li_2S electrode. (e) CV curves of the $Li_2S@TiS_2$ electrode at various scan rates (0.1 mV s^{-1}, 0.2 mV s^{-1}, 0.3 mV s^{-1}, 0.4 mV s^{-1}, and 0.5 mV s^{-1}). (f) Plots of CV peak current for the anodic oxidation process (peak 3: $Li_2S \rightarrow S_8$) versus the square root of the scan rates. All the cells are tested at 60°C. (g) Energy profiles for the oxidation of bare Li_2S and of Li_2S on TiS_2. The optimized geometries of TiS_2 with adsorbates (Li_2S^*, $Li_2S_2^*$, $Li_2S_4^*$, $Li_2S_6^*$, $Li_2S_8^*$, and S_8^*) are shown in the inset (titanium: blue; sulfur: yellow; and lithium: green).

CV evaluation on the as-assembled cells provides additional evidence for the catalytic effect of TiS_2 in ASSLSBs. When compared to bare Li_2S electrodes, the $Li_2S@TiS_2$ electrodes demonstrate a lower oxidation potential and higher reduction potential (Figure 110c-d), suggesting that the TiS_2 coating significantly reduces the electrode polarization by catalyzing Li-S redox reactions. Additionally, the CV curves of the as-prepared electrodes at various scan rates are used to study the electrode kinetics with respect to the Li-ion diffusion coefficient, as shown in Figure 110e. The CV peak current versus the square root of the scan rates for both $Li_2S@TiS_2$ and Li_2S electrodes (Figure 110f) shows a linear relationship. Notably, the slope of $Li_2S@TiS_2$ curve is larger than that of the bare Li_2S. According to the classical Randles-Sevcik equation for a diffusion-limited process, a larger slope of the curve for $Li_2S@TiS_2$ electrode indicates a faster lithium diffusion within the $Li_2S@TiS_2$ electrode compared to the bare Li_2S electrode, which further facilitates sulfur transformation reactions. To attain an in-depth understanding of the catalytic effect of TiS_2 coating for the improved charge reaction kinetics in ASSLSBs, the overall reaction mechanism for Li_2S oxidation is simulated theoretically. First-principles calculations propose detailed energetics and kinetics of reaction steps for the TiS_2 modulated Li_2S oxidation. As shown in Figure 110g, TiS_2 modulated Li_2S oxidation becomes the energetically favored reaction, which results in the enhanced electrochemical performance of the Li-S batteries.

Patents/Publications/Presentations

The project has no patents, publications, or presentations to report this quarter.

Task 5.4 –Investigation of Sulfur Reaction Mechanisms (Enyuan Hu, Brookhaven National Laboratory; Deyang Qu, University of Wisconsin, Milwaukee)

Project Objective. The primary objectives are as follows:

- To continue conducting fundamental research on the mechanism of the sulfur redox reaction, especially those on the interplay of the dissolved polysulfides in electrolyte and those in the solid phase in cathode during charging.
- To continue developing the polymeric sulfur electrode, adequate anode, and corresponding electrolyte to achieve high-energy-density, long-cycle-life Li-S batteries. The team will focus on the overall dissolution of polysulfide in an electrolyte and the effectiveness of polymeric sulfur electrodes.
- To develop the alternative anode materials having low reactivity with dissolved polysulfide ions.
- To continue to develop and optimize creative electrode making processes to improve processability and aerial capacity (for example, dry process and thick electrodes).

Project Impact. Further understanding of the mechanisms of all reactions in a Li-S cell will lead to mitigation of the "shuttle effect." The project results will thus guide development of sulfur cathode and Li-S designs with significant increase of energy density and of cycle life and with reduction of cost. This will greatly accelerate deployment of EVs and reduce carbon emission associated with fossil fuel consumption.

Approach. This collaborative project involves the following: (1) continue to synthesize cross-linked polymerized sulfur compounds, in which a sulfur is attached to the conductive backbone with covalent bonds; therefore, the polysulfides can be immobilized within the matrix, (2) investigate the sulfur redox reaction mechanism in the solid phase, (3) continue exploring the alternative anode materials that can cycle well and do not react with dissolved polysulfide and sulfur in the electrolyte to mitigate the "shuttle effect," and (4) develop an engineering process for high sulfur loading electrodes.

One-Year Goals. In FY 2021, the interim goal is to develop a Li-S battery with sulfur-containing cathode of 600-800 mAh/g capacity with mitigation of the "shuttle effect."

Collaborations. The PI works closely with beamline scientists at synchrotron facilities to develop novel Li-S characterization tools. The PI and co-PI collaborate closely with top scientists at ANL, LBNL, and PNNL, as well as U. S. industrial collaborators at GM, Duracell, Clarios, etc. The PI and co-PI also collaborate with scientists in China, Japan, and South Korea. These collaborations will be strengthened and expanded to give this project a vision on both today's state-of-the-art technology and tomorrow's technology in development, with feedback from the material designer and synthesizers upstream and from industrial end users downstream.

Milestones

1. Synthesize new polymeric sulfur compounds. Conduct preliminary electrochemical, optical, and synchrotron based testing of sulfur redox reaction in the solid phase (in cathode). (Q1, FY 2021; Completed)
2. Test alternative anode materials with both sulfur and polymeric sulfur electrodes and determine interaction with dissolved polysulfide ions and overall electrochemical performance. (Q2, FY 2021; Completed)
3. Investigate sulfur redox reaction in the solid phase in cathode. Test the newly synthesized polymeric sulfur materials. (Q3, FY 2021; Completed)
4. Test full cell in either coin-cell or pouch-cell format with polymeric sulfur cathode and alternative anode. (Q4, FY 2021; In progress)

5. Conduct preliminary investigations of sulfur redox reaction mechanism in the solid phase in cathode and the interplay between dissolved polysulfide ions in electrolyte and sulfide compounds in the solid. Complete and continue testing of polymeric sulfur cathode and alternative anode in full-cell format. (Annual Milestone; In progress)

Progress Report

In previous quarters, the team concluded that the polymeric sulfur compounds, which have better ability to restrain both elemental sulfur and long-chain polysulfides within the cathode, can retain the cycling capacity of a Li-S battery. This quarter, the sulfur organic polymers were thoroughly characterized, and the success and complete inverse vulcanization was validated. Although there was a small amount of elemental sulfur remaining in the polymers, most sulfur was attached to the polymer backbones.

On grinding the chunks of sulfur polymers into fine powders, the color changed from dark brown to yellowish and light-brown, which was similar in the case of elemental sulfur. It is known that some S-containing polymers will gradually decompose after synthesis. XRD and DSC were used to verify if the chemical structure of sulfur polymers was altered by mechanical grinding. As shown in Figure 111a, the diffraction patterns of crystalline S_8 were not observed in the XRD. The endothermic peaks at 104.6°C, 119.9°C, and 168.9°C were not observed in the DSC scans, either (Figure 111b). The peaks were associated with the transition of S_8 from an orthorhombic state to a monoclinic state, the melting of monoclinic sulfur, and the λ transition of liquid sulfur, respectively. Evidentially, no apparent decomposition of the sulfur polymers was observed after mechanical grinding, since S_8 was one of the products of decomposition. The content of extractable sulfur in the polymers was also measured by a solvent (DME) extraction. Interestingly, elemental sulfur was clearly detected in the extractant, as shown in Figure 111c. However, the extracted elemental sulfur only represented less than 2% (wt) of the sulfur, which indicated most of the sulfur was in a stable polymeric form.

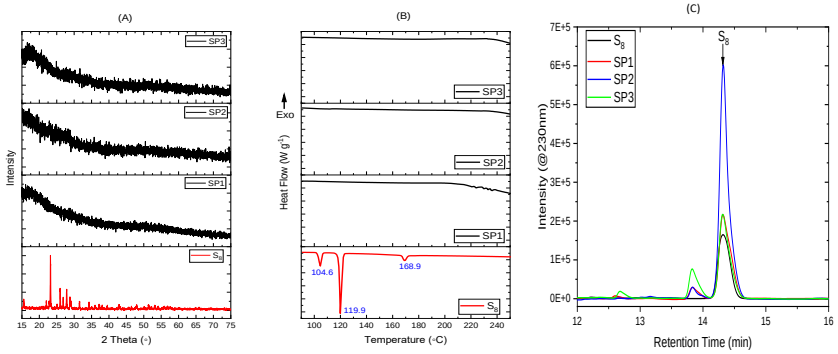

Figure 111. X-ray diffraction patterns (a) and differential scanning calorimetry curves (b) of elemental sulfur and three sulfur/organic polymers (after grinding); high performance liquid chromatograms of elemental sulfur contents in extraction solvent (c) after grinding and stirring for 72 hours in a pure DME solvent and pure elemental sulfur in DME.

The galvanostatic discharge and charge profiles for the Li-S polymer batteries are shown in Figure 112. There are two discharge plateaus and two charge plateaus for the three Li-S polymer batteries. The results were consistent with those of the Li-S polymer batteries in ether-based electrolytes reported in the literature. The discharge and recharge curves were very similar with those of traditional Li-S battery, as shown in Figure 112. It is worth pointing out that SP1 sulfur polymer material was also tested in a carbonate-based electrolyte, but unlike the sulfur polymers synthesized at high temperature, SP1 could not be cycled.

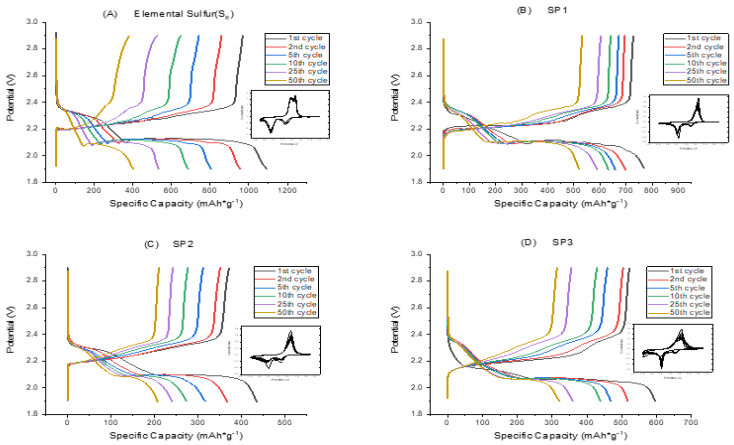

Figure 112. The discharge/charge profiles and cyclic voltammograms of a Li-S battery (a), and three Li-S polymer batteries (b-d). Specific capacities are based on the sulfur contents.

Patents/Publications/Presentations

The project has no patents, publications, or presentations to report this quarter.

Task 5.5 – New Electrolytes for Lithium-Sulfur Battery (Gao Liu, Lawrence Berkeley National Laboratory)

Project Objective. The project objective is to develop new electrolytes, additives, and electrode compositions for Li-S battery with high ion-conductivity, stable toward polysulfide and promoting the polysulfide affiliation with the electrode substrate to prevent polysulfide dissolution.

Project Impact. This work will address the high cost and low energy density of Li-ion rechargeable batteries. The emerging Li-S batteries could feature both high energy density and low cost. This project enables applications of the low-cost, abundant sulfur element as a major chemical component for electrical energy storage. This project will develop new approaches for electrolytes and electrode compositions of Li-S rechargeable batteries.

Approach. This project aims to develop new electrolytes and additives for Li-S battery. The properties of the ideal electrolyte for sulfur electrode would be high ion conductivity, stable toward polysulfide, and promoting the polysulfide affiliation with the electrode substrate to prevent polysulfide dissolution. The project is designed to first understand the electrode substrate interaction with the polysulfides in different electrolytes. This will lead to better understandings of the polysulfide nucleation and precipitation mechanisms in common electrolytes. The second stage of the project will focus on chemically modifying the structures of the solvent and salt electrolyte molecules to increase electrolyte stability and ionic conductivity, to prevent polysulfide dissolution, and to promote polysulfides precipitation.

Out-Year Goals. The team will also investigate the contribution of Li-metal electrodes to overall Li-S battery performance and will develop methods to stabilize Li-metal surface.

Collaborations. This project collaborates with J. Guo and W. Yang (ALS/LBNL), A. Minor (National Center for Electron Microscopy at LBNL/UCB), L-W. Wang (LBNL), and P. B. Balbuena, Texas A&M University.

Milestones

1. Measure polysulfide dissolution in the new amphiphilic electrolytes. (Q1, FY 2021; Completed)
2. Map out the Li-ion diffusion path in sulfur materials. (Q2, FY 2021; Completed)
3. Develop optimized sulfur electrodes according to the electrolyte properties and Li-ion transport in sulfur materials. (Q3, FY 2021; Completed)
4. Investigate the Li-metal electrode properties in the Li-S cell. (Q4, FY 2021; In progress)

Progress Report

Sulfur electrode design and Li-metal anode stabilization are important aspects to ensure proper operation of the Li-S cells. The electrolyte is one of the determining factors to the morphology and composition of sulfur electrodes. When electrolyte solvents of high polysulfide solubility are chosen, such as DOL/DME, sulfur electrode needs to have high porosity and larger pore sizes to allow reversible sulfur and Li_2S dissolution and precipitation. The larger pore sizes facilitate polysulfide transportation and precipitation during the electrochemical process, especially at high current density operation. However, when an electrolyte of very low polysulfide solubilities is used, high porosity is important to accommodate volume change of the sulfur to Li_2S transformation, but larger pore sizes are no longer critically required. Here, the team demonstrates the performance characteristic of dissolved polysulfide solutions in a traditional sulfur electrode design when different concentrations of $LiNO_3$ are used to stabilize the Li-metal surface. It is known that $LiNO_3$ additive in the electrolyte can suppress the shuttling effect and enhance cycling stability of the Li-metal electrode, since it can form a good SEI layer on lithium anode and help to capture Li_2S_x on the cathode, decreasing the excessive electrolyte decomposition and Li-polysulfide migration to the anode, respectively. In addition, the LiTFSI-based electrolyte shows high conductivity, and $TFSI^-$ anion also can help to form stable SEI layer on the anode. Consequently, the 1.0 M LiTFSI in DME:DOL (1/1, v/v) with 1% $LiNO_3$ (~ 0.15 M) has become the standard electrolyte for Li-S batteries. However, the generated-SEI layer on lithium anode could be unstable, and the $LiNO_3$ continues to be consumed during the cycling process, along with the electrolyte decomposition by exposure to lithium metal, leading to overall decrease in performance of the batteries. The alternative approach of amphiphilic hydrofluoroethers electrolyte could prevent polysulfide dissolution and stabilize Li-metal anode. In the DOL/DME (1/1, v/v) based electrolyte, the molar ratio of LiTFSI and $LiNO_3$ should be varied to obtain optimized composition in terms of high conductivity, stable SEI layer formation, and sulfur utilization to compare the cell performance results based on amphiphilic hydrofluoroether electrolyte. Herein, the $LiNO_3$ concentration is fixed at 0.6 M first, and then the LiTFSI concentration is varied from 0.2-0.8 M in DOL/DME (1/1, v/v) system. From Figure 113a, it is observed that the Li-S cells with high LiTFSI concentration electrolytes, such as 0.6 and 0.8 M LiTFSI, exhibit low specific capacity. The low capacity of the cell with 0.2 M LiTFSI electrolyte could be because of the lower conductivity compared to other electrolytes. The 0.4 M LiTFSI – 0.6 M $LiNO_3$ electrolyte having a low capacity in early cycling state shows higher capacity compared to the commercial electrolyte 1.0 M LiTFSI with 1% $LiNO_3$ (~ 0.15 M) after 30 cycles and starts to decay in capacity after 70 cycles, which might be attributed to the exhaustion of $LiNO_3$ portion in the electrolyte. Although the 0.6 M and 0.8 M LiTFSI showed low capacity, high CE is observed for these electrolytes compared to the others, as shown in Figure 113b. In a dissolved polysulfide electrolyte system (such as DOL/DME), the stabilization of Li-metal electrode is another very important factor for achieving acceptable Li-S battery electrochemical performance.

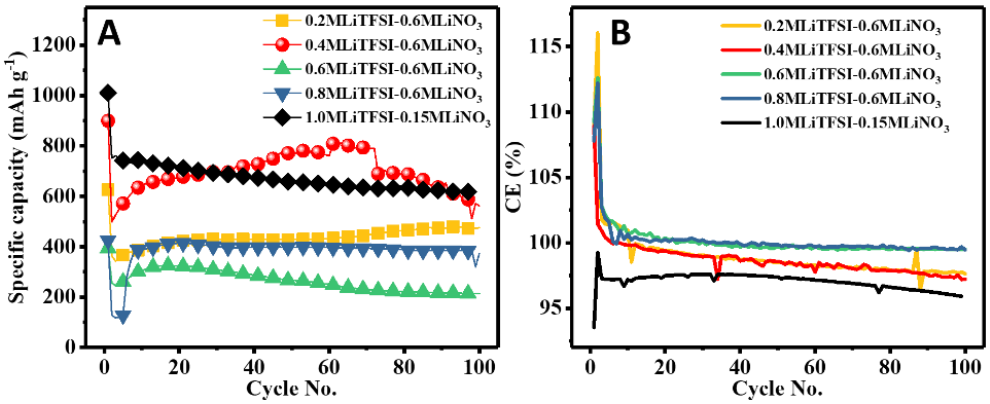

Figure 113. (a) Cycling performance of Li-S cells with different LiTFSI concentrations with 0.6 M $LiNO_3$ in DOL/DME (1/1, v/v). (b) Coulombic efficiency evolution during the cycling test.

Patents/Publications/Presentations

The project has no patents, publications, or presentations to report this quarter.

TASK 6 – AIR ELECTRODES / ELECTROLYTES

Team Lead: Ji-Guang Zhang, Pacific Northwest National Laboratory

Summary and Highlights

High-density energy storage systems are critical for EVs required by the EV Everywhere Grand Challenge. Conventional Li-ion batteries still cannot fully satisfy the ever-increasing needs because of their limited energy density, high cost, and safety concerns. As an alternative, the rechargeable lithium-oxygen (Li-O_2) battery has potential to be used for long-range EVs. The practical energy density of a Li-O_2 battery is expected to be ~ 800 Wh kg^{-1}. The advantages of Li-O_2 batteries come from their open structure; that is, they can absorb the active cathode material (oxygen) from the surrounding environment instead of carrying it within the batteries. However, the open structure of Li-O_2 batteries also leads to several disadvantages. The energy density of Li-O_2 batteries will be much lower if oxygen must be provided by an onboard container. Although significant progress has been made in recent years on fundamental properties of Li-O_2 batteries, research in this field is still in an early stage, with many barriers to be overcome before practical applications. These barriers include:

- Instability of electrolytes—The superoxide species generated during discharge or O_2 reduction process is highly reactive with electrolyte and other components in the battery. Electrolyte decomposition during charge or O_2 evolution process is also significant due to high over-potentials.
- Instability of air electrode (dominated by carbonaceous materials) and other battery components (such as separators and binders) during charge/discharge processes in an O-rich environment.
- Corrosion of Li-metal anode in an electrolyte saturated with oxygen.
- Low energy efficiency associated with large over-potential and poor cyclability of Li-O_2 batteries.
- Low power rate capability due to electrode blocking by the reaction products.
- Absence of a low-cost, high-efficiency oxygen supply system (such as oxygen selective membrane).

The main goal of this Task is to provide a better understanding on the fundamental reaction mechanisms of Li-O_2 batteries and identify the required components (especially electrolytes and electrodes) for stable operation of Li-O_2 batteries. This task will investigate several new approaches to improve stability of Li-metal anode in Li-O_2 batteries:

- Li-metal anodes will be protected using two approaches: (1) *in situ* formation of a stable SEI layer before Li-O_2 cell operation through various electrolyte formulations and treatment protocols, and (2) *ex situ* formation of stable inorganic/polymeric hybrid electrolyte layers through dip-coating or tape-casting method to coat the inorganic/polymeric hybrid electrolyte layer on Li-metal surface.
- A joint theoretical/experimental approach for design and discovery of new cathode and electrolyte materials will act synergistically to reduce charge overpotentials and increase cycle life. Synthesis methods, in combination with design principles developed from computations, will be used to make new cathode architectures. Computational studies will be used to help understand decomposition mechanisms of electrolytes and how to design electrolytes with improved stability.
- A new cathode will be developed based on high-efficiency catalyst such as 2D TM dichalcogenides (TMDs). These cathode materials will be combined with new electrolyte blends and additives that work in synergy to reduce charge potentials and increase stability of the Li-air system.

State-of-the-art characterization techniques and computational methodologies will be used to understand charge and discharge chemistries. Success of this Task will establish a solid foundation for further development of Li-O_2 batteries toward practical applications for long-range EVs. The fundamental understanding and breakthrough in Li-O_2 batteries may also provide insight on improving performance of Li-S batteries and other energy storage systems based on chemical conversion process.

Highlights. The highlights for this quarter are as follows:

- The ANL team (K. Amine, L. A. Curtiss, and J. Lu) synthesized Ir_3Li particles ranging from 200 nm to 5 μm in size using a thermal reaction between iridium and lithium metals at 800°C and fully characterized by XRD, conductive AFM, superconducting quantum interference device (SQUID), Raman, and electron paramagnetic resonance (EPR) measurements. The Ir_3Li particles in combination with rGO were used for a cathode in a Li-O_2 cell and found to result in a lithium superoxide discharge product with a low charge potential. The crystal lattice similarities of Ir_3Li to LiO_2 are consistent with its role as a template for LiO_2 formation.
- The PNNL team (J-G. Zhang and W. Xu) investigated the effect of dual catalysts [soluble: 2,2,6,6-tetramethyl-1-piperidinyloxy (TEMPO), and solid: ruthenium oxide (RuO_2) or ruthenium metal (Ru)] on the performance of Li-O_2 batteries. They found that the Li-O_2 batteries cells with dual catalysts and polymer-supported solid electrolyte interphase (PS-SEI) layer protected lithium anode led to much better cycling stability (180 cycles) than those with single catalyst with a PS-SEI layer protected lithium anode (130 cycles).
- The ANL/UIC team (L. A. Curtiss, A. Ngo, and A. Salehi-Khojin) investigated the use of a new redox mediator in conjunction with a 2D TMD catalyst, $Nb_{0.5}Ta_{0.5}S_2$, and a dimethylsulfoxide (DMSO) / IL electrolyte with an $KMnO_4$-based additive. They find that the manganate anion, MnO_4^{-2} with an oxidation potential of ~ 3.5 V (versus Li/Li^+), can serve as an effective redox mediator with the resulting permanganate anion, MnO_4^-, serving as an oxidizer for the efficient decomposition of the solid lithium peroxide.

Task 6.1 – Rechargeable Lithium-Air Batteries
(Ji-Guang Zhang and Wu Xu, Pacific Northwest National Laboratory)

Project Objective. The objective of this project is to develop rechargeable Li-O_2 batteries with long-term cycling stability through in-depth research on more stable electrolytes and highly efficient catalysts for air electrodes, protection of Li-metal anodes, and deeper understanding on the oxygen reduction reaction (ORR) and oxygen evolution reaction (OER) mechanisms behind the electrochemical performance of Li-O_2 cells. In FY 2021, the team will further improve the cycle life and safety of Li-O_2 batteries using novel polymeric colloidal localized high concentration electrolytes (PC-LHCEs), binder-free catalysts with a robust artificial SEI layer, and synthesis of stable solvents. The fundamental mechanism behind the enhanced stability of Li-O_2 batteries using these new materials will also be investigated.

Project Impact. The project will develop rechargeable Li-O_2 batteries with long-term cycling stability through in-depth research on more stable electrolytes and highly efficient catalysts for air electrodes and protection of Li-metal anodes. This fiscal year, the team will further investigate stability of electrodes with different types of catalysts to keep the reversible reactions during the Li-O_2 battery operation and electrolytes to build more stable Li-O_2 batteries with long-term cycling capability.

Approach. Develop highly stable electrolytes, including novel PC-LHCEs with an optimization of Li-metal surface protection and effective catalysts to prevent the irreversible parasitic reactions at the electrodes (cathode and anode). The electrochemical test of Li||Li symmetric cell containing above stable electrolyte will be first measured comparatively with typical ether (TEGDME) based electrolytes to evaluate the stability of the electrolyte itself and the artificial SEI layer. Then, the stability of proposed electrolytes at the cathode side with reactive oxygen species during ORR/OER will be further characterized in the Li-O_2 cells. In addition, with new synthesis of solvents to stabilize the electrolyte system, the team will find the key parameters for suitable electrolyte in Li-O_2 batteries.

Out-Year-Goals. The long-term goal of the proposed work is to enable rechargeable Li-air batteries with a specific energy of 800 Wh/kg at cell level, 1000 deep-discharge cycles, improved abuse tolerance, and less than 20% capacity fade over a 10-year period to accelerate commercialization of long-range EVs.

Collaborations. This project collaborates with C. Wang of PNNL on characterization of cycled air electrodes by TEM/SEM, with P. Gao of PNNL on computational calculations and simulations, and with J. Read of ARL on oxygen solubility tests.

Milestones

1. Develop binder-free electrocatalysts on the surface of air electrode with polymer-supported SEI and redox mediators. (Q1, FY 2021; Completed)
2. Develop PC-LHCEs using osmosis effect. (Q2, FY 2021; Completed)
3. Understand the interphase properties of PC-LHCE/electrode. (Q3, FY 2021; Completed)
4. Develop new solvents that are stable against oxidation and singlet oxygen species for reversible Li-O_2 battery systems. (Q4, FY 2021)

Progress Report

This quarter, Li-O_2 batteries with dual catalysts (soluble: TEMPO, and solid: RuO_2 or Ru; see Figure 114a) were developed to reduce the cell overpotential along with a lithium anode protection by generation of PS-SEI for long-term cycling stability. The Li-O_2 battery cells with dual catalysts and Li/PS-SEI layer lead to much higher open circuit voltage (OCV, 3.18 V) and smaller cell impedance (137 Ω) than the cells with TEMPO only (2.79 V and 193 Ω, Figure 114b). The dual catalysts with a PS-SEI also show much better cycling stability (180 cycles, Figure 114c) than the single catalyst with a PS-SEI cell (130 cycles) in the cut-off voltage range of 2 V to 5 V because the dual catalytic effect and the robust PS-SEI layer keep reversible OER to stabilize the Li-O_2 battery system for long-term operation.

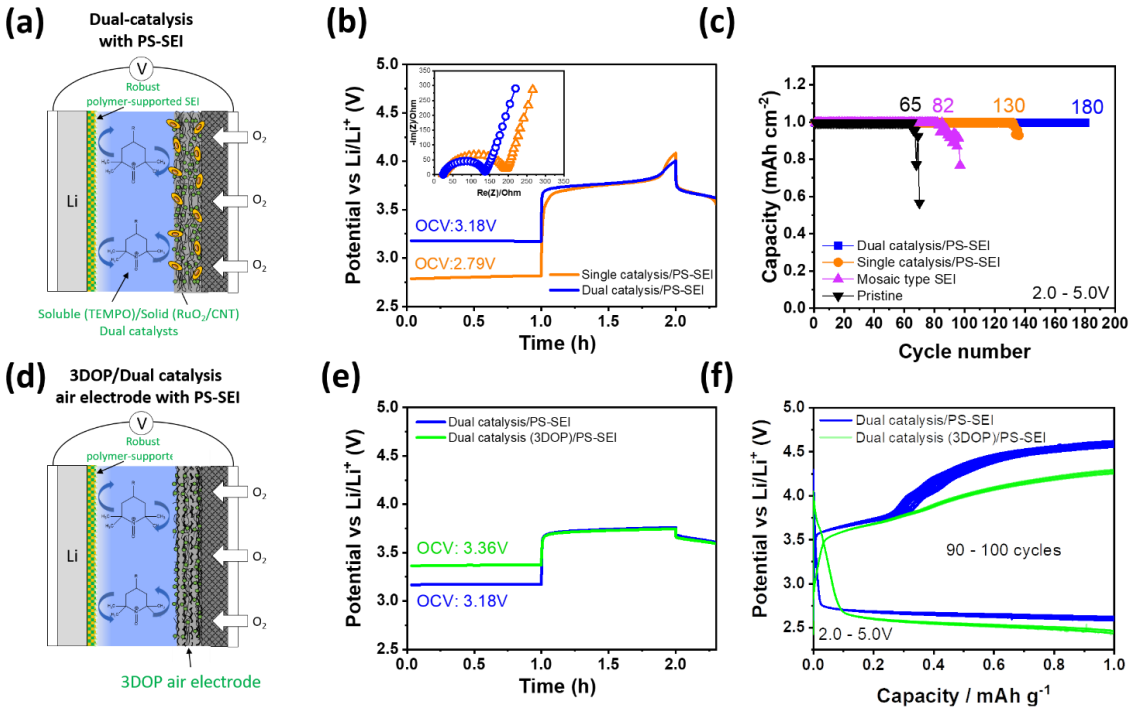

Figure 114. (a) Schematic illustration of the synergy effect of dual-catalysts with PS-SEI layer in Li-O_2 battery (LOB) cell. (b) Electrochemical impedance spectroscopy Nyquist plots (inset) of fresh Li-O_2 batteries with single and dual catalysts and their charge curves during pre-charging to 5 V. (c) Cycling stability of pristine lithium anode, Li/mosaic type SEI, Li / polymer-supported SEI (PS-SEI) with 0.1 M TEMPO, and Li/PS-SEI with 0.1 M TEMPO and RuO_2 fixed on the single-walled carbon nanotube (SWCNT) air electrode at a current density of 0.2 mA cm^{-2} under a capacity limited protocol of 1.0 mAh cm^{-2} in the operation voltage range of 2-5 V at 25°C. (d) Schematic illustration of the 3D ordered microporous (3DOP) / SWCNT air electrode with dual-catalysts and PS-SEI layer in a Li-O_2 battery cell. (e) Charge curves of Li-O_2 batteries with dual catalysts/PS-SEI layer and 3DOP/dual catalysts with PS-SEI layer during pre-charging to 5 V. (f) Charge-discharge profiles of Li-O_2 batteries with dual catalysts/PS-SEI and 3DOP/dual catalysts with PS-SEI layer at a current density of 0.2 mA cm^{-2} under a capacity limited protocol of 1.0 mAh cm^{-2} in the voltage range of 2-5 V at 25°C.

To enhance the effect of dual-catalysts during the long-term operation of Li-O_2 batteries, air electrode with three-dimensionally ordered microporous (3DOP) structure was generated using single walled carbon nanotube (SWCNT) by a templating method (Figure 114d). It is found that the Li-O_2 battery using an air electrode with 3DOP structure exhibits higher OCV (3.36 V) compared to those using non-3DOP air electrode (3.18 V); see Figure 114e. Li-O_2 batteries with 3DOP air electrode and dual-catalysts also show much lower over voltage during charge process and much better cycling stability after 100 cycles (Figure 114f) than those with dual-catalysts but without 3DOP air electrode. The synergic effect of the 3DOP structure and dual-catalysts system with PS-SEI layer is a new direction to further extend the cycling stability of Li-O_2 batteries.

Patents/Publications/Presentations

Presentation

- 239th ECS Meeting, Digital Meeting (May 30 – June 3, 2021): "A Stable Li Metal Anode with Electrochemically Treated Poly(Ethylene Oxide) Coating for Lithium Oxygen Batteries"; H-S. Lim, W-J. Kwak, S. Chae, S. Wi, L. Li, J. Hu, C. Wang, W. Xu, and J-G. Zhang.

Task 6.2 – Lithium-Air Batteries
(Khalil Amine, Larry A. Curtiss, and Jun Lu; Argonne National Laboratory)

Project Objective. This project will develop new cathode materials and electrolytes for Li-air batteries for long cycle life, high capacity, and high efficiency. The goal is to obtain critical insight that will provide information on the charge and discharge processes in Li-air batteries to enable new advances to be made in their performance. This will be done using state-of-the-art characterization techniques combined with state-of-the-art computational methodologies to understand and design new materials and electrolytes for Li-air batteries.

Project Impact. The instability of current nonaqueous electrolytes and degradation of cathode materials limits performance of Li-air batteries. The project impact will be to develop new electrolytes and cathode materials that are stable and can increase energy density of electrical energy storage systems based on lithium.

Approach. The project is using a joint theoretical/experimental approach for design and discovery of new cathode and electrolyte materials that act synergistically to reduce charge overpotentials and increase cycle life. Synthesis methods, in combination with design principles developed from computations, are used to make new cathode architectures. Computational studies are used to help understand decomposition mechanisms of electrolytes and how to design electrolytes with improved stability. The new cathodes and electrolytes are tested in Li-O_2 cells. Characterization, along with theory, is used to understand the performance of materials used in the cell and to make improved materials.

Out-Year Goals. The out-year goals are to find catalysts that promote discharge product morphologies that reduce charge potentials and to find electrolytes for long cycle life through testing and design.

Collaborations. This project engages in collaboration with K. C. Lau (UC at Norridge), Y. Wu (OSU), D. Zhai (China), and R. Shahbazian-Yassar (UIC).

Milestones

1. Design functionalized cathodes to achieve high electrochemical performance of Li-O_2 batteries. (Q1, FY 2021; Completed)
2. Characterize cathode materials and investigate electrochemical behaviors. (Q2, FY 2021; Completed)
3. Develop a new catalyst for a lithium superoxide-based battery based on template mechanism. (Q3, FY 2021; Completed)
4. By understanding the effects, engineer new catalysts with improved catalytic performance and suppressed side reactions. (Q4, FY 2021)

Progress Report

One major challenge for Li-oxygen batteries is the high charge overpotential, which results in low energy efficiency. It has recently been shown that lithium superoxide, which is a good electronic conductor and has a low charge overpotential, can be formed in a Li-O_2 battery using iridium as a catalyst. It was speculated that an Ir_3Li alloy forms, which acts as an effective template for growth of the LiO_2. In this work, Ir_3Li was thermally synthesized in bulk prior to implementation on the rGO cathode of a Li-O_2 cell.

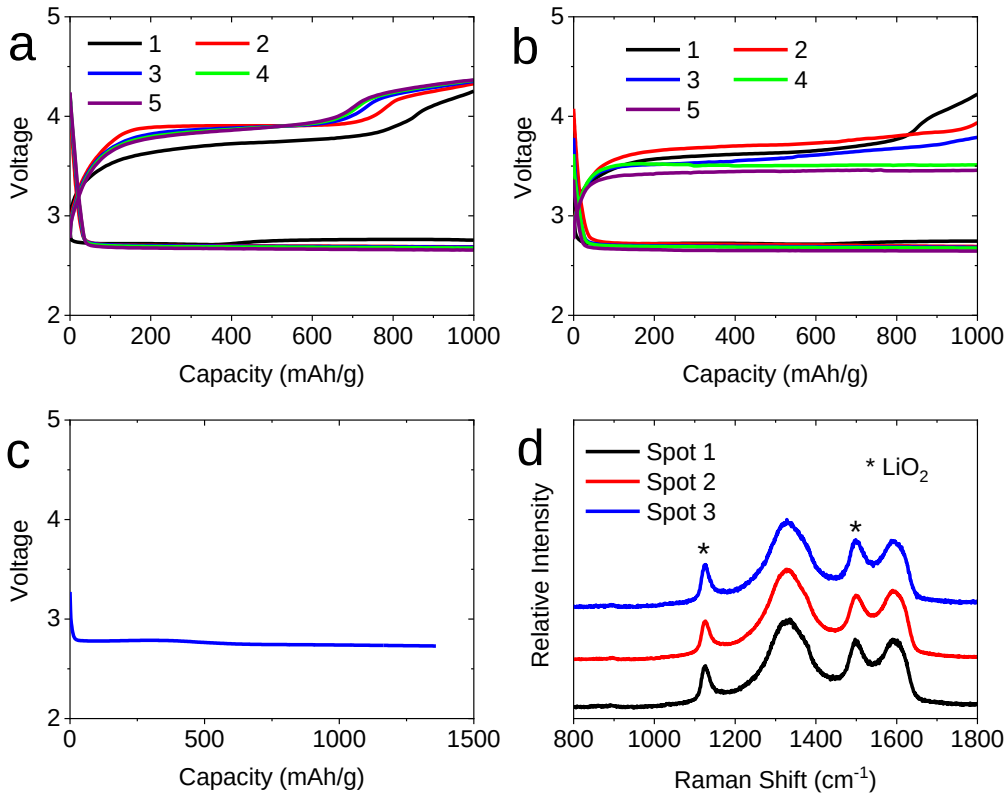

Figure 115. : (a) The first five cycles of a Li-O_2 cell with rGO / gas diffusion layer (GDL) cathode with a current density 0.05 mA/cm^2. (b) The first five cycles of a Li-O_2 cell with Ir_3Li-rGO/GDL cathode. (c) Deep discharge of Ir_3Li-rGO cathode in a Li-O_2 cell. (d) Raman spectra of deep discharged Ir_3Li-rGO cathode in a Li-O_2 cell showing strong LiO_2 peaks at different areas.

Ir_3Li particles ranging from 200 nm to 5 μm were synthesized using a thermal reaction between iridium and lithium metals at 800°C. The powder was characterized using XRD and was demonstrated to be phase pure. A comprehensive characterization of the electronic properties of Ir_3Li was conducted to determine its properties and relevance for use as a LiO_2 battery cathode. The characterization from conductive AFM, SQUID, and EPR measurements revealed that the synthesized Ir_3Li has metallic-like character with an affinity to O_2 adsorption, which is needed to act as an appropriate ORR/OER catalyst. XPS analysis supported by DFT calculations indicated that the iridium is negatively charged, likely enhancing its catalytic properties for ORR/OER. Raman studies demonstrated that the Ir_3Li material was stable in air exposure up to four weeks. In summary, the bulk Ir_3Li was found to have comparable electrical conductivity to iridium metal, possess metal-like magnetic properties, and have an affinity toward O_2 adsorption.

An Ir_3Li and rGO 1:1 mixture was added to a gas diffusion layer (GDL) electrode using a PVDF binder to form an Ir_3Li-rGO cathode. The resulting cathode was assembled in a Swagelok type Li-O_2 cell with a Li-metal anode and a 1 M lithium triflate in TEGDME-soaked glass fiber separator. For comparison, a similar Li-O_2 cell with rGO/GDL cathode was also assembled. Both cells were cycled at a current density of 0.05 mA/cm^2 and capacity

of 1000 mAh/g. The first five electrochemical discharge-charge cycles are shown in Figure 115a-b for the rGO/GDL and Ir_3Li-rGO/GDL cells, respectively. For the Li-O_2 cell with the rGO/GDL cathode, two charge plateaus at ~ 3.6-3.8 V and 4.2 V were observed. For the Li-O_2 cell with the Ir_3Li-rGO/GDL cathode, the charging potential remained mostly below 3.5-3.7 V, except toward the end of the 1st charging cycle. For detailed discharge product characterization on the Ir_3Li-rGO/GDL cathode, a different cell was discharged at 0.05 mA/cm^2 current density to a capacity of 1360 mAh/g. The larger capacity experiment was performed to increase the mass of the discharge product deposited on the cathode to enable Raman and titration analysis of the discharge product(s). The voltage profile during cycling of the cell is shown in Figure 115c.

After discharge, the cell was disassembled inside an Ar-filled glovebox. The cathode with discharge product(s) was dried inside the glovebox, cut in half, and subjected to micro-Raman and titration analysis with Ti(IV)OSO_4 followed by ultraviolet-visible spectroscopy of the titrant to determine the chemistry of the discharge product. The micro-Raman spectra is shown in Figure 115d. The titrant absorbance value indicated that the presence of Li_2O_2 was negligible on the discharged cathode. Raman spectra were collected on several different areas and demonstrated strong LiO_2 characteristic peaks at 1125 cm^{-1} and 1505 cm^{-1}, along with the characteristic rGO/graphitic peaks at 1328 cm^{-1} and 1596 cm^{-1}. These results indicate that LiO_2 was the dominant discharge product. TEM also confirmed the LiO_2 discharge product.

The noble metal-like properties of the Ir_3Li catalyst determined in this study, along with its crystal lattice similarities to LiO_2 demonstrated through DFT analysis, will help enable design guidelines for future catalysts to be implemented in Li-O_2 batteries.

Patents/Publications/Presentations

Publication

- Li, J., X. Bi, K. Amine, and J. Lu. "Understanding the Effect of Solid Electrocatalysts on Achieving Highly Energy-Efficient Lithium – Oxygen Batteries." *Advanced Energy and Sustainability Research* (2021): 2100045.

Task 6.3 – Lithium Oxygen Battery Design and Predictions
(Larry A. Curtiss / Anh Ngo, Argonne National Laboratory; Amin Salehi-Khojin, University of Illinois, Chicago)

Project Objective. The objective of this work is to develop new materials for Li-O_2 batteries that give longer cycle life and improved efficiencies in an air environment. New electrolyte blends and additives will be investigated that can reduce clogging and at the same time promote the cathode functionality needed to reduce charge overpotentials. New cathode and anode materials will be investigated that can work in conjunction with the electrolytes to improve cycle life in the presence of air components.

Project Impact. Li-air batteries are considered as a potential alternative to Li-ion batteries for transportation applications due to their high theoretical specific energy. The major issues with the existing Li-O_2 systems include degradation of the anode electrode, reactions with air components, clogging of the cathode, and electrolyte instability. Thus, this project is using a comprehensive approach to improve cycle life and efficiency through developing new materials for electrodes, anodes, and electrolytes that work in synergy.

Approach. The experimental strategy is to use cathode materials based on 2D TMDs that the team has found to be among the best ORR/OER catalysts. These cathode materials will be combined with new electrolyte blends and additives that work in synergy to reduce charge potentials and increase stability of the Li-air system. DFT and AIMD simulations are used to gain insight at the electronic structure level of theory of the electrolyte structure, and function both in bulk and at interfaces with the cathode, anode, and discharge product. CMD is used to obtain understanding at longer length and time scales of processes occurring in the electrolyte and growth mechanisms of discharge products. The team will also utilize a HT screening strategy based on experiment and theory to develop a large database of properties and outcomes of electrolyte combinations that can be analyzed using ML to predict electrolytes and additives with the best performance.

Out-Year Goals. The out-year goals are to find electrolytes that give high capacities and long cycle life in an air atmosphere using HT screening.

Collaborations. This project engages in collaboration with R. Assary, J. G. Wen, and S. Tepavcevic of ANL; B. Narayanan of University of Louisville; T. Li of Northern Illinois University; and F. Khalili-Araghi and R. Klie of UIC.

Milestones

1. Use a conductive metal-organic framework (MOF) for Li-O_2 battery to increase the number of active sites in cathode materials based on MOFs as well as localize them in pores. (Q1, FY 2021; Completed)
2. Utilize new TMD alloy catalyst for Li-O_2 batteries to increase charge/discharging rates. (Q2, FY 2021; Completed)
3. Investigate new concepts in electrolyte additives that work with the new TMD alloy catalyst to increase charge/discharge rates. (Q3, FY 2021; Completed)
4. Investigate new electrolyte additives that work with the TMD alloy catalyst to give anode protection. (Q4, FY 2021; Initiated)

Progress Report

Li-O_2 batteries are considered as an advanced energy storage system that could provide a much higher specific energy than Li-ion batteries for electrical transportation. However, there are major issues with the existing Li-O_2 systems, including degradation of the anode electrode, poor volumetric energy density, poor charge/discharge rates, electrolyte instability, and high charge overpotential. This work is focused on finding a combination of electrolytes, additives, and cathode catalysts to enable a Li-O_2 battery that can operate in an air atmosphere with a low charge potential while maintaining a long cycle life. Last quarter, the team presented results for a new catalyst, a new binary TMD alloy, $Nb_{0.5}Ta_{0.5}S_2$. This catalyst was found to facilitate both ORR and OER occurring during discharge and charge processes, respectively.

This quarter, the team investigated the use of a new redox mediator for use in conjunction with the $Nb_{0.5}Ta_{0.5}S_2$ catalyst. The new redox mediator is $KMnO_4$ in a DMSO/IL electrolyte, with the IL being 1-ethyl-3-methylimidazolium tetrafluoroborate (EMIM-BF_4). During the electrolyte preparation, there is a reaction between $KMnO_4$ and DMSO resulting in the formation of colloidal MnO_2 particles and K_2MnO_4, with some remaining unreacted $KMnO_4$ in the resulting electrolyte. The manganate anion, MnO_4^{-2}, has an oxidation potential of ~ 3.5 V (versus Li/Li^+); thus, it can serve as a redox mediator with the resulting permanganate anion, MnO_4^-, serving as an oxidizer for the decomposition of the solid lithium peroxide [$(Li_2O_2)_s$] in a two-step process (where the subscript s denotes a solid phase) that regenerates the MnO_4^{-2} :

$$MnO_4^- + (Li_2O_2)_s \rightarrow MnO_4^{-2} + (Li_2O_2\text{-}LiO_2)_s + Li^+$$
$$MnO_4^- + (Li_2O_2\text{-}LiO_2)_s \rightarrow MnO_4^{-2} + O_2 + (Li_2O_2)_s + Li^+$$

This process results in the decomposition of the Li_2O_2 and release of O_2. The feasibility of the first step of the decomposition reaction has been studied by AIMD simulations, where the $KMnO_4$ extracts a lithium from Li_2O_2, as shown in Figure 116. The results of the simulation indicate that the lithium migrates from the Li_2O_2 surface without any barrier in the presence of $KMnO_4$. The final state has energy lower than the initial state by 1.4 eV. In a previous similar study for the redox mediator of LiI, the LiI_3 has a barrier of ~ 0.5 eV for the first step in the decomposition of Li_2O_2. In that case, the oxidizer reaction is $LiI_3 + Li_2O_2 \rightarrow 3LiI + O_2$. In addition, the team has carried out DFT calculations based on cluster representations of Li_2O_2. In those calculations the thermodynamics for the reaction of $KMnO_4$ (or $LiMnO_4$) to decompose Li_2O_2 clusters are very favorable, energetically in agreement with the AIMD calculations.

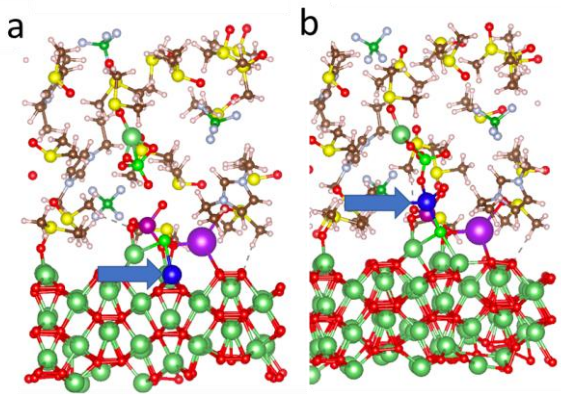

Figure 116. (a) Density functional theory simulation of DMSO/IL electrolyte on a Li_2O_2 surface with $KMnO_4$ shows lithium (blue) initially located at interface Li_2O_2. (b) After optimization, the lithium ion migrates from Li_2O_2 surface to electrolyte without any barrier, and the final structure has an energy lower than the initial state by 1.4 eV.

The redox mediator property of the $KMnO_4$ additive is evident from a comparison of experimental results with an electrolyte with no $KMnO_4$ additive. For example, the charge potential for a cell with the $KMnO_4$ electrolyte at 0.1 $mA.cm^{-2}$ (1000 $mAh.cm^{-2}$ capacity) is 3.55 V (at the end of the 20^{th} cycle), compared to 4.25 V for a cell with a LiTFSI salt, as shown in Figure 117 under the same conditions. The $KMnO_4$ electrolyte has a similar charge potential as one with an LiI additive, a well-studied redox mediator (that is, 3.55 V versus 3.50 at 0.1 $mA.cm^{-2}$ after 20 cycles and 3.75 V versus 3.85 V at 0.5 $mA.cm^{-2}$ after 20 cycles). When the cell is run with the

$KMnO_4$ redox mediator at the higher rates of 0.5 mA/cm^{-2} and 1 mA/cm^{-2} and higher capacities, a second plateau at a higher voltage starts appearing at 20-40 cycles, which also appears for the LiI cell, but at less cycles. It is not clear what causes the second plateau, but a different mechanism may govern the charge process. The team also notes that the appearance of the second plateau may be related to the higher capacities used for the higher rates since when the rate of 1 mA/cm^{-2} is used with the small capacity of 1000 mAh/cm^{-2}, the second plateau does not occur.

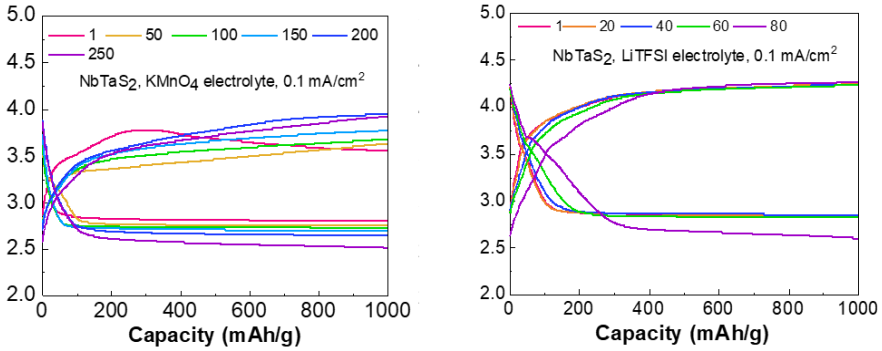

Figure 117 Comparison of performance of $KMnO_4$ additive (left) and LiTFSI additive with $Nb_{0.5}Ta_{0.5}S_2$ catalysts at 0.1 mA.cm^{-2} current density with all conditions the same.

In summary, this work has found a new redox mediator for Li-O_2 batteries that works in synergy with a TMD catalyst.

Patents/Publications/Presentations

The project has no patents, publications, or presentations to report this quarter.

TASK 7 – SODIUM-ION BATTERIES

Team Lead: Xiao-Qing Yang, Brookhaven National Laboratory

Summary

The Na-ion battery will require investigations to identify optimal electrode materials, electrolytes, separators, and binders to reach full potential. The BMR program will therefore have a limited effort directed toward identifying Na-ion battery materials that have potential value for vehicle applications. During FY 2019, the BMR added several new projects in the area of Na-ion batteries, four of which have been continuously funded in FY2020 and FY2021. Progress on these projects this quarter is described in this report.

Highlights. The highlights for this quarter are as follows:

- The ANL team (C. Johnson and K. Amine) investigated the solid-state synthesis of sodium layered oxide cathode using *in situ* high-energy XRD and successfully synthesized high-purity O3-phase layered oxide cathodes. The cathode exhibited high specific capacity of ~ 180 mAh/g and high CE of 95%.
- The BNL team (X-Q. Yang and Z. Shadike) has applied advanced diagnostic techniques such as XANES and 2D XANES mapping to the investigation and improvement of the new high-capacity and high-C rate multi-component sodium cathode materials $NaMnFeCoNiO_2$ (NMFCN). The XANES and XANES mapping results are consistent with the CV test showing that no Ni^{2+}/Ni^{3+} redox is observed in the 1st charging process.
- The LBNL team (M. Doeff) used hard XAS to probe the electronic and structural changes in a layered lepidocrocite-type titanate as a function of drying temperature, and as function of SOC (for the material dried at 60°C).
- The PNNL team (J-G. Zhang) analyzed the compositions of SEI and CEI layer formed on the anode and cathode in cycled high voltage (4.2 V) carbon||$NaNi_{0.68}Mn_{0.22}Co_{0.10}O_2$ (NaNMC) cells. They found that the use of high concentration sodium bis(fluorosulfonyl)imide – triethyl phosphate (NaFSI-TEP) electrolyte not only can form an inorganic rich SEI layer to stabilize hard carbon anode, but also effectively suppress dissolution of TMs in cathode, therefore improving the electrochemical performance of Na-ion batteries.

Task 7.1 – Exploratory Studies of Novel Sodium-Ion Battery Systems (Xiao-Qing Yang and Zulipiya Shadike, Brookhaven National Laboratory)

Project Objective. To meet the challenges of powering PHEVs and BEVs, new rechargeable battery systems with high energy and power density, low cost, good abuse tolerance, and long calendar and cycle life need to be developed. The primary objective of this project is to develop new advanced synchrotron-based material characterization techniques and apply these techniques to study the new rechargeable battery systems beyond the Li-ion batteries, namely the Na-ion battery systems for EVs.

Project Impact. The results of this project will be used for developing technologies that will significantly increase the energy density and cycle life and reduce the cost of beyond Li-ion battery systems. This will greatly accelerate deployment of EVs and reduce carbon emission associated with fossil fuel consumption and will help in the direction of building U. S.-based energy storage manufacture chains.

Approach. This project will use the synchrotron-based *in situ* X-ray diagnostic such as *in situ* XRD and *in situ* XAS tools, combined with TEM, STEM, and TXM imaging techniques developed at BNL to evaluate the new materials and redox couples to obtain in-depth understanding of the reaction mechanisms of these materials, aiming to improve existing materials and to provide guidance for new materials and new technology development for Na-ion battery systems.

Out-Year Goals. The out-year goal is to complete the synchrotron-based XRD, XAS, and XANES mapping studies of new cathode materials P2-$Na_{0.66}[Mn_{0.61}Ni_{0.28}Sb_{0.11}]O_2$ and P2-$Na_{0.7}Mg_{0.2}[Mn_{0.6}Fe_{0.2}\square_{0.2}]O_2$ (□ here representing TM vacancy) and a high-capacity, high-C rate, multi-component cathode material.

Collaborations. The BNL team has been closely working with top scientists on new material synthesis at ANL, LBNL, and PNNL, with U. S. industrial collaborators at GM and Johnson Controls, and with international collaborators.

Milestones

1. Complete XAS, including XANES and extended x-ray absorption fine structure (EXAFS) as well as 2D XANES mapping of the pristine P2-$Na_{0.66}[Mn_{0.61}Ni_{0.28}Sb_{0.11}]O_2$ cathode material at nickel and manganese K-edge. (Q1, FY 2021; Completed)
2. Complete nickel and manganese K-edge XAS (including XANES and EXAFS) of P2-$Na_{0.66}[Mn_{0.61}Ni_{0.28}Sb_{0.11}]O_2$ cathode material at different SOCs. (Q2, FY 2021; Completed)
3. Complete *ex situ* TEM, XRD study, and 2D XANES mapping of high-capacity high-C rate multi-component sodium cathode material with P2 type at different SOCs. (Q3, FY 2021; In progress)
4. Complete iron and manganese K-edge XAS of P2-$Na_{0.7}Mg_{0.2}[Mn_{0.6}Fe_{0.2}\square_{0.2}]O_2$ cathode material at different SOCs. (Q4, FY 2021; In progress)

Progress Report

This quarter, the team completed the third milestone and progressed on other milestones. Na-ion batteries with gravimetric energy density potentially comparable to some Li-ion batteries and the raw materials are widely available. They have been pursued persistently for grid energy storage and low-speed vehicles. Advanced diagnostic techniques developed by BNL have been successfully applied to the investigation and to improvement of the new high-capacity and high-C rate multi-component sodium cathode material NMFCN. Figure 118 shows the nickel K-edge 2D XANES mapping of the pristine material. Figure 118a shows the thickness map of pristine particles. Figure 118b-d shows the component mapping of Ni^{2+} and Ni^{3+} throughout the region of interest, which indicates that nickel predominantly exists as Ni^{3+} rather than Ni^{2+} in the pristine state. Figure 118c shows the spectrum integrated from the whole field of view shown in Figure 118a, which confirms that the averaged valence state of nickel is closer to Ni^{3+}. The 2D XANES result is consistent with the CV test result shown in Figure 118e, where no Ni^{2+}/Ni^{3+} redox is observed in the 1st charging process.

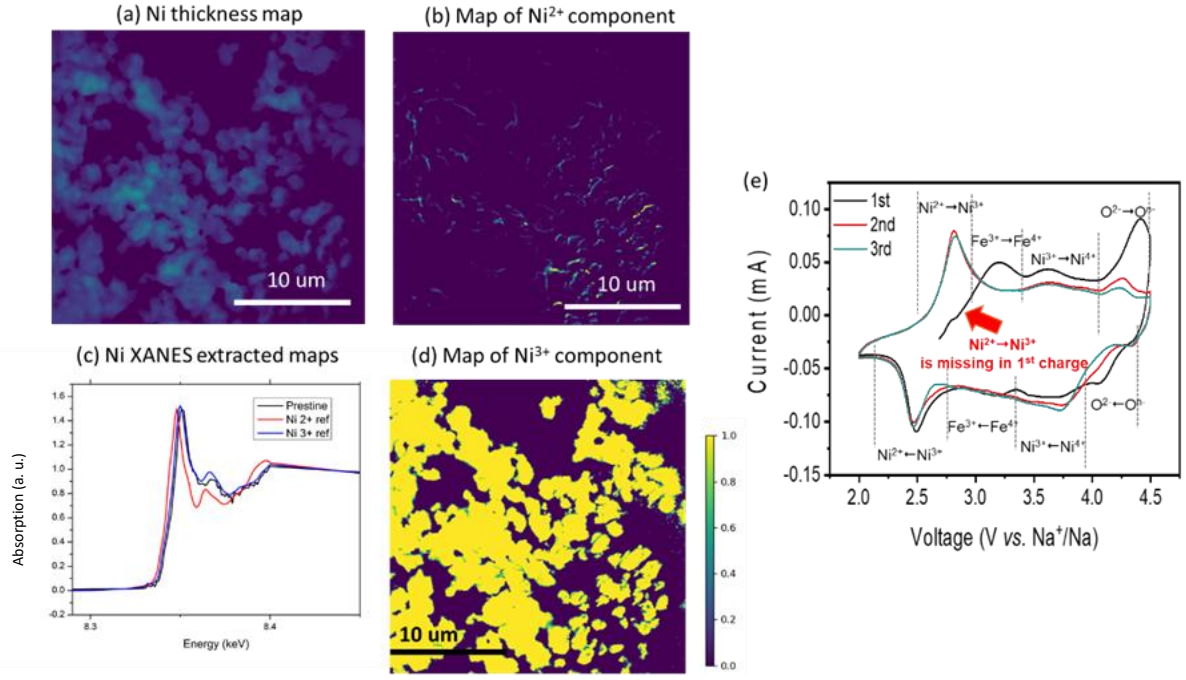

Figure 118. 2D X-ray absorption near-edge spectroscopy (XANES) mapping of pristine $NaMnFeCoNiO_2$ and cyclic voltammetry (CV) test. (a) Nickel thickness map. (b) Ni^{2+} composition map. (c) Nickel XANES integrated from the field of view in (a). (d) Ni^{3+} composition map. (e) CV test for the 1st, 2nd, and 3rd electrochemical cycles.

Patents/Publications/Presentations

Presentations

- MRS Spring Meeting, Virtual (April 17–23, 2021): "Oxygen Redox in P3 Cu-Based Sodium Battery Cathode"; E. Hu. Invited.
- MRS Spring Meeting, Virtual (April 17–23, 2021): "Anionic Redox Chemistry in Layered Chalcogenide Cathode Materials for Sodium Batteries"; Z. Shadike, T. Wang, D-R. Shi, E. Hu, Z-W. Fu, and X-Q. Yang.* Invited.

Task 7.2 – Development of a High-Energy Sodium-Ion Battery with Long Life (Chris Johnson and Khalil Amine, Argonne National Laboratory)

Project Objective. The project objective is to develop a high-energy Na-ion battery with long life. Moreover, the battery chemistry should utilize low-cost materials. The energy density target is 200 Wh/kg and/or 500 Wh/L, wherein the anode and cathode capacity targets are 600 $mAhg^{-1}$ and 200 $mAhg^{-1}$, respectively.

Project Impact. A Na-ion battery on par with the energy density of a Li-ion battery can have a high impact in the transportation sector with the assumption that the cost is significantly below $85/kWh and that the battery pack provides a 300-mile range. The consumer is not concerned about the battery chemistry employed if these metrics can be met. Development of these battery chemistries will situate the United States in a strong position as relates to new low-cost energy storage systems beyond lithium ion.

Approach. In a team approach, the Na-ion battery group will create a versatile Na-ion battery chemistry with beneficial advantages such as low cost, safety, recycling, and sustainability of materials used. The team will work synergistically so that the final design is the culmination of advances in phosphorus carbon composites mated with optimized lead or other highly dense metalloids, such as tin and/or antimony and derivatives thereof, for the recyclable anode. Synthesis and optimization of such blended composite anodes will be conducted in parallel to diagnostic characterization of structures, phase formation, and cycling stability. Cathode work will begin at the end of the first year and will involve gradient cathodes consisting of Fe-Mn compositions, as well as intergrowths of layer stacking sequenced oxides. If resources allow, the team also will attempt to stabilize cathode surfaces using ALD methods, particularly for the benefit of staving off dissolution of manganese and iron/electrolyte reactivity. Electrolytes will be partly procured from H. Li at PNNL.

Out-Year Goals. The state-of-the-art Na-ion battery in the literature has now been surpassed by this team, but performance is still too low for commercialization. Thus, the goal is to move forward and continually invent the most superior Na-ion battery chemistry that can compete worldwide through work output from this project.

Collaborations. Researchers from PNNL who are developing electrolytes for Na-ion batteries will provide this project with formulations to test with the various electrode combinations investigated at ANL.

Milestones

1. Doped red phosphorus (RP) anode with high specific capacity and stable cycle life. (Q1, FY 2021; Completed)
2. *In situ* characterization of layered cathodes during synthesis; synthesize Ni-based, Fe-based, and Mn-based sodium layered cathodes. (Q2, FY 2021; Completed)
3. Advanced characterization on developed cathodes and anodes during charge/discharge. (Q3, FY 2021; In progress)
4. Performance optimization of synthesized layered cathodes and demonstration of full-cell development using optimal phosphorus anode and developed/commercial cathodes. (Q4, FY 2021; In progress)

Progress Report

Among various phase structures in sodium layered oxide cathodes, O3 phase represents the structure with the highest sodium content and is thus a better cathode candidate than other types of cathodes for a practical Na-ion battery. However, its formation mechanism remains elusive. Hence, in this quarter, the team has used *in situ* high-energy X-ray diffraction (HEXRD) to probe the solid-state synthesis of O3 sodium layered oxide cathodes.

Figure 119a shows the 2D contour plot of *in situ* HEXRD patterns during the formation process of O3 $NaNi_{0.4}Mn_{0.4}Co_{0.2}O_2$ as a control cathode. The team decided that this control work will be used to compare trivalent cobalt with trivalent iron reactivity and its nature of sodium intercalation. The ultimate goal is to create a Fe-Mn based layered oxide cathode with O3 phase. Previous work has shown that Fe(IV) (that is, charged $Na_{1-x}FeO_2$) may be catalytic to decomposition of the ester-based carbonate electrolyte. It is likely that Co(IV) does not portray this high reactivity.

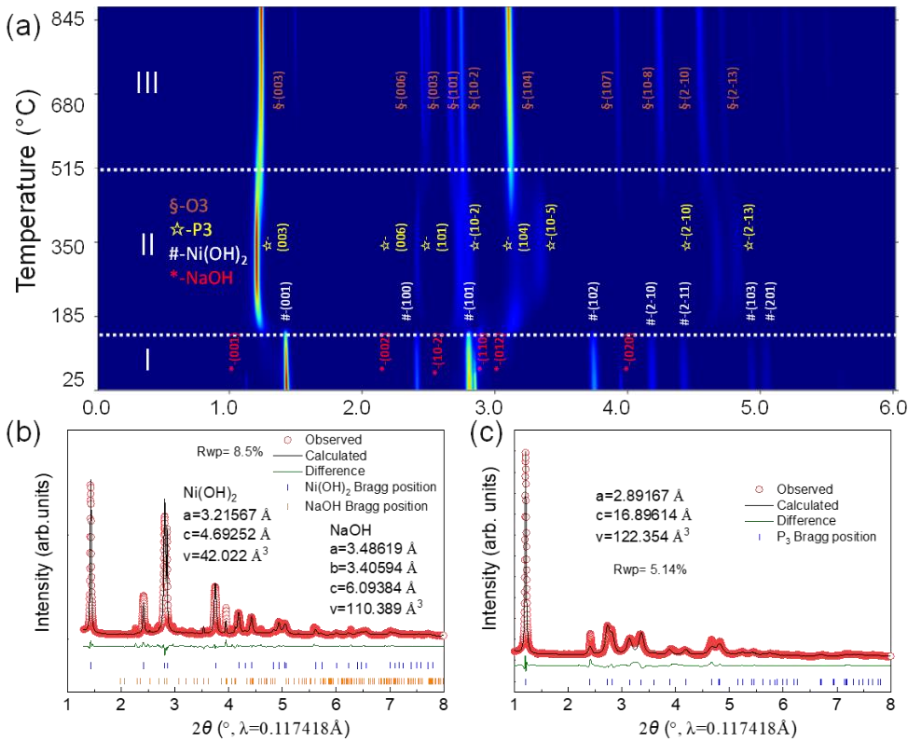

Figure 119. (a) 2D contour plot of *in situ* high-energy X-ray diffraction (HEXRD) patterns during solid-state synthesis of O3 $NaNi_{0.4}Mn_{0.4}Co_{0.2}O_2$. Rietveld refinement of HEXRD patterns of (b) starting material and (c) intermediate product at 350°C.

The Co-containing control starting material was a mixture of $Ni_{0.4}Mn_{0.4}Co_{0.2}(OH)_2$ and 5% excess mole of NaOH. As clearly shown, the major reactions started to occur at around 150°C and 350°C, respectively. Therefore, the formation process of O3 $NaNi_{0.4}Mn_{0.4}Co_{0.2}O_2$ can be classified into three regions according to their phase composition: 25-185°C (region I, starting material), 185-500°C (region II, intermediates), and 500-875°C (region III, final product). The Rietveld refinement in Figure 119b-c shows that the starting material can be well indexed as $Ni(OH)_2$ and NaOH, while the XRD pattern of the intermediate product at 350°C is consistent with that of P3-$Na_{0.8}Ni_{0.4}Mn_{0.4}Co_{0.2}O_2$. On further reaction beyond 500°C, more Na^+ was inserted into the layered structure and hence the structure of O3 phase started to evolve. Therefore, a high temperature of > 800°C is required to synthesize high-purity O3 phase. More detailed analysis on the changes of lattice parameter, Li^+/Ni^{2+} mixing, and crystalline size as a function of temperature will be made to obtain the optimal heating temperature and holding time.

The team found that quenching is necessary to maintain the O3 phase structure during cooling. With a slow cooling under air atmosphere, the obtained material exhibited a mixed phase of P1/P2/O3 (Figure 120a), which might be due to the surface reconstruction induced by slow cooling and thus lead to the formation of Na-deficient phase such as P1 and P2. In sharp contrast, the quenched sample exhibited high purity O3 phase. The morphologies of the quenched cathode are shown in Figure 120b, which exhibited characteristic conventional polycrystalline features. The electrochemical performance of the quenched $NaNi_{0.4}Mn_{0.4}Co_{0.2}O_2$ cathode was evaluated by using coin-cells with sodium metal as reference and counter electrode. Figure 120c shows the first charge/discharge curves within 2.0-4.4 V at 0.1C, which exhibited the characteristic features of O3 phase with multiple-step voltage plateaus. The 1st charge and discharge capacity were measured to be as high as 180.6 mAh/g and 171.9 mAh/g, leading to a low initial irreversible capacity loss of only 8.7 mAh/g and a high initial CE of 95%. This is extremely important for the practical application of sodium layered cathode. In addition, it exhibited an average working voltage of ~ 3.5 V. These results can lead to a high energy density of ~ 600 Wh/kg based on the material level. This is comparable with LFP cathode and $LiCoO_2$ cathode. However, on further charge/discharge, the capacity exhibited a continuous decrease. After 100 cycles, the reversible capacity was only ~ 50 mAh/g, resulting in a low capacity retention of 30% (Figure 120d). The team will conduct advanced characterization, particularly with electrolyte optimization, during charge/discharge to understand the degradation mechanism and develop corresponding strategies to stabilize O3 cathode during prolonged cycling.

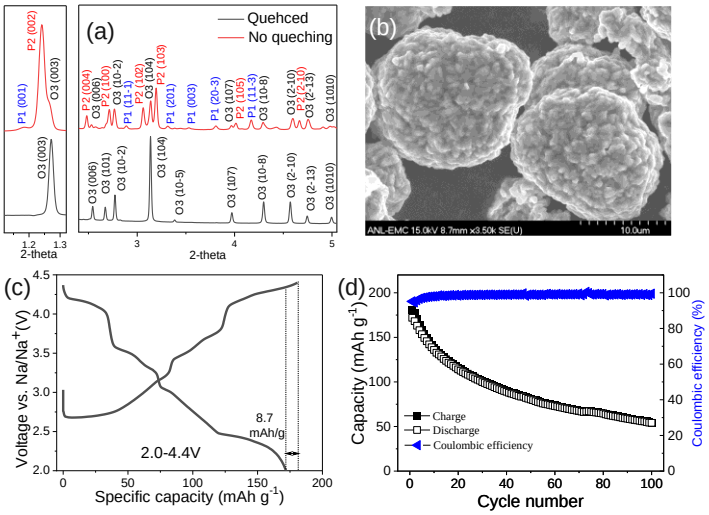

Figure 120. (a) High-energy X-ray diffraction (HEXRD) patterns of samples with/out quenching. (b) Scanning electron microscopy images of O3 $NaNi_{0.4}Mn_{0.4}Co_{0.2}O_2$. (c) The 1st charge/discharge curve and (d) the corresponding cycling performance of O3 $NaNi_{0.4}Mn_{0.4}Co_{0.2}O_2$ cathode at C/10.

Patents/Publications/Presentations

The project has no patents, publications, or presentations to report this quarter.

Task 7.3 – High-Capacity, Low-Voltage Titanate Anodes for Sodium-Ion Batteries (Marca Doeff, Lawrence Berkeley National Laboratory)

Project Objective. The objectives are to understand differences in the sodium intercalation mechanism of various sodium titanate anodes through an array of synthetic, electrochemical, and structural characterization techniques, and to overcome practical impediments to their use, such as the high 1st-cycle Coulombic inefficiencies that are currently observed. The ultimate goal is to produce a 200-250 mAh/g anode that cycles reversibly.

Project Impact. Although several suitable cathode materials for Na-ion batteries exist, there are few suitable anode materials due to low potential instabilities. Therefore, sodium titanate variations will be synthesized through different routes to develop materials with various morphologies and dopants. Decreasing the 1st cycle inefficiencies and improving cycling performance will allow enabling technology for a practical high-energy Na-ion battery.

Approach. Candidate stepped layered titanates will be synthesized by appropriate routes (hydrothermal, solid-state, etc.). Materials will then be characterized electrochemically and physically. Structure-function relationships will be built to correlate the effect of changing structure (for example, step size) on electrochemical properties.

Out-Year Goals. A series of synchrotron characterization techniques will be used to further develop sodium titanate anode materials with stable cycling while delivering high capacities.

Collaborations. TXM is done in collaboration with Y. Liu (SSRL). Synchrotron hard, soft XAS, and X-ray Raman efforts are in collaboration with D. Nordlund and D. Sokaras (SSRL). Electrolyte design is done in collaboration with K. Xu (ARL).

Milestones

1. Characterize lepidocrocite titanates. (Q1, FY 2021; Completed)
2. Optimize electrode. (Q2, FY 2021; Completed)
3. Assemble, test, and study full cells. (Q3, FY 2021; In progress)
4. *Go/No-Go Decision*: On lepidocrocite titanate, stop if problems are not solved. (Q4, FY 2021)

Progress Report

The possible changes of titanium oxidation state and structural modifications induced by heat treatment of sodium titanates were investigated this quarter by hard XAS. Regardless of the heating temperature, titanium ions in all the titanate samples demonstrate a tetravalent state (Figure 121a). Noticeable changes were observed in the pre-edge region: a gradual increase of A2/A2' peak intensity ratio and A3 peak intensity as the heating temperature increases (Figure 121b). The A2 pre-edge peak has been mainly attributed to a dipolar transition of $1s \rightarrow 3d\ (t_{2g}) - 4p$ hybridized states including a little $1s \rightarrow 3d\ (e_g)$ quadrupolar component, while the A3 peak has been ascribed to the pure dipolar transitions of $1s \rightarrow 3d\ (e_g) - 4p$ hybridized states.[1-2] The difference in oxygen CN of the titanium atom and the local structural symmetry of TiO_6 octahedra may explain the difference in A2/A2' peak intensity ratio and A3 peak intensity. Fourier transform EXAFS analysis also reveals changes of local structure after heat treatment: slight elongation of Ti-O distance and shortening of Ti-Ti distance (Figure 121c).

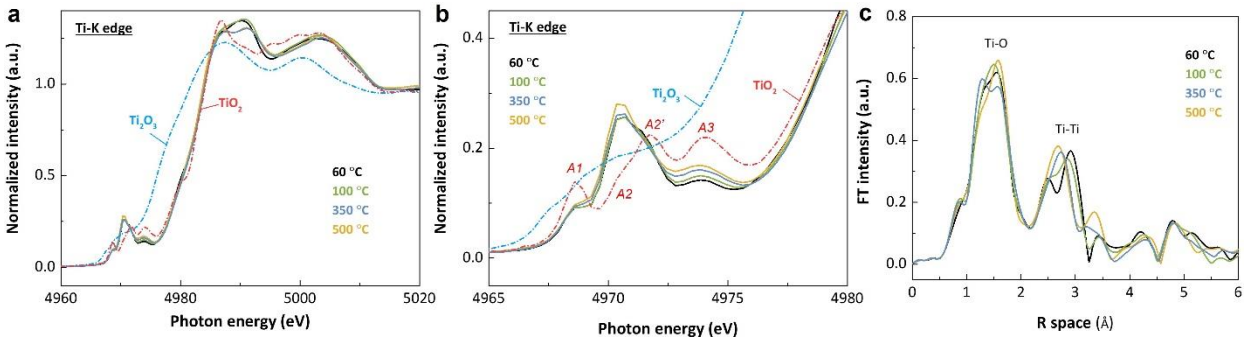

Figure 121. (a) Titanium K-edge spectra in the X-ray absorption near-edge spectroscopy region for $Na_{0.74}Ti_{1.815}O_4$ annealed at different temperatures from 60°C to 500°C, and (b) magnification of the pre-edge features. Titanium K-edge spectra of Ti_2O_3 and TiO_2 were also included for comparison. (c) Fourier-transformed magnitude of titanium K-edge extended X-ray absorption fine structure spectra for $Na_{0.74}Ti_{1.815}O_4$ annealed at different temperatures from 60°C to 500°C.

Hard XAS was also utilized to probe the electrochemical Na^+-ion storage mechanism in sodium titanate anodes. Figures 122 & 123 show the normalized XANES spectra of 60°C-annealed $Na_{0.74}Ti_{1.815}O_4$ electrodes on electrochemical cycling. The titanium K-edge shifts to lower energy on discharging to 0.1 V versus Na^+/Na, indicating a reduction of Ti^{4+} on sodiation (Figure 122b-c). The reduction of Ti^{4+} leads to longer Ti-O distance, as revealed by EXAFS analysis (Figure 122d). On recharging to 2.0 V versus Na^+/Na, the edge position shifts to higher energy, suggesting oxidation of titanium ions on desodiation (Figure 122e-f). The edge position of the electrodes at the fully charged states gradually shifts to lower energy on cycling ($1^{st} \rightarrow 10^{th} \rightarrow 67^{th}$ cycle, Figure 123), suggesting that the Coulombic inefficiency at each cycle (a small portion of Na^+ intercalated during discharge remains in the titanate anodes after charge) results in a gradual titanium reduction. Soft XAS will be utilized to further elucidate the redox behavior of sodium titanate anodes at the surface region. The assembly, testing, and optimization of full cell using sodium titanate anode and $Na_3V_2(PO_4)_3$ is continuing.

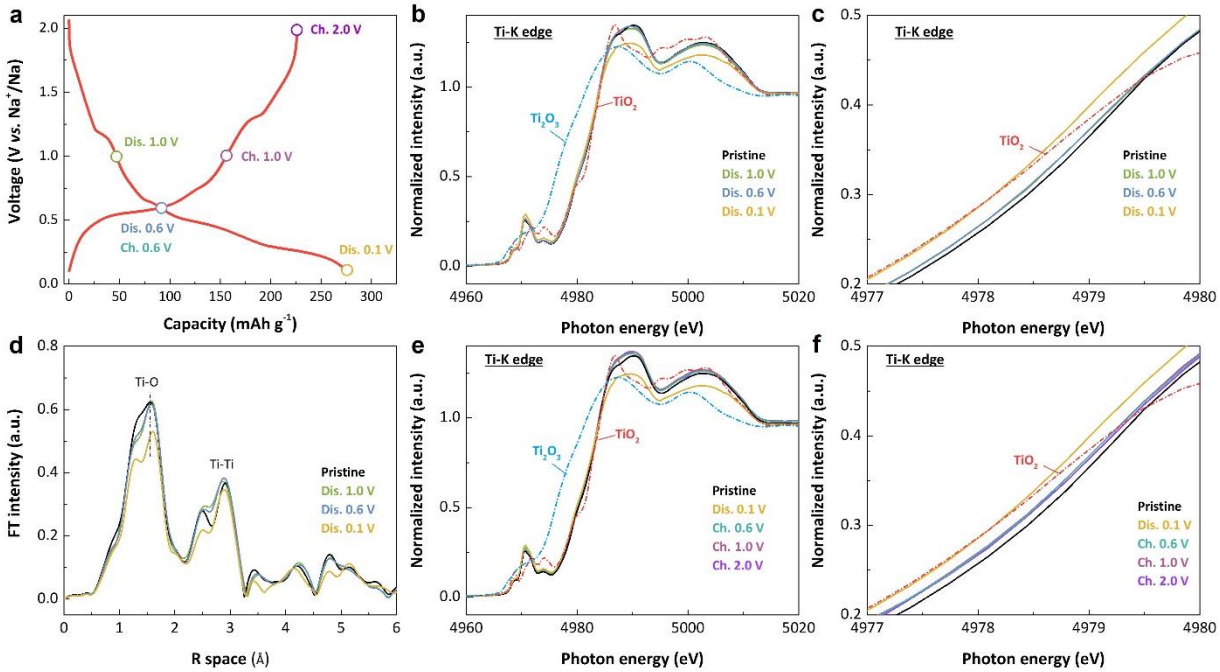

Figure 122. (a) 1st-cycle charge and discharge plots of 60°C-annealed $Na_{0.74}Ti_{1.815}O_4$ for *ex situ* X-ray absorption spectroscopy measurements. Titanium K-edge spectra in the X-ray absorption near-edge spectroscopy region for 60°C-annealed $Na_{0.74}Ti_{1.815}O_4$ electrodes at different states of (b) discharge and (e) charge, and their corresponding magnification view (c/f). (d) Fourier-transformed magnitude of titanium K-edge extended X-ray absorption fine structure spectra for 60°C-annealed $Na_{0.74}Ti_{1.815}O_4$ electrodes at different discharge states.

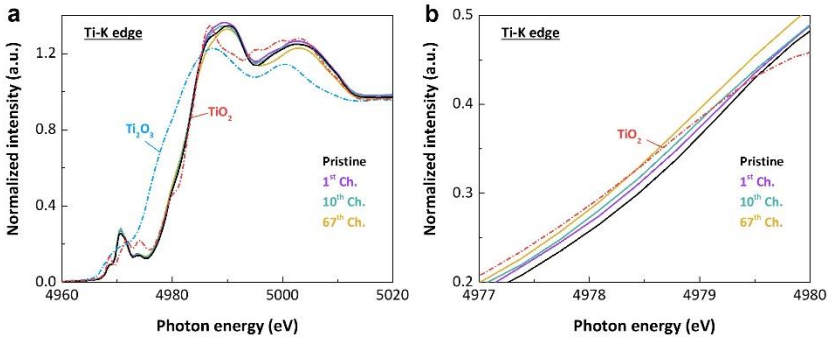

Figure 123. (a) Titanium K-edge spectra in the X-ray absorption near-edge spectroscopy region for 60°C-annealed $Na_{0.74}Ti_{1.815}O_4$ electrodes at fully charged states in different cycles, and (b) their corresponding magnification view. Titanium K-edge spectra of Ti_2O_3 and TiO_2 were also included for comparison.

References

[1] *Journal of Physical Chemistry C* 115 (2011): 6554–6560.

[2] *Applied Surface Science* 502 (2020).

Patents/Publications/Presentations

Publication

- Yin, W., J. Alvarado, G. Barim, M. C. Scott, X. Peng, and M. Doeff. "A Layered Nonstoichiometric Lepidocrocite-Type Sodium Titanate Anode Material for Sodium-Ion Batteries." *MRS Energy & Sustainability* (2021). doi: 10.1557/s43581-021-00008-6.

Task 7.4 – Electrolytes and Interfaces for Stable High-Energy Sodium-Ion Batteries (Ji-Guang Zhang, Pacific Northwest National Laboratory)

Project Objective. The Na-ion battery is a potential alternative energy source for EVs and grid applications due to the low cost and the natural abundance of sodium. The performance of Na-ion batteries largely depends on development of electrode materials and electrolytes. In recent years, a series of potential electrode materials has been developed. However, a fundamental understanding of the electrochemistry of Na-ion batteries, especially the stability of the electrode-electrolyte interface in these batteries, is still not well established. This project will develop innovative electrolytes to enable fundamental understanding on the interface between electrode and electrolyte for stable operation of high-energy Na-ion batteries. A high-capacity anode will also be developed. The proposed research will enhance the achievable capacities of both anode and cathode for Na-ion battery and improve the stability of electrodes/electrolyte interface, establish correlation (electrolyte design rule) between electrochemical performances of Na-ion batteries and the electrolyte/interface properties, and enable long cycle life and safe operation of high-energy Na-ion batteries.

Project Impact. Success of this project will provide a solid understanding on the electrolyte/electrode interphase of Na-ion batteries and significantly improve their energy density, cycle life, and safety. It will also accelerate the practical application of Na-ion batteries in both EV and stationary energy storage.

Approach. This project will optimize the electrolyte components and concentrations to develop innovative electrolytes and additives with improved electrochemical and physical properties. Ether-based electrolytes with different salt will be optimized toward both anode (sodium metal and hard carbon) and cathode. Phosphate-based LHCE will be optimized to improve cycling performance of Na-ion batteries. SEI/CEI components of Na-ion battery in ether and phosphate electrolytes will be studied using XPS and SEM/TEM techniques to reveal the fundamental mechanism behind the improved stable performance of Na-ion batteries. Electrolyte additives in carbonate electrolyte will also be investigated to improve the electrochemical cathode performance. These approaches will unravel the origin of the SEI at the dynamic interface, providing guidance for the electrolyte and interface design and enabling high capacity and long life of Na-ion batteries.

Out-Year Goals. This project will select the electrolyte compounds and identify the formation of interfacial SEI layer on hard carbon and CEI layer-on-layer oxide cathode and its effect on the electrode materials. It will also provide guidance on electrolyte optimization and to improve CE of sodium deposition/stripping to be more than 99%.

Collaborations. This project will collaborate with ANL, LBNL, and other leading scientists in the field of cathode and anode materials for Na-ion batteries. It will also collaborate with C. Wang and M. Engelhard of PNNL for TEM and XPS characterization.

Milestones

1. Develop high-capacity carbon anodes in Na-ion batteries with optimized electrolytes. (Q1, FY 2021; Completed)
2. Develop high-voltage electrolytes ($\geq$ 4.2 V) to increase energy density of Na-ion batteries. (Q2, FY 2021; Completed)
3. Characterize CEI/SEI interphase properties in optimized electrolyte to probe the mechanism of high-voltage cycling stability of Na-ion batteries. (Q3, FY 2021; Completed)
4. Develop electrolytes that are compatible with conventional polymer separators. (Q4, FY 2021)

Progress Report

To understand the mechanism behind the stable electrochemical performance of 4.2 V hard carbon||NaNMC cells in advanced nonflammable high-concentrated electrolyte (HCE, NaFSI:TEP = 1:1.5 in mole ratio) compared with BE [1 M $NaPF_6$/ propylene carbonate (PC)], the compositions of electrode/electrolyte interphases were analyzed by XPS. The results of XPS analysis on CEI layer formed on cycled NaNMC cathode surface are shown in Figure 124. In carbon 1s spectra of CEI formed in BE, the main species are C-C/C-H, C-O, C = O, CO_3, and PVDF, as shown in Figure 124a. In contrast, for the CEI layer formed in HCE, additional C-SO_x peak from NaFSI salt decomposition can be clearly identified, as shown in Figure 124d. The fluorine 1s spectra of CEI layers formed in both electrolytes contain NaF and C-F/P-F/S-F peaks. The phosphorus 2p and sulfur 2p spectra typically represent the contributions from inorganic components derived from the conductive salts ($NaPF_6$ or NaFSI). The intensity of sulfur 2p spectrum in NaFSI-TEP electrolyte was higher than phosphorus 2p spectrum in $NaPF_6$-PC electrolyte, indicating that more salt was decomposed to form CEI layer when HCE was used. XPS analysis revealed that the use of high concentration NaFSI-TEP electrolyte can effectively suppress dissolution of TMs in cathode, which is a significant advantage of this electrolyte. Figure 124g indicates that the atomic ratio of manganese in the CEI layer formed in NaFSI-TEP electrolytes is much less (0.46% versus 2.18%) than those formed in $NaPF_6$-PC electrolyte. Similarly, the atomic ratio of nickel in the CEI layer formed in NaFSI-TEP is also much less (0.11% versus 0.36%) than those formed in $NaPF_6$-PC electrolyte. This is consistent with Figure 124h-i that shows much less TMs can be found in NaFSI-TEP than in $NaPF_6$-PC electrolyte. These results clearly indicate that the inorganic-rich CEI layer formed in NaFSI-TEP electrolyte can effectively suppress the dissolution of TMs and stabilize CEI, therefore improving the electrochemical performance of Na-ion batteries.

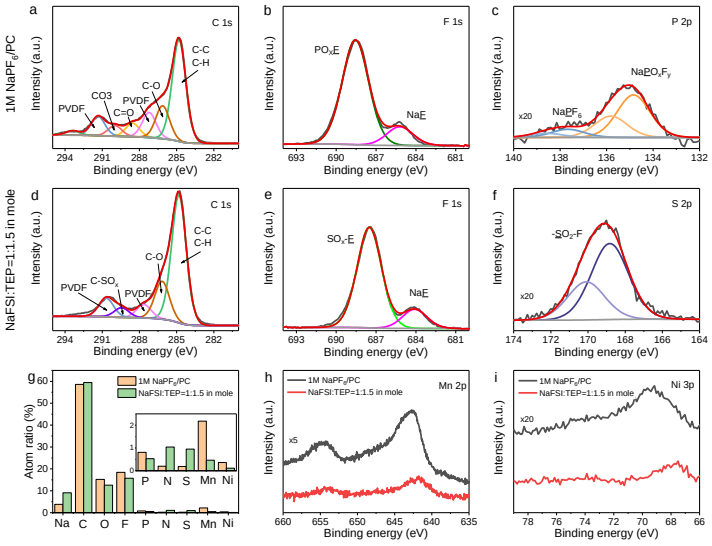

Figure 124. X-ray photoelectron spectra of CEI components on cycled NaNMC surface. (a/d) Carbon 1s spectra, (b/e) fluorine 1s spectra, (c) phosphorus 2p spectra, and (f) sulfur 2p spectra in $NaPF_6$-PC electrolyte (a-c) and NaFSI-TEP electrolyte (d-f). (g) Atomic composition ratios of CEIs in two electrolytes. (h/i) Manganese 2p and nickel 3p spectra in two electrolytes.

The XPS spectra and atomic ratios of cycled hard carbon anode in two electrolytes were also summarized in Figure 125. The organic species (carbon 1s) were similar in two electrolytes. However, the XPS spectra were different for inorganic elements, including phosphorus 2p from $NaPF_6$ salt, nitrogen 1s, and sulfur 2p from NaFSI salt decomposition. In NaFSI-TEP electrolyte, the intensity of nitrogen 1s and sulfur 2p peaks from NaFSI salt decomposition were much higher than phosphorus 2p peak from $NaPF_6$ salt decomposition in $NaPF_6$-PC electrolyte. In summary, in $NaPF_6$-PC electrolyte, the SEI components with inorganic and organic hybrid species were derived from both PC solvent and $NaPF_6$ salt decomposition. However, in NaFSI-TEP electrolyte, more NaFSI salt decomposition forms nitrogen, sulfur based inorganic SEI components, which can ensure a robust SEI layer and excellent cycling stability of hard carbon.

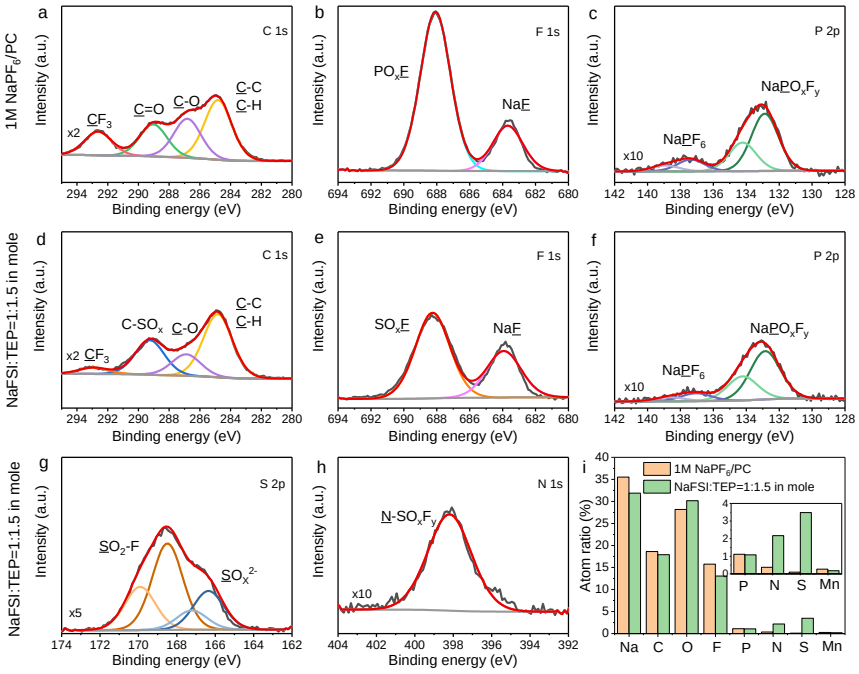

Figure 125. X-ray photoelectron spectra of SEI components on cycled hard carbon surface. (a/d) Carbon 1s spectra, (b/e) fluorine 1s spectra, (c/f) phosphorus 2p spectra, (g) sulfur 2p spectra, and (h) nitrogen 1s spectra in $NaPF_6$-PC electrolyte (a-c) and NaFSI-TEP electrolytes (d-h). (i) Atomic composition ratios of SEIs in two electrolytes.

Patents/Publications/Presentations

Presentation

- 239th ECS Meeting, Digital Meeting (May 2021): "Phosphate Electrolyte Design for Highly Reversible Sodium Ion Batteries"; Y. Jin,* P. L. M. Le, R. Yi, T. D. Vo, and J-G. Zhang.

Innovation Center for Battery500
(Jun Liu, Pacific Northwest National Laboratory; Yi Cui, Stanford University)

Project Objective. The project aims to develop commercially viable lithium battery technologies with a cell-level specific energy of 500 Wh/kg through innovative electrode and cell designs that enable the extraction of the maximum capacity from advanced electrode materials. In addition to achieving high specific energy, the project aims to be able to achieve 1,000 cycles for the developed technologies.

Project Impact. The Battery500 Consortium will develop next-generation lithium battery technologies that will significantly increase energy density, improve cycle life, and reduce cost. This will greatly accelerate deployment of EVs and reduce carbon emission associated with fossil fuel consumption. The consortium will utilize first-class expertise and capabilities in battery research in the United States and develop an integrated and multi-disciplinary approach to accelerate development and deployment of advanced electrode materials in commercially viable high-energy batteries. The advances made in this consortium will also benefit the improvement of current Li-ion battery technologies.

Approach. This project will utilize an assortment of national resources located at the national laboratory level and university level. The lithium anode combined with a compatible electrolyte system and two cathodes—one high-Ni $LiNi_xMn_yCo_zO_2$ and another sulfur—will be studied and developed to reach high energy density. The project focus is to design novel electrode and cell architectures to meet the 500 Wh/kg goal. The consortium will work closely with R&D companies, battery/materials manufacturers, and end users / original equipment manufacturers to ensure that the developed technologies are aligned with industry needs and can be transitioned to production.

Out-Year Goals. This project aims for the following out-year goals. First, fabricate and test a pouch cell capable of 350 Wh/kg and 350 cycles. Second, fabricate and test a pouch cell capable of 400 Wh/kg and 100 cycles.

Collaborations. Collaboration among consortium team members will be well coordinated by the leadership team, which includes the keystone project leads and co-leads along with PIs at all member institutions. Collaboration with the community outside of this consortium and with industry will be facilitated by the executive committee, the advisory board, and the industry committee.

Milestones

1. Benchmark Li-anode architecture with 50-µm lithium anode using protocols for 350 Wh/kg cells, and achieve over 200 cycles in coins. (Q1, FY 2021; Completed)
2. Optimize pressure effect for Li-S from coin cells. (Q2, FY 2021; Completed)
3. Provide new electrolyte formulation for Li-S (PNNL). (Q3, FY 2021; Completed)
4. Demonstrate 350 Wh/kg pouch cell with > 450 cycles; 400 Wh/kg > 100 cycles; and > 450 Wh/kg. Demonstrate good cycling of Li-S pouch cell at 300 Wh/kg. (Q4, FY 2021; In progress)

Progress Report

Keystone Project 1: Materials and Interfaces

The goal of Keystone 1 is to provide the materials and chemistry support for Keystone projects 2 and 3. Binghamton developed an approach to reduce 1st cycle loss by niobium doping. PNNL demonstrated extended calendar life (with a capacity recovery of 89.5% after 18-month storage at fully discharged state) of Li||NMC-811 cells with a fluorinated orthoformate (TFEO) based LHCE. UT Austin synthesized a lithiophilic matrix material as an alternative anode and validated it in coin full cells with a high-nickel $LiNi_xMn_yCo_{1-x-y}O_2$ (NMC) which has a high-capacity retention of 94% after 100 cycles. University of Washington (UW) identified proper boundary conditions for conserving mass in Li-metal battery models (both one-dimensional, or 1D, and 2D) for plating and stripping.

The Binghamton team verified that the 1st-cycle capacity loss of NMC cathode is mainly due to kinetic limitations for lithium insertion during discharge. This loss can be reduced by electrode calendering, increasing of temperature, constant current followed by constant voltage discharge kinetics control procedures. However, to solve this issue intrinsically at the material level, surface modification is recommended to enhance fast diffusion into the material and minimize the formation of more resistive surface impurities. Bulk substitution is also recommended to enhance capacity retention on extended cycling; this is believed to help the reduction of diffusion of non-lithium ions in the lattice, and therefore the reduction of oxygen loss. A Nb-based coating also assists in removing surface impurities, such as Li_2CO_3. As shown in Figure 126a, compared to pristine NMC-811, after Nb-coating, the 1st-cycle capacity loss was respectively reduced ~ 5 mAh g^{-1} and 12 mAh g^{-1} for the cut-off voltage of 4.4 V and 4.6 V, corresponding to an increase of ~ 2% and 5% on the CE. This benefit was not only observed for carbonate-based electrolyte, but also for the PNNL M47 LHCE (LiFSI-1.2DME-3TTE by mol); see Figure 126b.

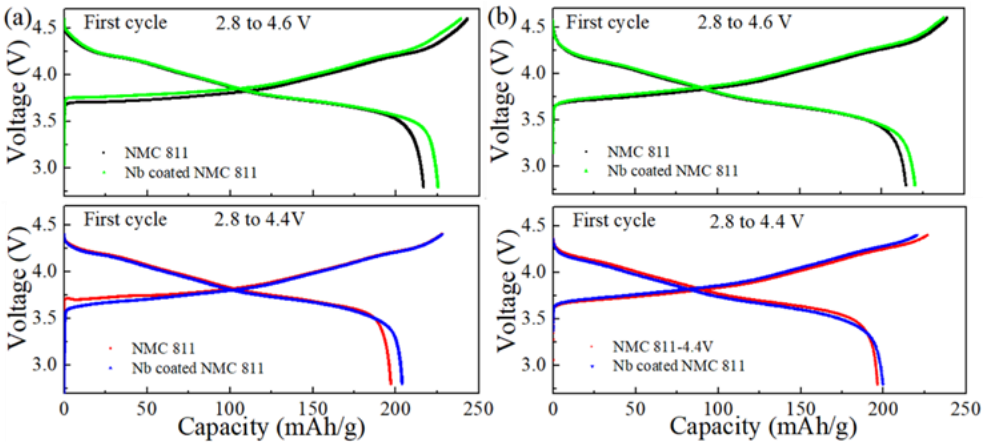

Figure 126. 1st Charge and discharge curves of pristine NMC-811 and Nb-coated NMC-811 within the voltage range of 2.8-4.6 V and 2.8-4.4 V, respectively, with (a) 1 M $LiPF_6$ in EC/DMC electrolyte and (b) Pacific Northwest National Laboratory's M47 localized high concentration electrolyte.

Al-substitution was also found to be effective in reducing the 1st-cycle loss. The team study showed that with 4% Al-substitution, the 1st capacity loss can be reduced from 35 mAh/g to 16 mAh/g, which can be attributed to the improved lithium diffusion, as shown in Figure 127. The impact of using different ions for the coating and for substitution will be further investigated.

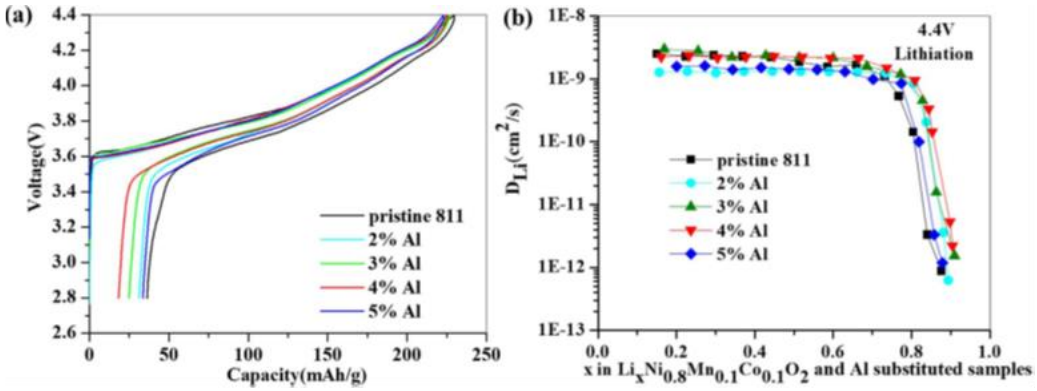

Figure 127. (a) The voltage profile of 1st cycle at 0.1C of NMC-811 and $LiNi_{0.8}Mn_{0.1-y}Co_{0.1}Al_yO_2$, (y = 0.02, 0.03, 0.04, 0.05) versus lithium in the voltage range of 2.8-4.4 V. (b) Calculated diffusion coefficients of lithium ion at different lithium compositions during the lithiation process with GITT measurement for all samples.

The PNNL team investigated the calendar life of Li||NMC-811 coin cells consisting of the NMC-811 cathode (4.2 mAh cm^{-2}), a thin lithium foil (50 µm), and the TFEO-based LHCE. The electrolyte amount was controlled at an electrolyte/capacity (E/C) ratio of 7 g (Ah)$^{-1}$. All cells were stored in 25°C temperature chambers and charged and discharged between 2.8 V and 4.4 V at C/10 rate, where 1C = 4.2 mA cm^{-2}. For the calendar life tests, cells were first cycled twice in the voltage range of 2.8-4.4 V at C/10 rate and then charged to the target SOC. As shown in the Figure 128a-c, three SOC conditions [that is, fully discharged state (0% SOC, rest after formation cycles), half charged state (50% SOC, with a specific capacity of 97 mAh g^{-1} charged at constant current mode), and fully charged state (100% SOC, where cells were charged to 4.4 V at constant current mode followed with an additional constant voltage step)] were selected for this study. The self-discharge capacity and the recoverable capacity of the cells were measured after selected storage periods (that is, 1 day, 1 week, 2 weeks, 3 weeks, 4 weeks, 2 months, 3 months, 6 months, 9 months, and 18 months) at 25°C. At each scheduled time, cells at fully discharged state were charged and discharged at C/10 for 1 cycle to check the recoverable capacity, as shown in Figure 128d. For the cells charged to 50% or 100% SOC, they were first fully discharged at C/10 to check the capacity loss (or self-discharge) during the selected rest period, and then charged back to the target SOC, as shown in Figure 128e-f, respectively. The last curve (18-month storage) in Figure 128e shows the discharge profile of a separate sample stored at 50% SOC for 18-months without intermediate steps. The self-discharge rate is defined as the capacity loss during the rest period divided by the storage time since the beginning of the last rest period. After 9 months of storage, the capacity recovery reduced slightly, indicating the calendaring degradation accelerated in this period. When the storage time is further prolonged to 18 months, 181.9 mAh g^{-1} (that is, 89.6% of initial capacity) can still be recovered. This result clearly demonstrates that great capacity recovery can be achieved in high-voltage Li||NMC-811 cells using the TFEO-based LHCE. For the cells stored at 50% SOC, the self-discharge rates are between 0.31- 0.82%/day during different storage periods with an average self-discharge rate of 0.42%/day for the whole storage time. For the cells stored at 100% SOC, the self-discharge rates are between 0.23-0.86%/day during different time periods with an average self-discharge rate of 0.26%/day. The slight variation of the self-discharge rates may come from the systematic error of the Land Battery Tester System used, which could be reduced in the long storage time. A fully charged battery would lose only 2.5% (5.7 mAh g^{-1}) of its initial capacity (227.5 mAh g^{-1}) for 1 week of storage. In addition, a fully charged cell can still retain more than half of the capacity [114.0 mAh g^{-1} of its previous charged capacity (216.8 mAh g^{-1})] after 9-month storage, which is excellent for practical applications such as EVs.

The UT Austin team synthesized a lithiophilic matrix material as an alternative anode, validated it in coin full cells with a high-Ni cathode at low N/P ratio [capacity ratio between the anode (negative electrode) and cathode (positive electrode)], and assembled pouch cells for further validation (Figure 129). The backbone of the lithiophilic host was a carbonized cotton (CC) matrix coated with silver nanoparticles, as the Li-Ag alloy displays fast diffusivity for Li^+ and presents a low nucleation barrier for lithium deposition. The lithiophilic matrix was further infiltrated with a SE $Li_{3.85}Sn_{0.85}Sb_{0.15}S_4$ (LSnS), which is ion-conductive, soluble in water and methanol, and stable in dry air. Finally, pentaerythritol tetraacrylate (PETEA) monomer was reacted with $Li_{3.85}Sn_{0.85}Sb_{0.15}S_4$ to improve its stability at the Li-metal interface. Coin full cells with a high loading of $LiNi_{0.9}Mn_{0.05}Co_{0.05}O_2$ (NMC) cathode (18.0 mg cm^{-2}, 4.0 mAh cm^{-2}) and a controlled N/P ratio of 1 were assembled, with lean LHCE electrolyte [5 µL $(mAh)^{-1}$] confined to the cathode and separator via *in situ* gelation with polymer. The coin full cells demonstrated a high capacity retention of 94% after 100 cycles at C/5 rate. For further testing, pouch full cells with a low stack pressure of 320 kPa have been assembled and are cycling with high capacity and good retention.

The BNL team applied synchrotron XRF mapping to understand the TM dissolution at high-voltage charging and consequent deposition on the Li-metal anode. This is closely related to the Battery500 goal of further increasing the cell energy density, which can be realized by increasing the charging voltage. However, high voltage can lead to serious TM dissolution on the cathode side, followed by TM migration through electrolyte and deposition on Li-metal anode, resulting in surface/interphase degradation and cell capacity fade. XRF mapping images with a spatial resolution ~ 30 µm were collected from the Li-metal anodes recovered from both BE and electrolyte that contains a new phosphorus-based additive after 90 cycles. As the fluorescence intensity can be directly related to the TM concentration, the deposited TM on Li-anode surface can also be mapped quantitatively, as shown in Figure 130a, in which the concentrations of nickel, manganese, and cobalt are represented by the color scale bar with the unit in µg mm^{-2}. Several interesting findings are noted. First, there are substantial inhomogeneities across the electrode, which apply to electrodes harvested from both

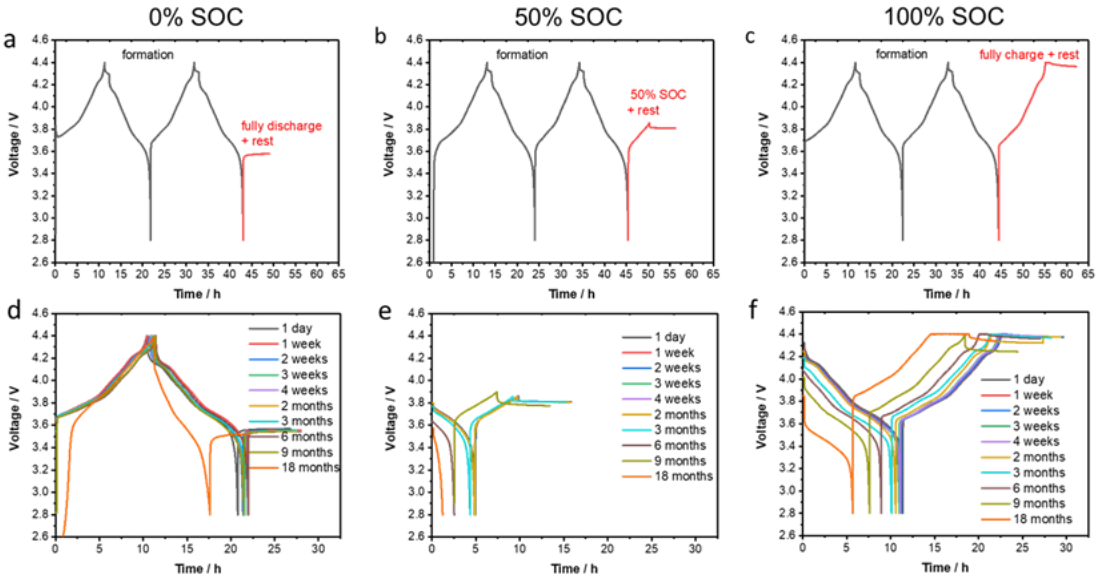

Figure 128. Electrochemical performance of cells at different SOCs. (a-c) Voltage profiles of the cells during the formation process and rest conditions: (a) cell rested at fully discharged state (0% SOC), (b) cell rested at half-charged state (50% SOC), and (c) cell rested at fully charged state (100% SOC). (d-f) Voltage profiles of the cells after different storage periods at different SOCs: (d) 0% SOC, (e) 50% SOC, and (f) 100% SOC.

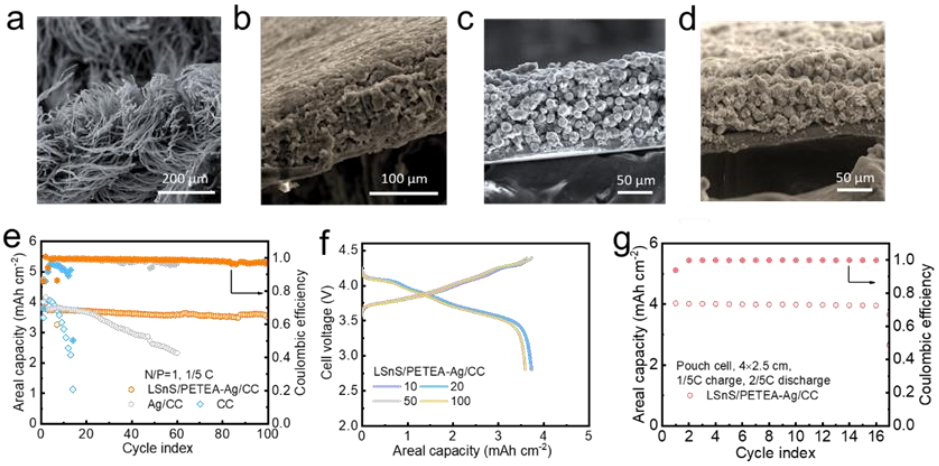

Figure 129. Full-cell performance of lithiophilic matrix | high-Ni NMC cells: Cross-sectional scanning electron microscopy (SEM) images of (a) Ag / carbonized cotton (CC) anode, (b) LSnS/PETEA-Ag/CC anode, (c) NMC cathode, and (d) NMC cathode infiltrated with LHCE-based gel polymer electrolyte. (e-f) Cyclability and voltage profiles of coin full cells assembled with LSnS/PETEA-Ag/CC anode and NMC cathode (N/P = 1). (g) Cyclability of pouch full cells assembled with LSnS/PETEA-Ag/CC anode and NMC cathode (N/P = 1).

baseline and additive-containing electrolytes. TM concentration in one area can be higher than another area by an order of magnitude. Such inhomogeneities demonstrate the necessity of considering TM dissolution in the length-scale of electrode-level instead of just at nanometric level; such electrode-level study has never been explored. Second, among all three TMs, nickel experiences the most severe dissolution. This is completely different from the widely accepted belief that manganese is the most dissolved element among nickel, manganese, and cobalt. One possible reason for such a difference is that this work evaluated the entire electrode, while previous work usually only focused on a randomly selected spot that may not be representative, given the high inhomogeneities of the deposition across the electrode. Third, the additive can very effectively suppress TM dissolution, as shown in Figure 130b. On average, the deposited TM is reduced by ~ 70% when the additive is present.

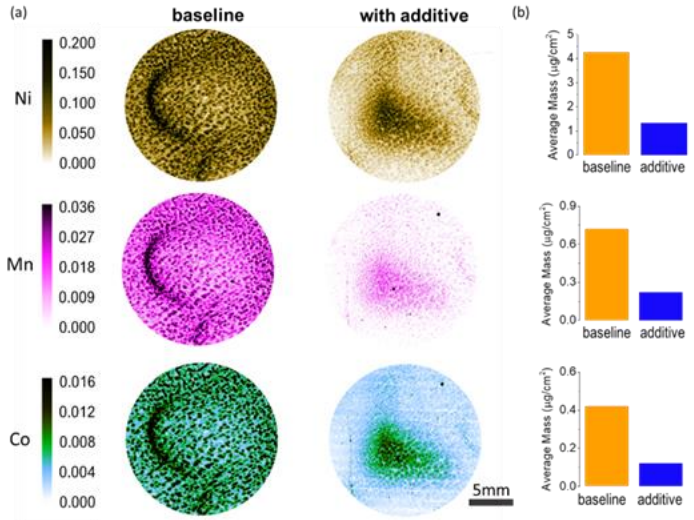

Figure 130. Electrode-level quantification of the deposited transition metal (TM) on lithium anode. (a) X-ray fluorescence mapping of the lithium anode with spatial resolution ~ 30 μm. The unit of the color scale bar is μg mm^{-2}. (b) Average deposited TM mass per unit area for the three TMs. In both (a) and (b), comparisons are made between the baseline electrolyte and the 'with additive' electrolyte.

Highlights of Keystone Project 1

The highlights for this quarter are as follows:

- Several approaches such as niobium surface coating and niobium bulk substitution have been recommended to reduce 1st-cycle loss of NMC cathode (Binghamton).
- Li||NMC-811 cells using a TFEO-based LHCE have demonstrated the capability to extend calendar life (capacity recovery was 89.5% after 18-month storage at fully discharged state) (PNNL).
- A lithiophilic matrix material as an alternative anode has been synthesized and validated in coin full cells with a high-Ni NMC cathode. These cells have high capacity retention of 94% after 100 cycles (UT Austin).
- XRF mapping studies were carried out to understand the TM dissolution at high-voltage charging and consequent deposition on the Li-metal anode. The quantitative analysis showed that nickel, rather than the widely believed manganese, is the most dissolved element among nickel, manganese, and cobalt; using a new additive can effectively suppress the dissolution of all of them (BNL).

Keystone Project 2: Electrode Architecture

The goal of Keystone 2 is to design, model, fabricate, and characterize the effect of electrode architecture on electrode and cell performance in support of reaching the project goal of 500 Wh kg^{-1} cell specific energy. Highlighted in this report for Keystone 2 are efforts on controlling the chemical corrosions of Li-metal anodes, sulfurized polyacrylonitrile (SPAN) cathode characterization, and binder effects on cycling performance of high-areal-capacity SPAN electrode (UCSD), and the development of models for lithium deposition growth (UW/UT).

Development of 1D and 2D Models for Lithium Deposition Growth with Mass Conservation

The UW/UT team has been developing 1D and 2D models to capture the movement of lithium during plating/stripping when it is cycled at various rates. This quarter, it was observed that the imperfect mass conservation in previous treatment is too significant to be ignored, especially for repeated charge/discharge cycles. The improper formulation for mass conservation in electrochemical models involving moving boundaries, if ignored, might lead to erroneous results for the variables of interest in a battery, and in turn affect the accuracy of predictions for battery degradation and cycle life. Figure 131 shows comparative results obtained after a careful implementation of an improved mass conservation formulation at the moving boundary at the electrode-electrolyte interface where an advective flux term has been included in the interface boundary condition based on the mass jump condition at moving interfaces. The 1D transport model example has been chosen as a base case to demonstrate and emphasize the importance of electrode-electrolyte interface mass balance and has also been incorporated into 2D models. Both the 1D and 2D models have been implemented in an efficient form—for example, 100 cycles of charge/discharge curves take less than a minute of CPU time.

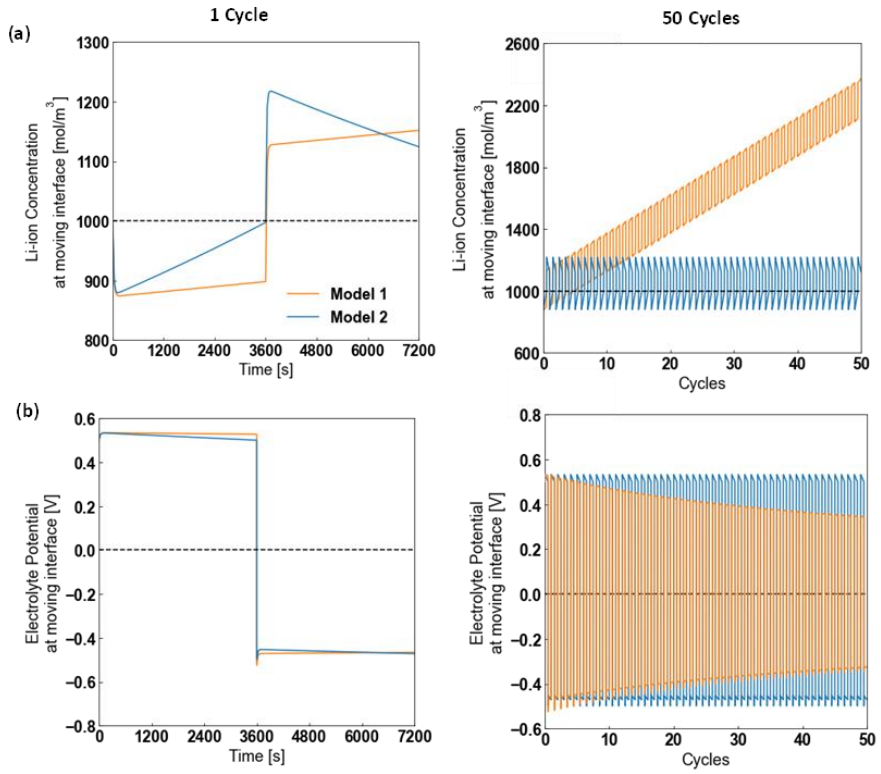

Figure 131. Comparative results for electrolyte (a) concentration and (b) potential over 50 cycles for the original model without advective flux (Model 1) and modified model with advective flux (Model 2) at moving interface at x = 0.

Controlling the Chemical Corrosion of Li-Metal Anodes

Although extensive studies have been performed trying to prolong the cycling life of Li-metal anode, the lack of comprehensive understanding of chemical stability between lithium metal and LEs, which causes the corrosion of lithium metal, has prevented it from having an extended calendar life. The UCSD team designed experiments to study the trend of lithium corrosion in LE. First, 0.318 mAh of lithium was plated onto a copper substrate at a rate of 0.5 mA cm^{-2} in a coin-cell setup with a high concentration "Bisalt" electrolyte (4.7 M LiFSI + 2.3 M LiTFSI in DME) and carbonate-solvent-based "Gen 2" electrolyte (1.2 M $LiPF_6$ in EC-EMC). After plating, the deposited lithium metal with the copper substrate was kept in coin cell with the corresponding electrolytes while the cell was under the open circuit condition (without being linked to a cycler). After a certain period of storage time, the cells were disassembled, and the titration gas chromatography (TGC) method was used to quantify the mass of metallic Li^0 remaining on the copper substrate.

The lithium mass retention (%) as a function of storage time is shown in Figure 132a/d. For lithium plated in both Bisalt and Gen 2 electrolytes, there was a sudden drop of Li^0 mass in the first 24 hours of resting. After that, the corrosion rate of lithium plated in Bisalt electrolyte slowed down, which resulted in a 26.0% loss of Li^0 mass after 5 weeks of resting. However, a more drastic loss of Li^0 mass was observed in the Gen 2 electrolyte. The continuous corrosion of lithium caused a 60.8% loss of Li^0 mass after 5 weeks of resting. The morphological study by Cryo-FIB/SEM further confirms the corrosion trend obtained by TGC. The lithium morphology in Bisalt electrolyte did not experience a significant change after 5 weeks of resting under open circuit (Figure 132b-c). The lithium retained mostly its granular shape even after the resting period, although there was a decrease of lithium thickness from 1.16 µm to 0.92 µm. As expected, a sharp change in the morphology of lithium plated in the Gen 2 electrolyte was observed by Cryo-FIB/SEM (Figure 132e-f). The freshly deposited lithium in Gen 2 electrolyte exhibited a whisker-like morphology, while the corroded lithium showed a porous and powder-like morphology. There was also a substantial decrease of lithium thickness from 2.93 µm to 1.02 µm, which again agreed with the loss of Li^0 mass quantified by TGC. The two fundamentally different electrolyte systems, Bisalt (high-concentration ether-based electrolyte) and Gen 2 (conventional carbonate-based electrolyte), showed two drastically different corrosion trends: Bisalt showed a fast corrosion during the first 24 hours, but stabilized quickly afterward; Gen 2 showed a continuous corrosion rate throughout the 5 weeks of resting period.

Based on results to date, there might be two possible reasons for the difference in the corrosion trends from the two electrolytes: (1) Li-metal surface chemistry; and (2) Li-metal porosity. More research will be performed to study which parameters have the most significant impact on the lithium corrosion rate.

STEM Analysis of SPAN

The UCSD team has been analyzing the structure of the SPAN material in an effort to understand its reaction mechanism and search for approaches to further improve its capacity. Last quarter, STEM EELS was used to probe the bonding environment evolution of nitrogen, sulfur, and carbon in SPAN cathode after 10 cycles. The team found that nitrogen played an active role during the lithiation process of the SPAN. This quarter, the nitrogen K-edge spectra of the pristine SPAN was simulated by the FEFF9 software to better understand the measured EELS spectra.

The pristine SPAN molecule structure was built in iQmol software based on the FTIR results of the pristine SPAN. There are two types of C-S bonds in the SPAN molecule: one is the C-S bond at position 4 on the pyridine ring, which is well known; the other is the C-S bond at position 2 on the pyridine ring, which will break the conjugation structure of the pyridine ring and add extra hydrogen atoms onto the ring. The newly proposed SPAN molecular structure is illustrated in Figure 133b.

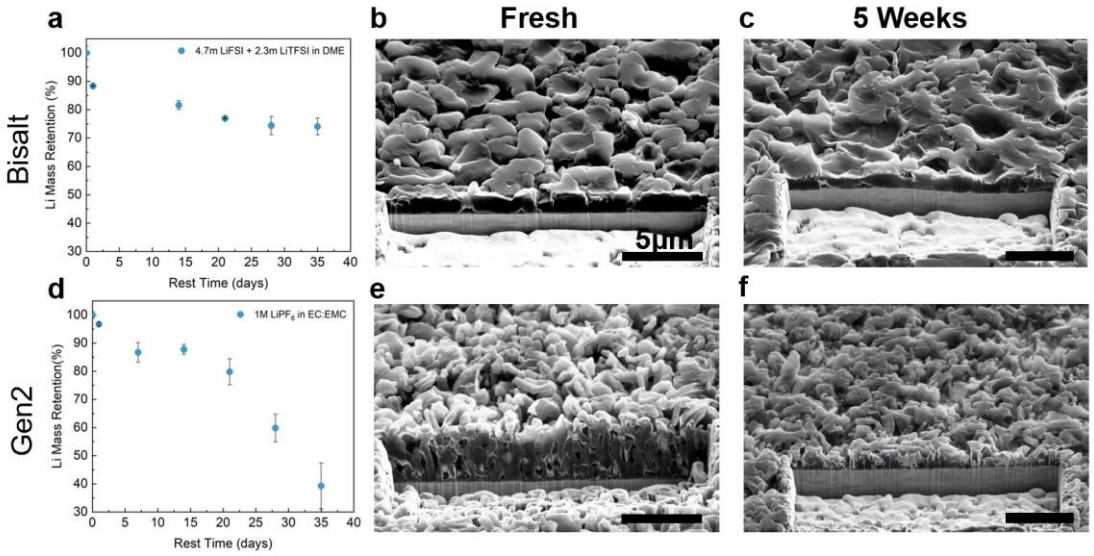

Figure 132. (a-c) The trend of Li-metal corrosion in high-concentration "Bisalt" electrolyte: (a) the Li^0 mass retention (%) as a function of resting time; and the scanning electron microscopy (SEM) images of the lithium morphology (b) before and (c) after 5 weeks of resting. (d-f) The trend of Li-metal corrosion in carbonate solvent based "Gen 2" electrolyte (1 M $LiPF_6$ in EC-EMC): (d) the Li^0 mass retention (%) as a function of resting time; and the SEM images of the lithium morphology (e) before and (f) after 5 weeks of resting. Total amount of 0.318 mAh of lithium is plated at a rate of 0.5 mA cm^{-2} in all samples.

EELS simulations for the nitrogen K-edge of the pristine SPAN were conducted using the FEFF9 software assuming four different types of nitrogen atoms, based on relative distance to the nearest C-S bond (Figure 133a). In location 2, where the nitrogen is surrounded by two sulfur atoms, the major peak is located at ~ 406 eV, which might be associated with the 1s to σ* transitions. In location 3, where the nitrogen has only one sulfur neighbor, there is a splitting in the peak that associated with the 1s to σ* transition. In location 4 and location 5, because nitrogen is not next to any sulfur atoms, the simulated nitrogen K-edge spectra show similar structure, where only one major peak is located at ~ 410 eV. Assuming a ratio of 0.05:0.8:0.1:0.05 for these four locations, the total nitrogen K-edge spectra was simulated, which was found to be close to the experimentally measured spectra (Figure 133c). The EELS results further confirm that there might be C-S at position 2 in the pristine SPAN pyridine ring. Further analyses by FTIR and XPS are in progress to decipher the reaction mechanism between lithium and SPAN.

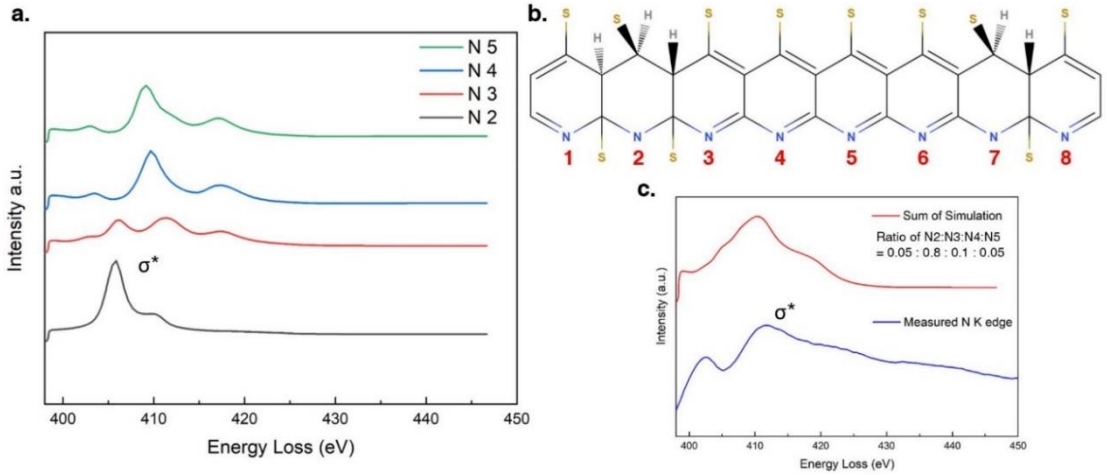

Figure 133. (a) The simulated nitrogen K-edge electron energy loss spectroscopy (EELS) spectra of the nitrogen atoms at different locations. The simulation was performed by FEFF9 software. (b) The proposed molecular structure of pristine sulfurized polyacrylonitrile (SPAN), with each nitrogen atom location marked. (c) The comparison between the sum of simulated nitrogen K-edge EELS spectra and the measured nitrogen K-edge of the pristine SPAN.

Binder Effects on Cycling Performance of High Areal Capacity SPAN Electrode

The UCSD team has systematically investigated the effect of binders on the cycling performance of high-areal-capacity SPAN cathodes (> 6 mAh cm^{-2}). They first tested the cycling stability of the SPAN electrode with active material loading of 1 mg cm^{-2}, which shows stable cycling, with no noticeable change of the voltage profiles throughout 60 cycles, indicating the SPAN material itself is highly stable (Figure 134a). However, the Li||SPAN cell shows a rapid capacity fading from 650 mAh g^{-1} to 400 mAh g^{-1} within 60 cycles when the electrode loading increases to 10 mg cm^{-2}; the corresponding voltage profiles indicate a fast polarization increase (Figure 134a-b). The morphology of the high-areal-capacity SPAN cathodes before and after cycling was studied by SEM. Figure 134d/h shows the top and cross-sectional view images of the pristine SPAN cathode. The presence of cracks is likely due to the stress generated during solvent evaporation for high loading electrodes. After 60 cycles, the electrode was delaminated from the current collector (optical image, Figure 134e inset). The cross-sectional image (Figure 134i) shows that the cathode thickness increases from 119 µm to 157 µm. More cracks have formed vertically from the bottom to the top of the electrode. The mechanical failures of cracking, delamination, and volume change are likely the root cause of the rapid capacity fading of the 10 mg cm^{-2} SPAN electrode. The mechanical disintegration of the thick SPAN electrode will lead to the breakage of the conductive network, which consequently causes either active material loss or polarization increase during cycling. Optimizing the polymer binder is a practical approach to improve the electrode mechanical integrity. The 6 mAh cm^{-2} SPAN cathode with a CMC binder exhibited stable cycling. It maintained 94.5% of its capacity (based on the 3rd cycle) at the 60th cycle, while the PVDF electrode at the 60th cycle only delivered a capacity retention of 66.7% (Figure 134a). The voltage profiles in Figure 134c also indicate that there was only a slight degradation with the electrode using CMC binder. Furthermore, the SEM images of the pristine and cycled electrodes in Figure 134f/g/j/k revealed no visible cracks or delamination in the electrode, proving durability with the CMC binder. This work proves the importance of binder on thick SPAN cathodes and paves the road for high-energy-density Li||SPAN cells with significantly improved cycling stability.

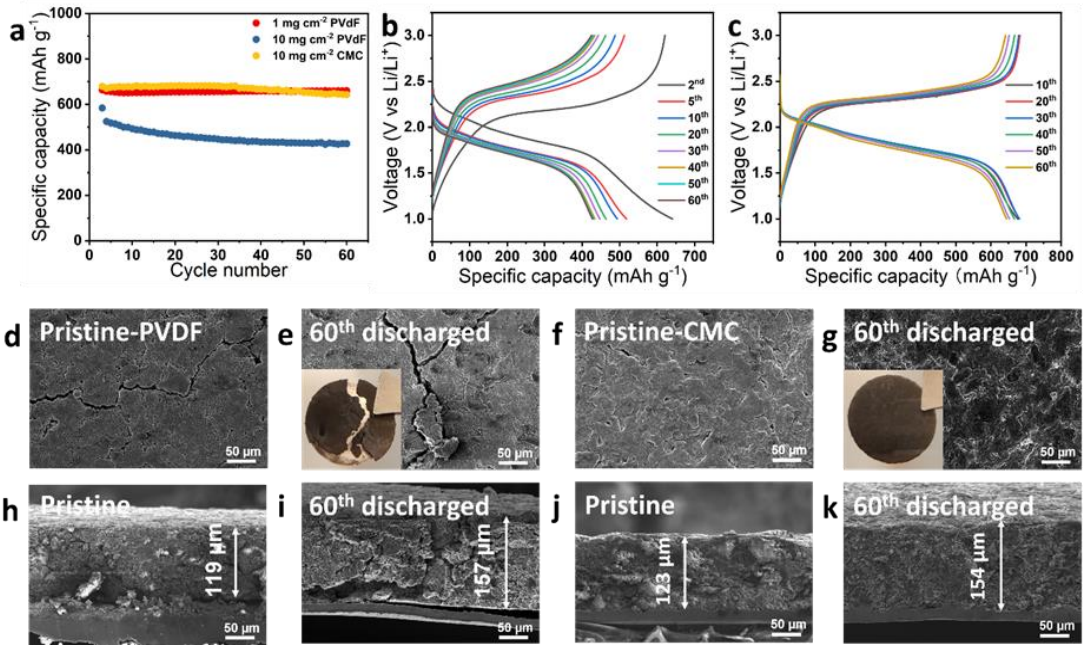

Figure 134. Comparison of cycling performance of SPAN cathodes with different areal mass loading. (a) Specific capacity of SPAN electrode. (b) Voltage profiles of 10 mg cm^{-2} SPAN cathode with PVDF binder. (c) Voltage profiles of 10 mg cm^{-2} SPAN cathode with carboxymethyl cellulose (CMC) binder. (d-k) Scanning electron microscopy images of high-areal-capacity SPAN cathode. With PVDF binder: Top-view images of (d) pristine and (e) after 60th discharge. Cross-sectional view images of (h) pristine and (i) after 60th discharge. With CMC binder: Top-view images of (f) pristine and (g) after 60th discharge. Cross-sectional view images of (j) pristine and (k) after 60th discharge. The cell was cycled under C/20 rate for two formation cycles and then cycled under C/5 rate.

Highlights of Keystone Project 2

The highlights for this quarter are as follows:

- UW/UT improved the Li-metal deposition model by including an advective boundary condition that better conserves the lithium mass, resulting in much better representation of the lithium cycling process.
- UCSD showed that lithium corrosion in a high-efficiency "Bisalt" electrolyte is fast in the initial 24 hours, but slows down dramatically afterward; in contrast, a constant-rate corrosion process takes place in a low-efficiency carbonated electrolyte.
- UCSD showed that binder choice is essential for the cycling stability of high loading SPAN cathode with the more elastic CMC being the preferred choice.

Keystone Project 3: Cell Fabrication, Testing, and Diagnosis

Keystone 3 continues to focus on the integration of advancements from Keystones 1 and 2, optimization of cell design, and the advancement of methods, to better understand cell aging and failure through advanced testing and diagnostics. This quarter, the team (1) advanced cell designs capable of extended cycle life (600+ cycles), (2) advanced understanding of the mechanical response of Li||S cells, and (3) compared analysis of loss of lithium in cells aged using either calendar or cycle life conditions.

Different than the Li||NMC batteries, where most of the mechanical changes take place in Li-metal anode, both the positive and negative electrodes in Li||S cells undergo mechanical expansion and contraction during cycling. Using similar techniques described in prior work for the Li-metal anode in NMC-based Li-metal batteries,[1] the Idaho National Laboratory (INL) team enhanced understanding of these two different mechanical aspects for Li-metal anode and S-cathode using single-layer pouch cells. For calendered sulfur electrodes at 7.8 kPa, it was observed that the normalized pressure can be divided into three zones corresponding to initial lithium loss zone (region 1), balanced lithium loss and structure evolution zone (region 2), and lithium anode structure evolution dominated zone (region 3). To further understand the link between capacity fade and cell mechanical response, the differential capacity (dQ/dV) and differential pressure (dP/dV) analysis were performed on cells using either non-calendered sulfur electrodes (NCSE) or calendered sulfur electrodes (CSE), as shown in Figure 135. The dQ/dV peak intensity at high voltage (~ 2.3 V) and low voltage (~ 2.1 V) is proportional to the specific capacities, and the ratio of 2.3 V / 2.1 V peak intensities follows the specific capacity trend (Figure 135a/c). However, the peak intensity of dP/dV does not follow the dQ/dV trend, since the dP/dV peak intensities are sensitive to pressure change with cycling (Figure 135b). The dP/dV peak intensity at ~ 2.1 V is higher than the dQ/dV intensity because of volume changes associated with the Li_2S formation on the cathode surface. The peak intensity gradually increases with cycling number as species accumulate on the cathode, in good agreement with charge polarization data. The overall dP/dV ratio of 2.3 V / 2.1 V peak intensities decrease (Figure 135c) with increasing cycling number because the amount of stripped lithium metal decreases. Comparing the results between the NCSE and CSE in Figure 135, it is clear that the CSE has better electrochemical and mechanical performance than its NCSE counterpart.

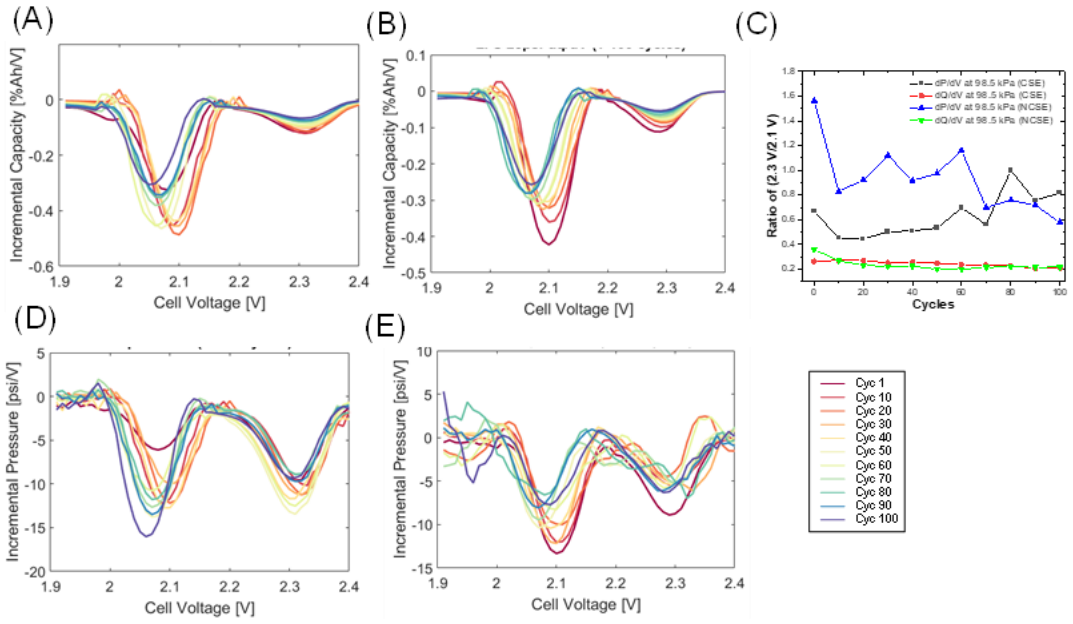

Figure 135. Comparison of non-calendered sulfur electrode (NCSE) or calendered sulfur electrode (CSE) cell differential capacity (dQ/dV) and differential pressure (dP/dV) as a function of cycles at 98.5 kPa. (a) NCSE dQ/dV. (b) NCSE dP/dV. (c) Comparison of ratio of high voltage (2.3 V)/ low voltage (2.1 V) dQ/dV and dP/dV peak intensities for NCSE and CSE cells. (d) CSE dQ/dV. (e) CSE dP/dV. (e) Comparison of normalized pressure for NCSE and CSE.

The PNNL team also continued to develop and implement new design principles to extend the life of Li-metal batteries and to understand the different degradation and failure mechanisms of them. As part of recently published work in *Nature Energy*, the team described 350 Wh kg^{-1} cells that achieved 600+ cycles while retaining 76% capacity retention (Figure 136e).[2] This advancement was achieved through a coordinated experimental design that used varying lithium thickness ranging from 0 µm (Li-metal free electrode) to 100 µm. Tuning the quantity of lithium at the negative electrode (shifting the cell N/P ratio) not only directly impacts cycle life, but also impacts the trajectory of capacity fade of these cells. Contrary to the commonly held belief, the use of more lithium in 50-µm and 100-µm lithium anode did not extend the cycle life, while the use of a balanced 20-µm thick lithium electrode resulted in the most extensive cycle life for this cell design. In this cell configuration, capacity fades in a gradual fashion, as opposed to a sudden rapid decay for thicker 50-µm and 100-µm lithium anodes. An even more rapid decay and shorter cycle life was observable when a Li-free negative electrode was used. These results provide valuable information for designing Li-metal batteries with high energy density and long cycle life.

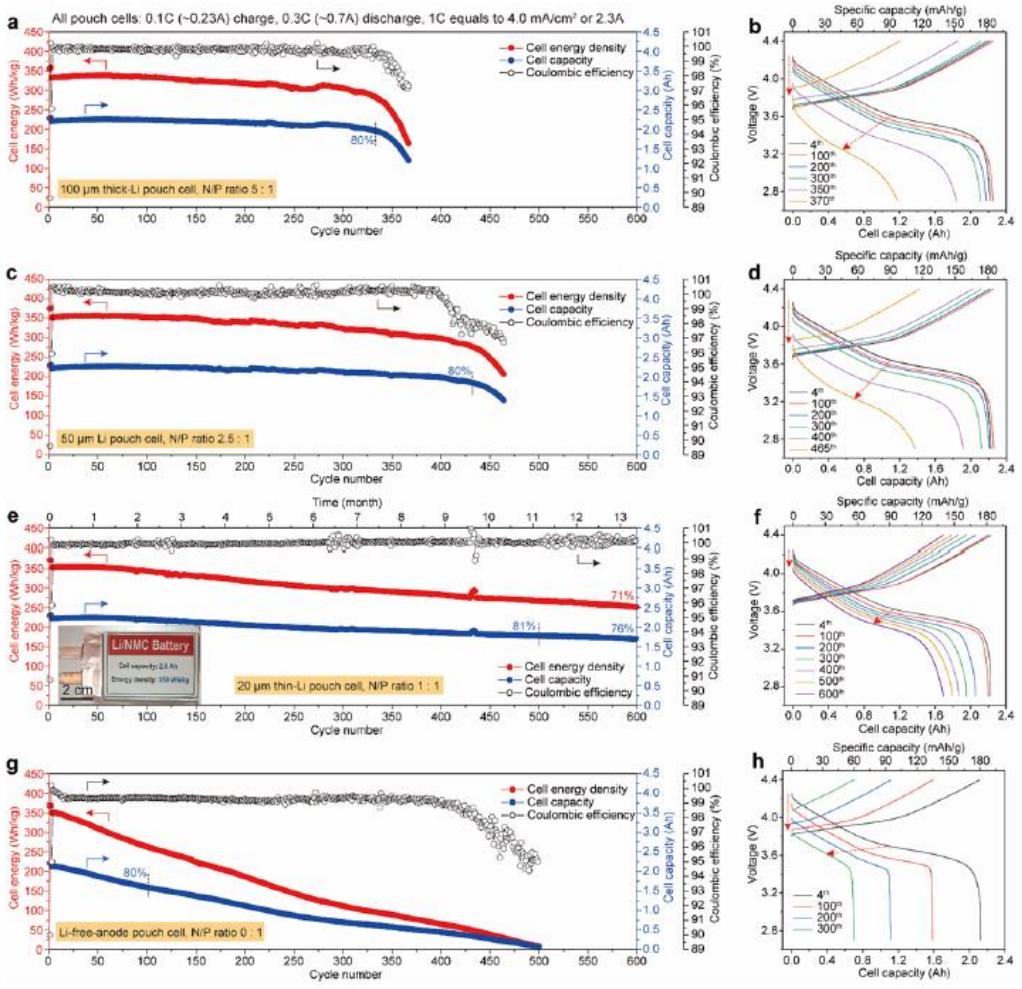

Figure 136. Capacity fade for different Li-metal battery designs for N/P ratios of 5:1 (a-b), 2.5:1 (c-d), 1:1 (e-f), and 0:1 (g- h).

The INL and PNNL teams worked together to compare the results between cycle aging and calendar aging using the Battery500 FY2020 cell design. Comparison was made on 350 Wh kg^{-1} pouch cells cycle-aged (using a standard C/10 charge and C/3 discharge) and calendar-aged (cells kept at 80% SOC for 14 days between reference performance tests, or RPTs). The results are shown in Figure 137. Both sets of cells show comparable loss of lithium inventory to SEI growth during aging. The cells that were maintained at rest for 14 days also

showed negligible fade over the course of the aging, though polarization did increase over the life of the cell, which resulted in a progressively lower SOC during the rest period. A key contributor of this shift was due to the cycles the cells underwent as part of the RPT. Based on these results, new evaluation methods and analysis protocols have been developed to decouple the impact of combined cycle and calendar aging effects.

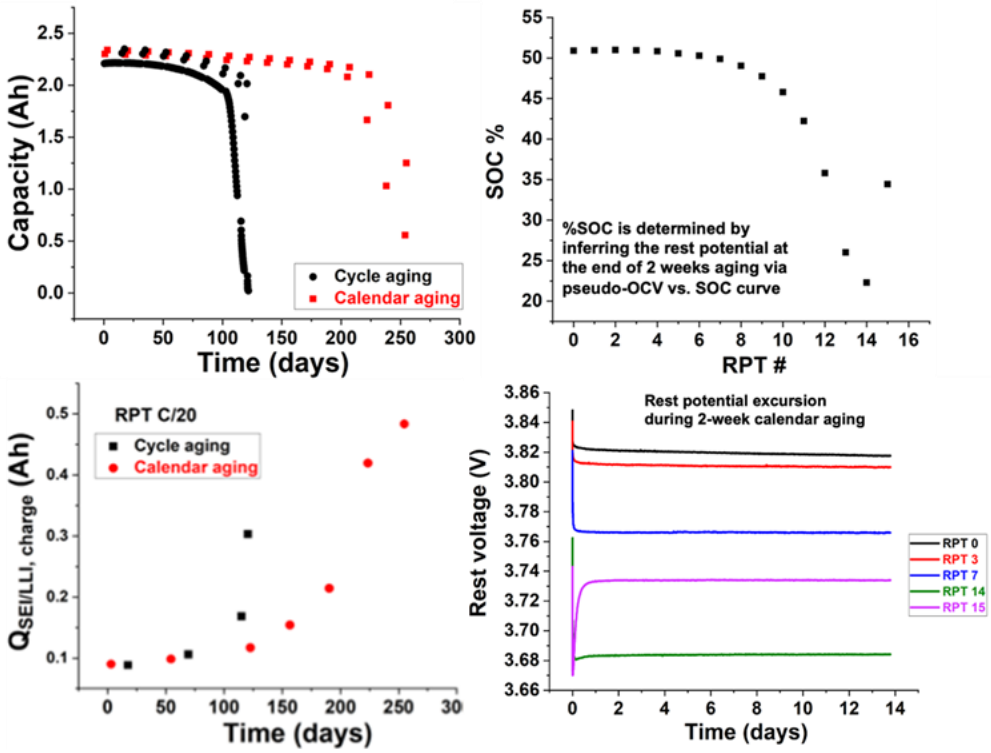

Figure 137. Comparison of calendar aging and cycle life aging for Li-metal batteries.

References

[1] Kim, S., et al. "Correlation of Electrochemical and Mechanical Responses: Differential Analysis of Rechargeable Lithium Metal Cells." *Journal of Power Sources* 463 (2020): 228180. doi: 10.1016/j.jpowsour.2020.228180

[2] Niu, C., et al. "Balancing Interfacial Reactions to Achieve Long Cycle Life in High-Energy Lithium Metal Batteries." *Nature Energy* 6 (2021): 723–732. doi: 10.1038/s41560-021-00852-3.

Highlights of Keystone Project 3

The highlights for this quarter are as follows:

- More detailed understanding on the different mechanical aspects for Li-metal anode and S-cathode were obtained using both dQ/dV and dP/dV analysis on single-layer pouch cells for Li||S, with both the lithium and sulfur electrodes (INL).
- An optimal anode-to-cathode capacity ratio of 1:1 was discovered comparing 0-µm, 50-µm and 100-µm thick lithium anodes. Contrary to conventional wisdom, long cycle life is observed by using ultra-thin lithium (20 µm) in balanced cells. A prototype 350 Wh kg^{-1} pouch cell (2.0 Ah) achieved over 600 long stable cycles with 76% capacity retention without sudden cell death (PNNL).

Patents/Publications/Presentations

Patent

- Yang, J., Y. Liu, X. Wu, X. Jiang, and J. Liu. "High Energy Li Batteries with Lean Lithium Metal Anodes and Methods for Prelithiation"; Patent Application PCT/US2021/039491, filed 6/29/2021, by University of Washington.

Publications

- Pei, B., H. Zhou, A. Goel, M. Zuba, H. Liu, F. Xin, and M. S. Whittingham.* "Al Substitution for Mn during Co-Precipitation Boosts the Electrochemical Performance of $LiNi_{0.8}Mn_{0.1}Co_{0.1}O_2$." *Journal of the Electrochemical Society* 68 (2021): 050532. doi: 10.1149/1945-7111/ac0020; Publication Date (Web): May 19, 2021.
- Lin, R.,* S-M. Bak,* Y. Shin, R. Zhang, C. Wang, K. Kisslinger, M. Ge, X. Huang, Z. Shadike, A. Pattammattel, H. Yan, Y. Chu, J. Wu, W. Yang, M. Whittingham, H. Xin,* and X-Q. Yang.* "Hierarchical Nickel Valence Gradient Stabilizes High-Nickel Content Layered Cathode Materials." *Nature Communications* 12 (2021): 2350. doi: 10.1038/s41467-021-22635w; Publication Date (Web): April 20, 2021.
- Zhou, H., B. Pei, Q. Fan, F. Xin, and M. S. Whittingham.* "Can Greener Cyrene Replace NMP for Electrode Preparation of NMC-811 Cathodes?" *Journal of the Electrochemical Society* 168 (2021): 040536. Publication Date (Web): April 27, 2021.
- Xu, B., X. Li, C. Yang, Y. Li, N. S. Grundish, P-H. Chien, K. Dong, I. Manke, R. Fang, N. Wu, H. Xu, A. Dolocan, and J. B. Goodenough.* "Interfacial Chemistry Enables Stable Cycling of All-Solid-State Li Metal Batteries at High Current Densities." *Journal of the American Chemical Society* 143, No. 17 (2021): 6542–6550. doi: 10.1021/jacs.1c00752; Publication Date (Web): April 27, 2021.
- Fang, R., B. Xu, N. S. Grundish, Y. Xia, Y. Li, C. Lu, Y. Liu, N. Wu, and J. B. Goodenough.* "Li_2S_6-Integrated PEO-Based Polymer Electrolytes for All-Solid-State Lithium-Metal Batteries." *Angewandte Chemie International Edition* (2021). doi: 10.1002/ange.202106039; Publication Date (Web): June 30, 2021.
- Zhou, H., H. Liu, X. Xing, Z. Wang, S. Yu, G. M. Veith, and P. Liu.* "Quantification of Ion Transport Mechanism in Protective Polymer Coatings on Lithium Metal Anodes." *Chemical Sciences* 12 (2021): 7023–7032. doi: 10.1039/D0SC06651F; Publication Date (Web): April 12, 2021.
- Lin, R., R. Zhang, C. Wang, X-Q. Yang, and H. L. Xin.* "TEMImageNet Training Library and AtomSegNet Deep-Learning Models for High-Precision Atom Segmentation, Localization, Denoising, and Deblurring of Atomic-Resolution Images." *Scientific Report* 11 (2021): 5386. doi: 10.1038/s41598-021-84499-w; Publication Date (Web): March 8, 2021. (This paper was published in Q2 of FY 2021, but not listed in the FY 2021 Q2 report.)
- Lu, B., E. Olivera, J. Scharf, M. Chouchane, C. Fang, M. Ceja, L. E. Pangilinan, S. Zheng, A. Dawson, D. Cheng, W. Bao, O. Arcelus, A. A. Franco, X. Li, S. H. Tolbert,* and Y. S. Meng.* "Quantitatively Designing Porous Copper Current Collectors for Lithium Metal Anodes." *ACS Applied Energy Materials* (2021). doi 10.1021/acsaem.1c00438; Publication Date (Web): June 18, 2021.
- Niu, C., D. Liu, J. A. Lochala, C. S. Anderson, X. Cao, M. E. Gross, W. Xu, J-G. Zhang, M. S. Whittingham, J. Xiao,* and J. Liu. "Balancing Interfacial Reactions to Achieve Long Cycle Life in High-Energy Lithium Metal Batteries." *Nature Energy* (2021): doi: 10.1038/s41560-021-00852-3; Publication Date (Web): June 28, 2021.

- Efaw, C., B. Lu, Y. Lin, G. Pawar, P. Chinnam, M. Hurley, E. Dufek, Y. S. Meng, and B. Li.* "A Closed-Host Bi-Layer Dense/Porous Solid Electrolyte Interphase for Enhanced Lithium-Metal Anode Stability." *Materials Today* (2021). doi: 10.1016/j.mattod.2021.04.018; Publication Date (Web): May 19, 2021.
- Kim, S. C., X. Kong, R. A. Vilá, W. Huang, Y. Chen, D. T. Boyle, Z. Yu, H. Wang, Z. Bao, J. Qin, and Y. Cui.* "Potentiometric Measurement to Probe Solvation Energy and its Correlation to Lithium Battery Cyclability." *Journal of the American Chemical Society* (2021). doi: 10.1021/jacs.1c03868; Publication Date (Web): June 29, 2021.
- Wang, H., Z. Yu, X. Kong, W. Huang, Z. Zhang, D. G. Mackanic, X. Huang, J. Qin, Z. Bao,* and Y. Cui.* "Dual-Solvent Li-Ion Solvation Enables High-Performance Li-Metal Batteries." *Advanced Materials* 33, No. 25 (2021): 2008619. Publication Date (Web): May 9, 2021.

Presentations (Invited)

- Morocco (April 7, 2021): "The Lithium Battery, From a Dream to Domination of Energy Storage"; M. S. Whittingham.
- Global Entrepreneurship Model United Arab Emirates (April 15, 2021): "My Journey to the Nobel Prize"; M. S. Whittingham.
- Chemistry Seminar, Stoffer Lecture, Missouri University of Science and Technology (April 16, 2021): "Li-Ion Batteries: From an Idea to Readiness to Take on Climate Change – Opportunities and Challenges"; M. S. Whittingham.
- MRS Spring Meeting, Virtual (April 22, 2021): "Batteries for Energy Storage to Green the Environment – Is There Another Battery Alternative?"; M. S. Whittingham.
- Nobel Prize Summit: Our Planet, Our Future; National Academy and Nobel Prize Institute (April 28, 2021): "Smart Cities and New Green Solutions"; M. S. Whittingham.
- New York State Energy Research and Development Authority Presents: Battery Energy Storage Systems – Key Considerations for Local Governments, Webinar #1: Battery Energy Storage Systems 101 (May 5, 2021): M. S. Whittingham.
- Israel Electrochemical Society (ISEL) Meeting (June 16, 2021): "Perspective on Lithium Battery Origins & Future Challenges/Opportunities"; M. S. Whittingham.
- Innovation Forum, LG Energy Solution (June 20, 2021): "Overview of Li Battery R&D"; M. S. Whittingham.
- Lindau Nobel Laureate Meeting (June 29, 2021): "Storage is Ready to Take-on Climate Change"; M. S. Whittingham.
- Mexican Energy Storage Network (May 21, 2021): "Model-Based Battery Management System for Current and Next-Generation Lithium Batteries"; V. R. Subramanian.
- 239th ECS Meeting, Digital Meeting (May 30 – June 3, 2021): "Robust 2D Simulation of Morphological Evolution in Lithium Metal Batteries"; T. Jang, L. Mishra, K. Shah, P. Mittal, A. Subramaniam, M. P. Gururajan, S. A. Roberts, and V. R. Subramanian.*
- Platinum Seminar Series, Monash University, Melbourne, Australia (June 2, 2021): "Sustainable Battery Chemistries for Electrical Energy Storage"; A. Manthiram.
- 239th Electrochemical Society Meeting, Chicago, Illinois (May 30 – June 3, 2021): "Low- and Zero-Cobalt Layered Oxide Cathodes for Lithium-Ion Batteries"; A. Manthiram.
- Distinguished Lecture Series, Phi Lambda Upsilon Student Organization, Kansas State University, Manhattan, Kansas (April 15, 2021): "Sustainable Battery Technologies for Renewable Energy Utilization and Vehicle Electrification"; A. Manthiram.

- European MRS (May 31, 2021): "Advanced Diagnostic Tools for Characterizing Lithium Metal Batteries and Solid-State Batteries"; Y. S. Meng.
- 239th ECS Meeting, Digital Meeting (May 30 – June 3, 2021): "Advances in Pyrolyzed Polymeric Sulfur Cathodes for Low-Cost Lithium Metal Batteries"; P. Liu.
- National Defense Industrial Association – Lithium Sulfur Battery Symposium (June 8, 2021): "Li-S Batteries with Pyrolyzed Polymer Sulfur Cathodes"; P. Liu.
- SAE International Battery Summit (June 15–16, 2021): "Going Beyond Today's Lithium-Ion Batteries"; P. Liu.
- MRS Spring Meeting (April 23, 2021): "Resolving the Controversy over the Elusive Components in Solid Electrolyte Interphase on Li Metal Anode"; E. Hu.
- DOE Office of Technology Transitions Entrepreneurship Program, Virtual Seminar (June 24, 2021): "From Fundamental Research to Technology Transfer"; J. Xiao.
- Department Seminar, University of Washington (June 2, 2021): "From Reproducible Coin Cells to Pouch Cell Design and Fabrication"; J. Xiao.
- MRS Spring Meeting, Virtual (April 21, 2021): "A Top-Down Approach to Understand and Address Fundamental Challenges in Rechargeable Lithium Metal Batteries"; J. Xiao.
- Beyond Li-Ion XIII, Argonne National Laboratory, Lemont, Illinois (June 9 – 11, 2021): "High-Throughput Diffraction Mapping of Li Metal Pouch Cell Batteries"; P. Khalifah.
- Virtual Seminar, Department of Mechanical Engineering, Massachusetts Institute of Technology (April 13, 2021): "Liquid Electrolytes for High-Voltage Lithium Metal Batteries"; W. Xu.
- ACS Spring Meeting, Virtual (April 12, 2021): "Building Advanced Electrode/Electrolyte Interphases for Stable Operation of High-Voltage Lithium Metal Batteries"; X. Ren, X. Zhang, H. Jia, X. Cao, J. Zhang, and W. Xu.*
- 239th ECS Meeting, Symposium A02 – LIBs Fast Charging, Digital Meeting (May 30 – June 3, 2021): "Can Fast Charging Rechargeable Lithium Batteries be a Reality?"; M. Li, C. Fang, Y. Zhang, B. Lu, Y. S. Meng, G. Pawar, Y. Lin, and B. Liaw.*

APPENDIX – ACRONYM GUIDE

Acronym	Full Description
1D	one-dimensional
2D	two-dimensional
3D	three-dimensional
3DOP	three-dimensionally ordered microporous
AC	alternating current
ACS	American Chemical Society
AFM	atomic force microscopy
AIMD	*ab initio* molecular dynamic
ALD	atomic layer deposition
ALS	Advanced Light Source
ANL	Argonne National Laboratory
ANN	artificial neural network
APS	Advanced Photon Source
ARL	U. S. Army Research Laboratory
ASR	area specific resistance
ASSB	all-solid-state battery
ASSLB	all-solid-state lithium battery
ASSLMB	All-solid-state lithium-metal battery
ASSLSB	all-solid-state lithium-sulfur battery
ATR	attenuated total reflectance
BE	baseline electrolyte
BEV	battery electric vehicles
β-LPS	β-phase Li_3PS_4
BNL	Brookhaven National Laboratory
BV	Butler-Volmer
CC	carbonized cotton
CCCV	constant current / constant voltage
CCD	critical current density
CE	Coulombic efficiency
CEI	cathode electrolyte interface
CMC	carboxymethyl cellulose
CMD	classical molecular dynamics
CN	coordination number
cNEB	climbing image nudged elastic band
CNT	carbon nanotube
CPE	composite polymer electrolytes
Cryo	cryogenic
cryo-FIB	cryogenic – focused ion beam
cryo-STEM	Cryogenic – scanning transmission electron spectroscopy
CSE	calendered sulfur electrodes
CV	cyclic voltammetry

Acronym	Full Description
DC	direct current
DCA	dicyanamide
DEB	double-end binding
DEMS	differential electrochemical mass spectrometry
DFE	defect formation energy
DFT	density functional theory
DIW	direct ink writing
DLR	Deutsches Zentrum für Luft- und Raumfaurt
DME	1,2-dimethoxyethane
DMSO	dimethylsulfoxide
DOE	U. S. Department of Energy
DOL	1,3-dioxolane
DOS	density of states
dP/dV	differential pressure
dPEO	dynamic bonds between polymer chains
dQ/dV	differential capacity
DRT	distribution of relaxation times
DSC	differential scanning calorimetry
E/C	Electrolyte/capacity
EC	ethylene carbonate
ECS	The Electrochemical Society
EDLi	electrochemically deposited lithium
EDS	energy dispersive X-ray spectroscopy (also known as EDX)
EELS	electron energy loss spectroscopy
eGF	exfoliated graphene fluoride
EIS	electrochemical impedance spectroscopy
eLi	engineered lithium
EMC	ethyl methyl carbonate
EMIM-BF_4	1-ethyl-3-methylimidazolium tetrafluoroborate
EPR	electron paramagnetic resonance
E/S	electrolyte/sulfur
EV	electric vehicle
EXAFS	extended X-ray absorption fine structure
FF	force field
FIB	focused ion beam
fs	femtosecond
FSI	bis(fluorosulfonyl)imide
FTIR	Fourier transform infrared
FZJ	Forschungszentrum Jülich
GB	grain boundary
gc	glass/ceramic
GDL	gas diffusion layer
GM	General Motors
GSE	glassy solid electrolyte
HAADF	high-angle annular dark-field
HCE	high-concentrated electrolyte

Acronym	Full Description
HEV	hybrid electric vehicles
HEXRD	high-energy X-ray diffraction
HOPG	highly oriented pyrolytic graphite
HPC	high-performance computing
HRTEM	high-resolution transmission electron microscopy
HT	high throughput
IL	ionic liquid
INL	Idaho National Laboratory
IR	Infrared
ISEL	Israel Electrochemical Society
ISU	Iowa State University
KB	Ketjenblack
KMC	kinetic Monte Carlo
LBNL	Lawrence Berkeley National Laboratory
LBO	Li_3BO_3
LCO	$LiCoO_2$
LE	liquid electrolyte
LFP	$LiFePO_4$
LGPS	$Li_{10}GeP_2S_{12}$
LHCE	localized high concentration electrolytes
LIC	lithium-ion conductor
LiPS	Li_7PS_6
LSiPCl	$Li_{9.54}Si_{1.74}P_{1.44}S_{11.7}Cl_{0.3}$
LLNL	Lawrence Livermore National Laboratory
LLZ	lithium – lanthanum – zirconium; also used to denote $Li_7La_3Zr_2O_{12}$
LLZO	$Li_7La_3Zr_2O_{12}$
LLZTO	Li-La-Zr-Ta-O
LMR-NMC	Li- and Mn-rich NMC
LPS	Li_3PS_4
LPSB	Li_3PS_4 + ½LiBr
LPSCl	Li_6PS_5Cl
LPSI	Li_3PS_4 + ½LiI
LSnS	$Li_{3.85}Sn_{0.85}Sb_{0.15}S_4$
LYC or LYCl	Li_3YCl_6
MC	Monte Carlo
MD	molecular dynamics
METS	multi-harmonic electrothermal spectroscopy
MGF	mixed glass former
MIC	molecular ionic composites
ML	machine learning
MOF	metal-organic framework
MOS	mixed oxy-sulfide
MOSN	mixed oxy-sulfide nitride
MPI	message-passing interface
MRS	Materials Research Society
MSD	mean square displacement

Acronym	Full Description
MSE	mean squared error
MYEGA	Mauro–Yue–Ellison–Gupta–Allan model
NaFSI	sodium bis(fluorosulfonyl)imide
NaNMC	$NaNi_{0.68}Mn_{0.22}Co_{0.10}O_2$
nano-FTIR	Fourier transform infrared nano-spectroscopy
NBR	nitrile butadiene rubber
NCM-622	$LiNi_{0.6}$-$Co_{0.2}$-$Mn_{0.2}O_2$
NCM-85105	$LiNi_{0.85}Co_{0.10}Mn_{0.05}O_2$
NCSE	non-calendered sulfur electrodes
ND	neutron diffraction
NEB	nudged elastic band
NMC	nickel – manganese - cobalt
NMC-622	$Ni_{0.6}Mn_{0.2}Co_{0.2}$
NMC-811	$Ni_{0.8}Mn_{0.1}Co_{0.1}$
NMF	nonnegative matrix factorization
NMFCN	$NaMnFeCoNiO_2$
NMR	nuclear magnetic resonance
NN	neural network
N/P ratio	capacity ratio between anode (negative electrode) and cathode (positive electrode)
NPCE	nonflammable polymer composite electrolytes
n-PDF	neutron diffraction and pair distribution function
NPT	constant number of atoms (N), pressure (P), and temperature (T)
ns	nanosecond
NVE	constant number (N), volume (V), and energy (E)
OCV	open circuit voltage
OER	oxygen evolution reaction
OMSH	ordered microporous sulfur host
ORNL	Oak Ridge National Laboratory
ORR	oxygen reduction reaction
OSU	Ohio State University
PAH	polycyclic aromatic hydrocarbon
PBDT	poly(2,2'-disulfonyl-4,4'-benzidine terephthalamide)
PC	propylene carbonate
PCA	principal component analysis
PCC	Pearson correlation coefficient
PC-LCHE	polymeric colloidal localized high concentration electrolyte
PDMS	polydimethylsiloxane
PE	polyelectrolyte, or polymer electrolyte
PEG	poly(ethylene glycol)
PEGDA	poly(ethylene glycol) diacrylate
PEGMA	poly(ethylene glycol) methacrylate
PEO	Poly(ethylene oxide)
PES	photon emission spectroscopy
PETEA	pentaerythritol tetraacrylate (PETEA
PFIB	plasma focused ion beam

Acronym	Full Description
PFG	pulsed field gradient
PGE	polymer gel electrolyte
PHEV	plug-in hybrid electric vehicle
PI	principal investigator
PMMA	polymethyl methacrylate
PNNL	Pacific Northwest National Laboratory
POSS	polyhedral oligomeric silsesquioxane
PS-SEI	polymer-supported solid electrolyte interphase
PSU	Pennsylvania State University
PTFE	polytetrafluoroethylene
pTFSI	triflimide-based polyion
PVDF	polyvinylidene (di)fluoride
Py	pyrrolidinium
RDF	radial distribution function
ReaxFF	reactive force field
RF	random forest
rGO	reduced Gr oxide
RMSE	root mean square error
RP	red phosphorus
RPT	reference performance tests
SAXS	small angle X-ray scattering
SE	solid electrolyte
SEB	single-end binding
SEI	solid electrolyte interphase
SEM	scanning electron microscopy
SEO	polystyrene-*b*-poly(ethylene oxide) block copolymer
SIC	single ion conductor
SIL	solvate ionic liquid
SLAC	Stanford Linear Accelerator Center
SOC	state of charge
SPAN	sulfurized polyacrylonitrile
SPE	Solid Polymer Electrolyte
SPM	scanning probe microscopy
SQUID	superconducting quantum interference device
SSB	solid-state battery
SSE	solid-state electrolyte
SSI	Solid-state ion
SSLB	solid-state lithium batteries
SSLMB	solid-state Li-metal batteries
SSRL	Stanford Synchrotron Radiation Lightsource
STEM	scanning transmission electron microscopy
SWCNT	single walled carbon nanotube
TEGDME	tetraethylene glycol dimethyl ether
TEM	transmission electron microscopy
TEMPO	2,2,6,6-tetramethyl-1-piperidinyloxy
TEP	triethyl phosphate

Acronym	Full Description
TFC	thin-film composite
TFSI	trifluoromethanesulfonimide
TGA	thermal gravimetric analysis
TGC	Titration Gas Chromatography
TM	transition metal
TMD	Transition metal dichalcogenide
TOF-SIMS	time-of-flight secondary ion mass spectrometry
TRL	technology readiness level
TXM	transmission X-ray microscopy
UCB	University of California, Berkeley
UCSD	University of California, San Diego
UH	University of Houston
UM	University of Michigan
UMD	University of Maryland
UT	University of Texas
UV	ultraviolet
UW	University of Washington
VASP	Vienna *ab initio* simulation package
VBM	Valence band maximum
VTO	Vehicle Technologies Office
XANES	X-ray absorption near edge structure
XAS	X-ray absorption spectroscopy
x-PDF	synchrotron X-ray diffraction and pair distribution function
XPS	X-ray photoelectron spectroscopy
xPEO	crosslinked PEO
XRD	X-ray diffraction
XRF	X-ray fluorescence
XRT	X-ray tomography